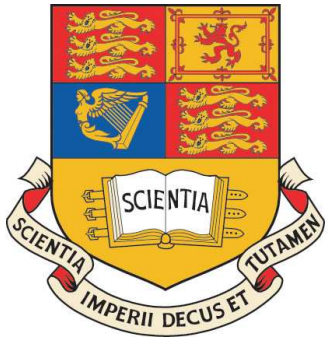
Martensitic transformation in TiNi based shape memory alloys – a first principles study



Appala Naidu Gandi

Department of Materials

Imperial College London

A thesis submitted for the degree of

Doctor of Philosophy

December 7, 2012

Supervisors: Professor Mike Finnis and Dr. David Dye

Abstract

The martensitic transformation in TiNi-based shape memory alloys has been investigated using various theoretical methods. The direct method for *ab initio* lattice dynamics is used for calculating phonon dispersion relations in austenite (B2) and martensites (B19, B19′). Normal mode symmetries in a B2 crystal are determined. Vibrational modes in the B2 crystal are labelled according to symmetry properties of their polarisation vector. Normal modes with imaginary frequencies are observed at the locations of experimentally observed soft modes. While labelling normal modes, the published mode symmetry label of a soft transverse acoustic (TA_2) mode with a $\langle 1\bar{1}0\rangle$ polarisation at $\frac{2\pi}{a}[\frac{1}{3}, \frac{1}{3}, 0]$ is corrected to Σ_2. Irreducible representations of the soft modes are used for determining the order parameters for various martensitic transformation paths experimentally observed using group theoretical methods. Accuracy of the interpolated frequencies in the phonon dispersion relations is assessed by using three different supercell sizes and by calculating the elastic constants from the slopes of the acoustic branches at the Brillouin zone.

Born et al. derived a relation between the force constants and elastic constants for a general crystal. Further simplification of this relation is possible for a B2 crystal because of its symmetry. This simplification is derived by applying elementary group theory. Elastic constants calculated with the simplified relation are in agreement with the elastic constants calculated from the slopes of the dispersion relations.

The self-consistent *ab initio* lattice dynamics (SCAILD) formulation is derived for an ordered compound. Precautions that need to be taken while practically implementing this formulation are discussed.

The effect of Hf or Zr addition to a binary Ti-Ni system is studied by considering one configuration at each of five compositions from 0 to 25 at.% Hf or Zr. Elastic constants are calculated following a

homogeneous deformation method. Selected normal mode frequencies are calculated using the direct method.

Declaration of Originality

I hereby declare that this thesis and the work reported herein was composed by and originated entirely from me. Information derived from the published and unpublished work of others has been acknowledged in the text and is presented as a list in the references.

Appala Naidu Gandi,
December 7, 2012.

To my parents

Acknowledgements

I thank Professor Mike Finnis for giving me an opportunity to study under his supervision. I learnt a lot during discussions with him. His way of addressing every issue that come across while solving a problem is very impressive. And it gave me a lot of motivation, especially when things are not going according to the plan. Also, I thank him for giving me the freedom to work in different directions without constraining in one direction. I would like to thank my co-supervisor Dr. David Dye for guidance and constant support. I am grateful to the UK India Education and Research Initiative (UKIERI) for sponsoring this project.

I would like to acknowledge all the people who directly or indirectly worked on the studies described in the references. All their efforts helped me to understand the problem at hand more clearly.

I thank all my friends and staff in Thomas Young centre for providing a friendly environment during my stay at Imperial College. I am thankful to teachers at Indian Institute of Science, Bangalore for their teachings and guidance, which encouraged me to pursue a PhD.

I would like to thank all my friends in London, Kondala Rao, Ravi, Suresh Dayanithi, Isaac Anand, and Mahadevan Krishnan, who gave me an enjoyable company and support.

I am indebted to my parents, Naidu and Kanaka Maha Laxmi, for providing me constant encouragement and allowing me to pursue my goals. I am very thankful to them for giving this freedom. I would like to thank both my lovely sisters, Rama devi and Suryakala, for their support, love and encouragement.

Contents

Contents vi

List of Figures ix

List of Tables xii

Nomenclature xiv

1 Introduction 1

1.1 Overview of the thesis . . . 5

2 Literature review 7

2.1 Structure of austenite . . . 8

2.2 Structure of martensites . . . 9

2.3 Softening of a normal mode . . . 13

2.3.1 Experiments . . . 13

2.3.2 DFT studies . . . 17

2.3.3 Electron-phonon interactions . . . 17

2.3.4 Phonon-phonon interactions . . . 20

2.4 Elastic softening . . . 21

2.4.1 Theoretical studies . . . 24

2.5 Ternary alloys . . . 24

3 Theoretical methods 31

3.1 Density Functional Theory (DFT) . . . 34

3.1.1 Hohenberg-Kohn theorems . . . 35

3.1.2 Kohn-Sham equations . . . 36

3.1.3 The exchange-correlation functional . . . 39

3.1.4 Pseudopotential approximation . . . 43

3.1.5 Projector augmented wave method . . . 44

3.1.6 Periodicity . . . 47
3.1.7 Forces on atoms . . . 50
3.2 Lattice dynamics in the harmonic approximation . . . 51
3.2.1 Small displacement method . . . 54
3.2.1.1 Periodicity of the supercell . . . 56
3.2.1.2 Dynamical matrix and dispersion relations . . . 56
3.2.1.3 Thermodynamic properties . . . 57
3.2.1.4 Elastic constants from dispersion relations . . . 59
3.2.1.5 Force constants and elastic stiffness tensor elements 60
3.2.2 Soft mode analysis with group theory . . . 65
3.3 Self consistent *ab initio* lattice dynamics (SCAILD) . . . 66
3.4 Homogeneous deformation method . . . 71

4 Results: binary alloys 74
4.1 Structure relaxation . . . 75
4.1.1 B2 . . . 75
4.1.2 B19 . . . 76
4.1.3 B19′ . . . 76
4.1.4 R . . . 77
4.2 Electronic properties . . . 79
4.2.1 Fermi surface . . . 82
4.3 Homogeneous deformation . . . 83
4.4 Harmonic phonon dispersion relations . . . 87
4.4.1 B2 . . . 87
4.4.2 B19 . . . 98
4.4.3 B19′ . . . 100
4.5 SCAILD method implementation . . . 103

5 Results: ternary alloys 108
5.1 Simulation details and lattice parameters . . . 109
5.2 Electronic properties . . . 110
5.3 Elastic constants . . . 114
5.4 Phonon dispersion . . . 118

6 Conclusions and outlook 123
6.1 Conclusions . . . 123
6.2 Outlook . . . 126
6.2.1 A Gaussian approximation potential (GAP) . . . 126

6.2.2 Self consistent harmonic approximation 127
6.2.3 Thermodynamic integration 129

A Normal mode symmetries in a CsCl crystal **130**
A.1 Irreducible representations 130
A.2 Compatibility relations 136

B Homogeneous deformation method **138**
B.1 Bulk modulus calculation 140
B.2 C' calculation 140
B.3 C_{44} calculation 141

References **142**

List of Figures

1.1 Schematic representation of a one way shape memory effect. . . . 2
1.2 Schematic representation of different temperatures associated with the martensitic transformation. . . . 3
1.3 Schematic representation of superelasticity observed during loading and unloading of a shape memory alloy. . . . 3

2.1 Binary Ti-Ni equilibrium phase diagram. . . . 8
2.2 Martensitic transformation temperatures as a function of Cu content in Ti-Ni-Cu alloys. . . . 11
2.3 Schematic unit cells of different phases involved in the martensitic transformation. . . . 12
2.4 Normal mode softening observed in the B2 of TiNi-based alloys as the alloys are cooled towards the M_s. . . . 15
2.5 Elastic softening observed in TiNi-based shape memory alloys. . . . 22
2.6 Isothermal section of the ternary Ti-Ni-Zr phase diagram at 700 °C. 26
2.7 Pseudobinary sections: NiTi-NiZr, HfNi-NiTi. . . . 26
2.8 Martensitic peak temperatures as a function of Hf in $Ti_{51-x}Ni_{49}Hf_x$ alloys. . . . 27
2.9 Martensitic start temperatures as a function of Zr in $Ti_{50-x}Ni_{50}Zr_x$ alloys. . . . 28

3.1 Schematic representation of separating the sum over unit cells into sum over co-ordination polygons. . . . 62

4.1 Total density of states in four structures. . . . 80
4.2 Electronic band structure in four phases. . . . 81
4.3 Electronic band structure in B2 calculated using the *Quantum Espresso*. . . . 82

4.4 Fermi surfaces of band 15 (green contours) and band 16 (blue contours) in a B2. . . . 83
4.5 Cross-sections of Fermi surfaces correspond to band 15 and band 16 at $k_z = 0.0$. . . . 84
4.6 Cross-sections of Fermi surfaces correspond to band 15 and band 16 at $k_z = 0.0769$. . . . 84
4.7 The energy variation with strain from different calculations for determining the elastic tensor elements. . . . 86
4.8 The stress variation with strain from different calculations for determining the elastic tensor elements. . . . 86
4.9 Phonon dispersion relations in a B2 obtained from 2×2×2 supercell calculations. . . . 90
4.10 Atomic displacements corresponding to a transverse acoustic mode (TA_2) at a wave vector $\frac{2\pi}{a}[\frac{1}{2}, \frac{1}{2}, 0]$. . . . 90
4.11 Phonon dispersion relations in a B2 obtained from 3×3×3 supercell calculations. . . . 96
4.12 Phonon dispersion relations in a B2 obtained from 4×4×4 supercell calculations. . . . 97
4.13 Squared frequencies of vibrational modes in B2 at exact wave vectors as a function of volume. . . . 98
4.14 First Brillouin zone of a B19 ($Pmcm$) and labels of high symmetry points in it. . . . 99
4.15 Phonon dispersion relations in B19 along $[\xi, 0, 0]$, $[0, \xi, 0]$, and $[0, 0, \xi]$ directions. . . . 101
4.16 Phonon dispersion relations in B19 along $[\xi, \xi, 0]$, $[\xi, 0, \xi]$, $[0, \xi, \xi]$, and $[\xi, \xi, \xi]$ directions. . . . 101
4.17 First Brillouin zone of a B19′ and labels of high symmetry points in it. . . . 102
4.18 Phonon dispersion relations in B19′ along $[\xi, 0, 0]$, $[0, \xi, 0]$, and $[0, 0, \xi]$ directions. . . . 102
4.19 Phonon dispersion relations in a B19′ along $[\xi, \xi, 0]$, $[\xi, 0, \xi]$, $[0, \xi, \xi]$, and $[\xi, \xi, \xi]$ directions. . . . 103
4.20 Order parameters of various martensitic transformation paths in TiNi-based shape memory alloys. . . . 104
4.21 Phonon dispersion in B2 at 350 K from calculations done using a 2×2×2 supercell. . . . 106
4.22 Vibrational free energy as a function of iteration number. . . . 107

5.1 Possible configurations in the Ti sub-lattices of a β' or a β_1 supercell as a function of alloying. 110
5.2 Density of states in the β_1 as a function of Hf content. 111
5.3 Spin-up density of states at the Fermi level in a β_1 or a β'phase as a function of ternary alloying. 112
5.4 Density of states in the β' as a function of Zr content. 113
5.5 Energy variation as a function of strain in different elastic constants calculations in austenite of $Ti_{50-x}Ni_{50}Hf_x$ alloys as a function of Hf content. 115
5.6 Energy variation as a function of strain in different elastic constants calculations in austenite of $Ti_{50-x}Ni_{50}Zr_x$ alloys as a function of Zr content. 116
5.7 Bulk modulus as a function of Hf or Zr content in ternary alloys. . 116
5.8 C′ as a function of Hf or Zr content in ternary alloys. 117
5.9 C_{44} as a function of Hf or Zr content in ternary alloys. 117
5.10 Dispersion relations in β_1 phase as a function of Hf content. . . . 119
5.11 Dispersion relations in β' phase as a function of Zr content. 120
5.12 Soft mode frequency as a function of Hf or Zr content in ternary alloys. 121

A.1 First Brillouin zone of a B2 crystal and labels of high symmetry points in it. 132

List of Tables

4.1 Structural parameters of a B19 unit cell 76
4.2 Structural parameters of a B19′ unit cell 77
4.3 Structural parameters of a R unit cell 78
4.4 Total energies of the equilibrium structures 79
4.5 Total spin-up density of states at the Fermi level in different structures 81
4.6 Elastic tensor elements of austenite calculated by following the homogeneous deformation method and from the literature 85
4.7 Exact wave vectors in the first Brillouin zone of a B2 in different supercell calculations 89
4.8 Order parameters for a $Pm\bar{3}m$(B2) $\xrightarrow[\Gamma_1^+,\Gamma_3^+,\Gamma_5^+]{M_5^-}$ $Pmma$(B19) transition 91
4.9 Order parameters for a $Pm\bar{3}m$(B2) $\xrightarrow[\Gamma_1^+,\Gamma_3^+,\Gamma_5^+]{M_5^-}$ $P2_1/m$(B19′) transition 92
4.10 Relationship between wave propagation velocities of the acoustic modes at the zone center and elastic constants in a cubic crystal . 93
4.11 Possible transition paths in TiNi-based shape memory alloys due to the soft mode instability at $\frac{2\pi}{a}[\frac{1}{3},\frac{1}{3},0]$ and corresponding primary order parameters 95
4.12 Secondary order parameters for the four transition paths in Table(4.11) 95
4.13 Elastic constants of a B2 calculated from the slopes of the dispersion relations. 97
4.14 Order parameters for a $Pmcm$(B19) $\xrightarrow[3\Gamma_1^+]{\Gamma_3^+}$ $P2_1/m$(B19′) transition 100

5.1 Lattice parameters of ternary supercells as a function Hf content in $Ti_{50-x}Hf_xNi_{50}$ alloys 112
5.2 Lattice parameters of ternary supercells as a function Zr content in $Ti_{50-x}Zr_xNi_{50}$ alloys 112

A.1 Character table for irreps at Γ 133
A.2 Character table for irreps at R 133
A.3 Character table for irreps at M 134
A.4 Character table for irreps at X 134
A.5 Character table for irreps at $\frac{2\pi}{3a}[1,1,0]$ 135
A.6 Character table for irreps at $\frac{2\pi}{3a}[0,1,0]$ 136
A.7 Character table for irreps at $\frac{2\pi}{3a}[1,1,1]$ 136
A.8 Compatibility relations at Γ for representations in B2 crystals . . 136
A.9 Compatibility relations at X for representations in B2 crystals . . 137
A.10 Compatibility relations at M for representations in B2 crystals . . 137
A.11 Compatibility relations at R for representations in B2 crystals . . 137

B.1 Equivalence of indices in the tensor notation and the matrix notation 138

Nomenclature

Acronyms

AE	All electron
BCC	Body centred cubic
BCO	Base-centred orthorhombic
BZ	Brillouin zone
DFT	Density functional Theory
DOS	Density of states
FBZ	First Brillouin zone
FLAPW	Full-potential linearised augmented plane wave
GAP	Gaussian approximation potential
GGA	Generalised gradient approximation
GOT	Grand Orthogonality Theorem
HA	Harmonic approximation
HTSMA	High temperature shape memory alloy
IFC	Inter-atomic force constant
Irrep	Irreducible representation
KS	Kohn-Sham
LA	Longitudinal acoustic
LDA	Local density approximation
LSD	Local spin density
MT	Martensitic transformation
PAW	Projector augmented wave
PS	Pseudo
QE	Quantum Espresso
QHA	Quasi-harmonic approximation
SCAILD	Self-consistent *ab initio* lattice dynamics
SCHA	Self-consistent harmonic approximation

SE	Schrödinger equation
SMA	Shape memory alloy
SME	Shape memory effect
TA	Transverse acoustic
TEM	Transmission electron microscopy
VASP	Vienna *ab initio* Simulations Package

Symbols

$\mathbf{a}$	Vector representing unit cell axis
A	Anisotropic factor
$\mathbf{A}$	Vector representing supercell axis
$\mathrm{A_s}$	Reverse transformation start temperature
$\mathrm{A_f}$	Reverse transformation finish temperature
$\mathbf{b}$	Vector representing reciprocal unit cell axis
$\mathbf{B}$	Vector representing reciprocal unit cell axis of a supercell
C_{ij}	Elastic modulus tensor in Voigt notation
C_{ijkl}	Elastic modulus tensor
$C_{\alpha\beta}(\mathbf{k}_{ss'})$	Dynamical matrix
$D_{\alpha\beta}(\mathbf{k}_{ss'})$	Dynamical matrix
e_{ij}	General strain tensor
$\mathbf{e}$	Polarisation vector
ϵ_0	The permittivity of vacuum
ϵ_i	Single orbital energies
ϵ_{ij}	Symmetric strain tensor
E	Total energy of a system
E_F	Fermi level
$f(x)$	Fermi distribution function
F	Helmholtz free energy of a system
$\mathbf{F}_\mathrm{I}$	Force on an atom I
$g^{\alpha}_{\mathbf{k}\mu,\mathbf{k}+\mathbf{q}\mu'}$	Fully renormalized self-consistent electron-phonon-interaction matrix element
$G(\mathbf{k}_j)$	Random Gaussian variable
$\hbar$	Plank's constant$\times\frac{1}{2\pi}$
$\hat{\mathcal{H}}$	Hamiltonian operator
j	Normal mode index

k_{B}	Boltzmann constant
$\mathbf{k}$	Wave vector
$\binom{\mathbf{k}}{j}$	Normal mode j at a wave vector $\mathbf{k}$
l, l'	Unit cell index in a supercell
$\binom{l}{s}$	s atom in the unit cell l
m	Mass of an electron
m_s	Mass of the s atom in the unit cell
$\mathrm{M_s}$	Martensitic transformation start temperature
$\mathrm{M_f}$	Martensitic transformation finish temperature
$\mathrm{M_d}$	Maximum possible martensitic transformation temperature under the application of stress
$n(x)$	Bose-Einstein distribution function
N	Number of unit cells in a supercell or Number of electrons in a system
$\mathbf{q}$	Wave vector
Q	Amplitude of a normal mode
s, s'	Atom in the basis of a unit cell
S	Entropy of a system
T	Temperature
$\mathrm{T_0}$	Equilibrium temperature at which both austenite and martensite have the same free energy
$\Delta\mathrm{T}$	Under cooling
$\hat{T}$	Kinetic energy operator
$\hat{\mathfrak{T}}$	Linear transformation operator
$\mathbf{u}$	Displacement vector
$v(\mathbf{r})$	Potential due to nuclei at a point $\mathbf{r}$
xc	Exchange and correlation
$\mathbf{x}$	Position vector
$\mathbf{y}$	Reciprocal lattice vector
Z	Partition function
Z_I	Charge of a nucleus I
0	Ground state

Greek symbols

$\alpha, \beta, \gamma,$	Cartesian directions
λ, ν	Cartesian directions

$\varepsilon_{\mathbf{k}\mu}$	Electronic eigenvalue at a wave vector $\mathbf{k}$ and in the band μ
$\rho(\mathbf{r})$	Electron density at a point $\mathbf{r}$
μ	Lagrange multiplier
ϕ_i	Single orbital wave functions
$\|\phi_i\rangle$	All electron partial waves
$\|\tilde{\phi}_i\rangle$	Smooth pseudo partial wave
Ψ	Many-body wave function
$\|\Psi_n^v\rangle$	Full one-electron wave function
$\|\tilde{\Psi}_n^v\rangle$	Smooth one-electron pseudo wave function
Φ	Potential energy
$\Phi_{\alpha\beta}$	Second order inter-atomic force constant
ω	Angular frequency
$\tilde{\omega}$	Renormalised angular frequency
$\bar{\omega}$	Symmetrised angular frequency
Ω	Volume of a unit cell
ϖ_{ij}	Anti-symmetric strain tensor

Chapter 1

Introduction

Shape memory alloys (SMAs) are a class of functional materials that can exhibit the *shape memory effect* (SME) and *superelasticity* [1]. Due to the presence of metallic bonds, these alloys have good strength, ductility, and other mechanical properties that make them suitable for structural applications. In addition, SMAs revert to a trained shape when heated to a certain temperature range. It is this ability of certain materials to regain the trained shape that is defined as the shape memory effect [2, 3]. It is a macroscopic effect of a thermally induced phase transformation. To exploit this phenomenon an additional function is added to a SMA structure by a suitable design. Both the SME and its related phenomenon of superelacticity are based on the same underlying kind of phase transformation, namely a *martensitic transformation* (MT), as described below.

The two phases involved in a MT are referred to as austenite and martensite. The austenite is a higher symmetry phase and is stable at higher temperatures, the martensite has a lower symmetry and is stable at lower temperatures. On cooling the austenite, the temperature at which it starts to undergo a MT is designated M_s and the temperature at which the MT completes during cooling is known as M_f. By its definition a MT is a diffusionless, first order transition. During the MT shearing and shuffling of atomic planes occur at very high velocities. A set of equivalent martensite crystals of different orientations, known as *variants*, forms the product phase. These variants are accommodated in such a way that the overall strain of the material is minimised, and are hence referred to as the *self-accommodating* variants. For this reason the macroscopic shape of the material will not change, although there is a change in its crystal structure.

The SME works as follows. The martensite can be deformed to another shape by applying a suitable stress. During this process reorganisation of the variants

may occur such that variants that are favourably oriented grow at the expense of others. Now if the material is heated after deformation, it will transform into the austenitic structure. The temperature at which this reverse transformation starts is designated A_s and its finish temperature is designated A_f. At A_f the heated material will have regained its original shape. This is known as a one way SME. It is schematically shown in Fig.(1.1) and various temperatures associated with the MT are shown in Fig.(1.2).

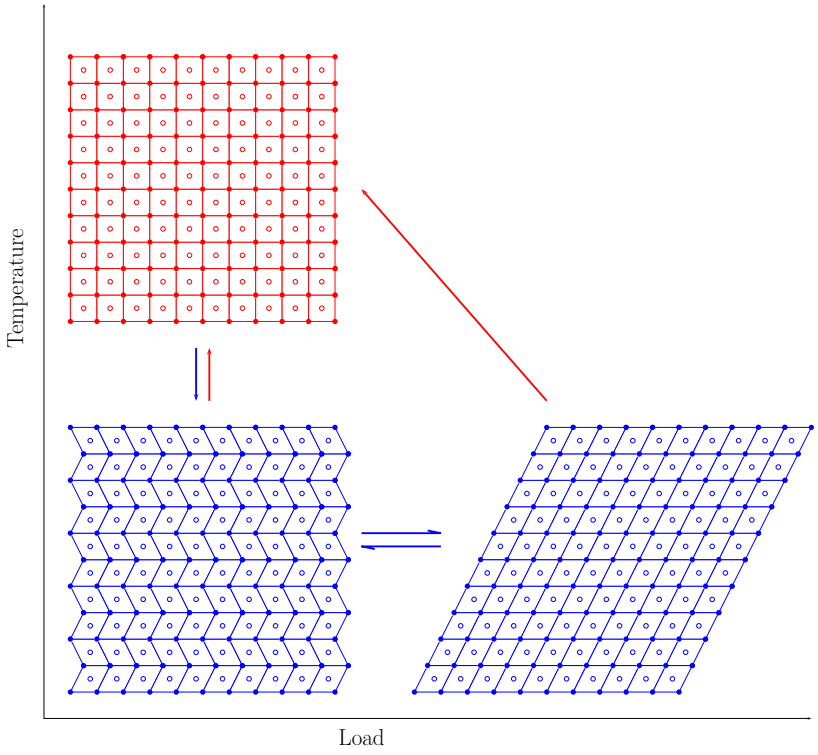


Figure 1.1: Schematic representation of a one way shape memory effect.

The superelasticity is closely related. Even at temperatures above A_f, where the austenite phase is stable, it is possible to cause the MT by applying stress. The austenite deforms elastically until the stress reaches a critical value, at which point the material starts to deform without any further increase in the stress level as the MT proceeds. The pseudoelastic deformation increases until the MT is complete. It is observed as a plateau in the stress-strain curves. The strains associated with this process are known as transformation strains. Transformation strains as high as 8% are observed in Titanium-Nickel based SMAs [2]. All strains, both elastic and transformation, will disappear on unloading. This is the phenomenon known

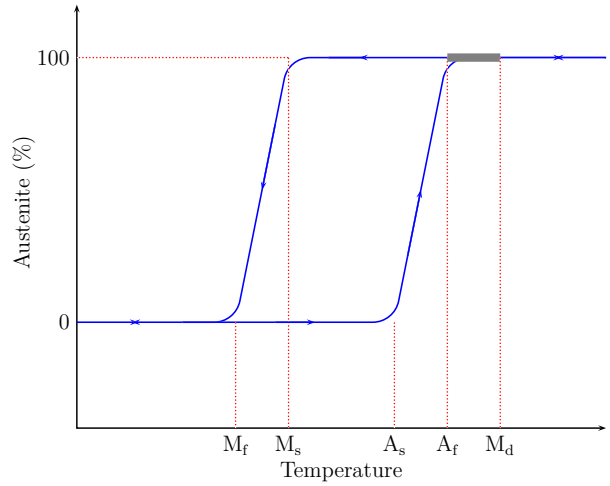


Figure 1.2: Schematic representation of different temperatures associated with the martensitic transformation.

as superelasticity and it is schematically illustrated in Fig.(1.3). Only variants which are favourably oriented to the applied stress are formed during the loading cycle. In this respect, the superelasticity is different from the SME where all the variants have the same probability of forming during the MT.

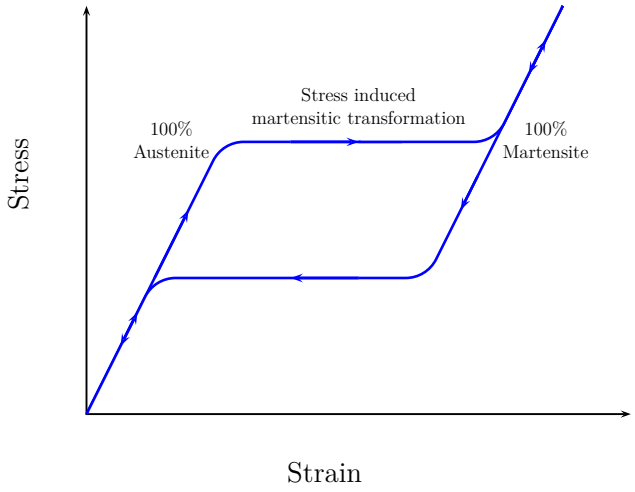


Figure 1.3: Schematic representation of superelasticity observed during loading and unloading of a shape memory alloy.

The critical stress required to initiate the superelasticity increases with increase in temperature as the relative stability of austenite increases with increase in temperature. When the critical stress reaches the yield strength of austenite,

the austenite starts to deform plastically and the superelasticity is not observed. The maximum temperature at which the superelasticity is observed is denoted M_d. The temperature range in which the superelasticity is observed is marked with a shaded gray region in Fig.(1.2) from A_f to M_d.

Transformation strains are also observed in temperature induced MT. But during a MT induced purely by cooling, different variants of martensite are accommodated in such a way that the macroscopic strain is negligible. Since the MT can be induced either by cooling or application of stress, it is also known as a thermoelastic phase transition [4].

The ability of some materials to revert to one shape when heated to a temperature above A_f and another shape when cooled to a temperature below M_f is known as a two-way SME. Thermomechanical treatments are used to impart the two way SME to SMAs [2]. In these treatments, known as training methods, the precipitates are nucleated and aligned in such a way that of all the possible variants of martensite only a few variants are preferentially formed during the MT. An oriented stress field associated with the precipitates helps in forming the trained shape when cooled below the M_f temperature.

Arne Ölander discovered a rubber-like elasticity in a Au-Cd alloy in 1932 [5]. Following this discovery, Ölander [6] and Byström [7] tried to identify various phases in the Au-Cd system and establish the Au-Cd phase diagram. These studies mark the beginning of attempts to understand the SME and the superelasticity. Since then many alloys, including Ti-Ni based alloys, exhibiting the SME and the superelasticity were discovered and studied. Buehler et al. observed that alloys with compositions near the equiatomic compound TiNi show unusual changes in dimensional and damping characteristics around 65 °C [8] .

Of all the alloys exhibiting the SME, TiNi-based shape memory alloys have the best combination of strength with ductility and can be formed into any desired shape [9]. Due to the presence of precipitates like Ti_2Ni, $TiNi_3$ and other metastable precipitates in the TiNi system it is possible to impart a wide range of mechanical properties to these alloys by thermomechanical treatments. TiNi-based SMAs can also be engineered to exhibit the two-way SME. These factors make the TiNi-based SMAs a good choice for practical applications, mainly in actuation and sensing [10]. TiNi-based alloys also have good bio-compatibility [11] and hence are used in many bioengineering and biomedical applications [12].

The temperature range in which the MT occurs is primarily determined by the composition of the alloy. Therefore, the composition decides the temperature range in which the SME can be applied. Binary Ti-Ni alloys have a maximum

M_s of 60 °C [3]. Pd, Pt,Au, Zr, and Hf additions increase the MT temperatures [10], while Fe, Co, V, Cr, Al, and Mn additions decrease the MT temperatures of TiNi-based SMAs [3]. Alloying addition also affects the structure of the martensite phase, hysteresis during the MT, strength, ductility, creep resistance, and corrosion resistance in Ti-Ni based SMAs. Otsuka et al. [3] have reviewed the experimental and theoretical studies carried to understand the MT in TiNi-based SMAs. Roland Noebe et al. [10] have reviewed the properties, applications, and potential applications of high temperature SMAs (HTSMAs).

Experimental studies determine various properties of a material as a function of composition, temperature, pressure, heat treatment, and thermomechanical history of the alloy. Results from the experimental studies are generally used for designing the processing methods, and determining practical applications of materials. On the other hand atomic level understanding of the MT can provide better insight into the relationship between the composition and properties of the material. It is experimentally verified that Pd, Pt,Au, Zr, and Hf addition increases the MT temperatures [10], but the exact changes these ternary additions cause at the atomic level are not known. Understanding of the MT in ternary alloys at atomic level is important for designing a HTSMA. Hf and Zr based HTSMAs are generally chosen for practical purposes because of their lower cost when compared to precious metal (Pt, Pd, Au) based alloys. Hence, the present study is carried on Hf, Zr based ternary alloys.

In the present work theoretical methods, primarily based on electronic structure calculations, have been used to further the understanding of the MT in Ti-Ni based SMAs. This study has two broad objectives:

- to understand the MT in binary Ti-Ni alloys,
- to study the effect of Hf and Zr addition to a binary Ti-Ni system.

We hoped that the results from this study would provide some useful inputs for designing the HTSMAs.

1.1 Overview of the thesis

This thesis is organised in the following way. In the Chapter 2, the structure of various phases involved in the MT are reviewed. The elastic properties and vibrational spectrum of the austenitic structure change in characteristic ways as the MT is approached from above. Experimental results related to elastic

softening and softening of phonon modes in TiNi-based SMAs are also presented the Chapter 2. Literature relevant to the Hf and Zr based HTSMAs is also reviewed in this chapter.

Density functional theory (DFT) codes have been used for performing electronic structure calculations. The principles of DFT, and various approximations made to implement DFT for calculating the properties of TiNi-based SMAs are presented in the Chapter 3. In Chapter 3 the homogeneous deformation method for calculating the elastic constants of crystals is described together with the finite displacement method for studying the lattice dynamics in crystals. The relationship between the methods is discussed, some shortcomings of the methods for calculating phonon spectra are elucidated. I investigate the discrepancy between the long-wavelength limit of calculated phonon dispersion curves and the corresponding elastic moduli and suggest how phonon frequencies can be obtained more accurately by judicious sampling of k-space. The use of group theoretical methods for assigning the symmetries of vibrational modes is discussed.

Results of the electronic structure calculations on binary TiNi system are presented in the Chapter 4. These results include electronic band structures, density of states, elastic constants, and phonon dispersion relations of various phases. Soft modes are identified in the calculated phonon dispersion relations. Symmetry of the soft modes are used for suggesting various MT paths in TiNi-based SMAs.

The effect of Hf and Zr additions on elastic constants and lattice dynamics is also studied. Results from these calculations are presented in the Chapter 5. Conclusions and outlook are described in the Chapter 6. Appendices are included to describe some mathematical details not previously derived or not readily available in the literature, including the relevant character tables for assigning the correct symmetry to normal modes.

Chapter 2

Literature review

The austenite phase has a CsCl type (B2) structure [13]. As suggested by Zener [14], more open body centered cubic structures have very low resistance to a $\{110\}\langle 1\bar{1}0\rangle$ shear and transform into close packed structures at low temperatures. Atomic vibrations at high temperature contribute largely to the entropy and stabilise these structures at high temperatures. As the alloy is cooled towards the M_s, the frequency of a particular mode of vibration decreases noticeably. This phenomenon is known as softening of a normal mode and the mode of vibration involved in this softening is known as the soft mode. When the soft mode frequency becomes zero, the structure become unstable to the atomic vibrations of the soft mode and a phase transition occurs. The short wave length lattice modulations of the soft mode, known as shuffle deformation [15], determine the structural information of the product phase. If there is a coupling between the soft mode and other modes of atomic vibrations, this coupling also determines the resulting structure.

Structures of various phases involved in the MT in TiNi-based SMAs are reviewed in the first section. Before the MT, some changes occur in the austenite phase. These changes decrease the stability of austenite. Experimentally these changes are observed as precursor phenomena to MT [3]. These phenomena include elastic softening, appearance of elastic peaks, softening of a mode of atomic vibration. Literature relevant to the normal mode softening and the elastic softening is reviewed in next sections. Results from the first principle electronic structure methods relevant to the present study are also reviewed. Literature relevant to the MT in ternary Ti-Ni-Hf and Ti-Ni-Zr alloys is discussed in the last section.

2.1 Structure of austenite

TiNi phase is an intermetallic compound. As can be seen from the phase diagram in Fig.(2.1), it undergoes a disorder to order transition at 1090 °C while cooling. The ordered phase involved in this transition is known as austenite. The austenite have a cubic symmetry. Its space group is $Pm\bar{3}m$. Philip et al. [16] first determined the structure of an ordered TiNi phase to be a B2 structure. They determined the lattice parameter of the austenite phase to be 3.015 Å at room temperature. Later, Chandra et al. [17] obtained X-ray diffraction patterns from an ordered phase in a Ti-50 at.% Ni alloy at 100 °C. By analysing the diffraction patterns, they also confirmed the structure of the TiNi as a B2 structure. Each unit cell contains two atoms: one Ni atom, and one Ti atom. Its basis is $(0, 0, 0)$ and $(\frac{1}{2}, \frac{1}{2}, \frac{1}{2})$.

Austenite, in all TiNi-based SMAs, transforms into a martensitic phase or an intermediate phase on further cooling due to soft mode instability. Structure of various phases formed due to the soft mode instability in various SMAs based on TiNi are reviewed in the next section.

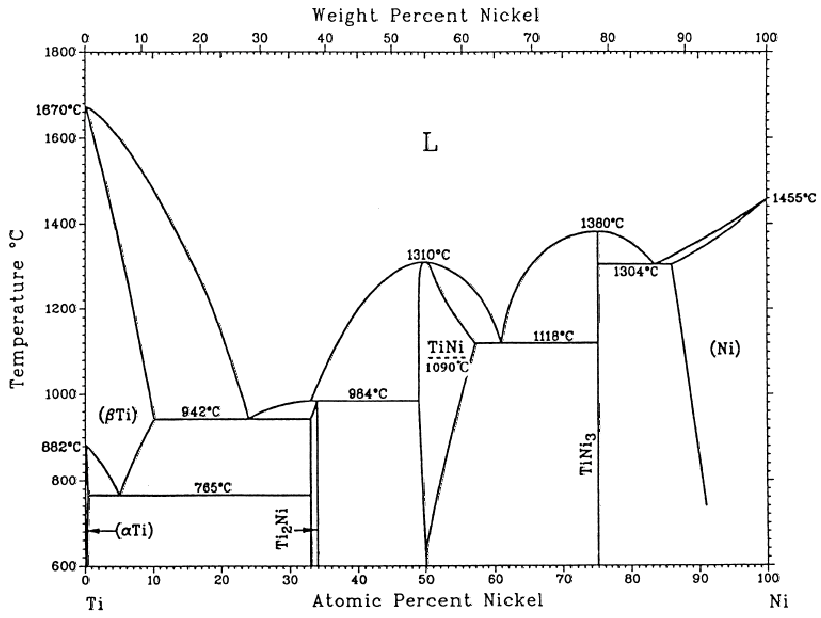


Figure 2.1: Binary Ti-Ni equilibrium phase diagram [18] as cited by Otsuka et al. [19].

2.2 Structure of martensites

Structure of the martensite depends on the soft mode characteristics, composition of the alloy, and thermomechnanical history of the alloy [3]. Product phases with trigonal, orthorhombic, and monoclinic symmetry were observed experimentally in TiNi-based SMAs. Structure of these phases are described in this section.

Monoclinic structure (B19′)

Ground state structure of TiNi-based binary SMAs have a monoclinic symmetry [3]. B19′ is formed during single stage MT observed in solutionised and quenched alloys. Austenite reaches ground state structure in two stages in cold worked and annealed alloys [20] or aged binary alloys [21]: B2 → trigonal phase → B19′. In these alloys B19′ is formed in the second stage during cooling from an intermediate phase, known as R phase, with a trigonal symmetry. The R observed in TiNi-based SMAs is reviewed in the next subsection.

Bührer et al. [22] used a neutron diffraction method to establish the structure of martensite observed in a Ni-50.7at% Ti alloy. They have determined the M_s temperature as 340 K by measuring electrical resistivity of the alloy as a function of temperature. This alloy was annealed at 1270 K and quenched in the water. The martensite diffraction pattern was obtained at 10 K. Its structure was found to be monoclinic with space group $P2_1/m$. Later Kudoh et al. [23] confirmed the structure of a B19′ phase by studying the X-ray diffraction patterns from a single martensitic crystal. The single crystal of martensite was formed by stress induced MT in a Ni-50.8at%Ti alloy. The unit cell has four atoms. In equiatomic TiNi alloy, they are : two Ni atoms, and two Ti atoms.

Trigonal structure (R)

As can be seen from the equilibrium phase diagram in Fig.(2.1), TiNi phase has more solubility for Ni than Ti. TiNi phase in off-stoichiometric Ni rich alloys decomposes into $TiNi_3$ and TiNi phase mixture on reaching equilibrium at low temperatures. However, solutionised and quenched Ni rich alloys contain excess Ni in TiNi. During the ageing process excess Ni precipitates as coherent metastable Ti_3Ni_4 precipitates [21, 24]. Formation of the metastable precipitates cause the MT to occur in two stages. Since the precipitation changes the composition of the TiNi phase, it also changes the MT temperatures [24].

The dislocation density in the SMAs is increased by cold working and an-

nealing procedure. Stress field is associated with the dislocations, in case of cold worked and annealed alloys, and the coherent precipitates, in case of aged Ni rich alloys, effect the MT. Effect of the stress fields on the MT is minimum if the transformation strains are less [25]. Transformation strains associated with a B2 to R transition are smaller than a B2 to B19′ transition. Therefore, the stress fields increases the stability of the R more than the B19′. Hence, the R is formed during the first stage of MT and on further cooling R transforms into a B19′.

In addition to the cold worked and annealed or aged binary TiNi SMAs, R is also observed in TiNi-based ternary SMAs contain either Fe [26] or Co [27]. Hara et al. [28] determined the structure of R observed in a Ti-50.23at.% Ni and a Ti-47.75at.% Ni-1.50at.% Fe alloy using the powder X-ray diffraction method and the electron diffraction method. They determined its structure as trigonal with space group $P3$ in both alloys. Later, Goryczka et al. [29] studied the structure of a R observed in a cold worked and annealed Ni-48.8 at.%Ti alloy and a Ni-50at.%Ti-3at.%Co alloy using a X-ray diffraction method. They determined the R structure as $P\bar{3}$. Three models structures were generally considered while refining the R phase structure with a Rietveld method. They are: $P3$, $P\bar{3}$, and $P31m$. The unit cell of a R phase in a stoichiometric TiNi alloy contains eighteen atoms. They are: nine Ni atoms, and nine Ti atoms.

Orthorhombic structure (B19)

Martesites with an orthorhombic symmetry are observed in Ti-Ni-Cu SMAs with Cu content greater than 7.5 at.% [30]. Saburi et al. determined the symmetry of a B19 as an orthorhombic symmetry by studying the X-ray diffraction patterns from a Ti-40.5at.%Ni-10at.%Cu alloy at 31 °C [31]. Detailed study of the MT in Ti-Ni-Cu SMAs was carried by Nam et al. [30, 32]. They have used electrical resistivity measurements and digital scanning calorimetry to determine the MT temperatures and identified composition dependent MT paths. The MT paths as a function of Cu content are shown in Fig.(2.2).

If the Cu content is between 7.5 at.% and 15 at.%, the MT occurs in two stages. In the first stage, the austenite transforms into an orthorhomic martensite : B2→B19. Later, the orthorhomic martensite transforms into a monoclinic martensite : B19→B19′. Transformation start temperature of first stage is denoted as M_s' and of second stage is denoted as M_s in the Fig.(2.2). The M_s' is slightly increasing with Cu addition, where as the M_s is strongly decreasing with increase in Cu content. In alloys with Cu content 20 at.% or more second stage

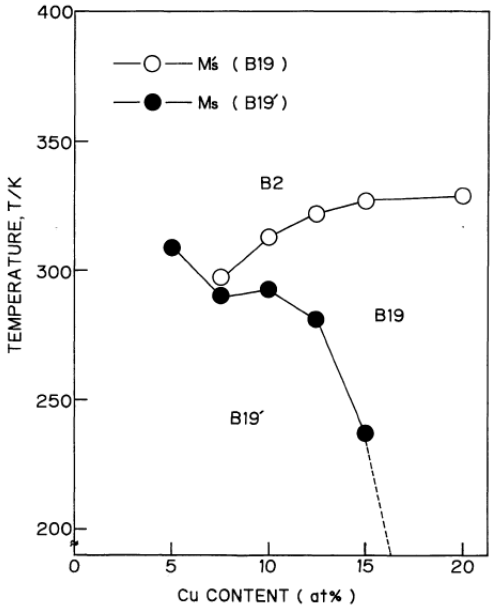


Figure 2.2: Martensitic transformation temperatures as a function of Cu content in Ti-Ni-Cu alloys [30].

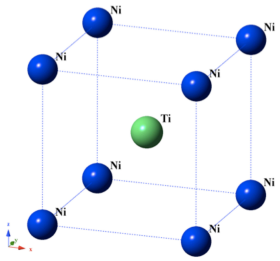
MT is not observed.

The lattice parameters of B19 unit cell as a function of Cu content were determined by Nam et al. using the X-ray diffraction method [32]. Later, Potapov et al. [33] determined the structure of a B19 observed in a Ti-25 at.%Ni-25at.%Cu alloy using transmission electron microscopy (TEM) and the X-diffraction method. B19 space group is *Pmmb*. There are four atoms in its unit cell. Schematic B2, B19, R, and B19′ unit cells are shown in Fig.(2.3).

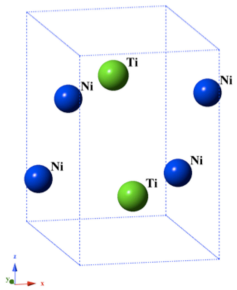
Base-centred orthorhombic structure (B33)

B33 is a theoretically predicted ground state phase of TiNi from DFT based total energy calculations. Huang et al. [34] calculated the total energies of B2, B19, B19′, and B33 of a TiNi alloy after full relaxation of internal degrees of freedom. Of all the phases B33 had a minimum total energy. Its space group is *Cmcm* and have eight atoms in a unit cell. They also found that shear stresses of values between 7.7 kbar and 14 kbar stabilise the B19′ with respect to B33. Shear stresses of these magnitude are generally present at the twin and grain boundaries. According to Huang et al. [34] presence of internal stresses is the reason for the observation of B19′ as the ground state in the experimental studies.

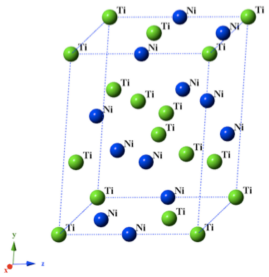
Huang et al. [34] also suggested that the shape information is stored in the internal stresses present in the micro structure. Internal stresses are present both



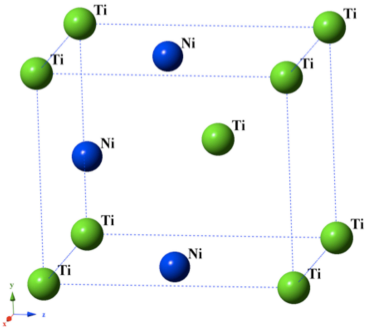
(a) B2 ($Pm\bar{3}m$)



(b) B19 ($Pmcm$)



(c) R ($P3$)



(d) B19′ ($P2_1/m$)

Figure 2.3: Schematic unit cells of different phases involved in the martensitic transformation.

in austenite and martensite. However, in a B2 only vacancies, dislocations, and grain boundaries are potential sources of internal stress field, and twin boundaries are not present. Therefore 'training' methods are used to increase the internal stress field, which aids in the formation of a few variants of martensite during MT, and hence the two way shape memory effect. In a martensite twin boundaries are also present. The stress field present associated with the dislocations, twin boundaries, and grain boundaries in martensite stores the shape information of austenite and aids the one-way shape memory effect.

2.3 Softening of a normal mode

In stable B2 all normal modes vibrate with a positive frequency. As the alloy is cooled towards the M_s, frequency of one or more normal modes of vibration decreases. Experimentally softening of normal modes is determined by inelastic neutron scattering. Experiments carried to study the softening of normal modes in TiNi-based SMAs are reviewed in this section.

2.3.1 Experiments

TiNi

Tietze et al. measured the phonon softening in an equiatomic TiNi alloy at various temperatures as the alloy is cooled towards M_s [35]. Measured dispersion relations of acoustic branches at a few wave vectors along $\frac{2\pi}{a}[\xi, \xi, 0]$ and $\frac{2\pi}{a}[\xi, \xi, \xi]$ directions are shown in Fig.(2.4(a)). Data points on this plot are results from the experiments and the broken curves are the results from a model calculation by Bruinsma [36].

A minimum was observed in a transverse acoustic branch with a $[\bar{1}10]$ polarisation (TA_2) along $\frac{2\pi}{a}[\xi, \xi, 0]$ direction at $\frac{2\pi}{a}[\frac{1}{3}, \frac{1}{3}, 0]$ [35]. This mode frequency was observed to be decreasing to zero as the alloy is cooled from 250 °C to 65 °C. Tietze et al. suggested that the TA_2 soft mode amplitude would condense into a static displacement and an intermediate phase with a monoclinic symmetry ($P2/m$) form on further cooling [35, 37]. The lengths of the unit cell of the proposed intermediate phase, also called premartensitic phase, along *a, b* directions are three times the B2 unit cell parameter. But premartensitic phase with a unit cell that occupies nine times the volume of a B2 unit cell, having a $P2/m$ symmetry was not observed experimentally. The structure of the premartensitic

phase was determined to be R whose unit volume is approximately same as the unit cell of the proposed monoclinic phase. Ohba et al. [38] later confirmed the pronounced softening of TA_2 mode at $\frac{2\pi}{a}[\frac{1}{3}, \frac{1}{3}, 0]$ in the B2 of a TiNi alloy prior to the MT.

Normal behaviour was observed along the $\frac{2\pi}{a}[\xi, \xi, \xi]$ direction. A crossover of the longitudinal and transverse acoustic (TA_2) branches was predicted by Bruinsma along the $\frac{2\pi}{a}[\xi, \xi, \xi]$ direction [36]. Tietze et al. [35] did not observe any crossover along this direction and attributed the difference to a simplification assumed in the model calculation by Bruinsma [36]. However, a cross-over is present in the calculated dispersion relations of a B2 presented in this thesis and in the experimentally measured dispersion relations of three body centred cubic (BCC) crystals [39, 40, 41] along the $\frac{2\pi}{a}[\xi, \xi, \xi]$ direction. Moine et al. [42] tried to determine phonon dispersion in a B2 of a Ti-47 at.%Ni-3 at.%Fe alloy along the $\frac{2\pi}{a}[\xi, \xi, \xi]$ direction. But they were not able to successfully determine the three acoustic branches along this direction. Therefore, phonon dispersion relations along this direction are yet to be accurately determined.

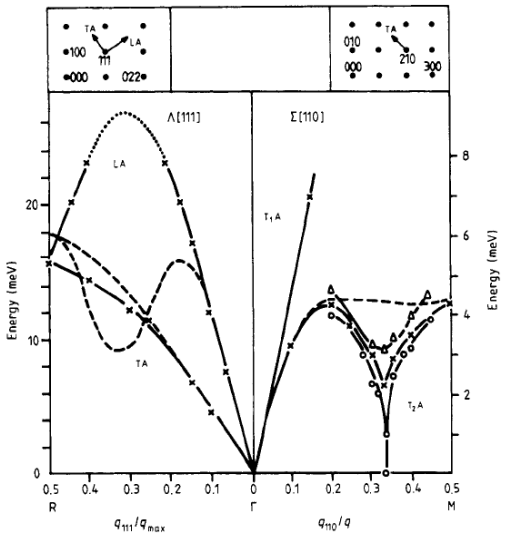
Ti-Ni-Fe

Normal mode softening in a Ti-47 at.%Ni-3 at.%Fe alloy was studied by Moine et al. [42]. They measured the phonon dispersion along $\frac{2\pi}{a}[\xi, 0, 0]$ and $\frac{2\pi}{a}[\xi, \xi, 0]$ directions. Normal mode softening was not observed along the $\frac{2\pi}{a}[\xi, 0, 0]$ direction. As shown in Fig.(2.4(b)), the entire TA_2 branch was found to be softening along the entire $\frac{2\pi}{a}[\xi, \xi, 0]$ direction as the alloy was cooled to 20 °C. And pronounced softening of the TA_2 mode was observed near $\frac{2\pi}{a}[\frac{1}{3}, \frac{1}{3}, 0]$ and at $\frac{2\pi}{a}[\frac{1}{2}, \frac{1}{2}, 0]$. Satija et al. [43] later confirmed the softening of TA_2 branch at $\frac{2\pi}{a}[\frac{1}{3}, \frac{1}{3}, 0]$ in the B2 of a Ti-46.8 at.%Ni-3.2 at.%Fe alloy.

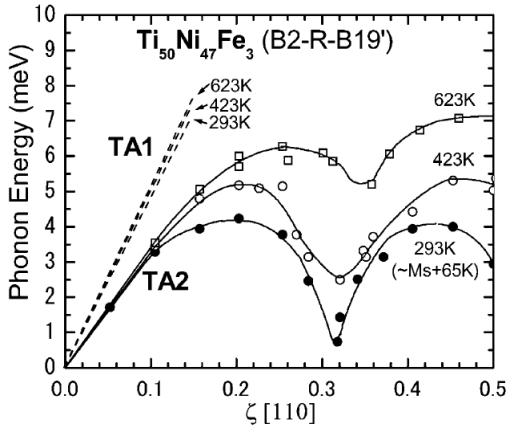
Ti-Ni-Cu

As cited by Otsuka et al. [3], Ren et al. [44] observed softening of the TA_2 branch along $\frac{2\pi}{a}[\xi, \xi, 0]$ direction in B2 of a Ti-30 at.%Ni-20 at.%Cu alloy prior to MT. As shown in Fig.(2.4(c)), normal mode softening is very noticeable at the zone boundary. All the three dispersion relation in Fig.(2.4) have a minimum at some point in the BZ.

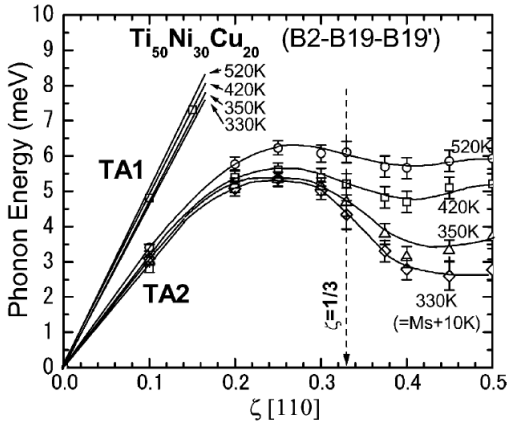
When the soft mode frequency becomes zero the B2 becomes dynamically unstable. Atomic vibrations corresponding to the soft mode become static dis-



(a) TiNi(△, 250 °C ; ×, 150 °C ;○, 65 °C) [35].



(b) TiNiFe [42].



(c) TiNiCu [3].

Figure 2.4: Normal mode softening observed in the B2 of TiNi-based alloys as they are cooled towards the M_s.

placements and a new structure forms. During this process some symmetry elements of the B2 are lost and a low symmetry product phase forms. Shuffle deformation of the soft mode is characterised by its wave vector, amplitude, and eigenvector. A soft mode also suggests that there are other soft modes at wave vectors in the star of the soft mode wave vector. And the relevant elastic constant also softens. Therefore, atomic displacements during the MT are described in terms of linear combinations of all the soft mode coordinates in Landau theory of phase transitions [45]. The distortions during the MT are described by an order parameter whose dimensionality is equal to the number of soft modes having the same frequency.

Group-subgroup relations as determined by group theory can be used to determine possible symmetries of the product phase from the soft mode symmetries [46]. Normal mode symmetries need to be determined for this purpose. Warren [47], by taking CsCl and Mg as examples, described a procedure for labelling of dispersion relations, determining mode symmetries at different points in the BZ, and determining the compatibility relations along different paths in the BZ. Soft mode symmetries can be determined using this procedure. However, as noticed by Saxena et al. [46], the mode symmetries at $\frac{2\pi}{a}[\frac{1}{2},\frac{1}{2},0]$(M) belong to M_5^-, M_3^-, and M_2^- irreducible representations (irreps) instead of M_5^-, M_2^-, and M_4^- irreps respectively in case of a CsCl crystal. It means the corresponding compatibility relations are also need to be corrected. Mode symmetries at high symmetry points and compatibility relations in the BZ of a CsCl crystal are derived in the Appendix A.

Barsch et al. [48, 49] analysed the structures of various martensites and results from inelastic scattering experiments. Using group theoretical symmetry criteria, they suggested order parameters and Landau free energy formulation for three ferroelastic transitions: B2$\xrightarrow{M_5^-}$B19, B2$\xrightarrow{\Sigma_4^{\frac{1}{3}}}$R, and B19$\xrightarrow{\Gamma_3^+}$B19′. Hatch et al. [50] determined the symmetries of all the normal modes that could be involved in a MT using group-subgroup relations for a given martensitic structure. They also determine the primary and secondary order parameters for every transition that could result in a B19′ or an R from a B2. TA_2 soft mode symmetry at $\frac{2\pi}{a}[\frac{1}{3},\frac{1}{3},0]$ was reported as belong to a $\Sigma_4^{\frac{1}{3}}$ irrep in most of the discussions in the literature [48, 51, 52]. However, as shown in the Appendix A, the $\Sigma_4^{\frac{1}{3}}$ irrep does not appear in the irrep decomposition at $\frac{2\pi}{a}[\frac{1}{3},\frac{1}{3},0]$. The soft mode symmetry at $\frac{2\pi}{a}[\frac{1}{3},\frac{1}{3},0]$ belong to a $\Sigma_2^{\frac{1}{3}}$ irrep.

2.3.2 DFT studies

Phonon dispersion relations in different phases, observed in TiNi-based SMAs, were calculated using theoretical methods based on electronic structure calculations [51, 53, 54]. Parlinski et al. [51] used a small displacement method for calculating the phonon dispersion relations in B2, B19, and B19′ using supercells of sizes 2×2×2, $2\times\sqrt{2}\times\sqrt{2}$, and $2\times\sqrt{2}\times\sqrt{2}$ respectively. By analysing the calculated dispersion relations in various phases at 0 K, they suggested different MT paths.

Consistent with the instability of a B2 at 0 K, there is a doubly degenerate normal mode having an imaginary frequency at M point in the BZ. Parlinski et al. [51] suggested the formation of a B19 due to soft mode instability at M : B2 $(Pm\bar{3}m) \xrightarrow{\mathrm{M}_5^-}$ B19 $(Pmcm)$. During this transition only one of the symmetry equivalent six soft modes drives the MT.

The soft mode at $\frac{2\pi}{a}[\frac{1}{3},\frac{1}{3},0]$ was found to have lower imaginary frequency than the soft mode frequency at M both in 2×2×2 and 3×3×3 supercell calculations of a B2 [51]. But experimentally pronounced softening of a normal mode was observed at $\frac{2\pi}{a}[\frac{1}{3},\frac{1}{3},0]$ in a TiNi alloy. Parlinski et al. [51] attributed the difference to anharmonic contributions at higher temperatures, which are not considered in the harmonic lattice dynamics. They also related the R observed in TiNi-based SMAs to the following MT, suggested by Barsch et al. [48], due to a soft mode instability at $\frac{2\pi}{a}[\frac{1}{3},\frac{1}{3},0]$: B2 $(Pm\bar{3}m) \xrightarrow{\Sigma_4^{\frac{1}{3}}}$ R $(P3)$.

Calculated dispersion relations of the B19 have an acoustic branch which has very low, but positive, frequencies near the BZ center. By assuming the softening of this acoustic mode at the BZ center, Parlinski et al. suggested a transition from B19 to B19′ : B19 $(Pmcm) \xrightarrow{\Gamma_3^+}$B19′$(P2_1/m)$. Lattice waves in the long wave limit are elastic waves. So the above transition can be considered to be due to a shear strain. In other words, it is a proper ferroelastic phase transformation as suggested by Barsch [48] in which the irrep Γ_3^+ represents a shear strain $\epsilon_5 = \epsilon_{xz}$. Imaginary modes of vibration are not found in the calculated dispersion relations of B19′ [51].

2.3.3 Electron-phonon interactions

Lattice vibrations at high temperature interact with the electrons and alter their energies. Varma et al. [55, 56] devised a method for studying the effect of changes in electronic eigenvalues, due a perturbation described by a wave vector **q**, on the

dynamical matrix. This method is suitable for studying the lattice dynamics in transition metals and transition metal compounds. In this method the dynamical matrix is written as a sum of $D^{(0)}(\mathbf{q})$, which is calculated from the energy of unperturbed system, $D^{(1)}(\mathbf{q})$, which arises from the first order corrections to the electronic eigenvalues due to second order atomic displacements, and $D^{(2)}(\mathbf{q})$, which arises from the second order corrections to the electronic eigenvalues due to the first order atomic displacements. Long range interactions contribute largely to $D^{(2)}(\mathbf{q})$ than $D^{(0)}(\mathbf{q})$. Varma et al. derived a relation for calculating major electron-phonon interaction contribution to the dynamical matrix, $D^{(2)}(\mathbf{q})$, from the electronic band structure:

$$D^{(2)}_{\alpha\beta}(\mathbf{q}) = -\sum_{\mathbf{k}\mu,\mathbf{k}+\mathbf{q}\mu'} \frac{g^{\alpha *}_{\mathbf{k}\mu,\mathbf{k}+\mathbf{q}\mu'} g^{\beta}_{\mathbf{k}+\mathbf{q}\mu',\mathbf{k}\mu}[f(\mathbf{k}\mu) - f(\mathbf{k}+\mathbf{q}\mu')]}{\varepsilon_{\mathbf{k}\mu} - \varepsilon_{\mathbf{k}+\mathbf{q}\mu'}}. \tag{2.1}$$

Here $\varepsilon_{\mathbf{k}\mu}$ is an electronic eigenvalue at a wave vector $\mathbf{k}$ and in the band μ, $f(\mathbf{k}\mu)$ is the Fermi distribution function, and $g^{\alpha}_{\mathbf{k}\mu,\mathbf{k}+\mathbf{q}\mu'}$ is a fully renormalized self-consistent electron-phonon-interaction matrix element. $g^{\alpha}_{\mathbf{k}\mu,\mathbf{k}+\mathbf{q}\mu'}$ is proportional to difference in velocities of electrons in states ($\mathbf{k}$ μ), ($\mathbf{k}$+$\mathbf{q}$ μ') : $g^{\alpha}_{\mathbf{k}\mu,\mathbf{k}+\mathbf{q}\mu'} \propto (v^{\alpha}_{\mathbf{k}\mu} - v^{\alpha}_{\mathbf{k}+\mathbf{q}\mu'})$, where $v^{\alpha}_{\mathbf{k}\mu}$ is equal to $\frac{\partial \varepsilon_{\mathbf{k}\mu}}{\partial k_\alpha}$.

Varma et al. [55, 56] used the above described method for studying the lattice dynamics in Nb, Mo, Nb-Mo alloys. They calculated the $D^{(2)}_{\alpha\beta}(\mathbf{q})$ from the electronic band structure obtained from the first principles calculations. A parametric form was assumed for nearest neighbours and next nearest neighbour force constants. Short range interactions, which contribute to $D^{(0)}_{\alpha\beta}(\mathbf{q})$ and $D^{(1)}_{\alpha\beta}(\mathbf{q})$, were described using these force constants. The parameters describing the force constants were determined in such a way that the diagonalization of $D^{(0)}_{\alpha\beta}(\mathbf{q})$+$D^{(1)}_{\alpha\beta}(\mathbf{q})$+ $D^{(2)}_{\alpha\beta}(\mathbf{q})$ produced a better fit with the experimental phonon dispersion relations. Results were analysed in relation to the phonon anomalies and various contributions causing the anomalies.

Phonon dispersion relations obtained after the fitting procedure correctly reproduced the experimentally observed anomalous phonon behaviours. All the anomalous phonon behaviour was found to be originating from scattering processes involving electronic states near the Fermi level, which contribute dominantly to the $D^{(2)}_{\alpha\beta}(\mathbf{q})$. Parallel Fermi surfaces separated by a nesting vector vector $\mathbf{q}$ provide large phase space of states ($\mathbf{k}\mu$) and ($\mathbf{k}$+$\mathbf{q}\mu'$) around the Fermi level. Scattering processes involving these states were found to be contributing largely to $D^{(2)}_{\alpha\beta}(\mathbf{q})$ and causing phonon anomalies at $\mathbf{q}$. As can be seen from the

dependence of $g^{\alpha}_{\mathbf{k}\mu,\mathbf{k}+\mathbf{q}\mu'}$ on $v^{\alpha}_{\mathbf{k}\mu}$, larger the electron velocity more is the contribution to $D^{(2)}_{\alpha\beta}(\mathbf{q})$. Therefore, Varma et al. [55, 56] also concluded that presence of sharp saddle points in the electronic band structure near the Fermi level cause phonon anomalies.

Bruinsma [36] used the method devised by Varma et al. for studying the lattice dynamics in TiNi. He used a simplified dynamical matrix in his calculations. Weak phonon anomalies were predicted along $\frac{2\pi}{a}[\xi,\xi,0]$ and $\frac{2\pi}{a}[\xi,\xi,\xi]$ directions with very slight softening at $\frac{2\pi}{a}[\frac{1}{3},\frac{1}{3},0]$ and a little softening at $\frac{2\pi}{a}[\frac{1}{3},\frac{1}{3},\frac{1}{3}]$ respectively. Large values of $D^{(2)}_{\alpha\beta}(\mathbf{q})$ at these wave vectors was found to be the reason for these anomalies. He also identified the phase space in the electronic band structure causing these anomalies. Experimentally, phonon softening was observed along the $\frac{2\pi}{a}[\xi,\xi,0]$ direction. Accurate phonon dispersion relations along the $\frac{2\pi}{a}[\xi,\xi,\xi]$ direction are yet to be determined.

Later, Zhao et al. [52] used the method of Varma et al. without any further simplifications to understand the lattice dynamics in TiNi along $\frac{2\pi}{a}[\xi,\xi,0]$ direction. They had used a self-consistent tight-binding method for evaluating the electronic band structure. By considering the electron-phonon interactions involving electronic states in only two bands crossing the Fermi level, they were able to obtain a better fit to the experimental phonon dispersion relations. The electron-phonon interaction was found to be strongly renormalising the longitudinal acoustic (Σ_1) and TA_2 (Σ_4) branches. Effect of $D^{(2)}_{\alpha\beta}(\mathbf{q})$ on the other transverse acoustic branch, TA_1, was found to be minimum. This model also accurately predicted the minimum in the TA_2 branch at $\frac{2\pi}{a}[\frac{1}{3},\frac{1}{3},0]$. Zhao et al. identified the nesting regions in the phase space of electronic states which were contributing dominantly to $D^{(2)}_{\alpha\beta}(\mathbf{q})$ at $\mathbf{q} = \frac{2\pi}{a}[\frac{1}{3},\frac{1}{3},0]$.

Thermal energy at high temperature smears the Fermi surface. Presence of defects, impurities, addition of alloying elements, thermal vibrations also changes the topology of Fermi surface. Zhao et al. [57] studied the effect of Fermi surface smearing using a Fermi-Dirac distribution function for the Fermi distribution function $f(\mathbf{k}\mu)$ in Eq.(2.1). After fitting the model dispersion relations to the experimental data, they studied the effect of increase in the temperature on the calculated dispersion relations. They found hardening of longitudinal acoustic (LA) branch and TA_2 branch along the $\frac{2\pi}{a}[\xi,\xi,0]$ direction with increase in temperature. Therefore, thermal smearing qualitatively explained the phonon softening with decrease in temperature.

2.3.4 Phonon-phonon interactions

Interactions between different normal modes of vibration contribute to the Hamiltonian and this contribution is termed as an anharmonic contribution. As pointed by Zener [14], BCC and other open structures are stabilised by entropic contribution from atomic vibrations at high temperatures. Within the harmonic approximation a subset of normal modes in these crystals have imaginary frequencies. These mode frequencies are renormalised by anharmonic effects at higher temperatures and more open structures are stabilised when all normal mode frequencies become positive. Souvatzis et al. [58] developed a supercell based self-consistent *ab initio* lattice dynamics (SCAILD) method from the self-consistent phonon method of Born [59]. In principle, this method is useful for studying the lattice dynamics at high temperatures in an approximate way. This method is explored, formulations is presented in the Chapter 3 and results are described in the Chapter 4.

Souvatzis et al. [60] used the SCAILD method for studying the lattice dynamics in B2 of a TiNi alloy using a 3×3×3 supercell. Simultaneous excitation of normal modes at the wave vectors commensurate with the size of the supercell was found to be stabilising the B2 at high temperatures. By analysing the phonon dispersion relations calculated at various temperatures in terms of TA_2 mode frequency at $\frac{2\pi}{a}[\frac{1}{3},\frac{1}{3},0]$ Souvatzis et al. predicted a phase transition of the B2 at 227 K. In agreement with the experimentally observed linear variation of squared soft mode frequencies with temperature, the squared renormalised frequencies in the stable B2 are found to be linearly varying with temperature.

Souvatzis et al. [60] also studied the effect of smearing of Fermi surface due to the phonon excitation at high temperatures. They calculated generalised mean-susceptibility along $\frac{2\pi}{a}[\xi,\xi,0]$ direction at 0 K and 300 K. Atomic displacements due to phonon excitation was found to be suppressing the susceptibility peak at $\frac{2\pi}{a}[\frac{1}{3},\frac{1}{3},0]$ to a lower value. They related the hardening of the TA_2 branch with increase in temperature to the suppression in the susceptibility. Zhao et al. [52] also calculated the generalised susceptibility for studying the phonon softening along the $\frac{2\pi}{a}[\xi,\xi,0]$ direction. As described by Varma et al. [56], this analysis assumes that the electron-phonon interaction matrix elements $g^{\alpha}_{\mathbf{k}\mu,\mathbf{k}+\mathbf{q}\mu'}$ are constants. However, as shown by Varma et al., this is not the case in general. Therefore, calculation of $D^{(2)}_{\alpha\beta}(\mathbf{q})$ is required for an accurate analysis of Fermi surface smearing on phonon softening.

2.4 Elastic softening

Transformation strains play an important role in determining the MT paths in TiNi-based SMAs. The martensite formed during MT, after self-accommodation of different variants, needs to be accommodated in the volume of austenite from which it is formed. Elastic energy associated with martensitic accommodation must be provided by decrease in the free energy due to the MT. Therefore, during the MT phases with low transformation strains are preferred over the ones with high transformation strains [25]. On contrary to the general behaviour, softening of elastic constants was observed before the MT in TiNi-based SMAs as they are cooled towards M_s [61, 62, 63]. This softening reduces the elastic energy of martensite accommodation and aids the MT. Softening of elastic constants occurs along with the normal mode softening. These results and the first order nature of the MT in TiNi-based SMAs suggest a coupling between lattice deformation due to atomic shuffles of the soft mode and the transformation strains [64]. Elastic softening observed in various TiNi-based SMAs is discussed in this section.

Mercier et al. [61], first, observed the elastic softening in a TiNi single crystal by measuring ultrasonic sound propagation velocities through a B2. M_s of this alloy was found to be $-5\,^{\circ}C$ by electrical resistivity measurements. The sound velocity was measured by a pulse-echo overlap method. The elastic constants were determined from the sound velocities between $80\,^{\circ}C$ and $-5\,^{\circ}C$. They found that the elastic constants C_{44} and C' are softening as the alloy is cooled towards the M_s.

Ren et al. [62] used a rectangular parallelopiped resonance method to measure the elastic constants in a Ti-30at.%Ni-20at.%Cu alloy as a function of temperature. Softening of C_{44} and C' was also observed in this alloy before the MT. Zhang et al. reported softening of C_{44} and C' prior to a B2 to R transition in a Ti-48 at.%Ni-2 at.%Fe alloy [63].

Softening of C' is observed in most of the SMAs before the MT [65]. But softening of C_{44} is observed only in the TiNi-based SMAs. In cubic crystals, C' determines the resistance to a $\{110\}\langle\bar{1}10\rangle$ shear and C_{44} determines the resistance to shearing of $\{100\}$ planes in an arbitrary direction [14]. Ren et al. [25, 65] critically analysed the elastic softening observed in TiNi-based SMAs. Ren et al. [25] calculated the elastic constants during the elastic softening in various alloys. Results are shown in Fig.(2.5). From these results they suggested the following empirical correlations between the changes in elastic constants and the structure of the product phase.

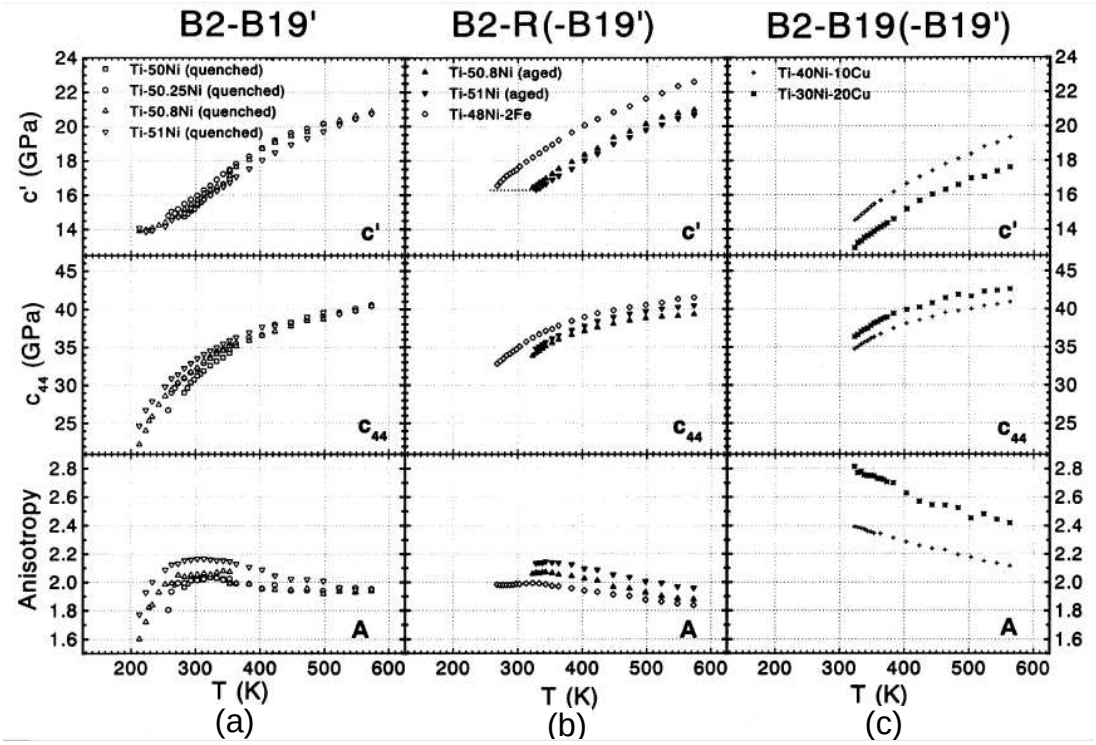


Figure 2.5: Elastic softening observed in TiNi-based shape memory alloys: (a) quenched Ti-Ni alloys, (b) aged Ti-Ni alloys, Ti-Ni-Fe alloys, and (c) Ti-Ni-Cu alloys [25].

- Although the C_{44} softening is observed in all TiNi-based SMAs, relative softening of C_{44} to C' determines the structure of the martensite.

- If the MT strains contain only a $\{110\}\langle\bar{1}10\rangle$ shear, then the final structure of martensite is B19. This is the case in Ni-Ti-Cu based SMAs with Cu content greater than or equal to 20 at.%.

- Occurance of a $\{110\}\langle\bar{1}10\rangle$ shear and a $\{001\}$ $\langle1\bar{1}0\rangle$ shear simultaneously or subsequently during the MT results in the formation of a B19′. Simultaneous occurrence of both shear is observed in the single stage MT observed in solutionised and quenched binary TiNi alloys.

- Two stage MT is observed in Ni-Ti-Cu alloys with Cu content less that 15 at.%. A $\{110\}\langle\bar{1}10\rangle$ shear occurs during the first stage and B19 forms. Softening in C' aids the shear occurring during first stage transition. The B19 transforms into a B19′ in the second stage. Softening in the elastic constant C_{44} aids this transition.

- MT in Ni-Ti-Fe alloys also proceeds in two stages. Simultaneous occurance of three different shears belonging to the family $\{110\}\langle\bar{1}10\rangle$ is required for the fomation of a R phase. This occur in the first stage and softening in C' aids this transformation. Softening in the C_{44} aids the R to B19′ transition occurring in the later stage. This is also the transformation sequence in the aged Ni rich binary, cold worked and annealed binary TiNi alloys.

- The tranformation strains observed during the formation of trigonal, orthorhombic and monoclinic phases increase in the same order. Because of this reason, the formation of trigonal phase is preferred over the monoclinic phase in the presence of precipitates and dislocation structure.

As can be seen from these suggestions, transition strains also play a role in determining the structure of the product phase. However, the elastic constants C' and C_{44} have positive values just before MT. It means the elastic softening is not complete before the MT. Austenite transforms to martensite due to the soft mode instability at low temperatures. The soft mode characteristics primarily determine the product phase. Therefore, shuffle deformation due to the soft mode instability is described by a primary order parameter while describing the MT using Landau theory of phase transitions [48]. The distortions due to transformation strains are described by a secondary order parameter.

2.4.1 Theoretical studies

Crystals, in general, expand on heating. Changes in elastic constants due to thermal expansion is a part of temperature dependence of elastic constants. Bihlmayer et al. [66] studied the variation of elastic constants due to volume change in the B2 of a TiNi alloy at 0 K using a homogeneous deformation method. They had used a full-potential linearised augmented plane wave (FLAPW) method for calculating the total-energy of strained atomic configurations. Calculated elastic constants satisfy the necessary stability criteria of elastic constants — $C_{11} > 0$, $C_{44} > 0$, and $C' > 0$ — required for the mechanical stability of a cubic crystal. The calculated elastic constants C' and C_{44} are found to stiffen a little with rise in the volume.

Wagner et al. [67] calculated the elastic constants of single crystals of experimentally observed phases (B2, B19, B19′), and a theoretically predicted ground state (B33). DFT based total energy calculations were performed for this purpose. The calculated elastic constants, which are otherwise difficult to measure experimentally, are valuable input to mesoscopic and microscopic modelling studies. They reported an instability of a B2 phase to a $\{110\}\langle\bar{1}10\rangle$ shear at 0 K — $C' < 0$. The calculated total energy of strained configuration was found to be decreasing with increase in the $\{110\}\langle\bar{1}10\rangle$ strain : the energy versus strain profile has a negative curvature at the equilibrium configuration. However, calculated elastic constants of a B2 phase from our study are satisfying the necessary stability criteria and contradicting the results from the study of Wagner et al. [67].

2.5 Ternary alloys

Binary TiNi-based SMAs have M_s in the range 0 to 60°C depending on the Ni content [3]. The SME and superelasticity of these alloys are exploited at temperatures around room temperature. However, materials with higher M_s are needed to make use of the two phenomenon in various devices operating at higher temperatures. Some of the ternary SMAs based on Pd, Pt, Au, Hf, and Zr have M_s values higher than the binary alloys [10]. Addition of these ternary elements up to a *critical* value between 0 and 10 at.% decreases the M_s, however, when the element is added in excess of the critical amount, the M_s value increases almost linearly with the alloying content. The critical amount depends on the ternary system. TiPt has the highest M_s at 1030 °C [68]. Having a high value of M_s may be a necessary initial requirement, but a useful HTSMA is also expected to have minimum

ductility and other properties. Since the MT occurs at higher temperatures in HTSMAs than in binary TiNi-based SMAs, diffusion activated processes such as recrystallisation, recovery and ageing also occur simultaneously [69]. These processes alter the composition and/or dislocation structure of different phases in the alloy and hence effect the MT. In addition, the HTSMAs are required to have oxidation resistance, creep resistance, high temperature strength, and fatigue life. In spite of many efforts to find a HTSMA satisfying all these requirements, very few alloys have been put into practical applications.

Precious metal based HTSMAs are very expensive. Commercial application of these alloys is not a viable option. Hence, the research has been focussed more on low cost Hf and Zr based HTSMAs. A section of the Ni-Ti-Zr phase diagram at 700 °C is shown in Fig.(2.6). The ternary λ phase in this diagram is a solid solution NiTiZr. As can be seen from this figure, the alloys in the system $Ti_{50-x}Ni_{50}Zr_x$ are alloys in the 50 at.% Ni isopleths of the Ni-Ti-Zr system. Pseudobinary section between NiTi and NiZr is shown in Fig.(2.7(a)). The β' phase in this diagram is a solid solution Ni(Ti,Zr) and it can dissolve up to 30 at.% Zr at 700 °C. Of the Ni-Ti-Hf system, only a pseudobinary section between HfNi and NiTi is available in the literature and is shown in Fig.(2.7(b)). The β_1 phase in this diagram is a solid solution Ni(Ti,Hf) with a solubility of 30 at.% Hf at 700 °C. The solid solutions β' and β_1 undergo a MT on cooling and are important phases for the present study. Both β' [70] and β_1 [71] has a $Pm\bar{3}m$ symmetry. Because of the solubility limit of Zr and Hf in β' and β_1 respectively, Zr or Hf addition can only be effective in changing the M_s up to 30 at.%. Excess addition results in the formation of a second phase, which does not affect the MT. Similarly, when the composition of the ternary alloy is off-stoichiometric from the compositions $Ti_{50-x}Ni_{50}Y_x$ (Y=Hf or Zr), second phase particles are present in the system along with the β' or β_1 before the MT.

AbuJudom et al. [74] invented the Hf, Zr based HTSMAs. For the same amount of ternary addition to a binary Ti-Ni system, the Hf increases the M_s more than the Zr. Angst et al. [75] determined the martensitic peak temperatures, M_p, using the differential scanning calorimetry in $Ti_{51-x}Ni_{49}Hf_x$ alloys as a function of Hf content. Here M_p is the temperature at which maximum heat of transformation is observed during the MT. The results are plotted in Fig.(2.8). Hf addition up to 7.5 at.% does not change the M_p appreciably. Addition of Hf in excess of 7.5 at.% causes significant increase in the M_p. The increment is linear with the Hf content. A maximum M_p value of 525 °C was observed at 30 at.% Hf. The method of sample preparation changes the behaviour somewhat;

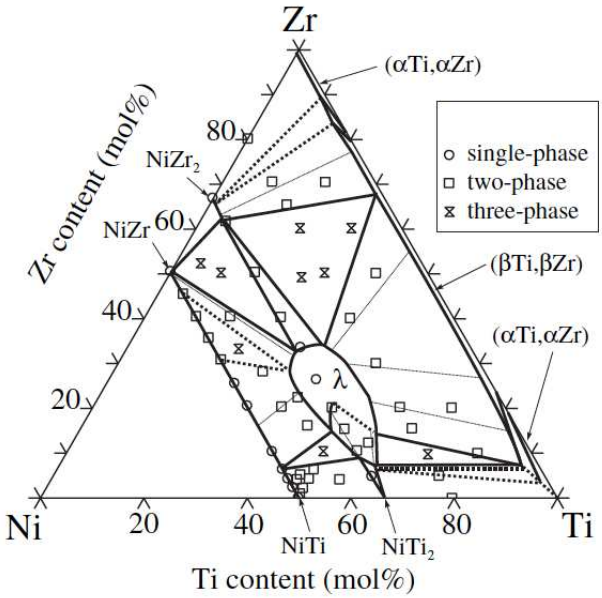
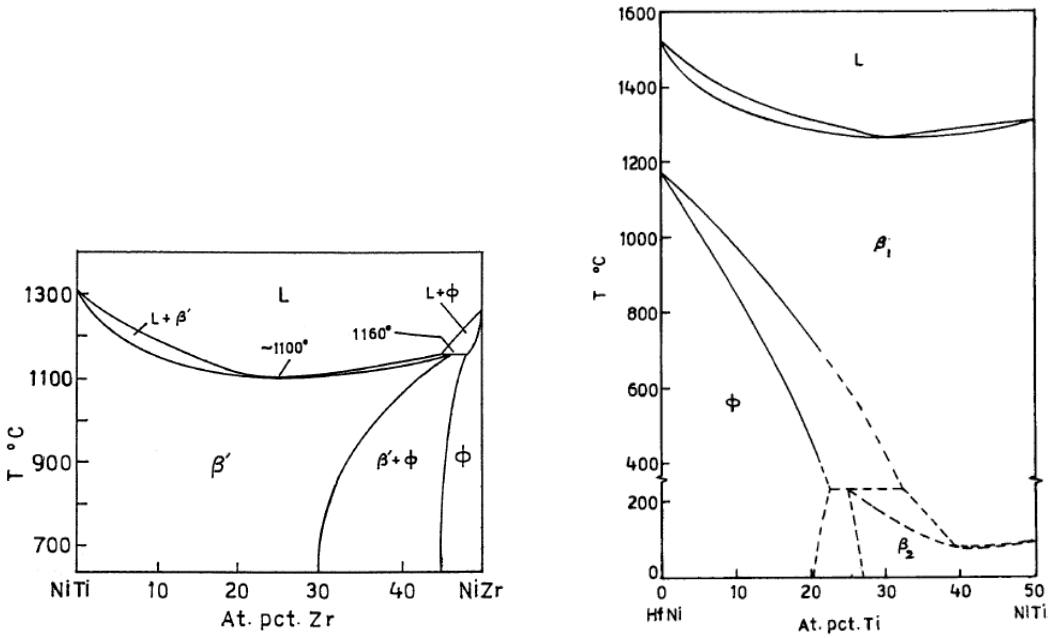


Figure 2.6: Isothermal section of the ternary Ti-Ni-Zr phase diagram at 700 °C [72] (reproduced from [73]).



(a) NiTi-NiZr [70]

(b) HfNi-NiTi [71]

Figure 2.7: Pseudobinary sections.

Sanjabi et al. [76] observed a *decrease* in the M_s in a ternary alloy with 5 at.% Hf, an increase in the M_s in ternary alloys with Hf content greater than 5 at.% in sputter-deposited $Ti_{50-x}Ni_{50}Hf_x$ thin films. They also observed formation of the R phase while cooling the alloys with Hf content less than 16 at.%.

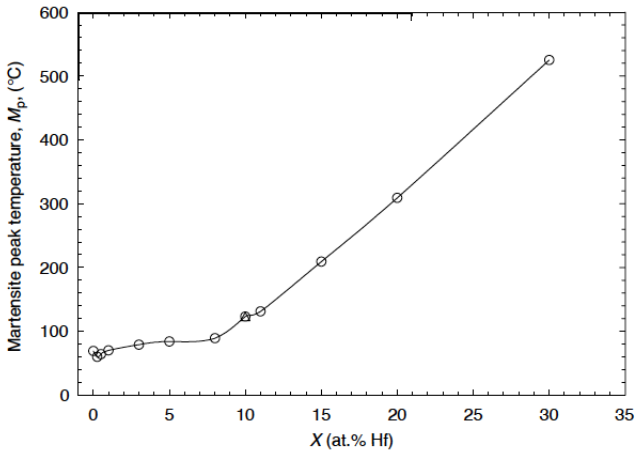


Figure 2.8: Martensitic peak temperatures as a function of Hf in $Ti_{51-x}Ni_{49}Hf_x$ alloys [75] (reproduced from [10]).

Potapov et al. [77] observed a reversible $\beta_1 \rightarrow$ B19′ MT in melt spun ribbons of $Ti_{50.2-x}Ni_{49.8}Hf_x$ alloys with Hf content between 8 and 25 at.%. The M_s temperatures and the thermal hysteresis (M_s-M_f) increases with the Hf content. The lattice parameter of the β_1 unit cell increases with increase in the Hf in Ti-Ni-Hf alloys [77]. Hf addition also increases the unit cell parameters *a, c,* monoclinic angle, and decreases the lattice parameter *b* of B19′ in both melt spun ribbons [77] and bulk [78] Ti-Ni-Hf alloys.

Thoma et al. [79] studied the effect of composition on the MT in $Ti_{90-x}Ni_xHf_{10}$ alloys with the Ni content ranging from 49.0 to 50.2 at.%. M_s remain almost same in alloys with Ni content between 49.0 and 50.0 at.% but decreases drastically when the Ni content is more than 50.0 at.%. This behaviour is similar to the binary Ti-Ni based SMAs.

Hf based HTSMAs have very poor shape memory properties and do not exhibit superelasticity [80]. The yield stress of β_1 is almost of the same magnitude as the stress required to induce the MT above the A_f temperature in Ti-Ni-Hf based SMAs. Hence, at temperatures just above A_f, the deformation proceeds from elastic deformation to dislocation mediated slip during the stress induced MT [81, 82]. The dislocation mediated slip causes work hardening and the plateau is not observed in the stress-strain curves. Because of the plastic deformation

during the stress induced MT, complete recovery is not observed in these alloys after unloading.

Pu et al. observed an increase in the M_s with Zr content in $Ti_{50-x}Ni_{50}Zr_x$ alloys [83] when the Zr content is more than 5 at.%. M_s temperatures from this study are plotted in Fig.(2.9). Similar trends in the M_s as a function of Zr content were observed by Hsieh et al. in $Ti_{53-x}Ni_{47}Zr_x$ alloys [84]. Beyer reported an increase in the monoclinic angle, lattice parameters *a, c,* and a decrease in the lattice parameter *b* of the B19′ with increase in the Zr content in Ti-Ni-Zr based HTSMAs [85]. This behaviour of changes in the lattice parameters of B19′ is consistent with the changes observed in lattice parameters of B19′ in Ti-Ni-Hf based HTSMAs. The M_s in these alloys decreases with Zr addition up to 4 at.% followed by an increase with further addition of Zr. Therefore, the *critical* alloying content is near 5 at.% and 7.5 at.% in $Ti_{50-x}Ni_{50}Zr_x$ and $Ti_{50-x}Ni_{50}Hf_x$ alloys respectively.

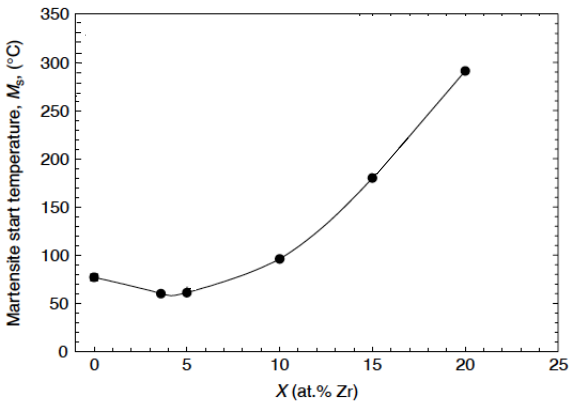


Figure 2.9: Martensitic start temperatures as a function of Zr in $Ti_{50-x}Ni_{50}Zr_x$ alloys [83](reproduced from [10]).

Stability of the Hf, Zr based HTSMAs also depends on the thermomechanical history of the alloy. The stability has been studied by subjecting the HTSMAs to thermal cycling, cold working and ageing treatments. Cold working in the martensitic state stabilises the martensite and increases the A_s [86]. When a Ti-Ni-Hf alloy is deformed in full martensitic state, the reorientation of different martensite variants occurs along with dislocation mediated slip. Plastic deformation that accompanies the martensitic reorientation degrades the SME performance [87]. Hence, for an optimum high temperature SME, plastic deformation must be avoided by keeping the deformation temperature well below the M_s [87, 88].

Thermal cycling without any application of stress relaxes the dislocation

structure and the associated stress field present in a material either due to a prior deformation or due to a training method [87]. During the initial thermal cycles, a new dislocation structure is introduced into the alloy. The new structure interacts with the existing structure and stabilises after a few thermal cycles. As a consequence the M_s decreases during the initial thermal cycles, reaching a constant value after stabilisation of the dislocation structure [69, 86, 87, 89].

The effect of ageing depends on the alloy composition and ageing temperature. For example, ageing in the martensitic state stabilises the martensite, resulting in a slight increase in the A_s in a $Ti_{30.5}Ni_{49.5}Zr_{10}Hf_{10}$ alloy. Hsieh et al. suggested that the pinning of the interface between martensite plates by interstitial atoms and quenched-in vacancies might be responsible for the martensitic stabilisation in this alloy [86]. Ageing of a $Ti_{36}Ni_{49}Hf_{15}$ alloy in the β_1 state stabilises the β_1 [90]. In this case M_s decreases rapidly with ageing time during the initial stage and reaches a constant value after ten hours of ageing. Ageing also effect the two-way SME. For example, in Ti-Ni-Hf alloys $(Ti,Hf)_2Ni$ particles grow with the ageing time. Growth of these second phase particles degrades the two-way SME in these alloys [87].

Hornbogen suggested that the MT temperature in an alloy can be written as a sum of two terms of independent physical origin: $M_s = T_0 - \triangle T$ [91]. Here T_0 is an equilibrium temperature at which both austenite and martensite have the same free energies and is a function of composition (c) of the alloys, the degree of order of the transforming phase. The undercooling $\triangle T$ depends on the factors affecting the nucleation and growth of martensite. These factors include external shear stresses, the resistance to MT shear. Strengthening of the alloy caused by point defects, dislocations, solute atoms, second phase particles ...etc increases the resistance to the plastic shear that occurs during the MT. The strengthening increases $\triangle T$ and decreases the M_s. Therefore, the HTSMAs needs to be treated by various methods like cold rolling, thermal cycling, ageing in such a way that the alloy would have a stable M_s before it is put into any practical applications at a high temperature.

Incomplete elastic softening occurs before the MT. Otsuka et al. [19] observed that the elastic constant C' softens to a critical value at the MT. The critical value is almost similar in all alloys and is independent of the alloy composition. Addition of an alloying element changes the elastic constants. The authors argued that since the critical C' before the MT is independent of the composition, the changes in the elastic constants due to the ternary additions change the MT temperatures accordingly [19]. If adding a ternary alloying element increases

the C′, the alloy needs to be cooled more before the MT so that the softened C′ reaches the critical value. Hence, the ternary alloy would have a low M_s compared to the binary alloy [69]. In other words the ternary alloy, which has more resistance to shear, requires more under cooling before the MT. As described in the previous paragraph, it is one of the many factors which determines the M_s of an alloy and it alone does not determine the M_s.

Addition of a ternary element affects both T_0 and $\triangle T$ of a binary TiNi alloy [91]:

$$dM_s(c) = \pm\Big\{\frac{\delta T_0}{\delta c}dc - \frac{\delta \triangle T}{\delta c}dc\Big\}. \tag{2.2}$$

If $\frac{\delta T_0}{\delta c} > \frac{\delta \triangle T}{\delta c}$, the M_s increases and vice-versa. In this study, I calculated the elastic constants of some ternary $Ti_{50\text{-}x}Ni_{50}Y_x$ (Y=Hf or Zr) alloys as a function of content of Y. Results were analysed to get some idea about the elastic hardening due to alloying additions. I also calculated the soft mode frequencies of β' and β_1 as a function of alloying content to get some insight into the effect of composition on the T_0.

Chapter 3

Theoretical methods

The configuration and properties of an aggregate of atoms depend on its constitutive elements and the interactions between them. The electronic structure of a material mainly determines these interactions, via the electron density. The information about electronic structure and density can be obtained in principle by solving the Schrödinger equation (SE). In practice a solution to this many-particle problem can only achieved approximately, and an approach that has proved especially successful is the Kohn-Sham method of Density Functional Theory. It is often referred to as an *ab initio* method, since from a user's point of view the input contains no empirical parameters. The theoretical achievement it represents is a reduction of the many-electron problem to a self-consistent set of one-electron Schrödinger-like equations (the Kohn-Sham equations). For use in this method, the Coulomb potential created by the atomic nuclei and the potential generated by core electrons are represented by effective potentials or pseudopotentials. Of particular interest here, the total energy of a system and a few higher order derivatives of the total energy with respect to certain parameters, such as nuclear positions, can be calculated. This approach has been used for calculating lattice parameters, and predicting crystal structures of lowest energy, for calculating the forces on atoms, elastic constants, interatomic force constants and phonon dispersion relations. These results have been used for studying the MT in TiNi-based SMAs. Principles of various theoretical methods used in my thesis work are presented in this chapter.

Schrödinger equation

Different atoms in a material are individually made of electrons and nuclei. The total energy of any material is determined by the interactions between these subatomic particles and their kinetic energies. These interactions are entirely Coulombic in nature, and comprise electron-electron interactions, electron-nucleus interactions and nucleus-nucleus interactions. The state of the electrons is controlled by the potential provided by nuclei of different atoms. The total energy of the system in its ground state is obtained in principle by solving the time-independent Schrödinger equation [92]

$$\hat{\mathcal{H}}\Psi = E\Psi. \tag{3.1}$$

Here $\hat{\mathcal{H}}$ denotes the Hamiltonian operator representing the kinetic energies of different subatomic particles and the interactions between them; E is the total energy of the system; Ψ is the many-body wave function. The ground state energy of a system is the total energy when the eigenvalue of Eq.(3.1) is at a minimum with respect to all electronic and nuclei coordinates. However, we shall be concerned firstly with the electronic ground state, which is obtained as follows.

The mass of a nucleus is more than 1900 times that of an electron, but the forces acting on the nuclei and electrons are almost same. Therefore, the relative velocity of electrons is very high, and for structural studies the nuclei can be treated as classical particles. It then becomes a good approximation to assume that the electrons respond to any motion of the nuclei instantaneously and reach a state of equilibrium dependent on the nuclear positions but not on their velocities. With this approximation, known as the *Born-Oppenheimer* approximation [93], it is possible to separate the electronic and nuclear coordinates in the many-body wave function. The electrons move in the potential due to frozen-in nuclei. For a fixed ionic configuration $\{\mathbf{R}_\mathrm{I}\}$ the electronic Hamiltonian operator can be written as

$$\begin{aligned}\hat{\mathcal{H}}_\mathrm{el} &= \sum_\mathrm{i} -\frac{\hbar^2}{2m}\nabla_\mathrm{i}^2 + \frac{1}{2}\sum_\mathrm{i}{\sum_\mathrm{j}}' \frac{e^2}{4\pi\epsilon_0|\mathbf{r}_\mathrm{i}-\mathbf{r}_\mathrm{j}|} + \sum_\mathrm{i}\sum_\mathrm{I}\frac{-e^2 Z_\mathrm{I}}{4\pi\epsilon_0|\mathbf{r}_\mathrm{i}-\mathbf{R}_\mathrm{I}|} \\ &= \hat{T} + \hat{V}_\mathrm{ee} + \hat{V}_\mathrm{ne}. \end{aligned} \tag{3.2}$$

Here the subscripts i and j denote electrons and I denotes a nucleus, m and e are

the mass and the charge of an electron respectively, Z_{I} is charge of the nucleus I, $\hbar$ is the reduced Plank constant, and ϵ_0 is the permittivity of vacuum. The first term in Eq.(3.2) is the kinetic energy of electrons denoted by an operator $\hat{T}$. The second term represents the electron-electron interaction energy and is denoted with $\hat{V}_{\mathrm{ee}}$. The prime on one of the summations in this term excludes the interaction of an electron with itself. The last term represents the electron-nucleus interaction energy and is denoted with $\hat{V}_{\mathrm{ne}}$. The total electronic energy E_{el} is obtained by solving the Eq.(3.3) for the electronic wave function Ψ_{el}.

$$\hat{\mathcal{H}}_{\mathrm{el}}\Psi_{\mathrm{el}} = E_{\mathrm{el}}\Psi_{\mathrm{el}}. \tag{3.3}$$

The total energy of a system E_{tot} is a sum of E_{el} and the nucleus-nucleus repulsion energy denoted with $\hat{V}_{\mathrm{nn}}$. Here

$$\hat{V}_{\mathrm{nn}} = \frac{1}{2}{\sum_{\mathrm{IJ}}}' \frac{Z_{\mathrm{I}}Z_{\mathrm{J}}e^2}{|\mathbf{R}_{\mathrm{I}} - \mathbf{R}_{\mathrm{J}}|}. \tag{3.4}$$

The Ψ_{el} is a function of all the electronic and nuclear coordinates. An infinite number of solutions exist for a given configuration of nuclei. Let us denote different wave function solutions by Ψ_{m} and the corresponding electronic energy value by E_{m}. The set of solutions $\{\Psi_{\mathrm{m}}\}$ is a complete set. The lowest energy state of the electronic system for given nuclear positions is also known as the ground state. Subscript 0 is used to denote this ground state: Ψ_0 is the ground state electronic wave function and E_0 is the ground state energy. All other states in the set $\{\Psi_{\mathrm{m}}\}$ are excited states. Ground state properties of a system are of major importance to the present study. Methods for finding the ground state of a system and its properties are often based on the variational principle, which is explained in the following section.

Variational principle

Consider a system in an electronic state Ψ. Measurement of the energy of the system results in one of the eigenvalues of the Hamiltonian. Average of many measurements of the energy $\langle E \rangle$ can be calculated using the following relation [94].

$$E[\Psi] = \frac{\langle \Psi|\hat{\mathcal{H}}|\Psi\rangle}{\langle \Psi|\Psi\rangle}. \tag{3.5}$$

Here $\langle \Psi|\hat{\mathcal{H}}|\Psi\rangle = \int \Psi^*\hat{\mathcal{H}}\Psi \, \mathrm{d}\mathbf{x}^N$ with $\mathbf{x}$ representing both the spatial and the spin

coordinates of an electron. The calculated energy from any trial wave function is always greater than or equal to the true ground state energy: $E[\Psi] \geq E_0$. Minimisation of the energy functional $E[\Psi]$ with respect to all the allowed electron wave functions Ψ gives the true ground state energy [94]:

$$E_0 = \min_{\Psi} E[\Psi]. \tag{3.6}$$

The electronic wave function which minimises the functional $E[\Psi]$ is the ground state electronic wave function Ψ_0. It is also the eigenstate which is associated with the lowest energy eigenvalue.

The functional $E[\Psi]$ needs to be minimised with respect to all the many-electron trial wave functions to determine the ground state energy and wave function : $\delta E[\Psi] = 0$. So as to ensure the normalisation of the final wave function, $\langle\Psi|\Psi\rangle = 1$, a method of Lagrange undetermined multipliers is used. The stationary values of a new functional G are determined in this method.

$$\delta[\langle\Psi|\hat{\mathcal{H}}|\Psi\rangle - E\langle\Psi|\Psi\rangle] = \delta G = 0. \tag{3.7}$$

Here E is the Lagrange multiplier. Out of all the solutions of Eq.(3.7), the lowest energy solution corresponds to the ground state. The wave function associated with the lowest energy is the ground state wave function.

For a 'N' electronic system, the Ψ is a function of '$3N$' spatial coordinates and 'N' spin coordinates. The computational cost of solving the Eq.(3.7) increases exponentially with the number of electrons in the system. Various approximate methods have been developed to reduce the computational cost. From the point of view of practical computation, the fastest methods reduce the problem to that of solving a single-electron Schrödinger equation within a potential that is a specified mean field created by all the electrons and nuclei. Density functional theory (DFT) based methods are the most successful of all these methods in the sense of their wide applicability and accuracy.

3.1 Density Functional Theory (DFT)

The electron density $\rho(\mathbf{r})$ is defined as the number of electrons per unit volume. It is a function of only three spatial coordinates and integration of this function over space gives the total number of electrons in the system. In DFT methods, the $\rho(\mathbf{r})$ is considered as the basic variable of a system.

3.1.1 Hohenberg-Kohn theorems

In 1965, Hohenberg and Kohn proved that the electronic charge density can be considered as the basic variable of a system. Their first theorem [95] states that the external potential can in principle be determined from the $\rho(\mathbf{r})$ within an additive constant. According to their second theorem [95], for any external potential an energy functional $E[\rho]$ can be defined in terms of the $\rho(\mathbf{r})$. The global minimum of the functional $E[\rho]$ is the ground state energy and the density corresponding to the ground state energy is the ground state density ρ_0. Hohenberg and Kohn therefore introduced a new variational method, expressed in terms of the $\rho(\mathbf{r})$, for determining the ground state energy. Since $\rho(\mathbf{r})$ determines the number of electrons and the external potential, the ground state wave function and all other electronic properties are determined in principle by the $\rho(\mathbf{r})$ alone. Therefore in DFT the electronic energy is written as a functional of the $\rho(\mathbf{r})$.

$$E_{\mathrm{v}}[\rho] = T[\rho] + V_{\mathrm{ee}}[\rho] + V_{\mathrm{ne}}[\rho] \tag{3.8}$$

$$= F^{\mathrm{HK}}[\rho] + \int \rho(\mathbf{r}) v(\mathbf{r}) \mathrm{d}\mathbf{r}. \tag{3.9}$$

Here $F^{\mathrm{HK}}[\rho]$ is the sum of kinetic energies of electrons and the electron-electron interaction energy. The subscript v to E denotes the explicit dependence of the electronic energy on the external potential v. An electron density ρ is said to be v representable if it is the density associated with an antisymmetric ground state wave function of a Hamiltonian of the form in Eq.(3.2) with some external potential v. In Hohenberg-Kohn theorems all the functionals are defined in terms of v representable densities.

Hohenberg and Kohn's second theorem is used to determine the ground state energy. Only those densities which would give the total number of electrons in the system on integration over space are considered in the variational method. If there are 'N' electrons in the system then $\int \rho(\mathbf{r})\mathrm{d}\mathbf{r} = N$. A new functional G is minimised to obtain the ground state energy:

$$\delta\big\{E_{\mathrm{v}}[\rho] - \mu\big[\int \rho(\mathbf{r})\mathrm{d}\mathbf{r} - N\big]\big\} = \delta G = 0. \tag{3.10}$$

Here μ is the Lagrange multiplier. The functional minimisation leads to an Euler-

Langrange equation

$$\mu = \frac{\delta E_{\rm v}[\rho]}{\delta \rho(\mathbf{r})} = v(\mathbf{r}) + \frac{\delta F^{\rm HK}[\rho(\mathbf{r})]}{\delta \rho(\mathbf{r})}. \tag{3.11}$$

Here $v(\mathbf{r})$ is the external potential due to nuclei. The $F^{\rm HK}[\rho]$ is independent of external potential. This functional is termed a 'universal functional' because the same functional can be used for any system. However, an exact functional form for the universal functional for an interacting electron system is not known, and generally regarded as impossible to know.

3.1.2 Kohn-Sham equations

Kohn and Sham (KS) [96] introduced an ingenious way to approximate $F^{\rm HK}[\rho]$ and hence to solve for the ground state properties of a system. For a given system of electrons and nuclei, consider a parallel auxiliary system, identical in every respect to the real system, except that the electrons do not interact with each other. I refer to the auxiliary system as a KS system. In order to reproduce the ground state density of the real system, the non-interacting electrons of the KS system move in an effective potential I refer to as the KS potential $v_{\rm KS}$. Therefore, the Hamiltonian of a KS system is free from the electron-electron interaction term. In Hartee atomic units e = 1, m = 1, $\hbar$ = 1, $1/(4\pi\epsilon_0) = 1$. Hartee atomic units are used in the following discussion. The Hamiltonian for a KS system is written as:

$$H_{\rm KS} = \sum_i -\frac{1}{2}\nabla_i^2 + \sum_i v_{\rm KS}(\mathbf{r}_i). \tag{3.12}$$

Let us suppose, for discussion purposes, that the material is non-magnetic, and contains an even number N of electrons, so that each of $N/2$ electronic orbitals is occupied by two electrons of opposite spin. The ground state wave function $\Psi_{\rm KS}$ of a KS system can be written as a Slater determinant of single orbital wave functions ϕ_i:

$$\Psi_{\rm KS} = \frac{1}{(N/2)!}\det[\phi_1\phi_2...\phi_{N/2}]. \tag{3.13}$$

The single particle orbitals are nothing other than the $N/2$ eigenfunctions corresponding to the $N/2$ lowest energy eigenvalues of the following equation.

$$\Big[-\frac{1}{2}\nabla^2 + v_{\rm KS}(\mathbf{r})\Big]\phi_i(\mathbf{r}) = \epsilon_i\phi_i(\mathbf{r}). \tag{3.14}$$

If the the single orbital wave functions are orthonormal, the kinetic energy of electrons $T_{\rm KS}$ in a KS system can be calculated from the orbital values:

$$\begin{aligned} T_{\rm KS} &= 2\langle\Psi_{\rm KS}|\sum_i^{N/2} -\frac{1}{2}\nabla_i^2|\Psi_{\rm KS}\rangle \\ &= 2\sum_i^{N/2}\langle\phi_i| -\frac{1}{2}\nabla^2|\phi_i\rangle \\ &= 2\sum_i^{N/2}\int \phi_i^*(\mathbf{r})(-\frac{1}{2}\nabla^2)\phi_i(\mathbf{r})\mathrm{d}\mathbf{r}. \end{aligned} \tag{3.15}$$

The charge density of a KS system can be calculated from the single particle orbitals:

$$\rho_{\rm KS}(\mathbf{r}) = 2\sum_i^{N/2}\phi_i^*(\mathbf{r})\phi_i(\mathbf{r}). \tag{3.16}$$

Since the KS electrons are non-interacting, the energy functional contains only the kinetic energy term and the electron-$v_{\rm KS}$ interaction energy term:

$$E[\rho_{\rm KS}] = T_{\rm KS}[\rho_{\rm KS}] + \int v_{\rm KS}(\mathbf{r})\rho_{\rm KS}(\mathbf{r})\mathrm{d}\mathbf{r}. \tag{3.17}$$

The ground state of a KS system is obtained by minimising this functional with respect to all densities that integrate over space to give 'N' electrons. It is done by minimising the following functional G.

$$G[\rho_{\rm KS}] = T_{\rm KS}[\rho_{\rm KS}] + \int v_{\rm KS}(\mathbf{r})\rho_{\rm KS}(\mathbf{r})\mathrm{d}\mathbf{r} - \mu\Big[\int \rho_{\rm KS}(\mathbf{r})\mathrm{d}\mathbf{r} - N\Big]. \tag{3.18}$$

As before, μ is the Lagrange multiplier associated with the constraint $\int \rho_{\rm KS}(\mathbf{r})\mathrm{d}\mathbf{r} = N$. The functional minimisation $\delta G[\rho_{\rm KS}] = 0$ leads to the following Euler-Lagrange equation.

$$\mu = v_{\rm KS}(\mathbf{r}) + \frac{\delta T_{\rm KS}[\rho_{\rm KS}]}{\delta\rho_{\rm KS}(\mathbf{r})}. \tag{3.19}$$

Now let us write the properties of an interacting N-electron system in terms of properties of a KS system containing the same number of electrons. Since the KS electrons do not interact with one another, the kinetic energy of KS electrons is not the same as that of interacting electrons. The second term in parenthesis

on the right-hand side of Eq.(3.20) contains this deviation.

$$T[\rho] = T_{\mathrm{KS}}[\rho] + (T[\rho] - T_{\mathrm{KS}}[\rho]). \tag{3.20}$$

Similarly the electron-electron interaction energy of an interacting system is written as a sum of two terms. One is the classical energy for a distribution of charge density J_{ee} and the other is a non-classical term containing the electronic exchange and correlation energies:

$$V_{\mathrm{ee}}[\rho] = J_{\mathrm{ee}}[\rho] + (V_{\mathrm{ee}}[\rho] - J_{\mathrm{ee}}[\rho]). \tag{3.21}$$

The J_{ee} can be easily calculated from the electron density:

$$J_{\mathrm{ee}}[\rho] = \frac{1}{2}\int\int \frac{\rho(\mathbf{r_1})\rho(\mathbf{r_2})}{|\mathbf{r_1} - \mathbf{r_2}|}\mathrm{d}\mathbf{r_1}\mathrm{d}\mathbf{r_2}. \tag{3.22}$$

Using the relations in Eqs. (3.22) and (3.21), the electronic energy functional of an interacting system in Eq.(3.8) can be written in terms of the energies of a KS system:

$$\begin{aligned} E[\rho] &= T_{\mathrm{KS}}[\rho] + J_{\mathrm{ee}}[\rho] + \int \rho(\mathbf{r})v(\mathbf{r})\mathrm{d}\mathbf{r} + (T[\rho] - T_{\mathrm{KS}}[\rho] + V_{\mathrm{ee}}[\rho] - J_{\mathrm{ee}}[\rho]) \\ &= T_{\mathrm{KS}}[\rho] + J_{\mathrm{ee}}[\rho] + \int \rho(\mathbf{r})v(\mathbf{r})\mathrm{d}\mathbf{r} + (E_{\mathrm{xc}}[\rho]). \end{aligned} \tag{3.23}$$

The last term in parentheses is termed the exchange-correlation energy E_{xc}. This functional is made of two contributions. The first one is the difference between the kinetic energies of electrons of an interacting system and its KS system. The second contribution is from the non-continuum part of the electron-electron interaction. The exact form of this functional is not known. Therefore approximate forms are used for E_{xc} in practice. The DFT of KS owes its success to the accuracy of these approximate exchange-correlation functionals, together with the fact that the kinetic energy of the KS system captures the essential physics of the true kinetic energy rather well. Widely used approximations for the exchange-correlation functionals are described in the next section.

In order to find the ground state density, the energy functional $E[\rho]$ needs to be minimised with respect to all densities that integrate to give 'N' electrons. It is done by minimising a functional G as in Eq.(3.10). This functional minimisation results in the following Euler-Lagrange equation.

$$\mu = v_{\text{eff}}(\mathbf{r}) + \frac{\delta T_{\text{KS}}[\rho]}{\delta \rho(\mathbf{r})}, \tag{3.24}$$

where

$$\begin{aligned} v_{\text{eff}}(\mathbf{r}) &= v(\mathbf{r}) + \frac{\delta J_{\text{ee}}[\rho]}{\delta \rho(\mathbf{r})} + \frac{\delta E_{\text{xc}}[\rho]}{\delta \rho(\mathbf{r})} && (3.25)\\ &= v(\mathbf{r}) + \int \frac{\rho(\mathbf{r}')}{|\mathbf{r} - \mathbf{r}'|} \mathrm{d}\mathbf{r}' + v_{\text{xc}}(\mathbf{r}) && (3.26)\\ &= v(\mathbf{r}) + v_{\text{H}}(\mathbf{r}) + v_{\text{xc}}(\mathbf{r}). && (3.27) \end{aligned}$$

Here $v(\mathbf{r})$ is the potential due to nuclei, $v_{\text{H}}(\mathbf{r})$, also known as a Hartree potential, is the local average classical Coulomb potential due to the electron charge distribution, and $v_{\text{xc}}(\mathbf{r})$ is the functional derivative of the exchange-correlation energy. On comparing Eq.(3.19) with Eq.(3.24), it is clear that the ground state density of an interacting electronic system would be same as the ground density of a non-interacting electronic system with a potential v_{KS} equal to v_{eff}. Therefore, the ground state density of an actual system can be calculated from the $N/2$ lowest energy single orbital wave functions obtained by solving Eq.(3.14) after replacing v_{KS} with v_{eff}. *i.e.*

$$\Big[-\frac{1}{2}\nabla^2 + v_{\text{eff}}(\mathbf{r}) \Big] \phi_i(\mathbf{r}) = \epsilon_i \phi_i(\mathbf{r}). \tag{3.28}$$

KS theory was extended to magnetic systems by U Von Barth et al. [97]. They derived the KS formulation for local spin density (LSD) calculations.

3.1.3 The exchange-correlation functional

Various approximations have been developed for this functional, on which the accuracy of the method rests. The simplest, successful, and still widely used approximation is the local density approximation (LDA) suggested by KS [96]. In this approximation, the exchange-correlation energy of an inhomogeneous electron gas is assumed to be local, meaning it can be written in the form:

$$E_{\text{xc}}^{\text{LDA}}[\rho] = \int \varepsilon_{\text{xc}}(\mathbf{r}) \rho(\mathbf{r}) \mathrm{d}\mathbf{r} \tag{3.29}$$

and the local exchange-correlation energy per electron ε_{xc} is assumed to be the same as that of a *homogeneous* electron gas whose density is the same as the density at the point $\mathbf{r}$: $\varepsilon_{\text{xc}}(\mathbf{r}) = \varepsilon_{\text{xc}}^{homo}(\rho(\mathbf{r}))$.

Dirac [98] derived an expression for exchange energy density ε_{x}, which is a part of $\varepsilon_{\mathrm{xc}}$, for a homogeneous electron gas:

$$\varepsilon_{\mathrm{x}}^{\mathrm{Dirac}}(\mathbf{r}) = 0.7386\rho^{\frac{1}{3}}(\mathbf{r}). \tag{3.30}$$

He proposed that the exchange effects could be incorporated into the electron density based methods using this relation. Later, improved approximations for exchange energy were developed by adopting the Dirac approximation to the exchange energy. Ceperley et al. [99] used a Quantum Monte Carlo simulation method for calculating the correlation energies $E_{\mathrm{c}}[\rho]$ of a homogeneous electron gas. The results from $E_{\mathrm{x}}[\rho]$ and $E_{\mathrm{c}}[\rho]$ calculations are used for determining fitting parameters in an approximated $E_{\mathrm{xc}}[\rho]$ functional.

The classical Coulomb electrostatic energy includes interaction of an electron with itself. This non-physical interaction is corrected by a part of $E_{\mathrm{xc}}[\rho]$. In LSD calculations this corrections is not perfect. Therefore Perdew et al. [100] proposed a correction to the energy functional $E[\rho]$. The correction is a sum of orbital dependent self interaction correction terms. This correction improved the accuracy of calculated electron densities, total energies, exchange-correlation energies. Self interaction correction is most important for elements with localised orbitals, but is more expensive to implement. However, conduction electrons in metallic systems are non-localised and efficient screening in these systems removes large part of error due to the self-interaction.

The LDA does not consider the corrections to $E_{\mathrm{xc}}[\rho]$ because of inhomogeneities in the electron densities in the neighbourhood of a point $\mathbf{r}$. Generalised gradient approximation (GGA) was introduced to correct this. In GGA the gradient of electron density is taken into account in addition to the local density at the point $\mathbf{r}$ [101]. In a second order GGA the $\varepsilon_{\mathrm{xc}}$ is written as a function of gradients up to second order [102]:

$$E_{\mathrm{xc}}^{\mathrm{GGA}}[\rho] \;=\; \int \varepsilon_{\mathrm{xc}}(\rho, |\nabla\rho|, \nabla^2\rho)\rho(\mathbf{r})\mathrm{d}\mathbf{r}. \tag{3.31}$$

When compared to a LSD approximation GGA improves total energies, energy barriers, structural energy differences [103, 104]. Calculated lattice parameters using a GGA are closer to the experimental values than those values calculated with a LDA but tend to overestimate them, whereas LDA tends to underestimate them. For all my calculations of the relative stability of various phases in a

binary TiNi system I used potentials constructed assuming a GGA [105] for the exchange-correlation functional.

Self-consistency

The objective of a DFT calculation is to find the charge density and associated ground state energy of an assembly of nuclei and electrons. The charge density depends on the wave functions through Eq.(3.16). For solving the single particle wave functions using the relation in Eq.(3.28), the effective potential must be known beforehand. The v_{eff} depends on the charge density. Therefore Eqs. (3.26), (3.28) and (3.16) are solved self-consistently [106]. An iterative method is used for this purpose. Various steps involved in each iteration are enumerated below.

1. An electron density generated by overlapping the spherically symmetric electron densities calculated for isolated atoms is used as the starting trial density $\rho_0^{\text{in}}(\mathbf{r})$.

2. Using the trial density, a trial Hartree potential $v_{\text{H}}(\mathbf{r})$ is obtained by solving the Poisson equation: $\nabla^2 v_{\text{H}}(\mathbf{r}) = -4\pi\rho_0^{\text{in}}(\mathbf{r})$.

3. A functional form for exchange correlation energy is assumed. Using this functional form and the trial density the exchange-correlation potential $v_{\text{xc}}(\mathbf{r})$ is calculated: $v_{\text{xc}}(\mathbf{r}) = \frac{\delta E_{\text{xc}}[\rho]}{\delta\rho(\mathbf{r})}$.

4. The $v_{\text{xc}}(\mathbf{r}), v_{\text{H}}(\mathbf{r})$ values are added to the external potential, $v(\mathbf{r})$, due to the nuclei to obtain an effective trial potential v_{eff}.

5. Using the v_{eff}, a set of single particle wavefunctions is obtained by solving the KS Eqs. (3.28).

6. A new electron density, referred to as the output density, of KS electrons is calculated from the single particle wave functions using the relation in Eq.(3.16).

7. A new trial electron density is constructed by mixing the output density and the previous trial density, and the next iteration of this cycle can be entered with this new input density.

8. An updated value of the total electronic energy is calculated according to:

$$E[\rho] = 2\sum_{i}^{N/2}\epsilon_i - \frac{1}{2}\int\int\frac{\rho(\mathbf{r_1})\rho(\mathbf{r_2})}{|\mathbf{r_1}-\mathbf{r_2}|}\mathrm{d}\mathbf{r_1}\mathrm{d}\mathbf{r_2} + E_{\mathrm{xc}}[\rho] - \int v_{\mathrm{xc}}(\mathbf{r})\rho(\mathbf{r})\mathrm{d}\mathbf{r}. \quad (3.32)$$

The steps (2) to (8) are followed in each iteration. The iterative procedure is stopped when the charge density is converged to a self consistent value within a specified tolerance. The self consistent density is the ground state density and the energy calculated with this charge density, which should also have converged to a satisfactory tolerance, is the ground state energy. So as to increase the speed of convergence various schemes have been proposed for mixing output and input charge densities or potentials.

Mixing methods

Mixing schemes suggested by Broyden [107] and Pulay [108] are based on a quasi-Newton-Raphson method for solving non-linear simultaneous equations. Paul Bendt et al. [109] applied the Broyden mixing method to a DFT problem and calculated the self-consistent-field in Si and ZnS in few iterations. In the Pulay mixing scheme an optimised charge density at a given iteration number n is calculated as a linear combination of input charge densities $\{\rho^{\mathrm{in}}_{\mathrm{n\text{-}i}}(\mathbf{r})\}$ from a few previous iterations:

$$\rho^{\mathrm{opt}}_{\mathrm{n}}(\mathbf{r}) = \sum_{\mathrm{i}=0}^{\mathrm{s\text{-}1}}\alpha_{\mathrm{i}}\rho^{\mathrm{in}}_{\mathrm{n\text{-}i}}(\mathbf{r}). \quad (3.33)$$

Here $\sum_{\mathrm{i}=0}^{\mathrm{s\text{-}1}}\alpha_{\mathrm{i}} = 1$. The difference between output density $\rho^{\mathrm{out}}_{\mathrm{n}}(\mathbf{r})$ and input density $\rho^{\mathrm{in}}_{\mathrm{n}}(\mathbf{r})$ is the error and is denoted with residue $\mathrm{R_n}(\mathbf{r})$. It is assumed that the error $\mathrm{R_n}(\mathbf{r})$ is a linear combination of errors from previous iterations with the same linear coefficients in Eq.(3.33):

$$R^{\mathrm{opt}}_{\mathrm{n}}(\mathbf{r}) = \sum_{\mathrm{i}=0}^{\mathrm{s\text{-}1}}\alpha_{\mathrm{i}}R_{\mathrm{n\text{-}i}}(\mathbf{r}). \quad (3.34)$$

The coefficients α_{i} are determined by minimising $\langle R^{\mathrm{opt}}_{\mathrm{n}}|R^{\mathrm{opt}}_{\mathrm{n}}\rangle$ with a constraint $\sum_{\mathrm{i}=0}^{\mathrm{s\text{-}1}}\alpha_{\mathrm{i}} = 1$ [110]. So as to efficiently cover the solution space, the $\rho^{\mathrm{opt}}_{\mathrm{n}}$ is mixed with the output charge density $\rho^{\mathrm{out}}_{\mathrm{n}}$ to create an input charge density for the next

iteration:

$$\rho^{\text{in}}_{\text{n+1}}(\mathbf{r}) = (1-\beta)\rho^{\text{opt}}_{n}(\mathbf{r}) + \beta\rho^{\text{out}}_{n}(\mathbf{r}). \tag{3.35}$$

Here β is a mixing parameter. The convergence of this method strongly depends on the choice of β.

3.1.4 Pseudopotential approximation

Core electrons in materials are nearer to the nuclei and are strongly attracted to the nuclei when compared to valence electrons. In general the core electrons do not take part in bonding. Most of the physical properties related to bonding and cohesion are determined by the valence electrons. Therefore the wave functions of core electrons in crystalline materials are often approximated by the free atom wave functions. And only the wave functions of valence electrons are assumed to be modified according to the wave functions of valence electrons in the neighbouring atoms. According to this approximation the nuclei and the core electrons are considered to be fixed and the valence electrons feel a screened potential from the nuclei [111]. This approximation is known as a frozen core approximation and it reduces the number of wave functions in electronic structure calculations.

The valence electron wave functions feel a strong potential from the nuclei in the core region, and the valence wave functions are orthogonal to the wave functions of core electrons. For these two reasons, the valence electronic wave functions have an oscillatory nature near the nucleus and in the region of the core electrons [112]. In interstitial regions between the cores the potential is very weak and slowly varying. Therefore, the valence wave functions are much smoother in the interstitial regions. If a plane wave basis is used for expanding the wave functions, a larger basis set is needed to describe the oscillatory nature of the valence wave functions in the core region [111]. The computational cost increases with the size of the plane wave basis. However, the core oscillations of valence wave functions interact less with other valence wave functions and are therefore less important for bonding.

In a pseudopotential method, the system of nuclei and core electrons are replaced with an effective, and much smoother potential [106], which is used instead of the external potential $v(\mathbf{r})$ in the KS equations. Since the core electrons are absent, and the pseudopotential is shallower than the real potential in the core region, the 'pseudo' wavefunctions, which replace the real single-particle valence electron wave functions do not need to oscillate so much, and a much smaller plane wave basis is enough to describe the wave functions. The pseudopotentials

are constructed in such a way that the pseudo wave functions calculated using them have the same energies as the true wave functions in an isolated atom. Furthermore the pseudo wave function and the true wave function of a valence electron should be identical outside a certain core radius [112].

If the charge density calculated from the real wave function is same as that calculated from the pseudo wave function at every point in space and the pseudo wave function is normalised, the pseudopotential ensuring these two conditions is called a *norm conserving pseudopotential* [113]. Norm conservation avoids the problem of an excess charge in the core region that previous pseudopotential methods had to deal with. The KS formulation using a norm conserving pseudopotential approximation is well described by Yin et al. [111]. A momentum space formulation of KS equations under the pseudopotential approximation is described by Ihm et al.[114].

A serious disadvantage of all traditional pseudopotential methods is that the information about the charge density and wave functions near the nucleus is lost, or it can only be recovered by an additional computation. An associated disadvantage of purely plane wave methods, even with a pseudopotential approximation, is that they still require quite a large basis set to accurately describe the first row elements, transition metals and rare earth elements [115], in which the wave functions of the important electrons are not nearly free electron like. One way forward is to use a mixed basis of plane waves and localized orbitals [116, 117, 118], however the most widely used approach is probably the PAW method described below.

3.1.5 Projector augmented wave method

The projector augmented wave (PAW) method, which I decided to use for most of the calculations described in this thesis, combines advantages of all-electron methods and pseudopotential methods. In the PAW method the 'real' single particle wave functions of valence electrons are calculated from a corresponding auxiliary pseudo wave function by a linear transformation. The transformation operator is chosen in such a way that the all electron (AE) wave function has the nodal structure of a true valence electron wave function in the core region. The pseudo (PS) wave function is a smooth wave function obtained by solving a modified single particle KS equations [115, 119]. This method was proposed by Blöchl [120]. Let us define $|\tilde{\Psi}_n^v\rangle$ as the smooth PS wave function and $|\Psi_n^v\rangle$ as the AE wave function. The linear transformation operator $\hat{\mathcal{T}}$ is defined in such a way

that $|\Psi_n^v\rangle = \hat{\mathcal{T}}|\tilde{\Psi}_n^v\rangle$.

In a PAW method space is divided into two regions: an *augmentation* region around each nucleus, and interstitial region between the augmentation regions known as an *envelope* region. In the envelope region, the AE wave function is the same as the PS wave function. The augmentation region around each atom 'a' is confined by a sphere of radius $r_{\rm a}^{\rm c}$ from its nucleus at $\mathbf{R}_{\rm a}$. The $r_{\rm a}^{\rm c}$ values are generally chosen as half of the nearest neighbour distance. Each augmentation region contributes to the transformation operator:

$$\hat{\mathcal{T}} = 1 + \sum_{\rm a} \hat{\mathcal{T}}^{\rm a}. \tag{3.36}$$

Here $\hat{\mathcal{T}}^{\rm a}$ is an operator representing contribution from the augmentation region around an atom 'a'. It is expressed in terms of partial waves of valence electrons of isolated atoms.

For an isolated atom the single particle wave functions can be obtained by solving the SE. In the frozen core approximation, the core states are localised in the core region in isolated atoms and do not change much in multi-atom environments. Therefore, core states are treated separately. From the wave function solutions of an isolated atom, only the valence wave functions which are orthogonal to the core states are considered for defining the operators $\hat{\mathcal{T}}^{\rm a}$. Let us call these wave functions as AE partial waves $|\phi_i\rangle$. For each AE partial wave, a smooth PS partial wave $|\tilde{\phi}_i\rangle$ is determined by solving the SE of isolated atom after replacing the external potential with an adjustable pseudo potential [120]. The adjustable parameter in the potential is chosen in such a way that the PS partial wave energy is equal to the AE partial wave energy. And, the $|\tilde{\phi}_i\rangle$ is equal to the $|\phi_i\rangle$ in the envelope region: $|\tilde{\phi}_i\rangle = |\phi_i\rangle$ when $|\mathbf{r} - \mathbf{R}_{\rm a}| > r_{\rm c}^{\rm a}$.

The partial waves $|\tilde{\phi}_i\rangle$ and $|\phi_i\rangle$ are used to define the transformation operator. Application of the transformation operator to the PS partial waves must result in the AE partial waves: $|\phi_i\rangle = \hat{\mathcal{T}}|\tilde{\phi}_i\rangle$. Within the augmentation region around atom 'a' only $\hat{\mathcal{T}}^{\rm a}$ contributes to the operator $\hat{\mathcal{T}}$. This fact is used to define the operator $\hat{\mathcal{T}}^{\rm a}$.

$$|\phi_i^{\rm a}\rangle = (1 + \hat{\mathcal{T}}^{\rm a})|\tilde{\phi}_i^{\rm a}\rangle \quad i \in \text{a and } |\mathbf{r} - \mathbf{R}_{\rm a}| < r_{\rm a}^{\rm c} \tag{3.37}$$

$$\hat{\mathcal{T}}^{\rm a}|\tilde{\phi}_i^{\rm a}\rangle = |\phi_i^{\rm a}\rangle - |\tilde{\phi}_i^{\rm a}\rangle = \sum_j (|\phi_j^{\rm a}\rangle - |\tilde{\phi}_j^{\rm a}\rangle)\langle\tilde{p}_j^{\rm a}|\tilde{\phi}_i^{\rm a}\rangle. \tag{3.38}$$

Here $\langle\tilde{p}_j^{\mathrm{a}}|$ are projector functions. The projector functions are localised to the augmentation region and have orthogonal relations with the PS partial waves: $\langle\tilde{p}_i^{\mathrm{a}}|\tilde{\phi}_j^{\mathrm{a}}\rangle = \delta_{i,j}$ for $i, j \in \mathrm{a}$. The projector functions are used for expanding the PS wave functions within the augmentation region and hence must form a complete set within the augmentation region. The projector functions must fulfil the condition $\sum_i |\tilde{\phi}_i^{\mathrm{a}}\rangle\langle\tilde{p}_i^{\mathrm{a}}| = 1$ with the PS partial waves [120]. The atom centred transformation $\hat{\mathcal{T}}^{\mathrm{a}}$ does not have any effect outside the augmentation region.

The complete transformation operator is written as the summation of local transformation operators in the augmentation using the relations in Eqs. (3.38) and (3.36):

$$\hat{\mathcal{T}} = 1 + \sum_{\mathrm{a}} \sum_{i} (|\phi_i^{\mathrm{a}}\rangle - |\tilde{\phi}_i^{\mathrm{a}}\rangle)\langle\tilde{p}_i^{\mathrm{a}}|. \tag{3.39}$$

The AE true wave function is calculated from the valence PS wave function using this transformation.

$$|\Psi_n^v\rangle = |\tilde{\Psi}_n^v\rangle + \sum_{\mathrm{a}} \sum_{i} (|\phi_i^{\mathrm{a}}\rangle - |\tilde{\phi}_i^{\mathrm{a}}\rangle)\langle\tilde{p}_i^{\mathrm{a}}|\tilde{\Psi}_n^v\rangle \tag{3.40}$$

$$= |\tilde{\Psi}_n^v\rangle + \sum_{\mathrm{a}} \sum_{i} |\phi_i^{\mathrm{a}}\rangle\langle\tilde{p}_i^{\mathrm{a}}|\tilde{\Psi}_n^v\rangle - \sum_{\mathrm{a}} \sum_{i} |\tilde{\phi}_i^{\mathrm{a}}\rangle\langle\tilde{p}_i^{\mathrm{a}}|\tilde{\Psi}_n^v\rangle. \tag{3.41}$$

Within the envelope regions, the AE wave function is same as that of the PS wave function. Since $|\phi_i^{\mathrm{a}}\rangle = |\tilde{\phi}_i^{\mathrm{a}}\rangle$ within the envelope region, the last two terms in the right hand side of Eq.(3.41) exactly cancel each other. Within the augmentation regions, the first term and the last term on the right hand side of Eq.(3.41) exactly cancel each other and the atom centered AE partial waves determine the true wave function. Because of the orthogonality of the AE partial waves with the core states, the true wave function has a nodal structure ensuring the orthogonality with the core states. Therefore, the PAW method determines the exact wave function in all regions of space.

Since PAW method determines the wave function more accurately in all regions in space, all properties which depend on the wave function can be calculated more accurately. My task is to understand the MT in TiNi-based shape memory alloys. All elements in this study (Ni, Ti, Hf, and Zr) are transition metals. I used two codes *Vienna ab initio Simulations Package* (VASP) [110] and *Quantum Espresso* (QE) [121] for calculating the total energy. Both codes use a plane wave basis for expanding the wave functions. Using the PAW method it is pos-

sible to describe the transition metals more accurately with a small plane wave basis in the augmentation region [120]. Therefore, I used PAW potentials in all total energy calculations. PAW potentials are not readily available to use with the *Quantum Espresso*. Therefore the *atompaw* code developed by Holzwarth et al. [122] was used for generating the PAW potentials for use in the *Quantum Espresso* code. PAW potentials provided with the *VASP* package were used in all calculations with *VASP*.

3.1.6 Periodicity

In a crystal, the potential for the electrons is a periodic function of position $\mathbf{r}$. This periodicity has enormous simplifying consequences for the methods of calculation used in this project both for electrons and phonons. The single-particle wave functions of electrons moving in a periodic potential are written as the product of a wavelike part and a lattice periodic part as a consequence of Bloch's theorem [123, 124]. *i.e.*

$$\phi_{\mathbf{k}}(\mathbf{r}) = \exp[i\mathbf{k}\cdot\mathbf{r}]\eta_{\mathbf{k}}(\mathbf{r}) \tag{3.42}$$

Here $\eta_{\mathbf{k}}(\mathbf{r})$ has the periodicity of the lattice and $\mathbf{k}$ is identified as the wavevector and one of the labels of the eigenstates of the KS equation. Using this form for wave functions, a single particle wave function at any point in a crystal can be written in terms of its value inside any single unit cell. The cell-periodic part of a wave function $\eta_{\mathbf{k}}(\mathbf{r})$ is expanded in a suitable basis. A plane wave basis contains plane waves at the reciprocal lattice vectors ($\mathbf{y}$), $\eta_{\mathbf{k}}(\mathbf{r})$ has the form of a Fourier series in this basis:

$$\eta_{\mathbf{k}}(\mathbf{r}) = \sum_{\mathbf{y}} c_{\mathbf{k}+\mathbf{y}} \exp[i\mathbf{y}\cdot\mathbf{r}] \tag{3.43}$$

and hence

$$\phi_{\mathbf{k}}(\mathbf{r}) = \sum_{\mathbf{y}} c_{\mathbf{k}+\mathbf{y}} \exp[i(\mathbf{y}+\mathbf{k})\cdot\mathbf{r}]. \tag{3.44}$$

Here $\mathbf{y}$ is a discrete lattice vector in reciprocal space as defined below. The formalism for the normal modes of vibration is entirely analogous; a normal mode can also be characterized by an amplitude and direction for each atom within the unit cell, analogous to $\eta_{\mathbf{k}}(\mathbf{r})$, modulated by a plane wave $\exp[i\mathbf{k}\cdot\mathbf{r}]$ [125].

Real and reciprocal lattices

The unit cell of the crystal lattice is defined by lattice vectors $(\mathbf{a}_1, \mathbf{a}_2, \mathbf{a}_3)$ and the reciprocal lattice of the crystal by $(\mathbf{b}_1, \mathbf{b}_2, \mathbf{b}_3)$, where

$$\mathbf{b}_i = \frac{2\pi\epsilon_{ijk}\mathbf{a}_j \times \mathbf{a}_k}{\Omega} \tag{3.45}$$

and the unit cell volume is

$$\Omega = \mathbf{a}_1 \cdot \mathbf{a}_2 \times \mathbf{a}_3. \tag{3.46}$$

Hence

$$\mathbf{a}_i \cdot \mathbf{b}_j = 2\pi\delta_{ij}. \tag{3.47}$$

A reciprocal lattice vector $\mathbf{y}$ as used in the expansion of a wave function in Eq.(3.44) therefore has the form

$$\mathbf{y} = n_1\mathbf{b}_1 + n_2\mathbf{b}_2 + n_3\mathbf{b}_3 \tag{3.48}$$

where the $\{n_i\}$ are integers.

For the purpose of defect calculations as well as the calculation of phonon frequencies it is useful to define periodic *supercells* which fill space with periodic boundary conditions on the atomic coordinates. Finite crystals, with periodic boundary conditions, are described by a supercell with edges $\mathbf{A}_1, \mathbf{A}_2, \mathbf{A}_3$, which in a perfect bulk crystal are integer multiples of the unit cell sides:

$$\mathbf{A}_i = N_i\mathbf{a}_i. \tag{3.49}$$

The total number of unit cells in the supercell is given by

$$N = N_1N_2N_3. \tag{3.50}$$

Unit cells within the supercell are indexed by the integer l, where $0 < l \leq N$ and located with their origins at the lattice vector $\mathbf{x}(l)$. Thus

$$\mathbf{x}(l) = l_1\mathbf{a}_1 + l_2\mathbf{a}_2 + l_3\mathbf{a}_3 \tag{3.51}$$

where the integers l_i are in the range $0 \leq l_i < N_i$.

Constraint of supercell periodicity

For calculating the displacements and frequencies of normal modes (phonon frequencies) with DFT by the most direct method, all pattens of displacement within a supercell must be periodically repeated. Thus the only accessible k-vectors are those describing waves with the periodicity of the superlattice. That is, $\mathbf{k}$ must be a reciprocal lattice vector *of the superlattice* in the same way as $\mathbf{y}$ is a reciprocal lattice vector of the lattice. If the reciprocal basis vectors of the superlattice are defined by $(\mathbf{B}_1, \mathbf{B}_2, \mathbf{B}_3)$, by analogy with Eq.(3.45)

$$\mathbf{B}_i = \frac{2\pi\epsilon_{ijk}\mathbf{A}_j \times \mathbf{A}_k}{N\Omega} \tag{3.52}$$

and the unit cell volume of the superlattice is

$$N\Omega = \mathbf{A}_1 \cdot \mathbf{A}_2 \times \mathbf{A}_3. \tag{3.53}$$

The $\mathbf{B}_i$ can be expressed in terms of the lattice vectors of the crystal using Eqs. (3.49) and (3.50):

$$\mathbf{B}_i = \frac{2\pi\epsilon_{ijk}\mathbf{a}_j \times \mathbf{a}_k}{N_i\Omega} \tag{3.54}$$

$$= \mathbf{b}_i/N_i. \tag{3.55}$$

Thus the allowed k-vectors are given by

$$\mathbf{k} = \frac{n_1}{N_1}\mathbf{b}_1 + \frac{n_2}{N_2}\mathbf{b}_2 + \frac{n_3}{N_3}\mathbf{b}_3. \tag{3.56}$$

The upper and lower bounds on the integers $\{n_i\}$ are determined by the condition that $\mathbf{k}$ is in the first Brillouin zone (FBZ), that is:

$$-\frac{1}{2} < \frac{n_i}{N_i} \leq \frac{1}{2}. \tag{3.57}$$

Any k-vector in this set satisfies

$$\mathbf{k} \cdot \mathbf{A}_i = 2\pi n_i. \tag{3.58}$$

The number of allowed wave vectors increases proportionally to the volume of a superlattice. For an infinite solid the exact wave vectors span a continuous vector space in the FBZ. The application of Bloch's theorem to an infinite solid

converts the problem of solving for an infinite number of wave functions to a problem of solving for a finite number of occupied states at an infinite number of k-vectors in the FBZ [106]. The occupied states at every wave vector in the FBZ contribute to the charge density and determine the potential. Therefore, in principle the occupied wave functions need to be calculated at an infinite number of k-vectors. On the other hand, the form of a wave function varies continuously with its k-vector. Therefore, any quantity that is integrated over all the wave functions in the FBZ can be represented by a weighted sum over a set of k-points in the FBZ, with an accuracy that improves with the size of the sample.

An approximate electron density and effective potential are therefore always calculated from the wave functions at discrete set of k-points. Various methods have been developed for obtaining more accurate potential and contribution to the total energy from the filled electronic states by sampling the k-points in the FBZ. The accuracy of an approximation, e.g. the early sampling method of Chadi et al. [126], can be systematically increased by adding more points to the k-point set. Monkhorst and Pack [127] suggested simply a set of uniformly spaced points in the FBZ, and theirs is the sampling method I have used in all the total-energy calculations described here.

The summation in Eq.(3.44) contains an infinite number of basis functions. The kinetic energy of a plane wave $\exp[i(\mathbf{k}+\mathbf{y})\cdot\mathbf{r}]$ is $(1/2)|\mathbf{k}+\mathbf{y}|^2$. Electrons with a lower kinetic energy are more important than those with a higher kinetic energy [106]. Hence, the plane wave expansion is truncated at a certain cut-off value (E_{cut}). Only $\mathbf{y}$ vectors satisfying the following condition are included in the expansion in Eq.(3.44).

$$\frac{1}{2}|\mathbf{k}+\mathbf{y}|^2 \leq E_{\text{cut}}. \tag{3.59}$$

This criterion determines the number of basis functions and makes the basis finite.

3.1.7 Forces on atoms

The forces acting on atoms in a given atomic configuration are required for efficient and accurate geometry optimisation (minimization of energy with respect to atomic coordinates) and for calculating the interatomic force constants (IFCs). The force on a particular atom I is defined in a static lattice as the derivative of the total energy with respect to its displacement, with the self-explanatory notation:

$$\mathbf{F}_{\mathrm{I}} = -\frac{\partial E_{\mathrm{tot}}}{\partial \mathbf{u}(\mathbf{R}_{\mathrm{I}})}. \tag{3.60}$$

The IFCs are defined as the second derivatives of the total energy with respect to nuclear displacements, evaluated about the equilibrium positions of the nuclei. The Hellmann-Feynman theorem [128, 129] is exploited for calculating the electronic contribution to the forces on the nuclei.

$$\begin{aligned} \mathbf{F}_{\mathrm{I,el}} &= -\frac{\partial E}{\partial \mathbf{u}(\mathbf{R}_{\mathrm{I}})} = -\frac{\partial \langle \Psi | \hat{\mathcal{H}} | \Psi \rangle}{\partial \mathbf{u}(\mathbf{R}_{\mathrm{I}})} \\ &= -\int \mathrm{d}\mathbf{r} \rho(\mathbf{r}) \frac{\partial v_{\mathrm{eff}}}{\partial \mathbf{u}(\mathbf{R}_{\mathrm{I}})}. \end{aligned} \tag{3.61}$$

The force of repulsion on a particular atomic nucleus from the nuclei of all other atoms is given by the derivative of

$$V_{\mathrm{I}}(\mathbf{R}_{\mathrm{I}}) = \sum_{J}{}' \frac{Z_{\mathrm{I}} Z_{\mathrm{J}}}{|\mathbf{R}_{\mathrm{I}} - \mathbf{R}_{\mathrm{J}}|}. \tag{3.62}$$

$$\mathbf{F}_{\mathrm{I,ion}} = -\frac{\partial V_{\mathrm{I}}(\mathbf{R}_{\mathrm{I}})}{\partial \mathbf{u}(\mathbf{R}_{\mathrm{I}})} \tag{3.63}$$

which is evaluated using an Ewald method [114]. The total force on an atom is a sum of electronic and ionic contributions: $\mathbf{F}_{\mathrm{I}} = \mathbf{F}_{\mathrm{I,el}} + \mathbf{F}_{\mathrm{I,ion}}$. To obtain an equilibrium geometry of a structure, all the atoms are relaxed until the forces on all atoms become less than some convergence threshold. By the same method, the forces induced by a displacement of an atom from its equilibrium position can be calculated. The resulting forces on all the other atoms are used for calculating the *dynamical matrix*, from which the frequencies of normal modes of vibration are obtained as an eigenvalue problem. This is the 'small displacement' method for studying lattice dynamics in the harmonic approximation, which I discuss in the following section.

3.2 Lattice dynamics in the harmonic approximation

Although we refer to atomic positions and structural parameters, these are actually the averages over time. Atoms vibrate about their mean positions and atomic

vibrations are responsible for various dynamical properties of a material, including major contributions to electrical resistivity, thermal conductivity, superconductivity, thermal expansion, interaction with neutrons and electrons ...etc [130]. Atomic vibrations are also responsible for diffusion and are very important for most phase transition processes. MT involve a cooperative movement of atoms in a very short time and lattice dynamics play an important role in it. If the atomic displacements are small, which is the case at low temperatures, the atoms vibrate in a harmonic potential and the harmonic approximation (HA) is valid. This section describes the lattice dynamics in the HA in crystalline materials. The notation used by Max Born et al. [131] is adopted in this discussion.

Let us describe the unit cell of a crystalline material with its axes $\mathbf{a_i}$ (i=1,2,3) and assume that each unit cell has 'r' atoms in its basis. Any unit cell is chosen as a reference unit cell and all other unit cell are indexed with respect to the reference unit cell. Vectors $\mathbf{x}$ and $\mathbf{u}$ are used to denote the position vector and the displacement vector of an atom respectively. The origin of reference unit cell (O) is chosen as the reference origin for the crystal. The position vector of the origin of the reference unit cell is the zero vector: $\mathbf{x}(\mathrm{O}) = \mathbf{0}$. As described in the Section(3.1.6), each unit cell is denoted with a three index label l and the position vector from O to the origin of the unit cell determines the l_i. The atoms in the basis are denoted with a label 's' and $\mathbf{x}(s)$ denotes the position vector of atom 's' in the reference unit cell. With this notation the mean position vector of atom 's' in the unit cell indexed with 'l' is denoted $\mathbf{x}(^{l}_{s})$ and is given by $\mathbf{x}(l)$+$\mathbf{x}(s)$. Likewise, $\mathbf{u}(^{l}_{s})$ denotes the displacement of atom 's' in the unit cell 'l' from its mean position.

The classical Hamiltonian H_{n} of the nuclei contains kinetic energy and potential energy terms. The potential energy Φ is expanded as a Taylor series in atomic displacements from the mean positions. *i.e.*

$$H_{\mathrm{n}} = \frac{1}{2}\sum_{ls\alpha} m_s \dot{u}^2_\alpha(^{l}_{s}) + \Phi, \tag{3.64}$$

$$\Phi = \Phi_0 + \sum_{ls\alpha} \Phi_\alpha(^{l}_{s}) u_\alpha(^{l}_{s}) + \frac{1}{2}\sum_{ls\alpha}\sum_{l's'\beta} u_\alpha(^{l}_{s})\Phi_{\alpha\beta}(^{ll'}_{ss'})u_\beta(^{l'}_{s'}) + \ldots. \tag{3.65}$$

Here Φ_0 is the potential energy of the crystal when all atoms are in their mean positions. At equilibrium the forces $\Phi_\alpha(^{l}_{s})$ on all atoms must vanish [131]. If the atomic displacements are small, the third and higher degree terms in displacement can be neglected. This is a HA and is valid at low temperatures. In this

approximation

$$H_{\mathrm{n}}^{\mathrm{har}} = \frac{1}{2}\sum_{ls\alpha} m_s \dot{u}_\alpha^2\binom{l}{s} + \Phi_0 + \frac{1}{2}\sum_{ls\alpha}\sum_{l's'\beta} u_\alpha\binom{l}{s}\Phi_{\alpha\beta}\binom{ll'}{ss'}u_\beta\binom{l'}{s'}. \tag{3.66}$$

The expansion co-efficient $\Phi_{\alpha\beta}\binom{ll'}{ss'}$ is an IFC. It is one element of the second order force constant matrix corresponding to two atoms $\binom{l}{s}$ and $\binom{l'}{s'}$. In the HA, $\Phi_{\alpha\beta}\binom{ll'}{ss'}$ denotes the negative of the force on an atom $\binom{l}{s}$ in the α-direction when an atom $\binom{l'}{s'}$ is displaced by a unit distance along the β-direction [131]. If the $\Phi_{\alpha\beta}\binom{ll'}{ss'}$ values are known for all atom pairs in a crystal, the equation of motion (3.67) for all atoms can be solved simultaneously.

$$F_\alpha\binom{l}{s} = m_s\ddot{u}_\alpha\binom{l}{s} = -\frac{\partial\Phi}{\partial u_\alpha\binom{l}{s}} = -\sum_{l's'\beta}\Phi_{\alpha\beta}\binom{ll'}{ss'}u_\beta\binom{l'}{s'}. \tag{3.67}$$

Wave form for the displacements

Since Bloch's theorem is a consequence of the translational lattice symmetry of the Hamiltonian, and defines the form of the one-dimensional representations of the translation group, it is no surprise to find that the normal modes of vibration, regarded as travelling waves, can be classified in a similar way. Whereas in the theory of electronic states the Hamiltonian matrix, such as might represent the KS equations, is the object with the lattice symmetry, in the theory of lattice vibrations this role is played by the *dynamical matrix*, to be defined below. The normal modes can be classified as travelling waves with a wave vector $\mathbf{k}$ and an angular frequency ω. Quanta of energy associated with the atomic vibrations are termed phonons. In the plane wave form the displacement of all atoms in a crystal are related to the displacement of atoms in a reference unit cell ($l = [0,0,0]$) as follows [125].

$$u_\alpha\binom{l}{s} = u_\alpha\binom{0}{s}\exp[i\mathbf{k}\cdot\mathbf{x}\binom{l}{s} - i\omega t] \tag{3.68}$$

$$= \frac{1}{\sqrt{m_s}}w_\alpha\binom{0}{s}\exp[i\mathbf{k}\cdot\mathbf{x}\binom{l}{s} - i\omega t] \tag{3.69}$$

Here $w_\alpha\binom{0}{s}$ is the amplitude in direction α of an atomic displacement scaled by the square root of its mass. This quantity turns out to be more convenient to work with than the unscaled displacements, as we shall see. As in the theory of electron states, it suffices to find solutions at all the wave vectors in any single reciprocal unit cell, since the solutions in all reciprocal unit cells are the same.

The FBZ is generally chosen for this purpose because it is the most symmetric [131]. I used DFT to calculate the required IFCs, with the small displacement method described in the following section.

3.2.1 Small displacement method

In a small displacement method, a supercell is constructed by suitably repeating the unit cell in three directions, and the atoms are relaxed to their equilibrium positions. The direct displacement method for calculating IFCs is then a direct application of Eq.(3.67).

One atom in the supercell is displaced a small distance along a Cartesian axis. This displacement induces forces on all other atoms in the supercell. These forces are calculated using the formulation described in the Section(3.1.7). In the HA, forces are related to the IFC and the displacements through the following relation [131, 132]:

$$F_\alpha\binom{l}{s} = -\sum_\beta \Phi_{\alpha\beta}\binom{ll'}{ss'} u_\beta\binom{l'}{s'}. \tag{3.70}$$

Since only one atom in the supercell is displaced in a calculation, there are only three terms in the summation in Eq.(3.70). Hence, the IFC correspond to the displaced atom and all atoms in the supercell can be calculated from the forces and the displacements [133, 134].

$$\Phi_{\alpha\beta}\binom{ll'}{ss'} = -\frac{\partial F_\alpha\binom{l}{s}}{\partial u_\beta\binom{l'}{s'}} \approx -\frac{F_\alpha\binom{l}{s}}{u_\beta\binom{l'}{s'}}. \tag{3.71}$$

In connection with this method it is important to discuss the approximation introduced by using a supercell of finite size, since the forces in Eq.(3.71) are not exactly the forces induced by the displacement $u_\beta\binom{l'}{s'}$ of just one atom, but by the same displacements of all its periodic images too. We shall return to this difficulty. The other intrinsic approximation is that the summation in Eq.(3.67) implies that the motion of an atom $\binom{l}{s}$ depends on its interaction with all other atoms $\binom{l'}{s'}$ in space. In practice the $\Phi_{\alpha\beta}\binom{ll'}{ss'}$ may decay rapidly with the interaction distance, but this is system dependent. In any case the $\Phi_{\alpha\beta}\binom{ll'}{ss'}$, at least in metals, are assumed to be zero beyond a certain cut-off distance [135] and only terms up to the cut-off distance are included in the calculations. This means that the interaction range included in the dynamics is limited by the size of the supercell [136].

In a single run of the code, in which the forces on all atoms in the supercell

induced by a displacement of one atom is calculated, one column of the force constant matrix is obtained. Therefore, without exploiting symmetry, three such calculations are required for each inequivalent atom in the reference unit cell to obtain all the possible matrix elements. Symmetry elements of crystals can be used to reduce the number of calculations [135, 136].

The force constant matrices must be symmetric and must satisfy a translational invariance condition [131]. *i.e.*

$$\Phi_{\alpha\beta}\binom{ll'}{ss'} = \Phi_{\beta\alpha}\binom{l'l}{s's}, \quad \text{and} \tag{3.72}$$

$$\sum_{l's'\beta} \Phi_{\alpha\beta}\binom{0l'}{ss'} = 0 \qquad \text{for } s = 1,\ldots, \text{r.} \tag{3.73}$$

Since each column of the force constant matrix is obtained from a different calculation, residual errors in the electronic structure calculations may cumulate in the sum rule in Eq.(3.73). The finite range of the IFCs imposed by the supercell dimensions also means that the contribution of longer ranged IFCs is omitted from the Eq.(3.73). To ensure the constraints of symmetry are not violated by the inevitable numerical errors, the calculated force constant matrices are symmetrised by applying all the point group operations of the crystal [135]. Translational invariance requires simultaneous satisfaction of 'r' Eqs.(3.73). Hence, an iterative method is used to slightly modify the IFC until they satisfy the translational invariance condition [135, 136].

In electronic structure methods, errors in wave functions cause second order errors in the energy but first order errors in forces. Therefore, a larger basis set and a denser k-point mesh are required for an accurate force calculation compared to what one needs for a total energy calculation [136].

Small atomic displacements must be used in this method so that the HA is valid. However, the smaller the displacement the smaller the induced forces on the atoms, and the greater the relative error in those calculated forces. Displacements around 1% of the lattice parameter are generally used in practice [135]. By calculating forces induced by two displacements of opposite sign, and using these forces in the central difference formula for calculating the IFC, even order anharmonicity in the forces is eliminated [137]. Hence, the IFCs calculated from positive and negative displacements are more accurate. Ackland et al. have described various aspects of the small displacement method in more detail [136].

3.2.1.1 Periodicity of the supercell

As mentioned above, when an atom in the supercell is displaced, equivalent atoms in all the images of the supercell are also displaced by the same amount. Therefore, the calculated IFCs contain contributions from within the supercell and from its periodic images.

$$\Phi^{\mathrm{sc}}_{\alpha\beta}\binom{ll'}{ss'} = \sum_{\mathbf{L}} \Phi_{\alpha\beta}\binom{ll'+L}{s\ s'}. \tag{3.74}$$

Here '**L**' runs over the supercell and its periodic images. The calculated force constants $\Phi^{\mathrm{sc}}_{\alpha\beta}\binom{ll'}{ss'}$ are equal to the exact ones $\Phi_{\alpha\beta}\binom{ll'}{ss'}$ only if the interatomic force is sufficiently short ranged that the interactions need only include one term (or none) in the sum in Eq.(3.74). However, regardless of interaction distance the dynamical matrix calculated using the $\Phi^{\mathrm{sc}}_{\alpha\beta}\binom{ll'}{ss'}$ values is exact for the wave vectors that are commensurate with the size of the supercell [138]. These are values of $\mathbf{k}$ for which the displacement pattern at a given time of a mode within the supercell is the same for all images of that supercell in the infinite periodic system. As derived in Section(3.1.6), for a supercell with the *superlattice* vectors $\mathbf{A}_i$ such wave vectors denoted $\mathbf{k}_{\mathrm{sc}}$ satisfy the condition

$$\exp[i\mathbf{k}_{\mathrm{sc}} \cdot \mathbf{A}_i] = 1. \tag{3.75}$$

Thus, the finite displacement method will recover the exact modes and frequencies if their wave vectors are $\mathbf{k}_{\mathrm{sc}}$. At other k-vectors these calculated IFCs are the basis for interpolating the frequencies, but unfortunately in many practical cases, limited by the supercell size this interpolation is to values very far from the true ones, as we shall see.

3.2.1.2 Dynamical matrix and dispersion relations

The equation of motion for atoms in the reference unit cell are solved to calculate the dispersion relations $\omega(\mathbf{k})$. Since there are 'r' atoms in the unit cell, there are '3r' degrees of freedom and hence '3r' simultaneous equations. For a given wave vector $\mathbf{k}$, the simultaneous Eqs. (3.67) lead to the following equations when the wave form in Eq.(3.69) is assumed for atomic displacements:

$$\omega^2 w_\alpha\binom{0}{s} = \sum_{\beta s'} C_{\alpha\beta}\binom{\mathbf{k}}{ss'} w_\beta\binom{0}{s'}, \tag{3.76}$$

$$\text{where} \quad C_{\alpha\beta}\binom{\mathbf{k}}{ss'} = \sum_{l'} \frac{1}{\sqrt{m_s m_{s'}}} \Phi^{sc}_{\alpha\beta}\binom{0l'}{ss'} \exp[i\mathbf{k} \cdot \{\mathbf{x}\binom{l'}{s'} - \mathbf{x}\binom{0}{s}\}]. \tag{3.77}$$

The matrix $C_{\alpha\beta}(\begin{smallmatrix}\mathbf{k}\\ ss'\end{smallmatrix})$ is known as the *dynamical matrix*. The summation in Eq.(3.77) considers the interaction of an atom s in the reference unit cell with all atoms of type s' within the interaction range. Equation(3.76) is a matrix eigenvalue problem, which is solved by diagonalising the dynamical matrix [131]. These equations show why the displacements were scaled by the masses to define the variables $w_\alpha(\begin{smallmatrix}0\\ s\end{smallmatrix})$; the dynamical matrix is thereby Hermitian and therefore the squared frequencies are guaranteed to be real and the eigenvectors, of the normal modes, are orthogonal, or if they are degenerate they can be chosen to be orthogonal. They can also be normalised over a unit cell, which we assume to be the case. There are $3r$ solutions at each value of $\mathbf{k}$, and we can label them in order of increasing frequency with a mode index j. We can denote the normal modes or eigenvectors of the dynamical matrix as $\mathbf{e}\left(\begin{smallmatrix}\mathbf{k}\\ j\end{smallmatrix}\right)$, and their components are labelled with indices α, the Cartesian direction, and s. Thus writing out the components, the eigenvectors satisfy

$$\omega^2(\begin{smallmatrix}\mathbf{k}\\ j\end{smallmatrix})e_\alpha(s|\begin{smallmatrix}\mathbf{k}\\ j\end{smallmatrix}) = \sum_{s'\beta} C_{\alpha\beta}(\begin{smallmatrix}\mathbf{k}\\ ss'\end{smallmatrix})e_\beta(s'|\begin{smallmatrix}\mathbf{k}\\ j\end{smallmatrix})\,. \tag{3.78}$$

To summarize, eigenvalues of the dynamical matrix are the squared frequencies of different modes. The dependency of a particular mode on the wavevector is called a *dispersion relation*. Eigenvectors are the polarisation vectors of modes. To obtain a dispersion relation along a path in the FBZ one must calculate the eigenvalues of the dynamical matrix at (in principle) all k-vectors along the path.

3.2.1.3 Thermodynamic properties

Harmonic approximation

In the HA, the volume of a crystal is assumed to be constant at all temperatures and each phonon mode is considered as an independent harmonic oscillator. The equilibrium volume V_0 at 0 K is considered as the volume of the harmonic system. There are two contributions to the total Helmholtz free energy: static energy U_0 of the system when all atoms are in their mean positions, and the energy associated with the atomic vibrations.

$$F_{\text{tot}}^{\text{HA}}(T, V_0) = U_0(V_0) + F_{\text{vib}}^{\text{HA}}(T, V_0). \tag{3.79}$$

The contribution to the Helmholtz free energy from each mode of atomic vibration $F(\begin{smallmatrix}\mathbf{k}\\ j\end{smallmatrix})$ is calculated using the partition function [131]. Thus the total vibrational

free energy of a crystal can be calculated if the exact phonon frequencies are available at all k-points, or in practice at an adequate sample of k-points, in the FBZ. The vibrational free energy at any temperature is obtained by summing the contribution from all vibrational modes $(\mathbf{k}_j)$ [135]. *i.e.*

$$F_{\text{vib}}^{\text{HA}}(T, V_0) = \sum_{\mathbf{k}j} \frac{1}{2}\hbar\omega(\mathbf{k}_j) + \sum_{\mathbf{k}j} k_B T \ln\left[1 - \exp\left(\frac{-\hbar\omega(\mathbf{k}_j)}{k_B T}\right)\right]. \tag{3.80}$$

The Helmholtz free energy is related to the internal energy (E) and the entropy (S) [131] : F = E - TS. Using this relation the entropy can be calculated as the negative of the derivative of free energy. Likewise, the internal energy and isochoric heat capacity can also be calculated.

Quasiharmonic approximation

Materials in general expand on heating, and have different vibrational frequencies at different temperatures and volumes. These are effects of *anharmonicity*; the normal modes interact with each other at high temperatures, because the HA becomes invalid. At the quantum level anharmonicity can be regarded as phonon-phonon interactions. There is a contribution to the free energy from the thermal expansion and phonon-phonon interactions, which can be estimated rather accurately up to well over half the melting point with the *quasiharmonic approximation* (QHA). In the QHA, a number of accurate phonon dispersion relations are calculated in the HA, while constraining the system at a series of different volumes $\omega(V)$. From these relations the free energy $F(T, V)$ is calculated with the harmonic formula above as a function of temperature and volume [139].

$$F_{\text{tot}}^{\text{QHA}}(V, T) = U_0(V) + \sum_{\mathbf{k}j} \frac{1}{2}\hbar\omega(\mathbf{k}_j|V) + \sum_{\mathbf{k}j} k_B T \ln\left[1 - \exp\left(\frac{-\hbar\omega(\mathbf{k}_j|V)}{k_B T}\right)\right]. \tag{3.81}$$

The equilibrium volume at a given temperature is the volume at which the free energy is minimised. The thermal expansion coefficient can then be estimated from the theoretical data for this equilibrium volume versus temperature. The entropy and pressure can also be evaluated from the theoretical data using the following thermodynamic relations [140].

$$S = -\left(\frac{\partial F}{\partial T}\right)_V \quad \text{and} \quad P = -\left(\frac{\partial F}{\partial V}\right)_T. \tag{3.82}$$

Similarly the isobaric heat capacity, bulk modulus, Gibbs free energy and the Grüneisen parameter can be calculated as a function of temperature using various other thermodynamic relations [141, 142].

Codes

I have used two codes for studying the lattice dynamics: the PHONOPY code developed by Atsushi Togo et al. [143] and the PHON code developed by Dario Alfè [135]. These codes are used for pre-processing and post-processing DFT calculations for generating phonon dispersion curves with the the small displacement method. The pre-processing involves determining the set of atomic displacements required for a given symmetry of the crystal, and creating the required supercells with and without atomic displacements. The post-processing involves extracting the forces on atoms in the supercell for each atomic displacement, calculating the IFC, calculating the dispersion relations and plotting them. The thermodynamic properties can also be calculated using these codes.

3.2.1.4 Elastic constants from dispersion relations

At long wavelengths ($\mathbf{k} \rightarrow \mathbf{0}$) the lowest frequency branches of the dispersion curves, for which $\lim_{\mathbf{k}\rightarrow 0} \omega(\mathbf{k}) \rightarrow 0$, correspond to sound waves, and the slope of ω versus $\mathbf{k}$ at $\mathbf{k} = 0$ is a sound velocity [144]. By applying elasticity theory to a long wave sinusoidal displacement in crystalline materials, a relationship between the elastic constants and the sound propagation velocity in any direction can be obtained. Jules de Launay [145], see also Dove [130], derived these relations for longitudinal and transverse acoustic modes along high symmetry directions for cubic crystals. Therefore, elastic constants can be calculated from slopes of acoustic branches at the FBZ center, and indeed they are often obtained experimentally from measurements of ultrasound velocities [61, 146]. However, to obtain theoretical values of the elastic constants by this procedure would require accurate dispersion relations near $\mathbf{k} = 0$, the centre of the FBZ, also known as the Γ point. In practice it will always be more efficient and accurate to calculate them directly by the method of homogeneous deformation, discussed below. I have compared the accuracy of the methods below. Complete dispersion relations and in particular the slopes of the acoustic branches at the Γ point are determined by the IFCs. Therefore, it is possible to derive formulae for all elastic constants in terms of the IFCs. Max Born et al. [131] derived the general relationships between the IFC and the elastic constants. The symmetry of a B2

crystal further simplifies these relations, as I discovered while working with the B2 phase. This simplification is described in the following section.

3.2.1.5 Force constants and elastic stiffness tensor elements

Acoustic lattice wave solutions depend on the direction in which the FBZ center is approached. For a given wave propagation direction $\mathbf{k}$ and an acoustic branch j, the solutions vary continuously. Born et al. [131] used a perturbation method for solving the eigenvalue problem for an acoustic wave along a propagation direction. Wave vector $\mathbf{k}$ was written as $\epsilon\mathbf{k}$ in Eq.(3.76) to represent all vectors along the chosen direction.

$$\omega^2(\tbinom{\epsilon\mathbf{k}}{j})w_\alpha(s|\tbinom{\epsilon\mathbf{k}}{j}) = \sum_{\beta s'} C_{\alpha\beta}(\tbinom{\epsilon\mathbf{k}}{ss'})w_\beta(s'|\tbinom{\epsilon\mathbf{k}}{j}). \tag{3.83}$$

All quantities in Eq.(3.83) were expanded with respect to ϵ. The dynamical matrix expansion up to second order was written as

$$C_{\alpha\beta}(\tbinom{\epsilon\mathbf{k}}{ss'}) = C^{(0)}_{\alpha\beta}(ss') + i\epsilon\sum_\gamma C^{(1)}_{\alpha\beta,\gamma}(ss')k_\gamma + \frac{1}{2}\epsilon^2\sum_{\gamma\lambda} C^{(2)}_{\alpha\beta,\gamma\lambda}(ss')k_\gamma k_\lambda, \tag{3.84}$$

where

$$C^{(0)}_{\alpha\beta}(ss') = \frac{1}{\sqrt{m_s m_{s'}}}\sum_{l'}\Phi_{\alpha\beta}(\tbinom{0l'}{ss'}), \tag{3.85}$$

$$C^{(1)}_{\alpha\beta,\gamma}(ss') = \frac{1}{\sqrt{m_s m_{s'}}}\sum_{l'}\Phi_{\alpha\beta}(\tbinom{0l'}{ss'})\{x_\gamma(\tbinom{l'}{s'}) - x_\gamma(\tbinom{0}{s})\} \tag{3.86}$$

and

$$C^{(2)}_{\alpha\beta,\gamma\lambda}(ss') = \frac{-1}{\sqrt{m_s m_{s'}}}\sum_{l'}\Phi_{\alpha\beta}(\tbinom{0l'}{ss'})\{x_\gamma(\tbinom{l'}{s'}) - x_\lambda(\tbinom{0}{s})\}\{x_\lambda(\tbinom{l'}{s'}) - x_\lambda(\tbinom{0}{s})\}. \tag{3.87}$$

The acoustic lattice wave solutions were represented with the following expansions:

$$\omega(\tbinom{\epsilon\mathbf{k}}{j}) = \epsilon\omega^{(1)}(\tbinom{\mathbf{k}}{j}) + \frac{1}{2}\epsilon^2\omega^{(2)}(\tbinom{\mathbf{k}}{j}) + \ldots, \tag{3.88}$$

$$w_\alpha(s|^{\epsilon\mathbf{k}}_j) = w^{(0)}_\alpha(s|^{\mathbf{k}}_j) + i\epsilon w^{(1)}_\alpha(s|^{\mathbf{k}}_j) + \frac{\epsilon^2}{2} w^{(2)}_\alpha(s|^{\mathbf{k}}_j) + \dots . \tag{3.89}$$

Expansions in Eqs. (3.88),(3.89), and (3.84) were substituted in Eq.(3.83) and perturbation equations for powers of ϵ up to second order were separately written. These equations were solved up to second order in ϵ. A necessary condition for solving the second order perturbation equation results in a relation between the polarisation of a lattice wave, force constants, atomic information, wave vector, and frequency of wave propagation. By comparing the lattice wave solution with the elastic wave solution from macroscopic elasticity theory, Born et al. [131] derived a relation between the elastic stiffness tensor elements, IFC, and atomic information for a non-ionic, stress-free crystal. The resulting formula is:

$$C_{\alpha\gamma,\beta\lambda} = [\alpha\beta, \gamma\lambda] + [\beta\gamma, \alpha\lambda] - [\beta\lambda, \alpha\gamma] + (\alpha\gamma, \beta\lambda), \tag{3.90}$$

where $C_{\alpha\gamma,\beta\lambda}$ is one element of the elastic stiffness tensor, $[\alpha\beta, \gamma\lambda]$ is a function of $C^{(2)}_{\alpha\beta,\gamma\lambda}(ss')$, $(\alpha\gamma, \beta\lambda)$ is a function of $C^{(1)}_{\mu\alpha,\gamma}(ss')$ and $C^{(1)}_{\gamma\beta,\lambda}(ss')$. The presence of symmetries in crystals further simplifies this relation. Of particular relevance here is that due to the cubic symmetry of a B2 crystal $C^{(1)}_{\alpha\beta,\gamma}(ss')$ vanishes, which I can show with the help of some elementary group theory as follows.

$C^{(1)}_{\alpha\beta,\gamma}(ss')$ in a B2 crystal

For a given s and s' atoms in the $C^{(1)}_{\alpha\beta,\gamma}(ss')$, the summation on the right side of Eq.(3.86) includes the interaction of an atom at position s in the reference unit cell 0 with neighbouring atoms at position s' in all unit cells l' in the space. Each unit cell contains just one atom labelled s'. In crystals with the property that the point group symmetry of the set of atoms with the same label s' about atom s is cubic, which for the B2 structure is true for all s, I show in this section that the summation, and hence the term $C^{(1)}_{\alpha\beta,\gamma}(ss')$, vanishes.

In B2 crystals, it is evident that all equidistant neighbours from an atom s in the reference unit cell can be visualised to be at vertices of a regular coordination polyhedron (c.p.) centred on the s atom in the reference unit cell. For a given s atom, the first, second, third, and so on nearest neighbours would be on polyhedra of increasing sizes respectively. All atoms labelled $(^{l'}_{s'})$ in the lattice can be assigned to one of these polyhedra. Thus the summation over l' could be expressed as a sum over $\{c, l_c\}$, where c labels the polyhedron and l_c one of its vertices, all of which are occupied by atoms with the same label s'. For illus-

trative purposes, the first four nearest neighbours in a two dimensional square lattice are shown in Fig.(3.1). The summation over all unit cells l' in Eq.(3.86) can be expressed as the sum over vertices of co-ordination polyhedra of different sizes:

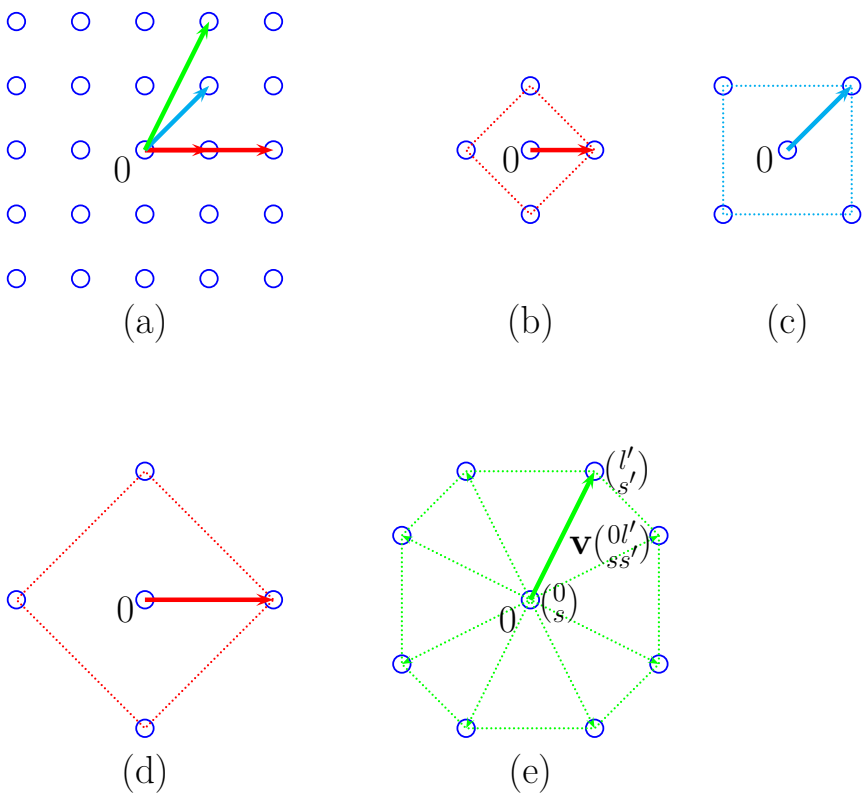


Figure 3.1: Schematic representation of separating the sum over unit cells into sum over co-ordination polygons: (a) two dimensional square lattice, (b) first nearest neighbour polygon, (c) second nearest neighbour polygon, (d) third nearest neighbour polygon, and (e) fourth nearest neighbour polygon.

$$C^{(1)}_{\alpha\beta,\gamma}(ss') = \frac{1}{\sqrt{m_s m_{s'}}} \sum_{c=1}^{\infty} \sum_{l_c} \Phi_{\alpha\beta}\binom{0l_c}{ss'} \{x_\gamma\binom{l_c}{s'} - x_\gamma\binom{0}{s}\}. \tag{3.91}$$

I now describe in turn the transformation properties of the two factors in Eq.(3.91), namely the vectors and the force constants, under operations of the point group. All vectors from an atom $\binom{0}{s}$ in the reference cell to atoms $\binom{l_c}{s'}$ at the corners of a given polyhedron are of the same length, and are related by the symmetry elements of the crystallographic point group. A similar algebra relates vectors in the star of a k-vector in the FBZ [147]. As denoted in the Fig.(3.1(d)), let $\mathbf{v}\binom{0l'}{ss'}$ be a vector from an atom $\binom{0}{s}$ to an atom $\binom{l'}{s'}$: $\mathbf{v}\binom{0l'}{ss'} = \mathbf{x}\binom{l'}{s'} - \mathbf{x}\binom{0}{s}$.

Some relevant concepts of group theory are summarised here. Let G_0 denote the set of point group elements of the crystal. Now consider symmetry elements $g \in \mathrm{G}_0$ which leave the vector $\mathbf{v}$ invariant and denote this set of elements with a subgroup $\mathrm{G}^{\mathbf{v}}$. If $\mathrm{G}^{\mathbf{v}}$ contains any other element in addition to an identity operation, the vector $\mathbf{v}$ is a special vector. Otherwise, $\mathbf{v}$ is a general vector. All the elements in G_0 can be partitioned between $\mathrm{G}^{\mathbf{v}}$ and cosets relative to $\mathrm{G}^{\mathbf{v}}$. Let $\{g_v\}$ be the set of coset representatives of this decomposition, including $\mathrm{G}^{\mathbf{v}}$ itself. They are equal in number to the number of vertices of the polyhedron, and themselves have a group structure (called a *quotient group*). For example, the set of vectors joining an atom $\binom{0}{s}$ and atoms $\binom{l_c}{s'}$, which are the vertices of a given polyhedron, are given by the set $\{g_v\mathbf{v}\}$; each of these cosets generates just one of the vertices, whichever of its operations acts on $\mathbf{v}$. The number of vertices is the ratio $|\mathrm{G}_0|/|\mathrm{G}^{\mathbf{v}}|$, where the numerator and denominator denote the number of elements in the full point group and the subgroup respectively, and this quotient is also called the *index* of $\mathrm{G}^{\mathbf{v}}$ in G_0. The number of cosets, that is the number of elements in the set $\{g_v\}$, or the *order* of the quotient group, is equal to this index. If all the point group operations in G_0 are applied to a vector $\mathbf{v}$, each vector in the set $\{g_v\mathbf{v}\}$ appears $|\mathrm{G}^{\mathbf{v}}|$ times.

Each component of $\mathbf{v}$ is a member of the three dimensional basis of the irrep T_1, which transforms like (x, y, z). Any vectors from the $\binom{0}{s}$ atom at the origin, the centre of a polyhedron, to a corner atom $\binom{l_c}{s'}$ can be generated from one of the others $\mathbf{v}\binom{0l'}{ss'}$ via the representation matrices of $\{g_v\}$:

$$v_\gamma\binom{0l_c}{ss'} = \sum_{\gamma'} T_1(g_v;\gamma,\gamma')v_{\gamma'}\binom{0l'}{ss'}. \tag{3.92}$$

Now I discuss the transformation properties of the force constants. The derivatives $\partial/\partial x_\gamma$ transform in the same way as the coordinates x_γ under operations of G_0. Thus $\Phi_{\alpha\beta}$ transforms like $x_\alpha x_\beta$, meaning that the same matrix representation of G_0 describes how they transform [148]. This is a six-dimensional representation $D^{(6)}$, with a basis of the form $x^2, y^2, z^2, xy, yz, zx$. When G_0 is a cubic group, this representation is reducible into the three irreps $A \oplus E \oplus T_2$, which are respectively the identity representation with basis $a \equiv x^2+y^2+z^2$, the two-dimensional representation with basis $(e_1, e_2) \equiv (2z^2 - x^2 - y^2, x^2 - y^2)$ and the three dimensional representation with basis $(t_1, t_2, t_3) \equiv (xy, yz, zx)$. Analogously to the vectors themselves, any force constant matrices $\Phi_{\alpha\beta}\binom{0l_c}{ss'}$ between the $\binom{0}{s}$ atom at the origin and one of the corners $\binom{l_c}{s'}$ can be calculated from the

force constant matrix connecting the origin to any of the other corners via the representation matrices of $\{g_v\}$:

$$\Phi_{\alpha\beta}\binom{0l_c}{ss'} = \sum_{\alpha'\beta'} D^{(6)}(g_v;\alpha\beta,\alpha'\beta')\Phi_{\alpha'\beta'}\binom{0l'}{ss'}. \tag{3.93}$$

Relations in Eqs. (3.92) and (3.93) can be used for writing the contribution to the $C^{(1)}_{\alpha\beta,\gamma}(ss')$ from each polyhedron:

$$\sum_{l_c} \Phi_{\alpha\beta}\binom{0l_c}{ss'} v_\gamma\binom{0l_c}{ss'} = \sum_{g\in\{g_v\}} \sum_{\alpha'\beta',\gamma'} D^{(6)}(g;\alpha\beta,\alpha'\beta')\Phi_{\alpha'\beta'}\binom{0l'}{ss'} T_1(g;\gamma,\gamma')v_{\gamma'}\binom{0l'}{ss'} \tag{3.94}$$

$$\equiv \frac{1}{|G^{\mathbf{v}}|}\sum_{g\in G_0} \sum_{\alpha'\beta',\gamma'} D^{(6)}(g;\alpha\beta,\alpha'\beta')\Phi_{\alpha'\beta'}\binom{0l'}{ss'} T_1(g;\gamma,\gamma')v_{\gamma'}\binom{0l'}{ss'}. \tag{3.95}$$

Let us define the product between $\Phi_{\alpha'\beta'}\binom{0l'}{ss'}$ and $v'_\gamma\binom{0l'}{ss'}$ as $S_{\alpha'\beta',\gamma'}\binom{0l'}{ss'}$. $D^{(6)}$ can be expressed in the basis of irreps. Hence, the summation over g in Eq.(3.95) can be written as:

$$\begin{aligned}\sum_{g\in G_0}\sum_{\alpha'\beta',\gamma'} D^{(6)}(g;\alpha\beta,\alpha'\beta')T_1(g;\gamma,\gamma')S_{\alpha'\beta',\gamma'}\binom{0l'}{ss'} \\ = \sum_{g\in G_0}\sum_{t'_i,\gamma'} T_2(g;t_i,t'_i)T_1(g;\gamma,\gamma')S_{t'_i,\gamma'}\binom{0l'}{ss'} \\ + \sum_{g\in G_0}\sum_{e'_i,\gamma'} E(g;e_i,e'_i)T_1(g;\gamma,\gamma')S_{e'_i,\gamma'}\binom{0l'}{ss'} \\ + \sum_{g\in G_0}\sum_{\gamma'} A(g;a,a')T_1(g;\gamma,\gamma')S_{a,\gamma'}\binom{0l'}{ss'}.\end{aligned} \tag{3.96}$$

Note that the factor $S_{\alpha'\beta',\gamma'}\binom{0l'}{ss'}$ can be taken outside the summation over g. By the Grand Orthogonality Theorem (GOT) every sum over group elements of the product of any matrix elements from different irreps vanishes [148]. Therefore, each line on the right-hand side of Eq.(3.96) reduces to zero, and the net contribution from each coordination polyhedron to $C^{(1)}_{\alpha\beta,\gamma}(ss')$ is zero. Hence,

$$C^{(1)}_{\alpha\beta,\gamma}(ss') = 0. \tag{3.97}$$

The $(\alpha\gamma,\beta\lambda)$ term on the right-hand side of the Eq.(3.90) is zero if all the

$C^{(1)}_{\alpha\beta,\gamma}(ss')$ elements are zero. Therefore, the relation between elastic constants and IFCs in the B2 simplifies to

$$C_{\alpha\gamma,\beta\lambda} = [\alpha\beta,\gamma\lambda] + [\beta\gamma,\alpha\lambda] - [\beta\lambda,\alpha\gamma], \tag{3.98}$$

where

$$[\alpha\beta,\gamma\lambda] = -\frac{1}{2\Omega}\sum_{ss'}\sum_{l'}\Phi_{\alpha\beta}\binom{0l'}{ss'}\{x_\gamma\binom{l'}{s'} - x_\gamma\binom{0}{s}\}\{x_\lambda\binom{l'}{s'} - x_\lambda\binom{0}{s}\}. \tag{3.99}$$

3.2.2 Soft mode analysis with group theory

Dispersion relations in various phases are routinely calculated at 0 K using *ab initio* lattice dynamics methods. Modes with imaginary frequencies are identified as soft modes. The phases with soft modes are unstable at 0 K, and if they are stabilized at high temperature by anharmonic effects, they would nevertheless have to undergo a phase transition on cooling, except in the unlikely case that anharmonicity is even significant at 0 K. Like the stable modes, each soft mode is associated with a k-vector and a polarisation vector. I used the ISOTROPY code developed by Stokes et al. [149, 150] to determine the possible martensitic structures from the soft mode instability.

Using the principles of group representation theory, this code lists all the possible irreducible representations associated with a k-vector in the FBZ of any crystal structure. For a given irreducible representation, the code determines all the possible isotropy subgroups and basic information regarding the transition to a particular subgroup. It can therefore be used to determine the number of distinct martensite domains that would form during a MT. Results from these studies and the results from the experimental studies in the literature are used to suggest the possible MT paths in binary TiNi-based SMAs.

Let us consider a macroscopic crystal of the parent phase with 'N' atoms, and represent the displacement of the atoms corresponding to the soft mode with a vector ϕ in a '$3N$' dimensional vector space. Let G be the crystallographic space group of the parent phase with crystallographic symmetry elements in the set $\{g\}$. According to Howard et al. [150], the space group of the product phase contains all the symmetry elements g which belong to the parent space group and which leave the distortion invariant. *i.e.*

$$g_h\phi = \phi. \tag{3.100}$$

Let us denote this subset of elements $\{g_h\}$ with a subgroup H. As described in Appendix A, each vibrational mode is associated with one of the irreps according to the symmetry properties of its polarisation vector. Equivalent soft modes used for characterizing the MT are defined in terms of components of an order parameter. For a given irrep, the order parameter is a representation of the crystallographic space group H of the product phase. ISOTROPY determines all possible product space groups and the corresponding order parameters. It also determines the unit cell dimensions and the relative orientation of the product phase with respect to the parent phase. In this analysis, it is assumed that the lattice translations in the martensite are also lattice translations in the B2 phase. This assumption is known as the *parent clamping* approximation [151]. It is only valid if the transformation strains associated with the MT are negligible or zero.

In fact, since the MT in TiNi-based SMAs is a ferroelastic transformation, it is associated with non-negligible transformation strains. Martensite variants are distorted and rotated according to these transformation strains. Hence, an accurate description of the MT must take into account the coupling between the amplitudes of soft modes and transformation strains. It is also possible to study this coupling with the help of ISOTROPY, with which the Landau free energy expansion can also be determined.

3.3 Self consistent *ab initio* lattice dynamics

Phonon-phonon interactions contribute largely to the entropy that stabilises the B2 structure at high temperatures. So as to incorporate these entropic effects, anharmonic effects need to be considered in the lattice dynamics. Souvatzis et al. [58, 152] proposed a self consistent *ab initio* lattice dynamics (SCAILD) method which considers the phonon-phonon interaction in a mean field approximation. This method is based on the self-consistent phonon approach developed by Born [59]. Souvatzis et al. described the SCAILD formulation for the case of a mono atomic crystal [153]. While implementing and testing it for the study of TiNi I learned much of importance about the method that is not discussed in the literature, and it is therefore worth including a more complete description of it in this thesis.

Atomic vibrations are treated as bosonic particle motion in quantum mechanics. The SCAILD method uses the Bose-Einstein distribution function for determining the phonon occupation number at high temperatures. Mode ampli-

tude values are calculated at a given temperature using this function. The effect of temperature is input through the mode amplitudes in the SCAILD method. The atoms are displaced according to the mode amplitudes. Thermal expansion of the crystal due to temperature increase is not considered in this method and the volume of the crystal at high temperature is held fixed. Forces are calculated on atoms using *ab initio* methods, although the method of force calculation is not fundamental to the principle of calculating the self-consistent phonon frequencies. The dispersion relation at the temperature under consideration is calculated from the mean force values on atoms. This process is repeated many times until the average dispersion relations are converged. So as to critically look into the SCAILD method, I re-derived the SCAILD formulation for a composite crystal. The formulation is expressed in normal coordinates, which are the normal coordinates of the *harmonic* crystal, and it is fundamental to the method that these are not changed, only their frequencies are renormalised.

In a SCAILD method, a supercell is used in the force calculations. Hence, the mode frequencies and wave solutions are exact only at the wave vectors commensurate with the size of the supercell. Normal coordinates describe the displacement of atoms in a supercell in terms of the lattice wave solutions at the exact wave vectors. The quantities involved, and the approach to diagonalization of a dynamical matrix are the same as in harmonic lattice dynamics. To establish the notation (see page xiv for most of the notation) I will describe these aspects first.

Let us define a reduced interatomic force constant matrix as

$$D_{\alpha\beta}\left(\begin{smallmatrix} ll' \\ ss' \end{smallmatrix}\right) = \frac{1}{\sqrt{m_s m_{s'}}} \Phi_{\alpha\beta}\left(\begin{smallmatrix} ll' \\ ss' \end{smallmatrix}\right). \tag{3.101}$$

The equation of motion, in the HA, can be expressed in terms of $D_{\alpha\beta}\left(\begin{smallmatrix} ll' \\ ss' \end{smallmatrix}\right)$ as

$$\frac{\partial^2 w_\alpha\left(\begin{smallmatrix} l \\ s \end{smallmatrix}\right)}{\partial t^2} = -\sum_{l's'\beta} D_{\alpha\beta}\left(\begin{smallmatrix} ll' \\ ss' \end{smallmatrix}\right) w_\beta\left(\begin{smallmatrix} l' \\ s' \end{smallmatrix}\right). \tag{3.102}$$

Let us make the ansatz of a travelling wave with the special form

$$\mathbf{w}\left(\begin{smallmatrix} l \\ s \end{smallmatrix}\right) = \mathbf{e}(s|\mathbf{k}) \exp\left\{i(\mathbf{k}\cdot\mathbf{x}(l) - \omega t)\right\}, \tag{3.103}$$

where $\mathbf{k}$ is one of the allowed k-vectors, giving the equation

$$\omega^2 e_\alpha(s|\mathbf{k}) \exp\{i\mathbf{k}\cdot\mathbf{x}(l)\} = \sum_{l's'\beta} D_{\alpha\beta}\binom{ll'}{ss'} e_\beta(s'|\mathbf{k}) \exp\{i\mathbf{k}\cdot\mathbf{x}(l')\}\,. \tag{3.104}$$

The corresponding eigenvalue equation is

$$\omega^2 e_\alpha(s|\mathbf{k}) = \sum_{s'\beta} D_{\alpha\beta}\binom{\mathbf{k}}{ss'} e_\beta(s'|\mathbf{k}), \tag{3.105}$$

where

$$D_{\alpha\beta}\binom{\mathbf{k}}{ss'} = \sum_{l'} D_{\alpha\beta}\binom{ll'}{ss'} \exp\{i\mathbf{k}\cdot[\mathbf{x}(l') - \mathbf{x}(l)]\}. \tag{3.106}$$

The lattice solutions at a wave vector $\mathbf{k}$ are obtained by diagonalising the dynamical matrix $D_{\alpha\beta}\binom{\mathbf{k}}{ss'}$:

$$\omega^2\binom{\mathbf{k}}{j} e_\alpha(s|^{\mathbf{k}}_j) = \sum_{s'\beta} D_{\alpha\beta}\binom{\mathbf{k}}{ss'} e_\beta(s'|^{\mathbf{k}}_j). \tag{3.107}$$

The eigenvectors $e_\alpha(s|^{\mathbf{k}}_j)$ satisfy the following orthonormality relations:

$$\sum_{s\alpha} e^*_\alpha(s|^{\mathbf{k}}_j) e_\alpha(s|^{\mathbf{k}}_{j'}) = \delta_{jj'}, \text{and} \sum_{j} e_\alpha(s|^{\mathbf{k}}_j) e^*_\beta(s'|^{\mathbf{k}}_j) = \delta_{ss'}\delta_{\alpha\beta}. \tag{3.108}$$

In the SCAILD method, I used the dispersion relations $\omega(\mathbf{k})$ calculated within the HA as the initial dispersion relations. The polarisation vectors of all vibrational modes are then assumed to be constant vectors equal to the initially calculated $e_\alpha(s|^{\mathbf{k}}_j)$ in the HA, even when their frequencies are imaginary.

Let us define reduced atomic displacements in the complete set of eigenvectors of D calculated at exact wave vectors as

$$\mathbf{w}\binom{l}{s} = \frac{1}{\sqrt{N}} \sum_{\mathbf{k},j} Q\binom{\mathbf{k}}{j} \mathbf{e}(s|^{\mathbf{k}}_j) \exp\{i\mathbf{k}\cdot\mathbf{x}(l)\}\,. \tag{3.109}$$

The expansion coefficients Q in this description are the *normal coordinates* [131]. In this description, the displacement of atoms in the supercell are

$$\mathbf{u}\binom{l}{s} = \frac{1}{\sqrt{m_s N}} \sum_{\mathbf{k}}^{N} \sum_{j}^{3r} \mathbf{e}(s|^{\mathbf{k}}_j) Q\binom{\mathbf{k}}{j} \exp\{i\mathbf{k}\cdot\mathbf{x}(l)\}. \tag{3.110}$$

In the SCAILD method, a set of Q values are generated using the standard relationship of harmonic lattice theory between the mean square amplitude values and mode frequencies [154]:

$$Q^2(\tbinom{\mathbf{k}}{j}) = \frac{\hbar}{\omega(\tbinom{\mathbf{k}}{j})}\Big[\frac{1}{2} + n\Big(\frac{\hbar\omega(\tbinom{\mathbf{k}}{j})}{k_B T}\Big)\Big], \tag{3.111}$$

where $n(x) = 1/\{(\exp(x) - 1)\}$ is the Bose-Einstein distribution function. A sample of atomic displacements at each iteration is generated by selecting new values of Q at random from a Gaussian distribution, with a width chosen to reproduce the above mean squared values. *i.e.*

$$Q(\tbinom{\mathbf{k}}{j}) = G(\tbinom{\mathbf{k}}{j})\sqrt{\frac{\hbar}{\omega(\tbinom{\mathbf{k}}{j})}\Big[\frac{1}{2} + n\Big(\frac{\hbar\omega(\tbinom{\mathbf{k}}{j})}{k_B T}\Big)\Big]}, \tag{3.112}$$

where $G(\tbinom{\mathbf{k}}{j})$ is a random Gaussian variable.

Although the description in the literature proceeds via an expansion of the Hamiltonian to third order in the normal coordinates, this is not essential to the understanding of the method, nor is it used in its implementation.

The essential idea is that in a mean field approximation the Hamiltonian is written in terms of harmonic oscillators whose frequencies are renormalised. In the mean field approximation, the harmonic force constants are replaced with effective force constants, which take into account the forces from anharmonic interactions [130].

My implementation of the SCAILD method included the following steps at each iteration.

1. Random values of the normal coordinates $Q(\tbinom{\mathbf{k}}{j})$ of all normal modes at the exact wave vectors are calculated using the initial mean square amplitude values in Eq.(3.111) and a Gaussian distribution function. If the wave vector is a general vector, diagonalising of the dynamical matrix $D_{\alpha\beta}(\tbinom{\mathbf{k}}{ss'})$ results in complex eigenvectors. The complex nature of the eigenvectors can be accommodated into the iterative method by making the $Q(\tbinom{\mathbf{k}}{j})$ a complex number. This is done by multiplying the $Q(\tbinom{\mathbf{k}}{j})$ with a random phase $\exp\{i2\pi x\}$, where x is a random number between 0 and 1. So as to ensure the real displacement of atoms in the supercell, the $Q(\tbinom{\mathbf{k}}{j})$ are further constrained to satisfy $Q(\tbinom{\mathbf{k}}{j}) = Q^*(\tbinom{-\mathbf{k}}{j})$. Corresponding atomic displacements in the supercell are then calculated using Eq.(3.110). Atoms in a supercell are displaced to these values.

simulate the atomic motion at a particular instant of time,

2. Hellmann-Feynman forces on all atoms in this perturbed supercell are calculated using the $VASP$ code. The displaced atomic configuration in the supercell corresponds to a configuration where all the normal modes are excited. Therefore, the forces contain an instance of the anharmonic contributions. The calculated forces are Fourier transformed [154].

$$F_\alpha(s|\mathbf{k}) = \sum_{j'} -\sqrt{m_s}Q(^{\mathbf{k}'}_{j'})e_\alpha(s|^{\mathbf{k}'}_{j'})\omega^2(^{\mathbf{k}'}_{j'}) - \frac{1}{2}\sum_{\mathbf{k}'j'}\sum_{\mathbf{k}''j''}\sum_{s'\beta}\sum_{s''\gamma}\Phi(^{\mathbf{k}\mathbf{k}'\mathbf{k}''}_{jj'j''})\frac{1}{\sqrt{m_{s'}m_{s''}}}e_\beta(s'|^{\mathbf{k}'}_{j'})Q(^{\mathbf{k}'}_{j'})e_\gamma(s''|^{\mathbf{k}''}_{j''})Q(^{\mathbf{k}''}_{j''}) + \dots. \tag{3.113}$$

3. Renormalised frequencies $\tilde{\omega}(^{\mathbf{k}}_{j})$ are calculated from the Fourier components of forces using Eq.(3.114):

$$\tilde{\omega}^2(^{\mathbf{k}}_{j}) = \sum_{s\alpha} -\frac{F_\alpha(s|\mathbf{k})e_\alpha(s|^{\mathbf{k}}_{j})}{Q(^{\mathbf{k}}_{j})\sqrt{m_s}}. \tag{3.114}$$

4. Since we are hoping to converge to an ensemble average, these 'raw' renormalised squared frequencies are now adjusted to respect symmetry. Frequencies calculated at different vectors in a star of $\mathbf{k}$ should be the same. But since we are calculating them on a perturbed lattice, the above raw renormalised frequencies at different vectors in a star of $\mathbf{k}$ are different. Hence in this step for each mode the frequencies are averaged over the different values on a star. The symmetrised frequencies $\bar{\omega}(^{\mathbf{k}}_{j})_i$ on a star of $\mathbf{k}$ in an iteration i are calculated using

$$\bar{\omega}^2(^{\mathbf{k}}_{j})_i = \frac{1}{|\{g^{\mathbf{k}}\}|}\sum_{g\in\{g^{\mathbf{k}}\}}\tilde{\omega}^2(^{g\mathbf{k}}_{j})_i. \tag{3.115}$$

Here $|\{g^{\mathbf{k}}\}|$ is the number of vectors in the star of $\mathbf{k}$, which is also the number of elements in the group $\{g^{\mathbf{k}}\}$, the quotient group of the full point group with respect to the group of $\mathbf{k}$, $G^{\mathbf{k}}$. All the elements $g \in G^{\mathbf{k}}$ leave the vector $\mathbf{k}$ invariant: $g\mathbf{k} = \mathbf{k} \quad \forall g \in G^{\mathbf{k}}$. The relevant group theory is summarised in Section(3.2.1.5). Note that there is an error in the literature, where this summation was described as being performed over the group elements of $G^{\mathbf{k}}$[58, 152, 153].

5. Another important adjustment must be made in the hope of approaching an ensemble averaged renormalised frequency. The squared frequencies $\langle\tilde{\omega}^2(\mathbf{k}_j)\rangle_i$ at the end of an iteration i are calculated from all the frequency values from previous iterations.

$$\langle\tilde{\omega}^2(\mathbf{k}_j)\rangle_i = \frac{1}{i}\sum_{x=1}^{i}\bar{\omega}^2(\mathbf{k}_j)_x. \tag{3.116}$$

This is essential because the configuration in each iteration represents a snapshot of the atomic vibrations at an instant of time. Therefore, the averaging in Eq.(3.116) should better represent a statistical averaging over time, or equivalently, a statistical averaging over a very large system. The $\langle\tilde{\omega}^2(\mathbf{k}_j)\rangle_i$ values are then used for determining the mode amplitudes for the next iteration, using Eq.(3.111), and the iteration steps are repeated.

Steps (1) to (5) are repeated until the average dispersion relations at the temperature under consideration are converged. The vibrational free energy is a single interesting quantity that depends on all the dispersion relations. It is therefore useful to continue the iterative procedure until the vibrational free energy is converged to the required accuracy.

3.4 Homogeneous deformation method

Elastic constants of a material determine its response to external stress. They also play an important role in the MT. In cubic crystals, elastic constant C′ determines the resistance to a shear on {110} planes in [110] directions. During the MT, shuffling and shearing of {110} planes occur. The periodicity of distortions is determined by the wave vector of the soft mode. Elastic softening of C′ is observed in TiNi-based SMAs with decrease in temperature as the alloys are cooled towards the transition temperatures. This elastic softening aids the shearing and shuffling of planes occuring during the MT. In this section, a homogeneous deformation method [155] for calculating the elastic constants is described. This method has been used here for calculating the elastic constants of all the alloys considered.

Let us consider a unit cell in periodic boundary conditions and subject it to a general small strain tensor e_{ij}. The strain tensor can be written as sum of a symmetric tensor $\epsilon_{ij} = \frac{1}{2}(e_{ij}+e_{ji})$ and an anti-symmetric tensor $\varpi_{ij} = \frac{1}{2}(e_{ij}-e_{ji})$. The tensor ϖ_{ij} describes a pure rotation and does not contribute any elastic energy in case of a single crystal. Therefore, the only strain tensor contributing to

the elastic strain energy is the symmetric strain tensor ϵ_{ij}. If a crystal is subjected to a homogeneous strain ϵ_{ij}, its energy increases by an amount equivalent to the elastic strain energy. Using the relation given by the Hooke's law, it is possible to write the elastic strain energy associated with the elastic distortion ϵ_{ij} in terms of its elements and elements of the elastic stiffness tensor:

$$E^{\text{ela}} = \frac{1}{2}\sum_{ijkl} \mathrm{C}_{ijkl}\epsilon_{ij}\epsilon_{kl}. \tag{3.117}$$

This relation is used to determine the elastic tensor elements in a homogeneous deformation method. The elastic stiffness tensor C_{ijkl} has 81 elements and it defines the elastic response of a material completely. Presence of symmetry reduces the number of independent elastic stiffness tensor elements. The symmetry elements of cubic crystals reduces the independent elastic tensor elements number to three. The unit cell of a given crystal structure is strained according to the applied strain. The strained cell parameters $\mathbf{a}_i'$ can be calculated from the equilibrium cell parameters $\mathbf{a}_i$ and the homogeneous strain tensor [155]:

$$\mathrm{a}'_{i\alpha} = \mathrm{a}_{i\alpha} + \sum_{\beta} \epsilon_{\alpha\beta}\mathrm{a}_{i\beta}. \tag{3.118}$$

The atoms in the strained unit cell are allowed to relax to their new equilibrium positions. The total energy of the system is calculated after complete relaxation. For a given strain tensor, this process is repeated for strains of different signs and magnitudes. The Hooke's law is valid only within the elastic region. Therefore to ensure that the applied strains are within the harmonic region, magnitude of strains ranging only from -0.02 to +0.02 are used. The total energy is plotted as a function of the magnitude of strain (γ) for a given strain tensor ϵ_{ij}. The analytic expression for the total energy of the strained unit cell can be written using the relation in Eq.(3.117).

$$E^{\text{tot}} = E^0 + \frac{1}{2}\gamma^2 \sum_{ijkl} \mathrm{C}_{ijkl}\epsilon_{ij}\epsilon_{kl} \tag{3.119}$$

Here E^0 is the energy of an unstrained crystal. For a given strain tensor it is possible to write total energy in terms of elastic tensor elements and γ. This expression relates the curvature value of the total energy versus strain profile, calculated at equilibrium configuration, to some combination of elastic tensor elements. For calculating the complete elastic stiffness tensor of a crystal the same procedure is repeated using different homogeneous strain tensors. If there

are 'p' independent elements in the elastic stiffness tensor of a crystal, 'p' different strain tensors need to be used. This procedure results in 'p' linear equations expressing some combinations of elastic constants in terms of curvature values. The curvature values are calculated from the energy versus strain profiles. The unknowns are the elastic tensor elements. The simultaneous linear equations are solved for elastic tensor elements using linear algebra methods. Strain tensors used for calculating the elastic constants are described in the Appendix B.

Chapter 4

Results: binary alloys

In a binary Ti-Ni system, alloys with compositions near equi-atomic TiNi undergo a MT. I used various theoretical methods described in the previous chapter to study the MT in TiNi-based SMAs. I will describe the results from these studies in this chapter. The motivation for the emphasis here on lattice dynamics is the general assumption that the MT in TiNi-based SMAs occurs due to a soft mode instability in the B2 structure. Four experimentally observed phases were considered in these studies: B2, B19, R, and B19′. I will describe the equilibrium structural information and discuss the relative stability of the four phases in the first section.

I calculated the electronic band structure and density of electronic states in each phase. The results will be presented in the second section. I will also discuss the stability of the four phases in terms of density of states (DOS) near the Fermi level. Fermi surfaces were calculated for B2. I will present the Fermi surfaces of two bands and identify the nesting regions separated by a soft mode wave vector.

Elastic constants of B2 were calculated by following a homogeneous deformation method. Results will be described and analysed in the third section. Harmonic phonon dispersion relations were calculated in three phases. I will present the results in the fourth section. Experimentally observed soft modes will be identified in the results. The irrep of the soft mode was used to determine the order parameters of various transformations that could be coupled to it. Order parameters for the experimentally observed MT paths will be presented. The quasi-harmonic approximation was used for studying the effect of thermal expansion on the unstable modes in B2. Results from these calculations will also be presented and discussed.

I tried to calculate the phonon spectrum at high temperatures by following

the SCAILD method. This revealed some important practical issues which have apparently not been discussed in the literature, and I will describe these in the fifth section.

Most of the electronic structure calculations presented in this thesis were done using the VASP code. The $3p$, $4s$, $3d$ electrons of Ni and $3s$, $3p$, $4s$, $3d$ electrons of Ti were considered as valence electrons. The cut-off for kinetic energy of electrons was chosen as 500 eV in all these calculations.

Linear response theory for calculating the harmonic phonon dispersion relations is implemented in the QE package [156], and this package also enables band structures and Fermi surfaces to be calculated and plotted easily. Hence I also used the QE package for calculating other properties of the B2 structure. Calculated harmonic phonon dispersion curves were in qualitative agreement with those calculated by the small displacement method. In addition to the valence electrons considered in the VASP calculations, the $3s$ electrons of Ni were also considered as valence electrons in QE calculations. The cut-off for the kinetic energy of electrons was set at 544.23 eV (40 Ry) in these calculations. Where the calculations were performed using QE, I explicitly mention the fact. All calculations were spin-polarised.

4.1 Structure relaxation

Four experimentally observed phases in the TiNi-based SMAs were considered. Experimentally available structural information was used for initializing the calculations. Unit cell parameters and atomic positions were relaxed until the forces on atoms were below the convergence threshold of 0.01 eV/Å. The equilibrium structures obtained after the relaxation were used for studying the material using other *ab initio* methods. The following part of this section presents the equilibrium structural parameters of the four phases.

4.1.1 B2

The energy of the B2 structure was calculated as a function of its lattice parameter, which was varied around the experimental lattice parameter [16]. Brillouin zone integration was done using a 20×20×20 **k**-point mesh in the total energy calculations. From the energy versus lattice parameter profiles, the equilibrium lattice parameter was calculated as 3.013 Å. This value is 0.07% less than the experimental value of 3.015 Å [71].

Table 4.1: Structural parameters of a B19 unit cell

Study	Symmetry	Lattice constants (Å)	Atomic positions
Present study (PAW-GGA)	*Pmcm*	a = 2.841 b = 4.593 c = 4.166	Ni(e) (0.0, 0.816, 0.25) Ti(f) (0.5, 0.277, 0.25)
Parlinski et al. (USPP-GGA)[51]	*Pmcm*	a = 2.800 b = 4.631 c = 4.190	Ni(e) (0.0, 0.780, 0.25) Ti(f) (0.5, 0.316, 0.25)
Huang et al. (PAW-LDA)[34]	*Pmcm*	a = 2.637 b = 4.557 c = 4.170	Ni(e) (0.0, 0.681,0.25) Ti(f) (0.5, 0.214, 0.25)

4.1.2 B19

Although B19 has not been observed in binary TiNi alloys, Parlinski et al. [51] relaxed the Ti and Ni atoms into a B19 structure. The hypothetical structure thus obtained was used for studying the MT. I used the atomic positions and lattice parameters of the hypothetical B19 as initial structural information for further relaxation. The space group symmetry of the reported B19 is *Pmcm* [51]. A 12 ×8 × 9 **k**-point mesh was used for BZ integration in structural optimisation calculations. Equilibrium cell parameters and atomic positions, expressed in absolute coordinates, are shown in Table(4.1). Structural information of a B19 unit cell from the literature is also presented in this table. Wyckoff position label is written next to each atom in the table.

4.1.3 B19′

Kudoh et al. [23] determined the structure of the B19′ observed in a Ti-49.2 at.%Ni alloy. Structural information from this study was used for initializing the calculations. A 12×10×8 **k**-point mesh was used for BZ integration in the structural optimisation calculations. Equilibrium cell parameters and atomic positions, expressed in absolute coordinates, are listed in Table(4.2). Structural information of a B19′ unit cell from the literature is also presented in this table. The relaxed monoclinic angle of the B19′ unit cell is 107.33 °, which is quite different from the experimentally determined 97.78 ° [23]. The equilibrium monoclinic angle of B19′ is in agreement with the 107.2 ° monoclinic angle predicted by Huang et al. [34] for the monoclinic structure. A B19′ structure with a 107.2 ° monoclinic angle can be visualised as a B33, base-centred orthorhombic (BCO),

Table 4.2: Structural parameters of a B19′ unit cell

Study	Lattice angles	Lattice constants (Å)	Atomic positions
Present study (PAW-GGA)	$\beta = 107.33\,^\circ$ $\alpha = \gamma = 90\,^\circ$	a = 2.923 b = 4.014 c = 4.925	Ni(e) (0.0855, 0.25, 0.6705) Ti(e) (0.3566, 0.25, 0.2138)
Kudoh et al. (Exp.) [23]	$\beta = 97.78\,^\circ$ $\alpha = \gamma = 90\,^\circ$	a = 2.898 b = 4.108 c = 4.646	Ni(e) (0.0372, 0.25, 0.6752) Ti(e) (0.4176, 0.25, 0.2164)
Parlinski et al. (USPP-GGA)[51]	$\alpha = \beta = 90\,^\circ$ $\gamma = 82.63\,^\circ$	a = 2.877 b = 4.686 c = 4.099	Ni(e) (0.9256, 0.7832, 0.0) Ti(e) (0.5374, 0.3242, 0.0)
Huang et al. (PAW-LDA) [34]	$\alpha = \beta = 90\,^\circ$ $\gamma = 107.2\,^\circ$	a = 2.851 b = 4.815 c = 3.921	Ni(e) (0.0851, 0.6708, 0.25) Ti(e) (0.3574, 0.2141, 0.25)

structure with an eight atom unit cell [34]. Equilibrium atomic positions in the B19′ are also in excellent agreement with the reported atomic positions in the BCO structure [34].

4.1.4 R

Hara et al. [28] determined the space group symmetry of R observed in TiNi binary alloys as $P3$. Structural information from this study was used for initializing the structure optimisation calculations. A 6×6×8 **k**-point mesh was used for BZ integration purposes in these calculations. Equilibrium cell parameters and atomic positions, expressed in direct coordinates, are shown in Table(4.3). Structural information of the R phase from the literature is also presented in this table.

Total energies of the four structures are compared in Table(4.4), which shows the relative total energies of the three phases with respect to B2 expressed per two-atom unit cell of the B2 structure. Calculated energy differences are in the same order as those reported in the literature [51, 34, 158]. But the calculated energies of various phases differ by a factor up to 2.7 times when compared with the reported energies in the literature. This differences in energies might be due to the differences in pseudopotentials, electronic kinetic energy cut-off values, k-point meshes used in various studies. Consistent with the experimental ground state, B19′ has the lowest energy. Also the total energy of the system is

Table 4.3: Structural parameters of a R unit cell

Study	Lattice angles	Lattice constants (Å)	Atomic positions
Present study (PAW-GGA)	$\alpha = \beta = 90\,^\circ$ $\gamma = 120\,^\circ$	a = 7.262 b = 7.262 c = 5.352	Ni(1a) (0.000, 0.000, 0.503) Ni(1b) (0.333, 0.667, 0.679) Ni(1c) (0.667, 0.333, 0.503) Ni(3d) (0.333, 0.978, 0.949) Ni(3d) (0.693, 0.026, 0.226) Ti(1a) (0.000, 0.000, 0.040) Ti(1b) (0.333, 0.667, 0.136) Ti(1c) (0.667, 0.333, 0.040) Ti(3d) (0.333, 0.987, 0.429) Ti(3d) (0.675, 0.008, 0.730)
Hara et al. (Exp.) [28]	$\alpha = \beta = 90\,^\circ$ $\gamma = 120\,^\circ$	a = 7.38 b = 7.38 c = 5.32	Ni(1a) (0.000, 0.000, 0.457) Ni(1b) (0.333, 0.667, 0.541) Ni(1c) (0.667, 0.333, 0.396) Ni(3d) (0.318, -0.022, 0.854) Ni(3d) (0.688, 0.021, 0.160) Ti(1a) (0.000, 0.000, 0.000) Ti(1b) (0.333, 0.667, 0.083) Ti(1c) (0.667, 0.333, 0.009) Ti(3d) (0.335, -0.004, 0.361) Ti(3d) (0.677, 0.010, 0.684)
Parlinski et al. (USPP-GGA) [51]	$\alpha = \beta = 90\,^\circ$ $\gamma = 120\,^\circ$	a = 7.257 b = 7.257 c = 5.383	Ni(1a) (0.000, 0.000, 0.542) Ni(1b) (0.333, 0.667, 0.630) Ni(1c) (0.667, 0.333, 0.542) Ni(3d) (0.333, -0.0159, 0.929) Ni(3d) (0.676, 0.009, 0.230) Ti(1a) (0.000, 0.000, 0.000) Ti(1b) (0.333, 0.667, 0.180) Ti(1c) (0.667, 0.333, 0.000) Ti(3d) (0.333, -0.021, 0.449) Ti(3d) (0.693, 0.026, 0.724)

decreasing along the experimentally observed MT paths: B2→B19→B19′, and B2→R→B19′.

Table 4.4: Total energies of the equilibrium structures

Structure	$E - E_{B2}$ (eV/two atoms)		
	Present study (PAW-GGA)	Parlinski et al. (USPP-GGA) [51]	Huang et al. (PAW-LDA) [34]
B2	0.0	0.0	0.0
B19	-0.1432	-0.0635	-0.088
B19′	-0.1484	-0.0860	-0.108
R	-0.0969	-0.0357	

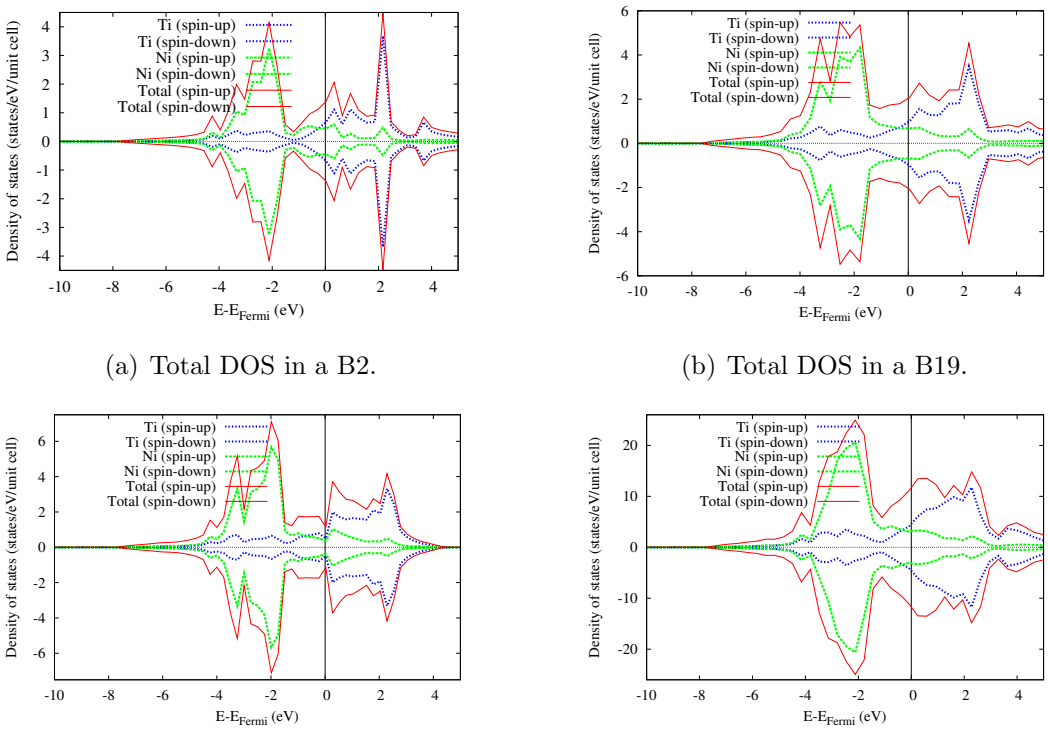
4.2 Electronic properties

Electronic states near the Fermi level E_F are most likely to undergo scattering processes and hence are more important for studying the stability of a material. The distribution of electronic states in energy is given by the density of states (DOS). The DOS were calculated here with the linear tetrahedron method [159]. Calculated DOS profiles in the four structures are shown in Fig.(4.1). The energy scale is defined here such that $E_F = 0$ eV in these profiles.

States near E_F have mainly d orbital character. For example, projected DOS onto a Ni and a Ti atom have 88% and 95% d character respectively at the Fermi level in B2. All the four DOS profiles have a number of peaks above E_F . These peaks are broader in B19, B19′, and R as compared to the peaks in B2. The four profiles differ in the fine structure around E_F, and notably there is a local minimum at E_F only in the most stable, B19′.

It is noteworthy that spin-polarization is not adopted in any of the structures. All the DOS exhibit a minimum at 1-2 eV below the Fermi level. The major contribution to the states below this minimum is from Ni d orbitals. Ti d orbitals are mainly contributing to the states well above E_F. States around the Fermi level are made up of orbitals from both Ni and Ti atoms. In B2 for example Ti atoms contribute approximately 60% to the states at E_F. Calculated DOS profiles in the four structures are in qualitative agreement with the theoretically calculated profiles in the literature [160, 161].

The DOS at the Fermi level, DOS(E_F), in a structure gives an indication of its stability. Generally, the lower the DOS at E_F the higher is the stability of a structure [162]. DOS(E_F) values in the four structures are listed in Table(4.5).



(a) Total DOS in a B2.

(b) Total DOS in a B19.

(c) Total DOS in a B19′.

(d) Total DOS in a R.

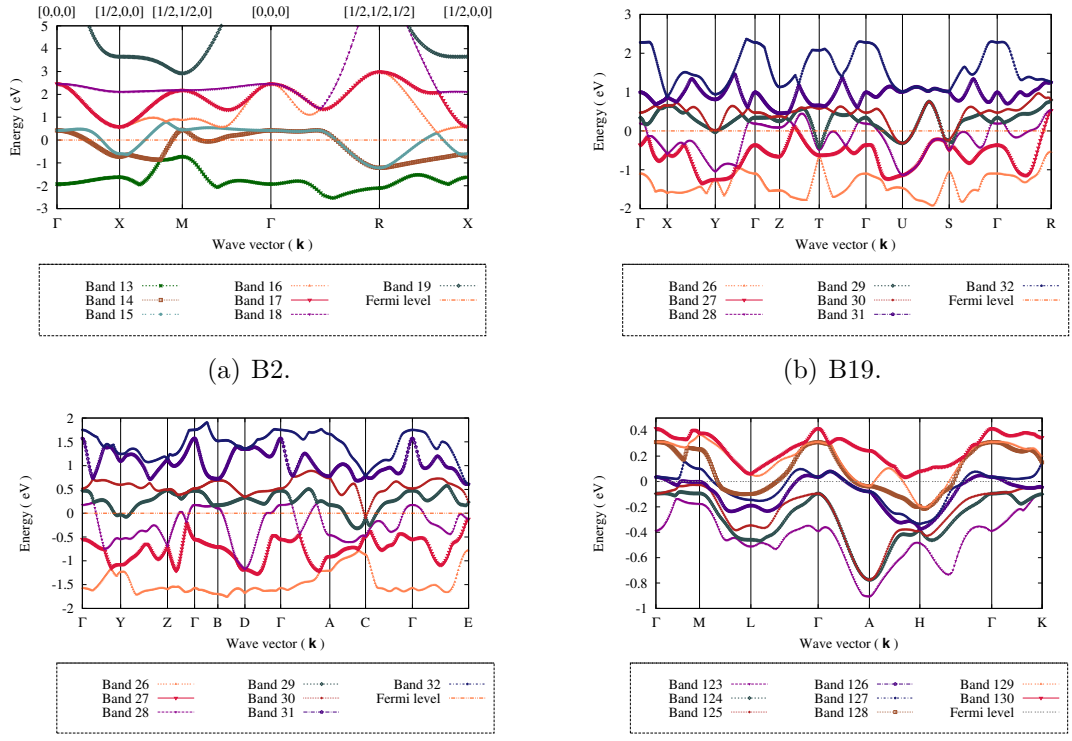
Figure 4.1: Total density of states in the four phases. Spin-down density of states are plotted as negative values.

The DOS(E_F) values decrease along the two transition paths: B2→B19→B19′, and B2→R→B19′. Hence the DOS(E_F) values accurately predict the relative stability of these four structures.

Table 4.5: Total spin-up DOS at the Fermi level in different structures

Structure	DOS(E_F) (States/eV/two atoms)
B2	1.3890
B19	1.0198
B19′	0.6027
R	1.2991

Electronic band structure provides a perspective of electronic states distribution along different paths in the BZ. Electronic band structures were calculated along high symmetry directions in the FBZ. Calculated band structures in the four phases are shown in Fig.(4.2).



(a) B2.

(b) B19.

(c) B19′.

(d) R.

Figure 4.2: Electronic band structure in various phases along high symmetry directions.

The B2 electronic band structure is in excellent agreement with the band structure calculated by Zhao et al. [57] and Bruinsma [36]. It is postulated

that parallel regions, often referred to as *nested*, on the Fermi surface might be responsible for the phonon anomalies at the wave vector by which they are separated. So as to identify such nesting regions, I calculated the Fermi surface in B2 using the QE code.

4.2.1 Fermi surface

The lattice parameter of the B2 structure was determined to be 3.045 Å(5.753 au). In these calculations a 16×16×16 **k**-point mesh was used for BZ integration. Electronic band structure was also calculated and it is plotted in Fig.(4.3). Since 3*s* electrons were also considered as valence electrons in the QE calculations, band 14 in QE calculations was equivalent to band 13 in VASP calculations and so on. This band structure is in qualitative agreement with the band structure in Fig.(4.2(a)). Two bands cross the Fermi level in Fig.(4.3), namely bands 15 and 16. Hence the two bands have both valence states and conduction states and the states within these two bands are likely to undergo interband or intraband scattering.

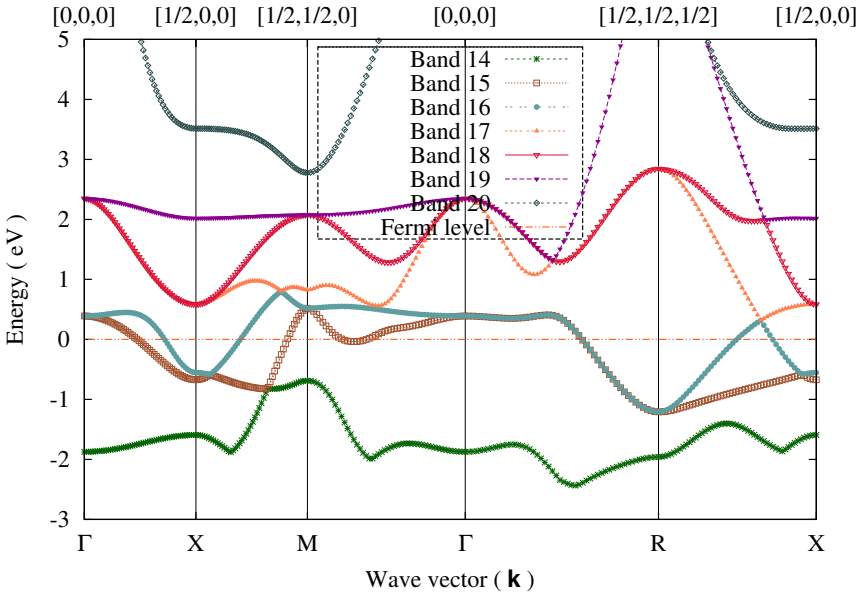


Figure 4.3: Electronic band structure in B2 calculated using the *Quantum Espresso*.

Three dimensional Fermi surfaces of band 15 and band 16 in the FBZ are shown in Fig.(4.4). The Fermi surfaces are in qualitative agreement with the Fermi surfaces calculated by Souvatzis et al. [60] and Hatcher et al. [163]. Regions

on Fermi surfaces separated by a phonon wave vector corresponding to the soft mode may contribute dominantly to the electron-phonon interaction [56]. Cross-sections of the Fermi surfaces are useful to identify these regions. Sections of Fermi surfaces corresponding to bands 15 and 16 at $k_z = 0.0$ and $k_z = 0.0769$ are shown in Figs. (4.5) and (4.6) respectively. Dotted regions in these plots denote the conduction states and empty regions denote the valence states. The boundaries between the conduction states and the valence states are the Fermi surface contours.

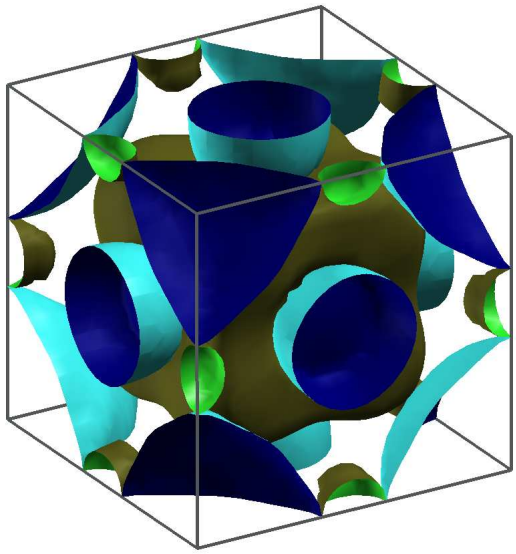


Figure 4.4: Fermi surfaces of band 15 (green contours) and band 16 (blue contours) in a B2.

Parallel regions on the Fermi surfaces of two bands separated by a wave vector close to the soft mode wave vector ($\frac{2\pi}{a}[\frac{1}{3}, \frac{1}{3}, 0]$) encompass many electronic states. Such regions are identified with arrows in Figs. (4.5) and (4.6). As shown by Zhao et al. [52, 57], interaction of the electron states in the nesting region with the phonon of wave vector $\frac{2\pi}{a}[\frac{1}{3}, \frac{1}{3}, 0]$ is responsible for a noticeable phonon anomaly in B2 at $\frac{2\pi}{a}[\frac{1}{3}, \frac{1}{3}, 0]$.

4.3 Homogeneous deformation

In order to determine the elastic constants of B2, I used the homogeneous deformation method. As described in the Appendix B, different strain tensors were used for calculating different elastic constants. The variation of energy with

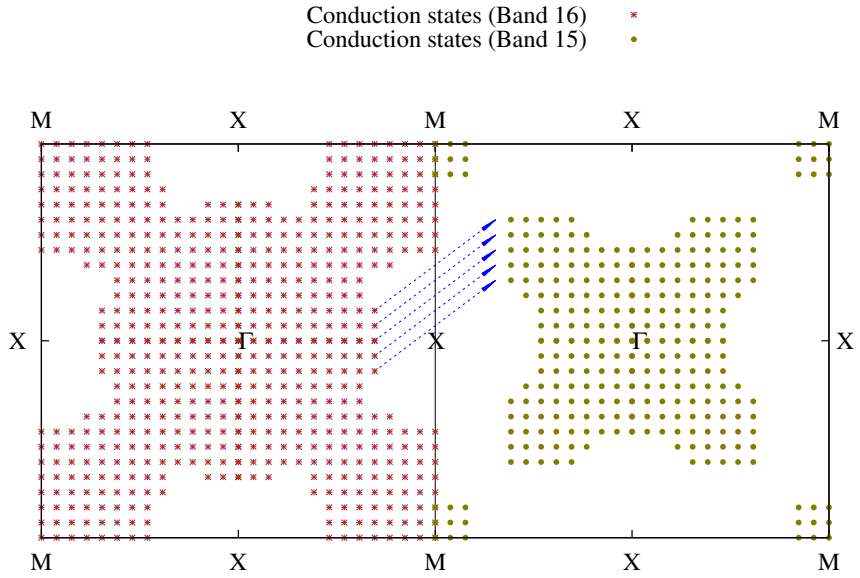


Figure 4.5: Cross-sections of Fermi surfaces correspond to band 15 and band 16 at $k_z = 0.0$.

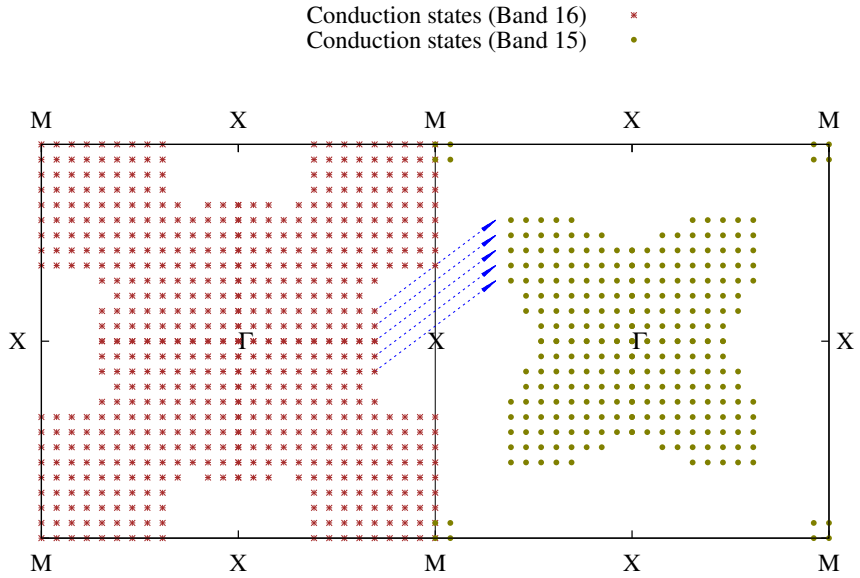


Figure 4.6: Cross-sections of Fermi surfaces correspond to band 15 and band 16 at $k_z = 0.0769$.

strain from these calculations is shown in Fig.(4.7). Elastic constants were calculated from the curvature at the minimum of each of these curves and listed in Table(4.6). The σ_1, σ_2, and σ_4 variation with strain in bulk modulus, C′, and C_{44} calculations respectively is shown in Fig.(4.8). Straight lines were fitted to the stress-strain curves and the elastic constants were calculated from the slopes. These values are also shown in the Table(4.6). Elastic constants calculated from the energy versus strain profiles and the stress versus strain profiles are agreeing with each other. The calculated elastic constants of the B2 from the literature are also presented in the Table(4.6) for comparison purpose. The experimental elastic constants presented in this table are from the study of Mercier et al. [61]. They calculated the elastic constants from the measurements of ultrasonic velocities by a pulse echo overlap method at the room temperature ($\sim 25\,^{\circ}$C). The elastic constants of a cubic crystal must satisfy the following requirements as a necessary condition for its mechanical stability [164]:

$$C_{11} > 0, \quad C_{44} > 0, \quad \text{and} \quad C' > 0.$$

The calculated elastic constants are all positive and satisfy the above stability criteria. This means that in B2, at 0 K, there is a natural restoring force against homogeneous deformation by shear or dilation. The elastic constants in Table(4.6) are in qualitative agreement with the calculated elastic constants by Bihlmayer et al. [66] and Wei Cai et al. [165]. This result contradicts the prediction by Wagner et al. [67] that there is an instability to homogeneous $\{110\}\langle 1\bar{1}0\rangle$ shear. Their result was also obtained with DFT. After careful checking of my calculations and their paper I believe they made a computational error, but I was unable to obtain definite confirmation of this from the authors.

Table 4.6: Elastic tensor elements of austenite calculated by following the homogeneous deformation method and from the literature

C_{ij}	Calculated value (GPa)		Literature (GPa)			
	Ene. vs str.	σ_i vs str.	Exp.[61]	Calc.[66]	Calc.[165]	Calc.[67]
C_{11}	190.94	188.01	162.44	178.2	165	138
C_{12}	142.32	144.25	129.24	147.6	125	169
C_{44}	51.20	50.98	34.77	49.0	38	40
C′	24.31	21.88	16.60	15.3	20	-15.5

Atomic vibrations may be described by normal modes of vibration. All normal modes vibrate with a positive frequency in a stable crystal, hence if the calculated frequency of any mode is imaginary at 0 K, the structure is unstable

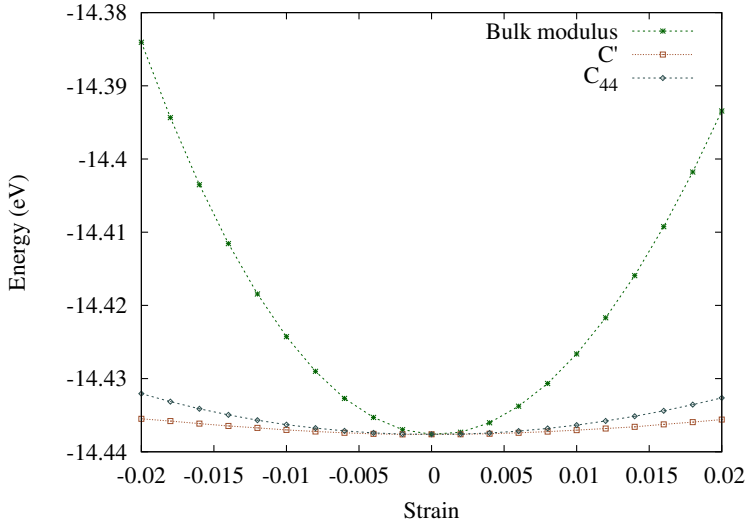


Figure 4.7: The energy variation with strain from different calculations for determining the elastic tensor elements.

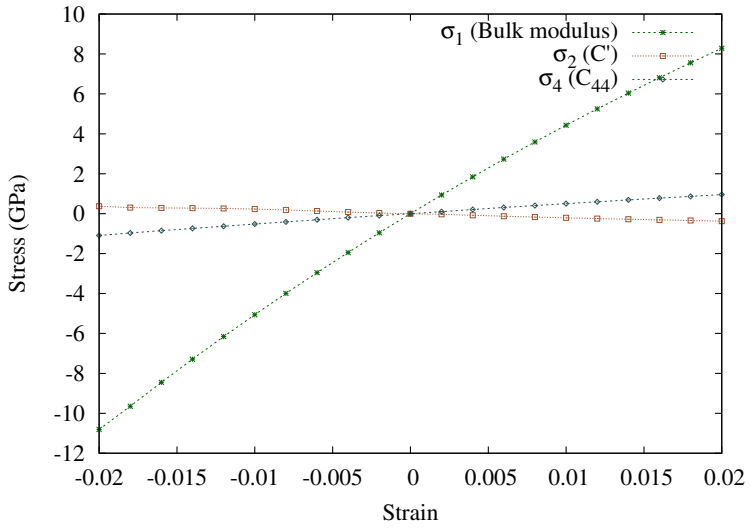


Figure 4.8: The stress variation with strain from different calculations for determining the elastic tensor elements.

to the atomic displacements of the mode. I calculated the phonon dispersion relations within the HA using a small displacement method. Results are described in the next section.

4.4 Harmonic phonon dispersion relations

Phonon dispersions were calculated in three phases. I will describe the results from these calculations in this section. The 'soft' modes are identified, *i.e.* the modes with imaginary frequencies. In the plots of phonon dispersion relations, which give frequency as a function of wave vector, their moduli are shown as negative frequencies. The experimentally observed soft modes are also analysed in this section.

4.4.1 B2

Phonon dispersion relations in B2 were calculated using three different supercell sizes. Since there are two atoms in the unit cell, there are six branches in the dispersion relations. The three branches which have zero frequency at the Γ point are acoustic modes and the rest are optic modes. In a small displacement method, the calculated frequencies are exact only at the wave vectors commensurate with size of the supercell. Exact wave vectors in calculations done with different supercells are listed in Table(4.7). It contains one vector from each star of exact wave vectors.

As described in the Section(3.2.1.2), frequencies and polarisation vectors of all normal modes at a given wave vector are obtained by diagonalising the dynamical matrix. Each normal mode belong to an irrep of the space group of the crystal according to the normal mode polarisation. Mode labelling is done according to the symmetry of the polarisation vector of normal modes and using the results derived in the Appendix A. Irreps of the soft modes are used for determining the symmetry of the product phases. The results are used for relating the experimentally observed MT paths to a particular soft mode.

The ISOTROPY code was used to determine the primary order parameters from the soft mode irrep (see Section(3.2.2) in Chapter 3) and to determine the secondary order parameters which describe the transformation strains of a MT. For a given irrep all possible product phases were determined. The product phases with unit cell volumes close to the experimentally-observed product phase unit cell volumes were considered for further analysis. Secondary order

parameters describing the transformation strains were determined for the chosen transformation path. I will describe the primary and secondary order parameters for the experimentally observed MT paths in the TiNi-based SMAs. All the determined order parameters are in agreement with the order parameters suggested by Barsch [48]. However, certain transformational strains which do not alter the symmetry of the product phase are added to the order parameters suggested by Barsch.

Symmetry coordinates are generally used for strain in the group theoretical analysis. The symmetry coordinates are obtained by reducing the six component strain basis. Let us define the strain variables $\{\eta_i\}$ which are obtained after reducing the components of the strain tensor with respect to cubic group operations [166]. $\eta_1 = \frac{1}{\sqrt{3}}(\epsilon_{11} + \epsilon_{22} + \epsilon_{33}), \eta_2 = \frac{1}{\sqrt{6}}(\epsilon_{11} + \epsilon_{22} - 2\epsilon_{33}), \eta_3 = \frac{1}{\sqrt{2}}(\epsilon_{11} - \epsilon_{22}), \eta_4 = 2\epsilon_{12}, \eta_5 = 2\epsilon_{13}$, and $\eta_6 = 2\epsilon_{23}$. The new strain symmetry coordinates $\{\eta_1\}, \{\eta_2, \eta_3\}$, and $\{\eta_4, \eta_5, \eta_6\}$ are basis functions of the irreps Γ_1^+, Γ_3^+, and Γ_5^+ respectively [46]. The secondary order parameter is described in terms of basis functions of the irreps Γ_1^+, Γ_3^+, and Γ_5^+.

In principle elastic constants can be calculated from the slopes of the dispersion relations at Γ, and I have evaluated them this way for comparison with the method of homogeneous deformation. Due to the small supercell size in the finite displacement method, in effect the dispersion curve is interpolated between Γ and the nearest exact k-point, which corresponds to a single wavelength that fits into the supercell. Hence the elastic constants calculated in this way turn out to be very inaccurate. I will also discuss the effect of the supercell size on their accuracy. Elastic constants can also be calculated directly from the force constants using the relation derived in the Section(3.2.1.5) in Chapter 3. As expected, these values are in agreement with those obtained from the long wavelength limit of the dispersion curves.

2×2×2 supercell calculations

Phonon dispersion relations calculated using a 2×2×2 supercell are shown in Fig.(4.9). A 6×6×6 **k**-point mesh was used for BZ integration in the force calculations. The harmonic frequencies at the exact wave vectors are in close agreement with the frequencies calculated by Parlinski et al. [51]. As can be seen from Fig.(4.9), there is a doubly degenerate acoustic mode which has imaginary frequency of $2.09i$ THz at the zone boundary wave vector M. One soft mode

Table 4.7: Exact wave vectors in the first Brillouin zone of a B2 in different supercell calculations

supercell size ↓	Exact points ↓
$2\times2\times2$	$\Gamma=\frac{2\pi}{a}[0,0,0]$, X $=\frac{2\pi}{a}[\frac{1}{2},0,0]$, M $=\frac{2\pi}{a}[\frac{1}{2},\frac{1}{2},0]$, R $=\frac{2\pi}{a}[\frac{1}{2},\frac{1}{2},\frac{1}{2}]$.
$3\times3\times3$	$\Gamma=\frac{2\pi}{a}[0,0,0]$, $\frac{2\pi}{a}[\frac{1}{3},0,0]$, $\frac{2\pi}{a}[\frac{1}{3},\frac{1}{3},0]$, $\frac{2\pi}{a}[\frac{1}{3},\frac{1}{3},\frac{1}{3}]$.
$4\times4\times4$	$\Gamma=\frac{2\pi}{a}[0,0,0]$, X $=\frac{2\pi}{a}[\frac{1}{2},0,0]$, $\frac{2\pi}{a}[\frac{1}{4},0,0]$, M$=\frac{2\pi}{a}[\frac{1}{2},\frac{1}{2},0]$, $\frac{2\pi}{a}[\frac{1}{4},\frac{1}{4},0]$, R$=\frac{2\pi}{a}[\frac{1}{2},\frac{1}{2},\frac{1}{2}]$, $\frac{2\pi}{a}[\frac{1}{4},\frac{1}{4},\frac{1}{4}]$.

belongs to a longitudinal acoustic (LA) branch and another to a TA_2 branch. Atomic displacements according to the polarisation vector of either of these two modes or a combination of them lower the energy of the system and the B2 would thereby transform into a new phase at low temperature. Symmetry of the doubly degenerate soft mode belongs to an irrep M_5^-. Atomic displacements in a $2\times2\times2$ supercell according to the polarisation vector of the TA_2 mode at M are shown in Fig.(4.10). This atomic displacement pattern is in agreement with the atomic displacement pattern of the same mode calculated by Huang et al. [53]. In this mode the atoms are moving only in the xy plane and not in the z direction.

As reported by Otsuka et al. [3], Ren et al. [44] observed pronounced softening of a TA_2 phonon at M before the MT in a Ti-30 at.%Ni-20at.%Cu alloy. B19 and B19′ were observed in TiNiCu based SMAs [32]. Parlinski et al. [51] suggested that the soft mode at M would transform B2 into B19: $Pm\bar{3}m(z=1)\xrightarrow{M_5^-}Pmma(z=2)$. Here z is the unit cell volume of a phase expressed in terms of the unit cell volume of B2. This transformation correctly describe the symmetry of the product phase. But it does not describe the transformation strains and volume change associated with the MT.

There are three vectors in the star of M and at each vector there is a doubly degenerate soft mode. Hence the primary order parameter is a six dimensional order parameter [49]. The primary order parameter and secondary parameters for a $Pm\bar{3}m\rightarrow Pmma$ transition are shown in Table(4.8). These order parameters correspond to a MT from B2 into one variant of B19. Secondary order parameters presented in this table describe the transformation strains, which do not alter the symmetry of the product. The undetermined components of the direction vectors in the Table(4.8) are measures of soft mode amplitudes and transformation

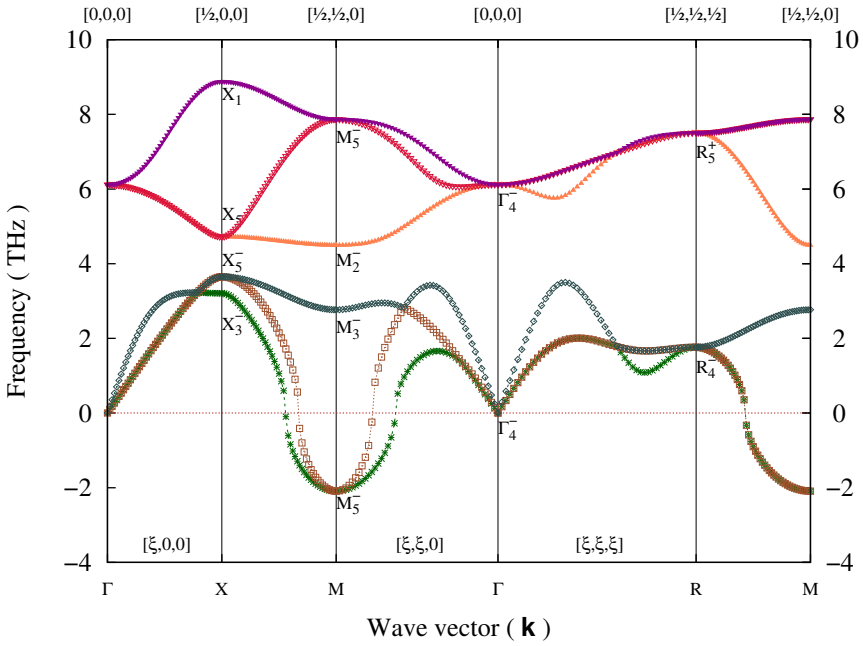


Figure 4.9: Phonon dispersion relations in a B2 obtained from 2×2×2 supercell calculations.

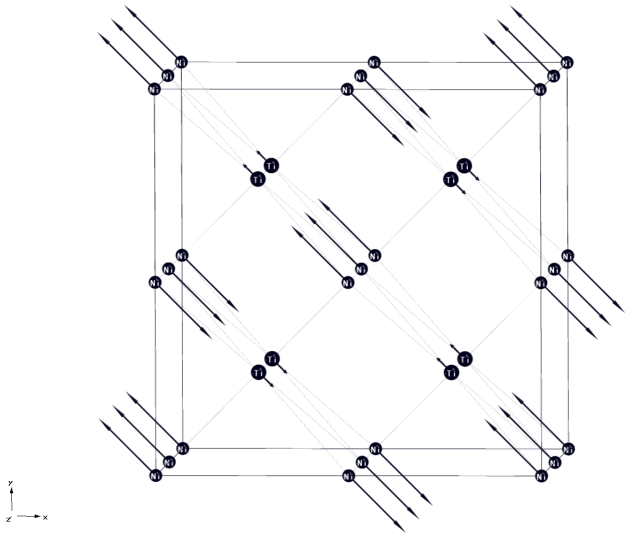


Figure 4.10: Atomic displacements corresponding to a transverse acoustic mode (TA_2) at a wave vector $\frac{2\pi}{a}[\frac{1}{2},\frac{1}{2},0]$.

strains: The component a is a measure of the soft mode amplitude, components b, c, d determine the transformation strains.

Table 4.8: Order parameters for a $Pm\bar{3}m$(B2) $\xrightarrow[\Gamma_1^+,\Gamma_3^+,\Gamma_5^+]{\mathrm{M}_5^-}$ $Pmma$(B19) transition

Primary order parameter	Direction vector
M_5^-	$\{a,0,0,0,0,0\}$
Secondary order parameters	**Direction vector**
Γ_1^+	$\{b\}$
Γ_3^+	$\{\frac{-1}{2}c, \frac{\sqrt{3}}{2}c\}$
Γ_5^+	$\{0,0,d\}$

The volume of a B19′ unit cell is approximately twice the volume of a B2 unit cell in binary TiNi SMAs [167] and TiNiCu based SMAs [32]. The symmetry of the B19′ phase is $P2_1/m$. A coupling between the soft mode at M and the shear strains could result in a product with a $P2_1/m$ symmetry. The order parameters corresponding to this MT are listed in Table(4.9). Notice the difference between the order parameters in Tables (4.8) and (4.9). The only difference is that the secondary order parameter describing the shear strains belongs to an irrep Γ_5^+. Therefore, a strong coupling between the soft mode at M and the shear strains belonging to the irrep Γ_5^+ might be responsible for the formation of B19′. C_{44} relates these shear strains to the elastic free energy.

It was empirically justified that the relative softening of the two elastic shear constants as measured by the anisotropy factor (A= C_{44}/C') is a predictor of the final symmetry of martensite [65]. If this ratio decreases as the alloy is cooled toward the M_s, B19′ forms during the MT. From the above symmetry arguments, coupling between shear strains having the symmetry of an irrep Γ_5^+ and the soft mode amplitudes could result in a B19′. This strong coupling might be causing the pronounced softening of C_{44} when the phonon mode is softening. The same coupling might be appearing as the correlation between C' and C_{44} because the same TA_2 branch is related to the C' in the long wave length limit.

Three products with trigonal symmetry (space groups $R3$, $R32$, and $R3m$) could form due to a M_5^- soft mode instability. This is because there are three possible combinations of the degenerate mode eigenvectors that can result in different symmetries. Unit cells of all three products have volumes twelve times the volume of B2. However, the experimentally observed R unit cell occupy approximately nine times the volume of a B2 unit cell. Therefore the R phase

Table 4.9: Order parameters for a $Pm\bar{3}m$(B2) $\xrightarrow[\Gamma_1^+,\Gamma_3^+,\Gamma_5^+]{\mathrm{M}_5^-}$ $P2_1/m$(B19′) transition

Primary order parameter	Direction vector
M_5^-	$\{a,0,0,0,0,0\}$
Secondary order parameters	Direction vector
Γ_1^+	$\{b\}$
Γ_3^+	$\{\frac{-1}{2}c, \frac{\sqrt{3}}{2}c\}$
Γ_5^+	$\{d,d,e\}$

observed in TiNi-based SMAs cannot form simply from the soft mode instability at M. In fact, experimentally the R phase was observed only in TiNi [20], TiNiCo [27], and TiNiFe [28] based SMAs but not in TiNiCu based SMAs. Pronounced phonon softening of a TA_2 mode near $\frac{2\pi}{a}[\frac{1}{3},\frac{1}{3},0]$ was experimentally observed in B2 prior to the MT in TiNi [35, 38] and TiNiFe [42, 43] based SMAs. In order to study the behaviour of the phonon at the wave vector $\frac{2\pi}{a}[\frac{1}{3},\frac{1}{3},0]$, dispersion relations were calculated using a 3×3×3 supercell. These results are presented in the next sub-section.

Acoustic waves in the long wave length limit ($\mathbf{k} \to \mathbf{0}$) represent sound waves. Dove [130] has derived the relationships between the propagation velocity of the acoustic waves at Γ and the elastic constants for a cubic crystal. These relations along a few high symmetry directions are given in Table(4.10). Elastic constants were calculated using these relations and slopes of the acoustic branches of the dispersion curves depicted in Fig.(4.9). These values are also listed in Table(4.10). The calculated elastic constants along different propagation directions are consistent with each other. However, it is important to note that the actual values are completely spurious! This is because the finite displacement method can give only a very poor representation of phonon dispersion curves in the long wavelength limit, as discussed later in this section.

As described in Section(3.2.1.5), the elastic constants are a linear combination of the IFC weighted by a function of the atomic positions. Force constant values determined in 2×2×2 supercell calculations were used for calculating the elastic constants. Following elastic constants were obtained : C_{11}=184.84 GPa, C_{44}=46.95 GPa and C_{12}=65.5 GPa. As expected these values are in excellent agreement with the elastic constants obtained from the slopes of dispersion relations, thus providing a useful check on our calculations.

Table 4.10: Relationship between wave propagation velocities of the acoustic modes at the zone center and elastic constants in a cubic crystal [130]. The elastic constants calculated using the slopes of acoustic branches at Γ along three directions in the Fig.(4.9).

$\mathbf{k} = [\xi,0,0]$	$\mathbf{k} = [\xi,\xi,0]$	$\mathbf{k} = [\xi,\xi,\xi]$
$\rho\ \omega^2_{[100]} = C_{11}\ \xi^2$	$\rho\ \omega^2_{[110]} = (\ C_{11}+C_{12}+2C_{44}\ )\ \xi^2$	$\rho\ \omega^2_{[111]} = (C_{11}+2C_{12}+4C_{44})\ \xi^2$
$\rho\ \omega^2_{[010]} = C_{44}\ \xi^2$	$\rho\ \omega^2_{[1\bar{1}0]} = (\ C_{11}\text{-}C_{12}\ )\ \xi^2$	$\rho\ \omega^2_{[1\bar{1}0]} = (C_{11}\text{-}C_{12}+C_{44})\ \xi^2$
$\rho\ \omega^2_{[001]} = C_{44}\ \xi^2$	$\rho\ \omega^2_{[001]} = 2C_{44}\ \xi^2$	$\rho\ \omega^2_{[11\bar{2}]} = (C_{11}\text{-}C_{12}+C_{44})\ \xi^2$
$C_{11} = 184.63$ GPa	$C_{11} = 184.51$ GPa	$C_{11} = 184.8$ GPa
$C_{44} = 46.95$ GPa	$C_{44} = 46.92$ GPa	$C_{44} = 46.7$ GPa
	$C_{12} = 65.47$ GPa	$C_{12} = 65.63$ GPa

3×3×3 supercell calculations

Dispersion relations obtained using a 3×3×3 supercell are shown in Fig.(4.11). The BZ integration was done using a 4×4×4 **k**-point mesh in the force calculations. The exact wave vectors are highlighted by vertical dotted lines in this figure. Compared to the calculations with a 2×2×2 supercell, there are two additional modes with imaginary frequencies: a TA_2 mode at $\frac{2\pi}{a}[\frac{1}{3},\frac{1}{3},0]$ having a frequency $2.02\imath$ THz and a LA mode at $\frac{2\pi}{a}[\frac{1}{3},\frac{1}{3},\frac{1}{3}]$ having a frequency $1.62\imath$ THz. The calculations accurately predicted the location of an experimentally observed soft mode at $\frac{2\pi}{a}[\frac{1}{3},\frac{1}{3},0]$. Although the soft mode frequency at M appears to be more imaginary than the soft mode frequency at $\frac{2\pi}{a}[\frac{1}{3},\frac{1}{3},0]$ in Fig.(4.11), the actual difference is only $0.07\imath$ THz. This is because the M point is not an exact wave vector in the 3×3×3 supercell calculations.

The calculated phonon dispersion relations do not have the contributions from anharmonic effects, which at finite tempeatures are very important in this system. The measured phonon frequencies, which are only available in the temperature range 65 °C – 250 °C [35, 38], depend on phonon-phonon interactions and electron-phonon interactions at higher temperatures. The calculated TA_2 mode frequencies at M and $\frac{2\pi}{a}[\frac{1}{3},\frac{1}{3},0]$ differ by $0.07\imath$ THz. However, the soft mode was observed experimentally only at $\frac{2\pi}{a}[\frac{1}{3},\frac{1}{3},0]$ in TiNi and TiNiFe based SMAs. These results suggest that the anharmonicity and changes in the Fermi surfaces at high temperature affect both the TA_2 modes in such a way that the TA_2 mode at $\frac{2\pi}{a}[\frac{1}{3},\frac{1}{3},0]$ is softer than the TA_2 mode at M in TiNi and TiNiFe

based SMAs.

There are twelve vectors in the star of $\frac{2\pi}{a}[\frac{1}{3},\frac{1}{3},0]$ and at each vector there is a soft TA_2 mode. Therefore, the order parameter has twelve components. The symmetry of the soft mode at $\frac{2\pi}{a}[\frac{1}{3},\frac{1}{3},0]$ belongs to an irrep Σ_2. The same symmetry has been reported to belong to a Σ_4 irrep in the literature [48, 51, 52]. This is incorrect. Isotropy subgroups belonging to the irrep Σ_2 include subgroups having orthorhombic symmetry (space groups $Pmm2$, $Amm2$, and $Pmmm$), monoclinic symmetry (space groups $P2$, $C2$, Pm, Cm, $P2/m$, and $C2/m$), and trigonal symmetry (space groups $P3$, $P3_1$, $R3$, $P\bar{3}$, $R\bar{3}$, $R32$, and $P31m$). All the unit cells of product phases with orthorhombic and monoclinic symmetries occupy three times or more the volume of a B2 unit cell. Therefore, B19 and B19′ observed in TiNi-based SMAs cannot form directly due to the soft mode instability at $\frac{2\pi}{a}[\frac{1}{3},\frac{1}{3},0]$.

Unit cells of four trigonal phases occupy approximately nine times the volume of a B2 unit cell. Space groups of the four product phases are: $P3$, $P3_1$, $P\bar{3}$, and $P31m$. Transition paths correspond to these four trigonal phases and primary order parameters of these transitions are shown in Table(4.11). Secondary order parameters describing the MT strains have same components in the four paths and are listed in Table(4.12). Unit cells of all other trigonal products occupy 27 times the volume of a B2 unit cell. The symmetry of the R phases observed in TiNi [29], TiNiFe [28], and TiNiCo [168] based SMAs was determined to be $P\bar{3}$, $P3$, and $P31m$ respectively. Each symmetry is related to a particular transition in Table(4.11). Therefore atomic displacements during a B2 $\rightarrow$ R transition in these alloys can be described by the corresponding primary order parameter in the Table(4.11) and the secondary order parameters in the Table(4.12).

The R phase transforms into B19′ on further cooling in TiNiCo based SMAs [27], cold worked and annealed TiNi-based SMAs [20, 24, 29]. The unit cell of the R phase contains eighteen atoms, while the unit cell of a B19′ contains four atoms. Therefore, since these are incommensurate it is not possible to study the R $\longrightarrow$ B19′ transition using the available group-subgroup relations. Hence calculation of phonon dispersion in R was not pursued.

4×4×4 supercell calculations

Increasing the supercell size increases the number of neighbours to which the calculated force constants are calculated with useful accuracy, since the periodic

Table 4.11: Possible transition paths in TiNi-based shape memory alloys due to the soft mode instability at $\frac{2\pi}{a}[\frac{1}{3},\frac{1}{3},0]$ and corresponding primary order parameters

Primary order parameter ↓	Transition path↓
$\{a,0,0,b,a,0,-b,0,0,0,a,-b\}$	$Pm\bar{3}m \xrightarrow[\Gamma_1^+,\Gamma_5^+]{\Sigma_2} P3$
$\{a,0,0,b,-\frac{1}{2}(a+\sqrt{3}b),0,-\frac{1}{2}(\sqrt{3}a-b),0,0,0,a,-b\}$	$Pm\bar{3}m \xrightarrow[\Gamma_1^+,\Gamma_5^+]{\Sigma_2} P3_1$
$\{a,0,0,0,a,0,0,0,0,0,a,0\}$	$Pm\bar{3}m \xrightarrow[\Gamma_1^+,\Gamma_5^+]{\Sigma_2} P\bar{3}$
$\{0,0,0,a,0,0,-a,0,0,0,0,-a\}$	$Pm\bar{3}m \xrightarrow[\Gamma_1^+,\Gamma_5^+]{\Sigma_2} P31m$

Table 4.12: Secondary order parameters for the four transition paths in Table(4.11)

Order parameter	Direction vector
Γ_1^+	$\{c\}$
Γ_5^+	$\{-d,d,-d\}$

boundary conditions mean that one is actually calculating a force constant between sublattices. At the same time we expect a larger supercell to improve the accuracy of the interpolated frequencies. In order to study these effects of interaction range, dispersion relations were also calculated using a 4×4×4 supercell. A **k**-point mesh of size 3×3×3 was used for the BZ integration in the force calculations. Calculated dispersion relations are shown in Fig.(4.12). In addition to the set of exact wave vectors in a 2×2×2 supercell, there are further exact **k**-points shown by the dotted vertical lines. As expected the calculated frequencies at the exact points on the zone boundary and at Γ match accurately the corresponding exact frequencies from the 2×2×2 supercell calculations. However, on comparing the dispersion relations in Figs. (4.9), (4.11) and (4.12), it appears that there is no general systematic increase in the accuracy of the interpolated frequencies with increase in the supercell size, the dispersion curves between the exact wave vectors should be regarded as unreliable.

This last point is reinforced by the elastic constants calculated from the slopes of the phonon dispersion curves of Figs. (4.9), (4.11) and (4.12). These values are listed in Table(4.13). The dispersion curves close to Γ, which were used for calculating the slopes, differ significantly between the supercells. For

this reason, the calculated elastic constants from the dispersion relations deviate significantly from the more reliable results from homogeneous deformation. Since there is no systematic change in the interpolated frequencies with increase in the supercell size, there is no systematic improvement in the calculated elastic constants with supercell size up to the largest possible with our fairly generous computational resources.

I also calculated the dispersion relations in the B2 following a linear response method as implemented in the QE [139, 156]. Dispersion relations were calculated at k-points in a set of points on a uniformly spaced 6×6×6 grid in the FBZ. Calculated dispersion relations are in qualitative agreement with the results from the small displacement method: Normal modes with imaginary frequencies were found at M, $\frac{2\pi}{a}[\frac{1}{3}, \frac{1}{3}, 0]$, and $\frac{2\pi}{a}[\frac{1}{3}, \frac{1}{3}, \frac{1}{3}]$.

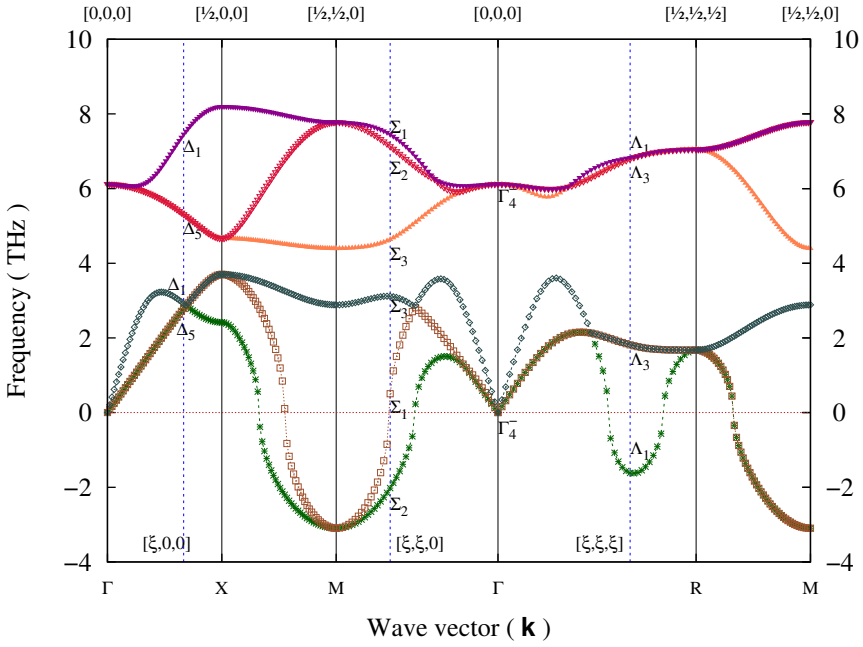


Figure 4.11: Phonon dispersion relations in a B2 obtained from 3×3×3 supercell calculations.

Quasi-harmonic approximation

Crystals expand on heating, demonstrating that phonons are intrinsically anharmonic. Nevertheless, the anharmonicity can be treated as renormalizing the frequencies associated with a set of harmonic normal modes. Following the simplest

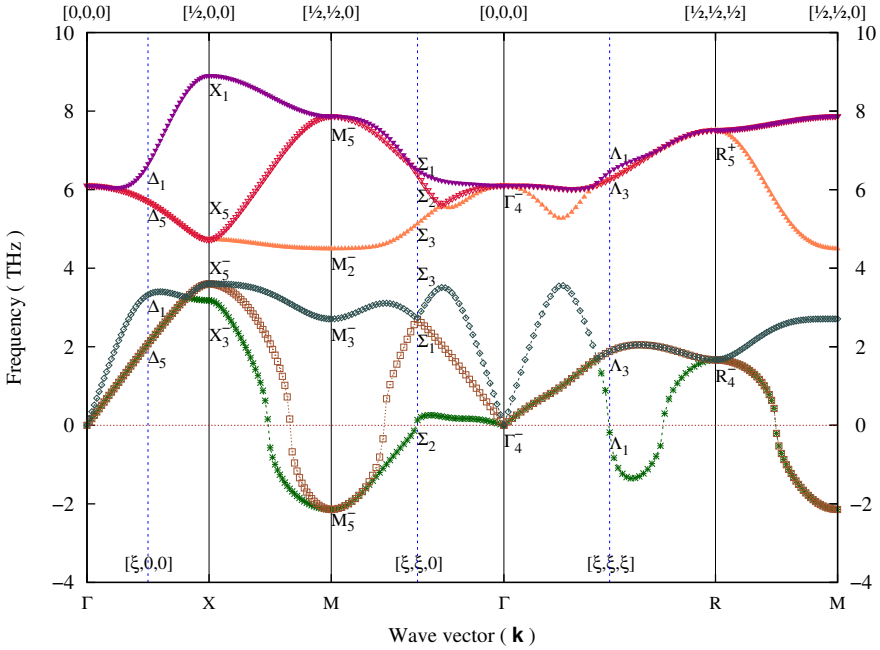


Figure 4.12: Phonon dispersion relations in a B2 obtained from 4×4×4 supercell calculations.

Table 4.13: Elastic constants of a B2 calculated from the slopes of the dispersion relations.

Elastic constant (GPa) ↓	2×2×2	3×3×3	4×4×4	Homogeneous Deformation
C_{11}	184.9	263.3	174.7	190.94
C_{12}	65.5	149.5	170.7	142.32
C_{44}	46.9	42.6	42.2	51.20

of all models, the quasi-harmonic approximation, the effect of thermal expanson on the harmonic phonons in B2 was calculated at different volumes. Uchil et al. measured the linear thermal expansion coefficient of B2 as $11 \times 10^{-6}/\,\mathrm{K}$ using a thermomechanical analyser [169]. Based on this value of the expansion co-efficient, the unit cell volume was calculated at eleven volumes between 0 K and 1000 K. For each volume the dispersion relations were calculated using a 2×2×2 supercell.

All the calculated dispersion curves exhibit the doubly degenerate imaginary mode at M. Calculated imaginary frequencies of soft modes do not change appreciably with volume. Squared frequency values at the exact points are plotted in Fig.(4.13). As can be seen from this figure, the frequencies of optic modes soften with thermal expansion while the soft mode frequencies are little affected by the volume change.

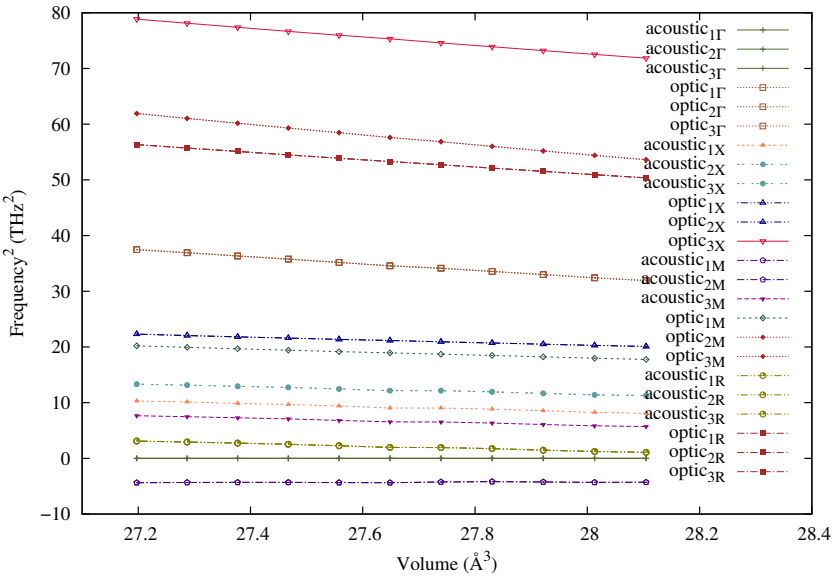


Figure 4.13: Squared frequencies of vibrational modes in B2 at exact wave vectors as a function of volume.

4.4.2 B19

Phonon dispersion relations in a B19 were calculated using a 2×2×2 supercell. Calculated dispersion relations are exact at Γ, X, Y, Z, S, T, U, and R wave vectors in the BZ. Locations of these k-points in the FBZ are shown in Fig.(4.14). A 6×4×5 **k**-point mesh was used for BZ integration in the force calculations. Results are plotted in Figs. (4.15) and (4.16). Since there are four atoms in the

unit cell, there are twelve branches in the dispersion relations.

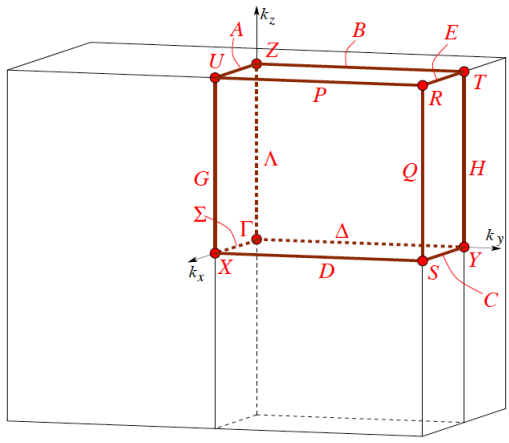


Figure 4.14: First Brillouin zone of a B19 ($Pmcm$) and labels of high symmetry points in it (generated on a crystallographic server [157]).

There is an unstable acoustic transverse mode at Y. All other mode frequencies at Y and all mode frequencies at other exact wave vectors are positive. The entire acoustic branch has imaginary frequencies along Γ to Y. Huang et al. [34] reported similar behaviour of one acoustic branch along Γ to $\frac{2\pi}{a}[010]$ in the dispersion relations of B19 with a $Pmcm$ symmetry. There are eight irreps associated with Y: Y_1^+, Y_2^+, Y_3^+, Y_4^+, Y_1^-, Y_2^-, Y_3^-, and Y_4^-. There is only one isotropic subgroup for each irrep. All the eight subgroups have an orthorhombic symmetry. Unit cells of all eight product phases have twice the volume of a B19 unit cell. Therefore, the soft mode at Y drives the transition from a B19 to an orthorhombic phase. And the unit cell of the product phase occupies two volumes of the B19 unit cell. Hence the product phase is not related to the experimentally observed B19 or B19′.

Parlinski et al. [51] calculated dispersion relations in a B19 ($Pmcm$ symmetry) using a $2 \times \sqrt{2} \times \sqrt{2}$ supercell. They reported a transverse acoustic branch having low but positive or zero frequencies along the Γ to $\frac{2\pi}{a}[0\frac{1}{2}0]$ direction. They suggested a transition from B19 to B19′ due to a low frequency acoustic branch near Γ; $Pmcm(z=2) \xrightarrow{\Gamma_3^+} P2_1/m(z=2)$. This transition is equivalent to a ferroelastic transition from a B19 to a B19′ due to a homogeneous shear suggested by Barsh et al. [48].

Γ and $\frac{2\pi}{a}[\frac{1}{2},0,0]$ are exact wave vectors in the B19 dispersion relations reported by Parlinski et al. [51]. Dispersion relations along a path from Γ to $\frac{2\pi}{a}[\frac{1}{2}$,0,0] in Fig.(4.15) are in qualitative agreement with the calculated dispersion relations by Parlinski et al. [51] along the same path.

The strain components reduce to six one dimensional representations under orthorhombic space group operations. The strain coordinates $\{\epsilon_{11}\}$, $\{\epsilon_{22}\}$, and $\{\epsilon_{33}\}$ are basis functions of three one dimensional irreps Γ_1^+. $\{\epsilon_{12}\}$, $\{\epsilon_{13}\}$, and $\{\epsilon_{23}\}$ are basis functions of irreps Γ_3^+, Γ_2^+, and Γ_4^+ respectively. As suggested by Barsch [48], a shear strain changes the symmetry of a B19 to the symmetry of a B19′. The Γ_3^+ label of the MT path $Pmcm(z=2) \xrightarrow{\Gamma_3^+} P2_1/m(z=2)$ can be considered to represent the transformation shear ϵ_{12}. This shearing does not change the volume of the unit cell appreciably. Hence the B19 and the B19′ involved in this process have approximately the same volume as required. Combining the ϵ_{12} shear and volume changing strains $\{\epsilon_{11}\}$, $\{\epsilon_{22}\}$, and $\{\epsilon_{33}\}$ does not change the symmetry of the product phase. Hence the strains which describe the volume change can be described as the secondary order parameters for a $Pmcm$(B19) $\longrightarrow$ $P2_1/m$(B19′) transition. The primary and secondary order parameters for this transition are listed in Table(4.14). The MT from a B19 to a B19′ phase in Cu-Ti-Ni based SMAs can be described in terms of these order parameters.

Table 4.14: Order parameters for a $Pmcm$(B19) $\xrightarrow[3\Gamma_1^+]{\Gamma_3^+}$ $P2_1/m$(B19′) transition

Primary order parameter	Direction vector
$\Gamma_3^+(\epsilon_{12})$	$\{a\}$
Secondary order parameters	Direction vector
$\Gamma_1^+(\epsilon_{11})$	$\{b\}$
$\Gamma_1^+(\epsilon_{22})$	$\{c\}$
$\Gamma_1^+(\epsilon_{33})$	$\{d\}$

4.4.3 B19′

Harmonic phonon dispersion relations were calculated in the B19′ structure using a 2×2×2 supercell. Calculated dispersion relations are exact at Γ, Y, Z, B, A, C, D, and E wave vectors in the BZ. High symmetry points in the FBZ are located and labelled for a B19′ crystal in Fig.(4.17). A 6×5×4 **k**-point mesh was used for BZ integration in the force calculations. Results are plotted in Figs. (4.18) and (4.19). Since there are four atoms in the unit cell, there are twelve branches in the dispersion relations.

All mode frequencies are positive at all the exact wave vectors. This result is

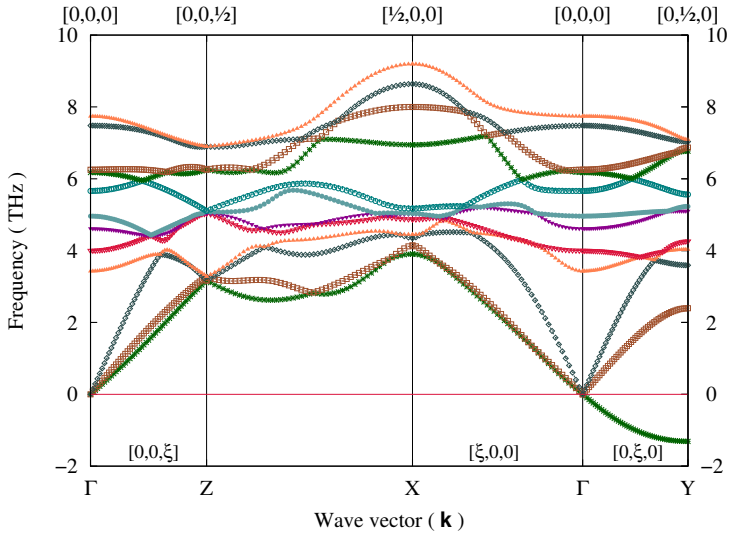


Figure 4.15: Phonon dispersion relations in B19 along $[\xi, 0, 0]$, $[0, \xi, 0]$, and $[0, 0, \xi]$ directions.

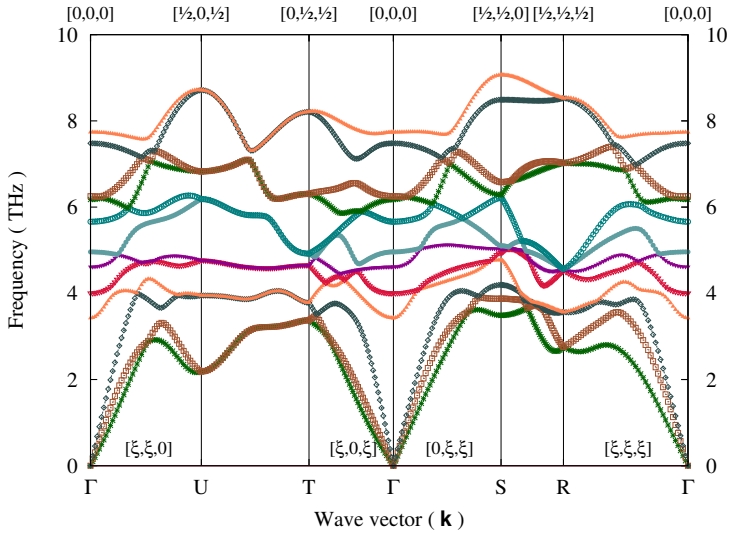


Figure 4.16: Phonon dispersion relations in B19 along $[\xi, \xi, 0]$, $[\xi, 0, \xi]$, $[0, \xi, \xi]$, and $[\xi, \xi, \xi]$ directions.

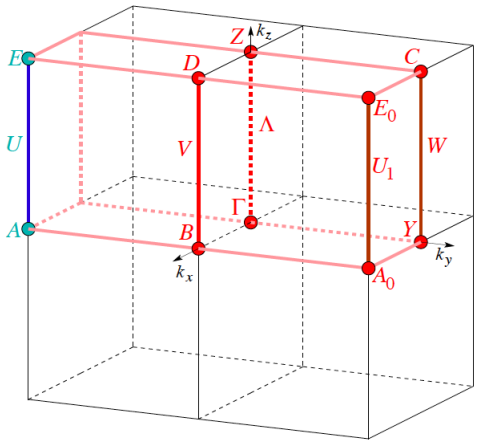


Figure 4.17: First Brillouin zone of a B19′ and labels of high symmetry points in it (generated on a crystallographic server [157]).

in consistent with the fact that B19′ is the ground state structure in TiNi-based SMAs. Parlinski et al. [51] calculated phonon dispersion in a B19′ phase using a $2 \times \sqrt{2} \times \sqrt{2}$ supercell. All mode frequencies are positive in their results as well.

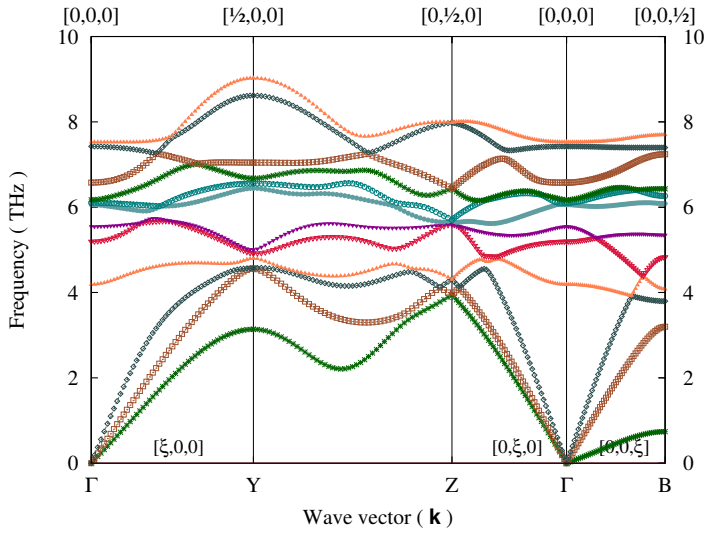


Figure 4.18: Phonon dispersion relations in B19′ along $[\xi, 0, 0]$, $[0, \xi, 0]$, and $[0, 0, \xi]$ directions.

The order parameters of various MT paths observed in TiNi-based SMAs are summarised in Fig.(4.20) which I have adapted from Fig.(4) in [48]. Order parameters describing the phonon amplitudes are shown with their irreps. The order parameters that determine the symmetry of the product phase are shown in a square (□) for each path. The strain components listed in a hexagon (⬡) do not change the symmetry of the product phase. But they are required to accurately

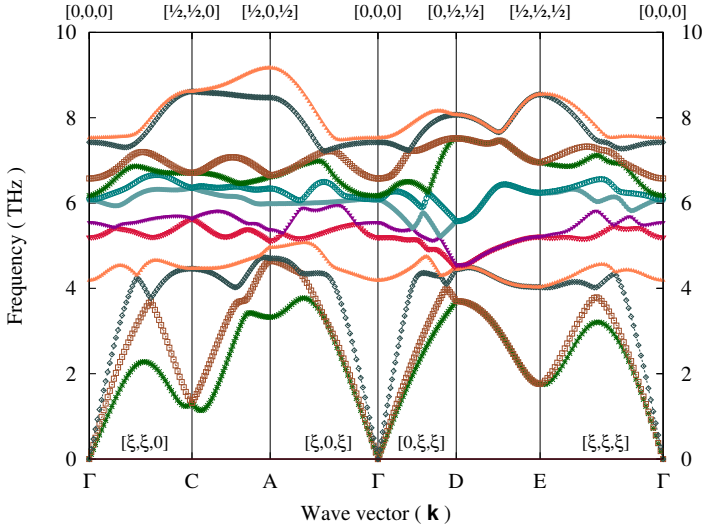


Figure 4.19: Phonon dispersion relations in a B19′ along $[\xi, \xi, 0]$, $[\xi, 0, \xi]$, $[0, \xi, \xi]$, and $[\xi, \xi, \xi]$ directions.

describe the atomic positions in the product phase.

4.5 SCAILD method implementation

As described in Section(3.3), the anharmonic effects at high temperatures can be incorporated into lattice dynamics in an approximately self-consistent way. I used a code developed by Souvatzis [170] for implementing the SCAILD method. I tried to calculate the phonon dispersion at high temperatures using a 2×2×2 supercell and a 3×3×3 supercell in a B2 phase. The SCAILD method is a computationally expensive method and I could not obtain a converged dispersion relation. I will describe the practical issues that occur while implementing the SCAILD method in this section. Each paragraph discusses one of the issues related to each step in the iterative procedure of the SCAILD method.

The harmonic frequencies were used for initiating the SCAILD method. The soft mode frequencies are imaginary frequencies in the HA. Absolute values of the imaginary mode frequencies were used for calculating the normal mode amplitudes. The provided code (version 4) was written in such way that a few normal modes would be excited in each iteration. By excited I mean only a few normal mode amplitudes are considered in the summation while determining the atomic displacements of atoms in the supercell in Eq.(3.110) described in the Section(3.3). For other normal modes, the mode amplitudes are assumed to

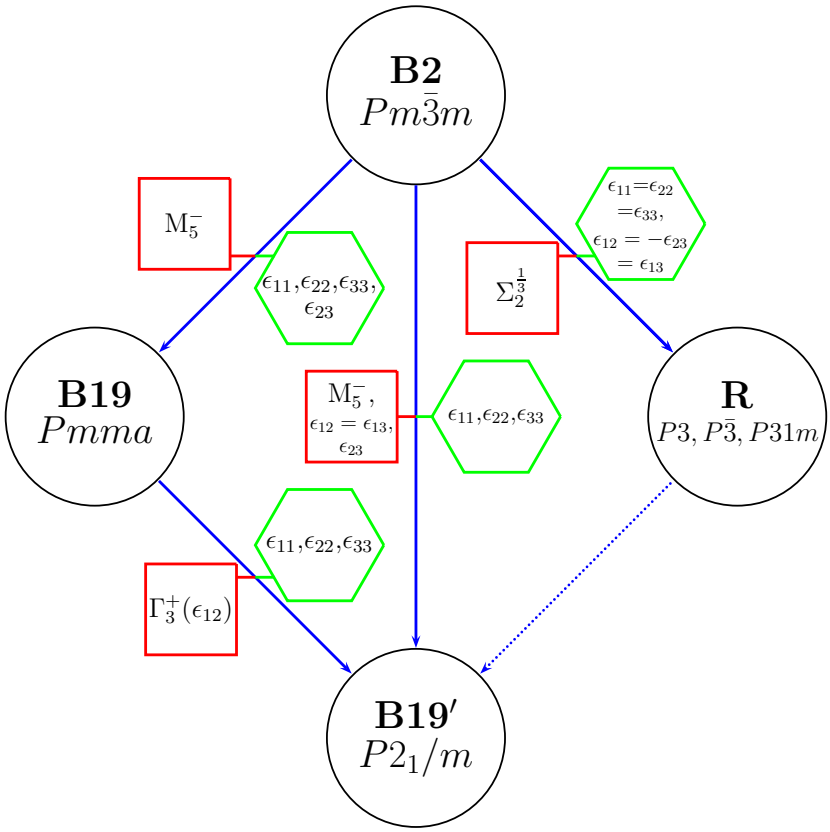


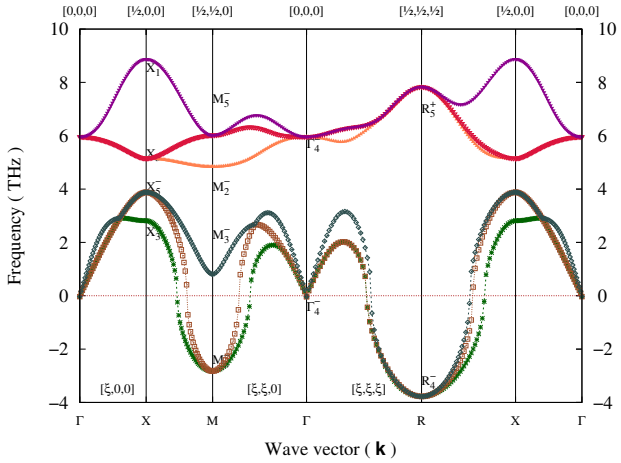
Figure 4.20: Order parameters of various martensitic transformation paths in TiNi-based shape memory alloys.

be zero and the frequencies in a given iteration are assumed to be equal to the corresponding average mode frequencies from previous iterations. But assuming excitation of only a few normal modes does not correctly simulate the atomic vibrations at a given temperature. Therefore, I modified this part of the code in such a way that all the normal modes at the exact wave vectors would be excited. As can be seen from Eq.(3.111), the mode amplitudes are larger when the mode frequency is close to zero frequency. It leads to instability and a phase transition while cooling the alloy. But I am trying to calculate the phonon dispersion of a B2 at high temperature. So as to avoid the unphysically large mode amplitudes, a logarithmic mean frequency was used for the mode frequency if it is close to zero. The logarithmic mode frequency was calculated from all the exact frequencies averaged up to a given iteration.

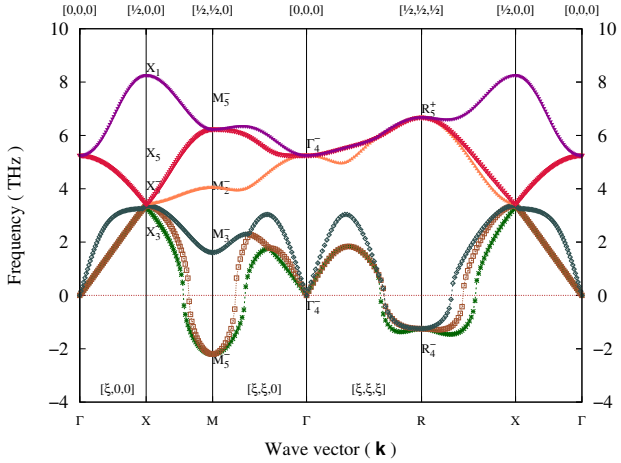
Since all the atoms are simultaneously displaced from their mean positions, the calculated Hellmann-Feynman force on an atom in the supercell is due to all these displacements. Accuracy of the calculated frequencies depends on the accuracy of the calculated forces. In a small displacement method, the amplitude of atomic displacements are kept small so that the HA is valid. At the same time the atomic displacements are chosen to be large enough so that the calculated forces are accurate. In the SCAILD method atomic displacements are determined independently and at random. Some atoms in the supercell are displaced less and others more. Accuracy of the calculated forces due to the difference in the displacements is not discussed in the literature. It is assumed that the calculated force on an atom due to all these displacements is accurate.

Renormalised frequencies are calculated from the Fourier components of forces using the Eq.(3.114). Some of the calculated renormalised square frequencies have imaginary components. However for every $\mathbf{k}$ there is a $-\mathbf{k}$ in the exact wave vectors and the square of mode frequencies at these two wave vectors are complex conjugates of each other: $\omega^2(^{-\mathbf{k}}_{j}) = \omega^{2*}(^{\mathbf{k}}_{j})$. On averaging the imaginary component disappears. And the average value is therefore taken as the estimate of the squared frequency. The calculated frequency of a mode in a given iteration is not expected to be equal to the average frequency of the same mode from previous iterations in the SCAILD method. However real, positive values are expected for all normal mode frequencies at each iteration for a stable crystal if the temperature is high enough. But some of the calculated square frequencies are negative in some iterations even at 350 K in the calculations done using a 2×2×2 supercell. Because of this reason, the averaged frequencies are imaginary even after 60 iterations as shown in Fig.(4.21(b)). Calculated vibrational free

energy from the average phonon dispersion is shown as a function of iteration number in Fig.(4.22)(see Section 3.2.1.3 in Chapter 3). Only real frequencies are considered while calculating the vibrational free energy. As can be seen from the Figs. (4.21) and (4.22), the average dispersion relation is very slowly converging at 350 K towards a stable phonon dispersion relation. However, as described before a few calculated mode frequencies are imaginary in some iterations. For a given mode, appearance of slow convergence is due to the fact that the number of times the calculated frequency is imaginary is less than the number of times the calculated frequency is real after certain number of iterations.



(a)



(b)

Figure 4.21: Phonon dispersion in B2 at 350 K from calculations done using a 2×2×2 supercell after (a) 30 iterations and (b) 60 iterations.

In some iterations the calculated mode frequencies are larger than normal. One such example is a calculated mode frequency equal to 27 THz. On averaging

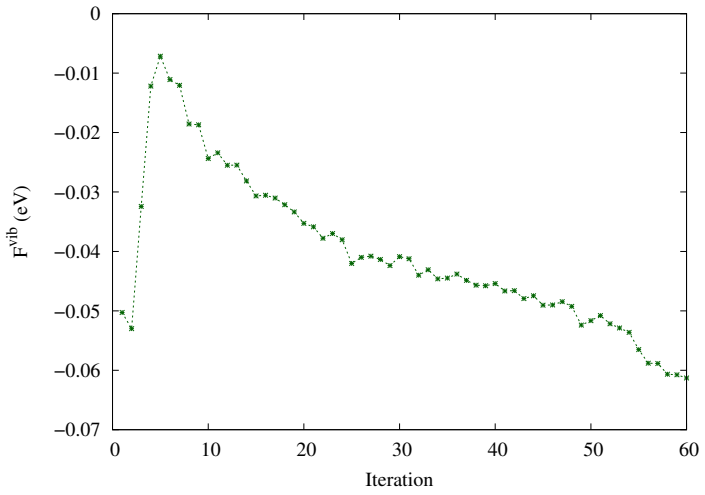


Figure 4.22: Vibrational free energy as a function of iteration number.

over a large number of iterations the set of exact frequencies appears to converge to a fixed set of values. But in order to achieve this precautions must be taken to avoid obtaining abnormal frequencies of this type at any iteration. Souvatzis et al. [60] estimated the transition temperature of B2 to be 227 K from the average dispersion relations calculated at different temperatures using the SCAILD method after 150 iterations. They had used a 3×3×3 supercell. I calculated the mode frequencies at 350 K over 60 iterations using a 2×2×2 supercell. But, I observed the above discussed abnormalities in the mode frequencies.

While practically implementing the SCAILD method a small set of k-points is used. The k-point sampling also affects the results. So as to study this effect a larger supercell needs to be used. Use of a large supercell increase the number of exact wave vectors. One needs to study the behaviour of calculated frequencies at each iteration in the calculations done with a large supercell. If satisfactory results are obtained, the SCAILD method can be used for studying the materials with the same or a larger supercell. For all these studies more computational resources are required. I used a 3×3×3 supercell for calculating the frequencies in ten iterations at 400 K. The above discussed abnormalities were also observed in the some of the mode frequencies calculated in these iterations. The SCAILD method does not converge for the size of supercell and the number of iterations that I could use within the scope of the computational resources available.

Chapter 5

Results: ternary alloys

I have studied the effect of ternary additions (Hf or Zr) on the elastic constants of β' and β_1 with the homogeneous deformation method, in a similar way to the binary alloys. Changes in the C′ and the C_{44} due to alloying affect the resistance to shear, which is believed to be an important contribution to $\triangle$T. Since the calculated elastic constants are valid only at 0 K, we are looking only for a correlation between the calculated values and the high temperature elastic constants of the transforming phases β' and β_1. The changes in elastic constants aid or suppress the shear that occurs during the MT and thereby affect the undercooling $\triangle$T. In particular the softening/stiffening of elastic constants due to alloying decreases/increases the strain energy associated with the accommodation of the martensite phase by the surrounding matrix. By this mechanism, the stiffening due to alloying would mainly act to slow the growth of martensite, and would not affect the initiation of the MT. The MT itself is thought to be due to a soft mode instability. The soft mode frequency depends on the composition and hence the soft mode frequency determines the M_s through its effect on the T_0.

Experimental phonon dispersion relations in Ti-Ni-Hf and Ti-Ni-Zr alloys are not reported so far. From the structures of martensites (R [76], B19′ [78, 85]) it appears that the soft mode wave vector is either $\frac{2\pi}{a}[\frac{1}{3}, \frac{1}{3}, 0]$ or M in Ti-Ni-Hf and Ti-Ni-Zr alloys. I tried to get some insight into the effect of alloying on the equilibrium temperature T_0 by calculating the soft mode frequency at M within the harmonic approximation. Calculated phonon dispersion relations and elastic constants of austenite as a function of ternary addition in $Ti_{50-x}Ni_{50}Hf_x$ and $Ti_{50-x}Ni_{50}Zr_x$ alloys are presented and analysed in this chapter. Trends in the results are qualitatively similar in $Ti_{50-x}Ni_{50}Zr_x$ and $Ti_{50-x}Ni_{50}Hf_x$ alloys. This is in agreement with the fact that addition of both Hf and Zr almost linearly increases

the M_s when added in amounts greater than 7.5 at.%. Hence, I will present and discuss the results together.

5.1 Simulation details and lattice parameters

A 2×2×2 supercell was created from the B2 unit cell. It contains sixteen atoms: 8 Ni and 8 Ti atoms. Simulation supercells of austenite in ternary alloys of 6.25, 12.5, 18.75, and 25 at.% ternary element (Hf or Zr) were generated by replacing 1, 2, 3, and 4 Ti atoms with the ternary alloying elements respectively. For a given alloy composition, there are a few possibilities for replacing the atoms in the Ti sub-lattice with ternary elements. These possibilities are shown in Fig.(5.1) as a function of alloying content. The 1a, 2b, 3c, 4f configurations in the Fig.(5.1) were chosen to represent the Ti sub-lattices of corresponding alloys. The new unit cells of 6.25, 12.5, 18.75, and 25 at.% ternary alloys have $Pm\bar{3}m$, $Imma$, $Pm\bar{3}m$, and $Fm\bar{3}m$ symmetry respectively. I will refer to these 16 atom unit cells as 'ternary supercells'. The three lengths of the sides of the supercell were varied, constraining the 90 ° angles and allowing the positions of all the atoms within the ternary supercell to relax. BZ integration was done using a 16×16×16 **k**-point mesh in the total energy calculations. $3p$, $3d$, and $4s$ electrons of Ni, $3s$, $3p$, $3d$, and $4s$ electrons of Ti, $5p$, $5d$, and $6s$ electrons of Hf, $4s$, $4p$, $4d$, and $5s$ electrons of Zr were considered as the valence electrons in these calculations.

Equilibrium lattice parameters of the ternary supercells of $Ti_{50-x}Ni_{50}Hf_x$ and $Ti_{50-x}Ni_{50}Zr_x$ alloys are listed in Tables (5.1) and (5.2) respectively. As can be seen from this tables, Hf or Zr addition increases the lattice parameters. Both Hf and Zr atoms are larger than a Ti atom [171]. When Ti atoms are replaced with either of these two atoms in ternary alloys, the unit cell volume increases [77, 78, 85, 70]. Therefore, the increasing trend of lattice parameters with ternary addition (Hf or Zr) is in agreement with the experimental observations, also shown in Tables (5.1) and (5.2). The lattice parameters of β' and β_1 phases are determined experimentally in a B2 structure. These values are doubled for the comparison purpose and shown in the tables. Lattice parameters at the compositions considered in the present study were not available experimentally in some cases. The lattice parameters for these compositions were obtained by interpolation and extrapolation, whichever is applicable, from the available experimental data.

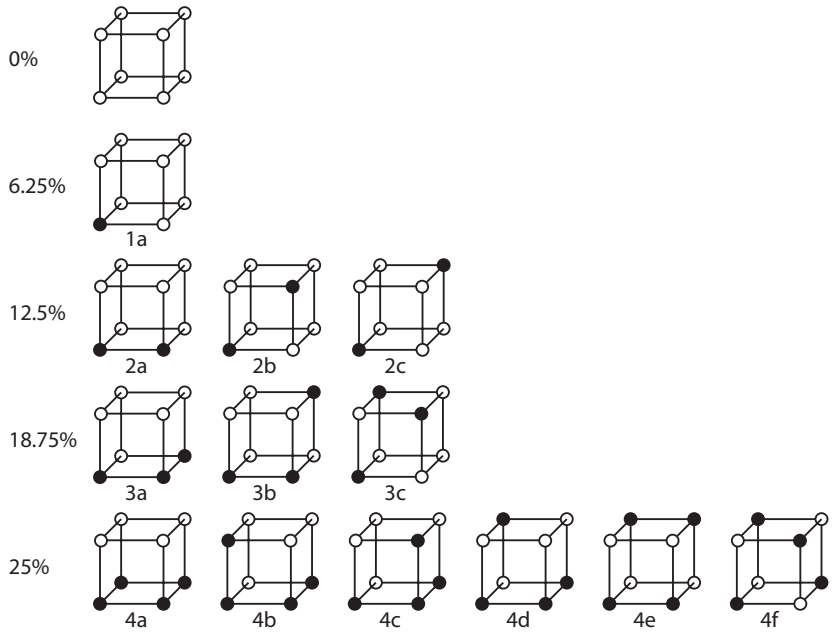
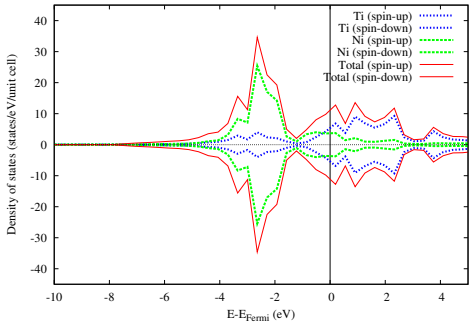


Figure 5.1: Possible configurations in the Ti sub-lattices of a β' or a β_1 supercell as a function of alloying. The open and closed circles represent Ti atoms and ternary alloying elements respectively.

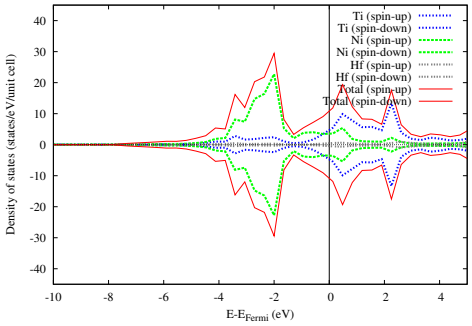
5.2 Electronic properties

Density of states in β_1 phase of the five alloys ($Ti_{50-x}Hf_xNi_{50}$ alloys) under study are plotted in Fig.(5.2). Major contribution to the states below the E_F (Fermi level) is from Ni atoms. Ti and Hf atoms contribute largely to the states above the E_F. Two alloys with Hf content 6.25 and 12.5 at.% have a broad major peak below the E_F. The same peak is narrow in alloys with 18.75 and 25 at.% Hf. There is a small peak near the E_F in all five compositions. The DOS at the Fermi level, DOS(E_F), in β_1 phase as a function of Hf content is depicted in Fig.(5.3). Alloys with 0 at.%, 12.5 at.% Hf have almost similar DOS(E_F) values. Other alloys have low DOS(E_F) values. But the variation of DOS(E_F) with Hf content is neither a consistent increase nor a consistent decrease.

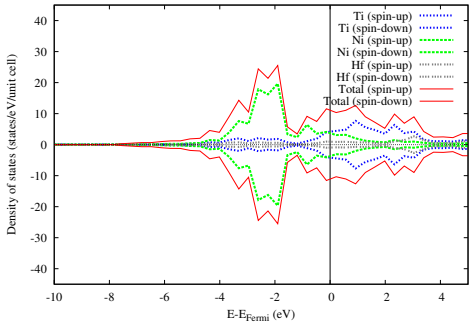
Density of states in β' phase of the five alloys ($Ti_{50-x}Zr_xNi_{50}$ alloys) under study are plotted in Fig.(5.4). Major contribution to the states below the E_F is from Ni atoms. Ti and Zr atoms contribute dominantly to the states above the E_F. There is a broad major peak below the E_F in two alloys with 6.25 at.% and 12.5 at.% Zr. The same major peak is narrow in the $Ti_{25}Zr_{25}Ni_{50}$ alloy. A small peak is present near the E_F in all five compositions. The DOS(E_F) in β' phase as a function of Zr content is shown in Fig.(5.3). Alloys with 0 at.%, 12.5 at.% Zr have almost similar DOS(E_F) values. Alloys with 6.25 at.%, 18.75 at.% have



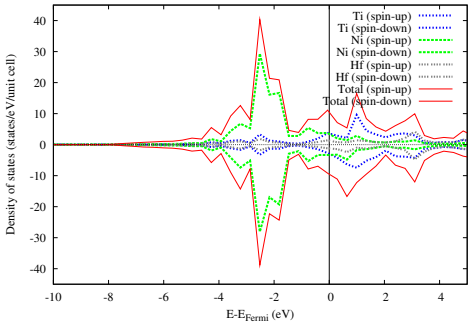
(a) 0 at.%



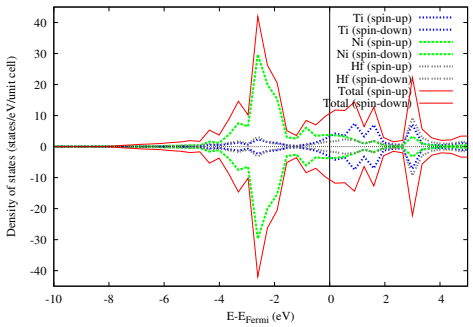
(b) 6.25 at.%



(c) 12.5 at.%



(d) 18.75 at.%



(e) 25 at.%

Figure 5.2: Density of states in the β_1 as a function of Hf content.

Table 5.1: Lattice parameters of ternary supercells as a function Hf content in $Ti_{50-x}Hf_xNi_{50}$ alloys

at.%Hf	Lattice parameter (Å)	
	Calc. value	Exp. value [77]
0.00	6.027	5.967
6.25	6.0720	6.054
12.50	6.117	6.125
18.75	6.161	6.179
25.00	6.205	6.234

Table 5.2: Lattice parameters of ternary supercells as a function Zr content in $Ti_{50-x}Zr_xNi_{50}$ alloys

at.%Zr	Lattice parameter (Å)	
	Calc. value	Exp. value [70]
0.00	6.027	5.967
6.25	6.083	6.016
12.50	6.138	6.075
18.75	6.194	6.133
25.00	6.246	6.20

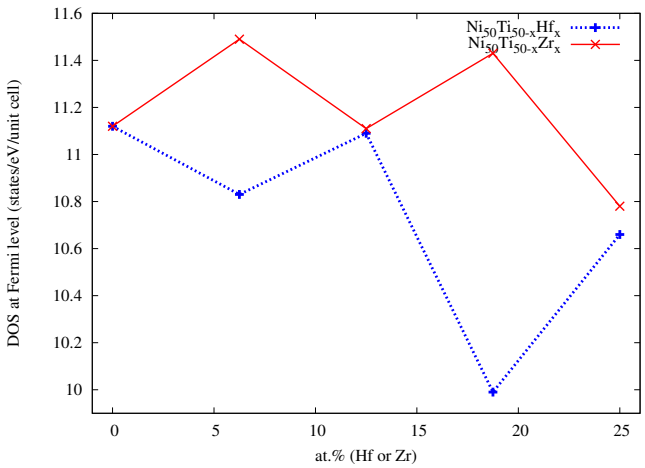
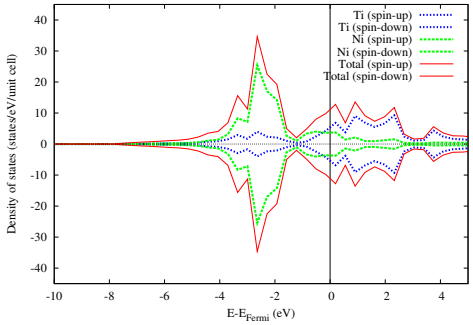
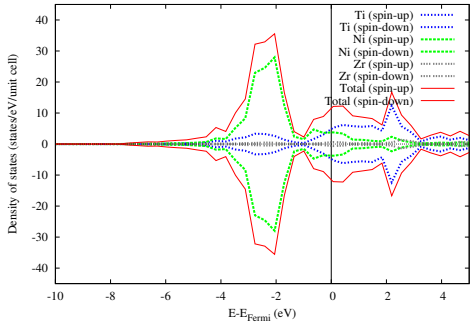


Figure 5.3: Spin-up density of states at the Fermi level in a β_1 or a β'phase as a function of ternary alloying.

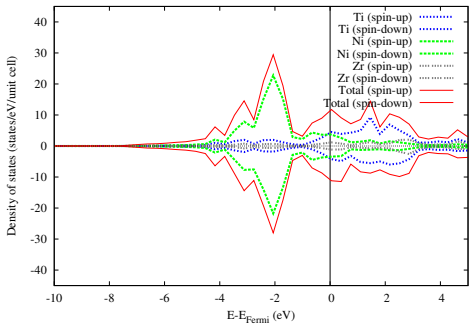
high density of states compared to a binary alloy. Low DOS(E_F) is observed in $Ti_{25}Zr_{25}Ni_{50}$ when compared to a binary alloy. Variation of the DOS(E_F) values with Zr content is neither a consistent increase nor a consistent decrease.



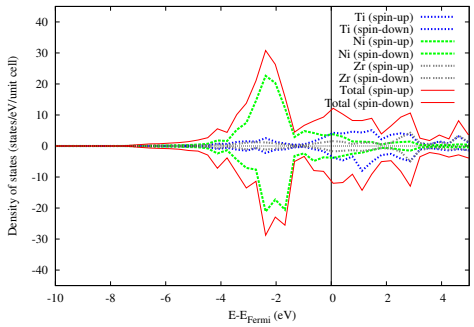
(a) 0 at.%



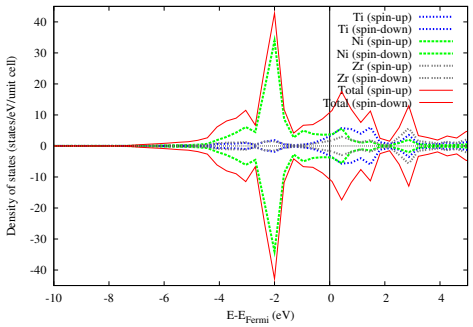
(b) 6.25 at.%



(c) 12.5 at.%



(d) 18.75 at.%



(e) 25 at.%

Figure 5.4: Density of states in the β' as a function of Zr content.

5.3 Elastic constants

I calculated the elastic constants of austenite represented by the five ternary supercells described above as a function of Hf and Zr content. Strain tensors, described in Appendix B, for calculating the elastic constants of a cubic crystal are used in these calculations. However some of the configurations have a non-cubic symmetry. In these configurations, applying a strain along x direction may not be symmetrically equivalent to applying a strain along y or z direction. The strain tensor chosen for C′ calculation has elements such that the strain energy for a given magnitude of strain might be different if the diagonal elements are interchanged in case of non-cubic crystals. In such cases three independent strain tensors (which are equivalent by symmetry in cubic crystals) are used. The strained energy of the crystal is obtained by averaging over the three independent strain states. Energy versus strain profiles from these calculations are plotted in Figs. (5.5) and (5.6). Elastic constants were calculated from the curvatures of the energy versus strain profiles determined at the equilibrium volumes.

Calculated bulk moduli as a function of alloying addition are plotted in Fig.(5.7). As can be seen from this plot, ternary alloying addition decreases the bulk modulus in $Ti_{50-x}Ni_{50}Hf_x$ and $Ti_{50-x}Ni_{50}Zr_x$ alloys.

C′ and C_{44} determine the resistance to shear in cubic crystals. Since the MT is a shear based transformation, these two elastic constants influence the degree of undercooling required before the MT. C′ values as a function of ternary alloying content are plotted in Fig.(5.8). Addition of 6.25 at.% Hf or Zr decreases the C′. When added in excess of 6.25 at.% the ternary Hf or Zr addition increases the C′. The predicted effect of this behaviour would be a decrease in the required undercooling with the initial ternary addition (x) of 6.25 at.% in $Ti_{50-x}Ni_{50}Hf_x$ and $Ti_{50-x}Ni_{50}Zr_x$ alloys, and an increase in the required undercooling when x is more than 12.5 at.%.

Although the highly ordered structures of our theoretical samples may not be representative of the real alloys, this result is at least consistent with the increase in the observed hardness of the $Ti_{50.5-x}Ni_{49.5}Zr_x$ and $Ti_{50.5-x}Ni_{49.5}Zr_{x/2}Hf_{x/2}$ alloys when the x value is greater than 10 at.% [86]. This strengthening enhances the bonding and stabilises the high temperature B2 structure, thereby lowering the M_s from the 'equilibrium' temperature T_0 [91]. However, as described in the Section(2.5) in Chapter 2, Hf or Zr addition in excess of 7.5 at.% increases the M_s. It means other factors such as, for example, changes in C_{44} or changes in the soft mode frequencies due to alloying might be acting effectively against the

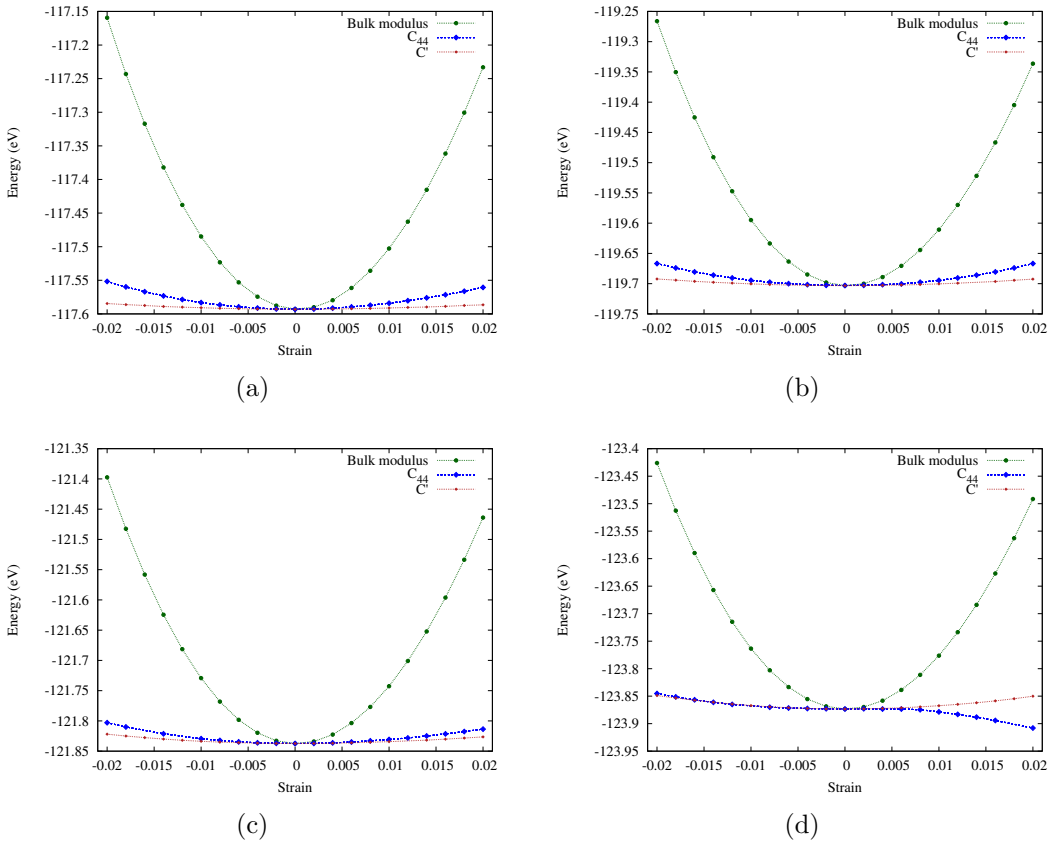


Figure 5.5: Total energy versus strain profiles in different elastic constants calculations in austenite of $Ti_{50-x}Ni_{50}Hf_x$ alloys as a function of Hf content : (a) 6.25 at.%Hf, (b) 12.5 at.%Hf, (c) 18.75 at.%Hf, and (d) 25 at.%Hf.

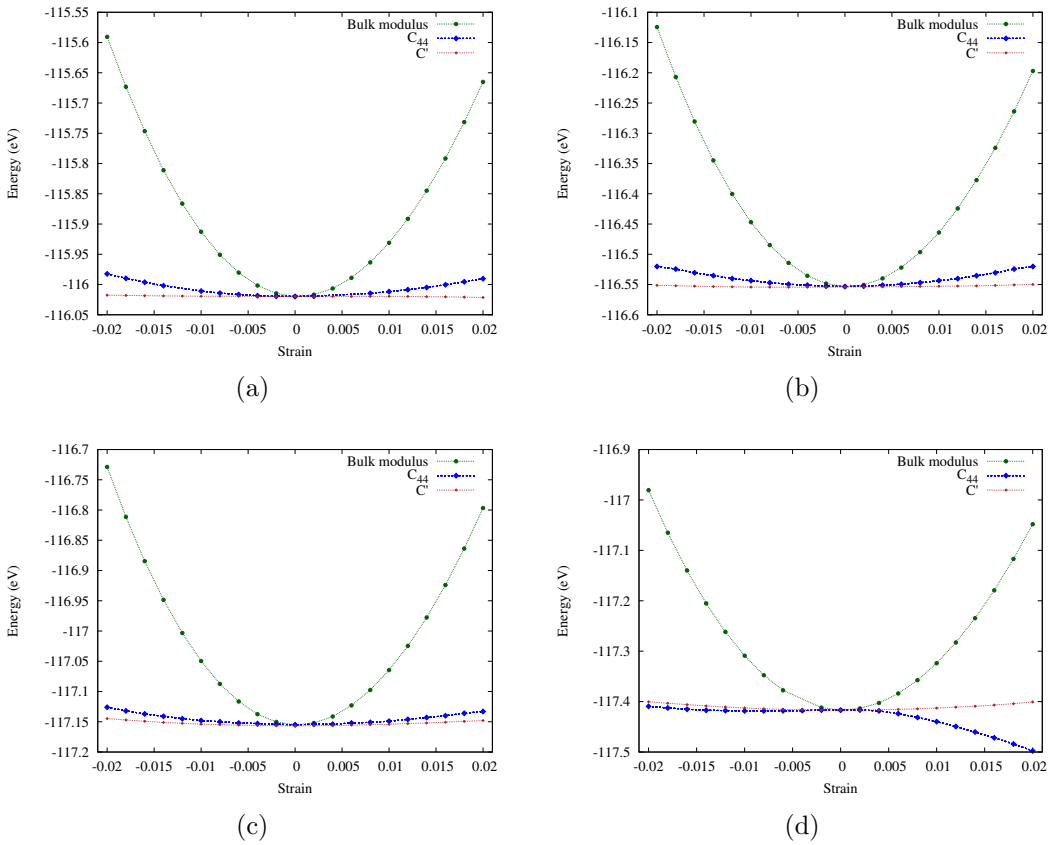


Figure 5.6: Total energy versus strain profiles in different elastic constants calculations in austenite of $Ti_{50-x}Ni_{50}Zr_x$ alloys as a function of Zr content : (a) 6.25 at.%Zr, (b) 12.5 at.%Zr, (c) 18.75 at.%Zr, and (d) 25 at.%Zr.

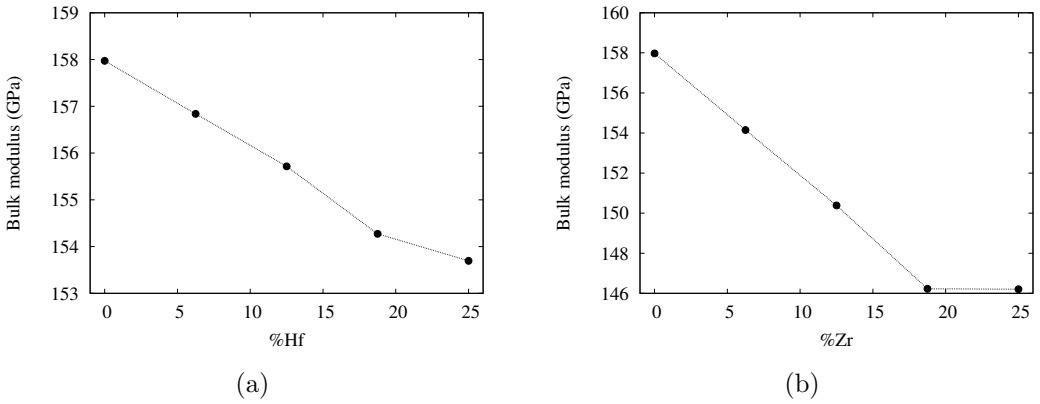
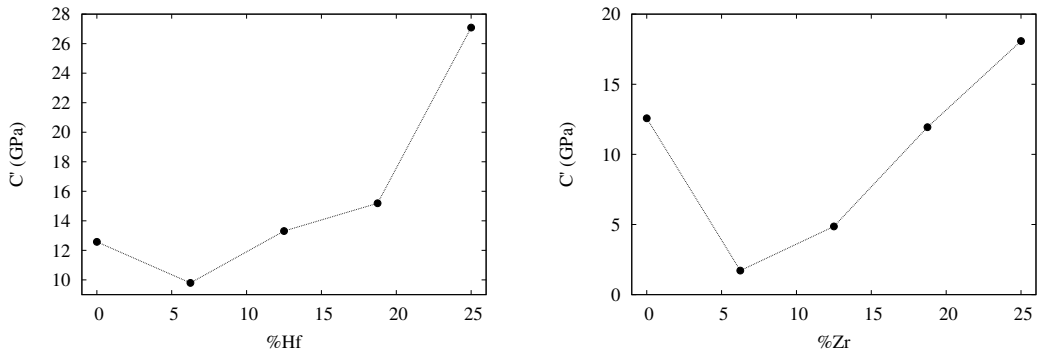


Figure 5.7: Bulk modulus as a function of Hf or Zr content in ternary alloys :(a)$Ti_{50-x}Ni_{50}Hf_x$ alloys (b)$Ti_{50-x}Ni_{50}Zr_x$ alloys.

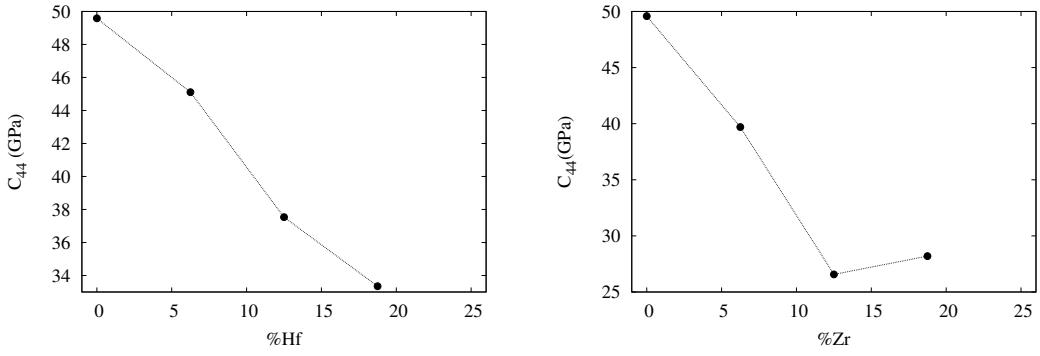


(a) (b)

Figure 5.8: C′ as a function of Hf or Zr content in ternary alloys :(a)$Ti_{50-x}Ni_{50}Hf_x$ alloys (b)$Ti_{50-x}Ni_{50}Zr_x$ alloys.

changes in the C′.

C_{44} values as a function of alloying are plotted in Fig.(5.9). Addition of Hf or Zr decreases the shear resistance C_{44}. If the alloying content is 25 at.%, the austenite is unstable with respect to a positive rhomobohedral shear. Decrease in the total energy of the system when a positive rhombohedral shear is applied to the ternary supercells can be seen from the Figs. 5.6(d) and 5.5(d). Softening of C_{44} decreases the undercooling required before the MT and favours the formation of B19′ (see Section(2.4) in Chapter 2). This might be the reason for the formation of only B19′ martensites in Ti-Ni-Hf [77, 78] and Ti-Ni-Zr [85] based HTSMAs.



(a) (b)

Figure 5.9: C_{44} as a function of Hf or Zr content in ternary alloys :(a)$Ti_{50-x}Ni_{50}Hf_x$ alloys (b)$Ti_{50-x}Ni_{50}Zr_x$ alloys.

The reductions in the C_{44} due to Hf or Zr addition contribute to an increase in the M_s whereas the predicted changes in C′ due to Hf or Zr addition would decrease the M_s. These conclusions must remain tentative, since we have calculated only a single sample at each composition, which may not be representative, nev-

ertheless they point the direction. The direct driving force for the MT however is a soft mode instability. The effect of alloying addition on a soft mode frequency at wave vector M is described in the next section.

5.4 Phonon dispersion

The effect of composition on the soft mode frequency can be studied by determining the phonon dispersion relations as a function of alloy composition. Experimental phonon dispersion relations in Ti-Ni-Hf or Ti-Ni-Zr alloys are not available in the literature. Inelastic neutron scattering experiments still need to be performed on these alloys to identify the soft mode and to study the variation of soft mode frequency as a function of composition. As a preliminary study of the effect of alloying addition on a soft mode frequency at M, I calculated the dispersion relations as a function of Hf and Zr content.

Dispersion relations were calculated by following the small displacement method in the ternary supercells. The volume of the first BZ of these ternary supercells is eight times smaller than that of β' or β_1, due to the doubling of the sides of the ternary supercells compared to the β' or β_1 unit cell. The Γ-point of the first BZ of the ternary supercell is the only exact wave vector in these calculations. In the usual β' or β_1 first BZ, the corresponding exact wave vectors are Γ, X, M, and R. So for comparison of the dispersion relations, the exact wave vectors are folded back to the Γ-point of the small BZ. I will denote the high symmetry points of the β' or β_1 BZ which are to be folded back to Γ in brackets.

A 8×8×8 **k**-point mesh was used for the BZ integration in the force calculations. Calculated dispersion relations in $Ti_{50-x}Ni_{50}Hf_x$ and $Ti_{50-x}Ni_{50}Zr_x$ alloys are plotted in Figs. (5.10) and (5.11) respectively.

The soft mode frequency of the austenite, even if its calculated value is imaginary, is taken to be an indicator for the stability of the actual austenite, in which imaginary frequencies can be renormalized to real, stable values by the high degree of anharmonicity. As usual, it is the negative modulus of the imaginary value which is plotted. Góra et al. [172] suggested that the MT occurs at a higher temperature in a phase with a large imaginary soft mode frequency than a phase with a small imaginary soft mode frequency. The calculated soft mode frequency at Γ as a function of Hf and Zr content is plotted in Fig.(5.12). There is no common trend in the soft mode frequencies as a function of alloying concentration in $Ti_{50-x}Ni_{50}Hf_x$, $Ti_{50-x}Ni_{50}Zr_x$ alloys through the whole range of

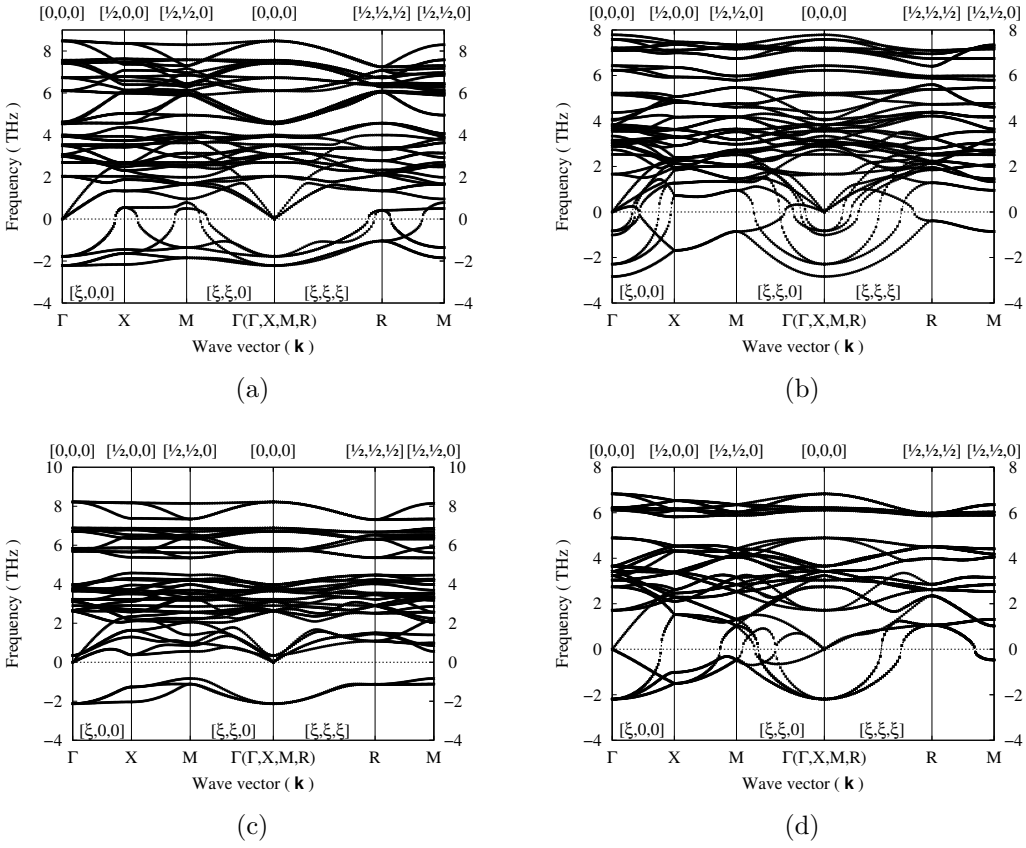


Figure 5.10: Dispersion relations in β_1 as a function of Hf content in $Ti_{50-x}Ni_{50}Hf_x$ alloys: (a) 6.25 at.%Hf, (b) 12.5 at.%Hf, (c) 18.75 at.%Hf, (d) 25 at. %Hf.

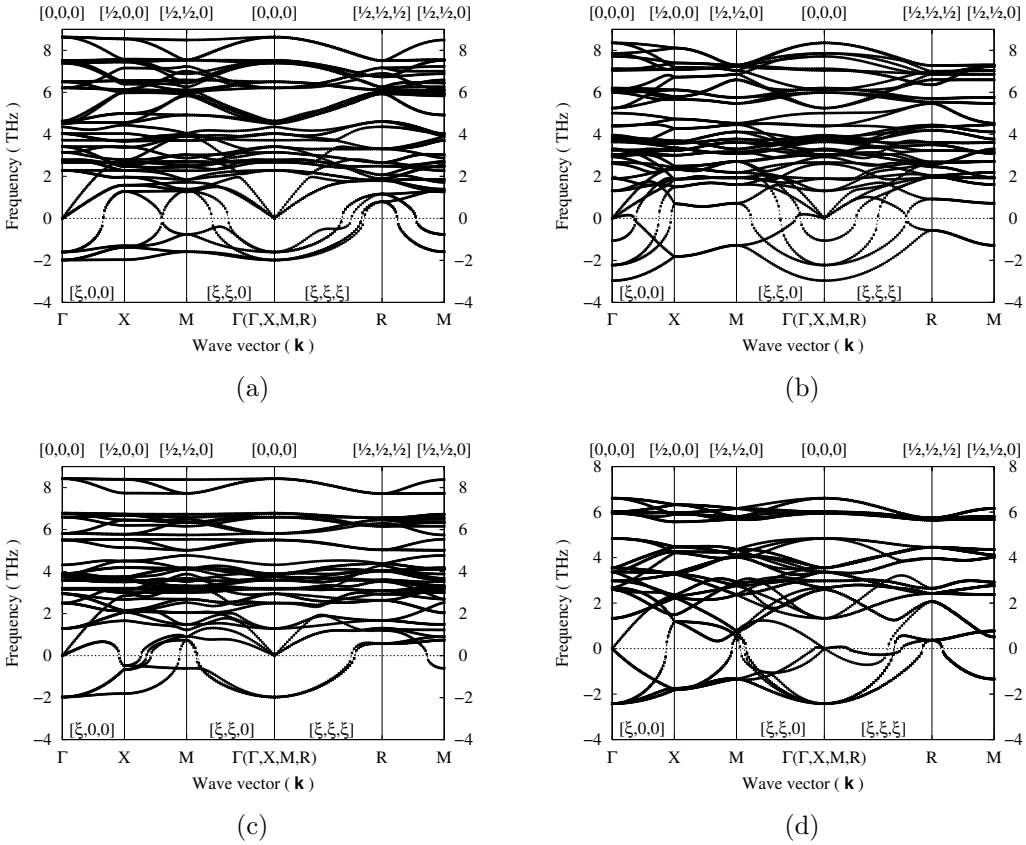
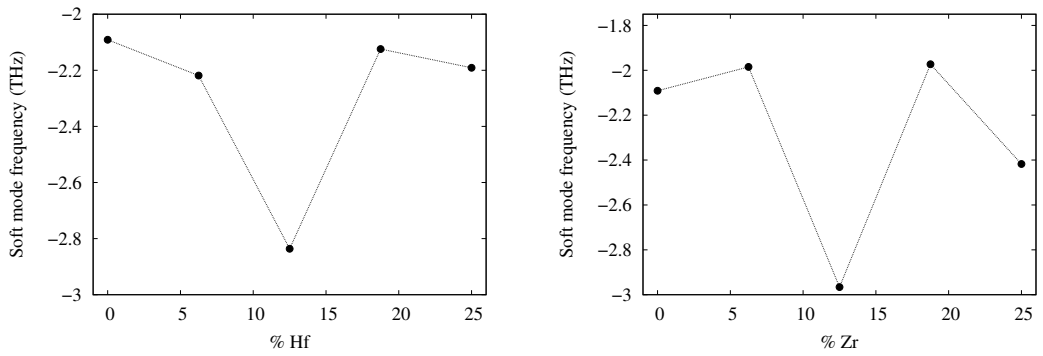


Figure 5.11: Dispersion relations in β' as a function of Zr content in $Ti_{50-x}Ni_{50}Zr_x$ alloys: (a) 6.25 at.%Zr, (b) 12.5 at.%Zr, (c) 18.75 at.%Zr, (d) 25 at. %Zr.

x; at 6.25% it seems that Hf is pulling down more imaginary modes, whereas at higher concentrations Zr is inducing more imaginary modes and with greater magnitude.

Soft mode frequency at M changes from $2.09\imath$ THz to $2.22\imath$ THz in a $Ti_{43.75}Ni_{50}Hf_{6.25}$ alloy when compared to a binary $Ti_{43.75}Ni_{50}$ alloy. The soft mode frequency become more imaginary ($2.84\imath$ THz) in a $Ti_{37.5}Ni_{50}Hf_{12.5}$ alloy. Alloys with 18.75 at.% Hf and 25 at.% Hf have soft mode frequencies $2.12\imath$ THz and $2.19\imath$ THz respectively, which are close to the to the soft mode frequency in binary alloys at M. The M soft mode frequencies in $Ti_{50-x}Ni_{50}Zr_x$ alloys with 6.25, 12.5, 18.75, and 25 at.% Zr are $1.99\imath$, $2.97\imath$, $1.97\imath$, and $2.42\imath$ THz respectively.



(a) (b)

Figure 5.12: Soft mode frequency as a function of Hf or Zr content in ternary alloys : (a) $Ti_{50-x}Ni_{50}Hf_x$ alloys (b)$Ti_{50-x}Ni_{50}Zr_x$ alloys.

The changes in the soft mode frequencies at M of the austenite as a function of Hf and Zr addition are not in agreement with the decrease in the M_s when the ternary alloying content is less than 7.5 at.% and increase in M_s when the alloy content is greater than 7.5 at.% [75, 10, 83]. One possible reason for the disagreement might be the soft mode wave vector is different from M in these alloys. And the agreement is expected only if the soft mode wave vector frequency is the dominating factor in determining the T_0. If the M is not the soft mode wave vector, phonon dispersion relations need to be calculated with a ternary supercells containing 54 atoms so as to study the effect of alloying addition on the soft mode wave vector at $\frac{2\pi}{a}[\frac{1}{3}, \frac{1}{3}, 0]$. The ternary supercells are build by creating a 3×3×3 supercell from a B2 unit cell and replacing some of the Ti atoms with Hf or Zr atoms. Calculations with 54 atoms ternary supercells allow us to vary the composition in steps of 1.85 at.% and hence sample the composition space more finely. However, there is also the problem of sampling configurations, for which an alternative method such as coherent potential approximation may

be the best way forward [173].

From the above discussed changes in the elastic constants and imaginary frequencies only trends can be observed. But, there is no way of quantifying the quantities $\frac{\delta \triangle T}{\delta c}$ and $\frac{\delta T_0}{\delta c}$ from these results. Alloying also effects the response of the alloy to cold working, ageing, and other thermomechanical treatments. Effects of alloying on thermomechanical treatments are not considered in the present study. Even if the effects of thermomechanical treatments are known as a function of ternary alloying addition, there is no way of combining in a quantitative way the effect of alloying on the soft mode frequencies, the elastic constants, and other factors. For this reason it is difficult to compare the changes in various factors due to alloying with the experimentally observed changes in the M_s, because they all act simultaneously and cooperatively. Nevertheless, if correlations between theoretical indicators such as those discussed here and experimental trends in MT temperatures can be discovered, they will be very useful in understanding the data.

Calculations are especially difficult for ternary alloys because of problem of configurational sampling. As shown in Fig.(5.1), there are different configurations of Ti sub-lattices for a given ternary alloy composition. Only one of these configurations is considered in the present study. An accurate representation of a given property can only be obtained by averaging the property over all the configurations, weighted by their probability of occurrence, for which a different technique would have to be employed.

Chapter 6

Conclusions and outlook

6.1 Conclusions

A martensitic transition is responsible for the shape memory effect and superelasticity in TiNi-based shape memory alloys (SMAs). The research described in this thesis was started with the objective of understanding this transition using the available theoretical methods. In particular, this study began with two objectives: to understand the martensitic transformation in TiNi-based binary alloys, and to study the effect of ternary alloying addition to a binary Ti-Ni system. We hoped that results from this study would provide some useful inputs while designing the high temperature shape memory alloys (HTSMAs). While the big scientific challenge of understanding enough to design a useful HTSMA remains, I have made some small steps in advancing the theory, which I can summarise as follows.

It is generally accepted that phonon dispersion and the softening of phonons has a key part to play in the existence and operating temperature of a reversible SMA. Normal mode symmetry is a very important property in the phonon dispersion relations, since it determines how the anharmonicity may couple lattice vibrations to each other and to elastic moduli. Applying density functional theory in the standard code VASP I have calculated the phonon dispersion relations in TiNi with the B2, B19, and B19′ structures within the harmonic approximation. I have labelled normal modes in B2 in the conventional manner according to the symmetry properties of their polarisation vector. Normal modes with imaginary frequencies are identified at the locations of the experimentally observed soft mode wave vectors.

The Landau theory of martensitic transformations is a phenomenological

approach to understanding the symmetry of martensitic phases in relation to that of their austenitic hosts. It requires the identification of order parameters characterised by soft modes that carry the symmetry of the martensitic crystal. I applied group theoretical methods to determine the order parameters for the experimentally observed martensitic transformation paths, making use of the normal mode irreps. Results are in agreement with the order parameters described in the literature, where available. Figures (4.9) and (4.11) show my normal mode labels along high symmetry directions and can be used in future as a reference for normal mode labelling in B2 crystals. In the process of deriving these normal mode symmetries, I corrected the published symmetry label of a transverse acoustic mode with a $\langle 1\bar{1}0\rangle$ polarisation (TA_2) at $\frac{2\pi}{a}[\frac{1}{3}, \frac{1}{3}, 0]$ to Σ_2.

The method I mainly used for calculating phonon frequencies is the widely used 'direct method', based on calculations of force constants using a periodically repeated supercell. Because force constants are thereby truncated in range, the dispersion curves are actually an interpolation between the values of rather few 'exact' **k**-vectors, meaning the **k**-vectors corresponding to an integer number of wavelengths within the supercell. I assessed the accuracy of these interpolated frequencies in B2 within the harmonic approximation by calculating the elastic constants from the slopes of the dispersion relations at the first Brillouin zone centre and by varying the size of the supercells from a single unit cell (2 atoms) up to $4 \times 4 \times 4$ unit cells (128 atoms). There is no systematic variation in the interpolated frequencies with the supercell size and some perhaps surprisingly large finite size errors in some of the frequencies, even for the largest supercells. The calculated elastic constant C' from the slopes of the dispersion relations are up to 145% in error compared to the value from the reliable method of homogeneous deformation.

A softening of elastic constants has been observed experimentally as the martensitic temperature is approached from above. One might therefore expect a higher transition temperature to be associated with softer elastic moduli. I have calculated elastic constants in the quasiharmonic approximation, but did not find any significant change due to the changes in volume that would be associated with the observed temperature range.

Experimentally it is observed that Hf or Zr addition up to 7.5 at.% does not affect the M_s much. When added in excess of 7.5 at.%, these two elements increase the M_s approximately linearly with atomic concentration. From the calculated shear constants of ternary systems I observed the following:

- at 6.25 at.% addition of Zr or Hf both C′ and C_{44} are softened,
- at $>$ 6.25 at.% addition of Hf or Zr C′ increases whereas C_{44} continues to soften with alloying content.

The first result is consistent with an increase in the M_s, but experimentally there is little change in the M_s when the ternary concentration is less than 7.5 at.%. Experimental increase in the M_s in ternary alloys with greater than 7.5 at.% Hf or Zr is not consistently predicted by the calculated C′ and C_{44} values, possibly because a large sample of configurations is required at higher alloy concentrations in order to reliably predict the elastic constants of a disordered alloy. While studying the effect of ternary alloying addition, only one configuration from a few possible configurations was considered for each alloy composition. Hence, the above described conclusions are tentative. For completing this study a representative sample of possible configurations should really be considered, which would require more computational time than was available to me. An alternative computational method needing less computational time, such as a coherent potential approximation or a virtual crystal approximation, will be worth exploring for this purpose.

The symmetry of a B2 crystal can simplify the relationship between the interatomic force constants and elastic constants derived by Born et al.[131] for a general crystal. I derived this simplification for the B2 structure by applying elementary group theory (using the properties of a quotient group and the Grand Orthogonality Theorem). The elastic constants derived using this relation are in agreement with the elastic constants measured from the slopes of the phonon dispersion relations. My formula (see Eq.(3.98)) may be useful in the future for analysing the effect of changes in force constants, e.g. in alloys within a mean field approximation, on elastic constants.

As a possible route to modelling sufficient anharmonicity to stabilize B2 at high temperature, I derived the SCAILD formulation for an ordered compound. Precautions that need to be taken while practically implementing the SCAILD method are also discussed in this thesis. In practice, a useful necessary criterion for the convergence of this method is the convergence of the vibrational free energy. In addition, the calculated vibrational frequencies should be manually checked at each iteration to make sure that all these frequencies are real at a given temperature before the phonon dispersion is accepted as converged at the temperature under consideration. I applied the SCAILD formulation for a temperature of 350 K in a 2×2×2 supercell. However, I was not able to obtain a

converged phonon dispersion relation after 60 iterations. Some of the calculated mode frequencies are imaginary in some iterations. I therefore have doubts about the validity of the claim in the literature, that by using SCAILD a value 227 K is the predicted transition temperature of B2.

In the following section, I will suggest some directions that I believe will be useful for future research.

6.2 Outlook

Several theoretical problems must be faced by future research on understanding the mechanism of martensitic transformations in shape memory alloys at the atomic scale. The first is the time it takes to make total energy and force calculations with the accuracy of DFT. The rapid increase in computer power is relieving this situation, nevertheless a lot more could be achieved with 2-3 orders of magnitude faster computations. New empirical potentials with something approaching DFT accuracy and robustness may make a significant impact on this problem. A second problem is efficient calculation of high temperature free energies. We have to deal with a regime in which the anharmonicity is more than a perturbation small enough to be treated by the quasiharmonic approximation. The austenite crystal structure is not even metastable at low temperature, so a more radical approach is required. Having tried and failed with the SCAILD method, I suggest that an alternative self-consistent phonon formulation or even a direct thermodynamic integration may be the best solution.

Three particular methods which might be of future use for understanding the martensitic transformation in TiNi-based shape memory alloys are suggested in this section. Beyond these, more mesoscopic aspects such as the role of interface energies, nucleation processes, accommodation strains, which probably require also modelling at the continuum level [174], still have to be addressed in any complete description.

6.2.1 A Gaussian approximation potential (GAP)

Interatomic potentials that can describe the phase stabilities and elastic properties are not available for a TiNi system [175]. Bartók et al. [176] developed a method for creating interatomic potentials, the GAP method, which seems to have the potential to do this. In this method, potentials are created from the highly accurate information about a system obtained from, mainly DFT based, quantum

mechanical calculations. A potential energy function is created not by fitting the parameters to data, as in conventional methods of generating potentials, but by applying information theory to fit parameters in a Bayesian approach, called a Gaussian process [177]. Such potentials are not cheap to compute, and require a lot of work to construct, but can be used for molecular dynamics or other methods, much more cheaply than using DFT directly.

A particular advantage of the Gaussian process is that its accuracy can be monitored and systematically improved if necessary at the fitting stage [178]. Another feature is that a crude model, such as the embedded atom model, can be used as a first approximation, and then the GAP potential can be fitted only to the difference between its predicted data and data for the same set of structures predicted by the full quantum mechanical model. In this way the major features of the potential landscape can be captured and the accuracy refined by tuning the GAP potential. If such a potential is successfully generated for TiNi and ternary alloys, it will be an efficient way to study the anharmonic lattice dynamics and phase transitions using the tools of atomistic simulation such as those mentioned below.

6.2.2 Self consistent harmonic approximation

The effect of anharmonicity is to renormalise the imaginary frequencies of the harmonic approximation, creating real frequencies and stabilising the B2 phase at high temperature. Rousseau et al. [179] suggested a variational method based on the self consistent harmonic approximation (SCHA) [59, 180] for estimating the renormalized phonon frequencies. In this method, the potential energy is expanded up to fourth order in atomic displacements. The harmonic approximation is obtained by truncating this expansion at second order, and for some normal modes it may lead to imaginary frequencies, which for the purely harmonic Hamiltonian implies that the crystal is mechanically unstable. In the SCHA, a trial harmonic term $\hat{U}_2^0$, which would give real phonon frequencies, is added and subtracted from the potential. The Hamiltonian $\hat{H}$ is written as a sum of two terms $\hat{H}_0$, $\hat{H}_1$:

$$\hat{H}_0 = \hat{T} + \hat{U}_0 + \hat{U}_2^0 \quad \text{and} \tag{6.1}$$

$$\hat{H}_1 = (\hat{U}_2 - \hat{U}_2^0) + \hat{U}_3 + \hat{U}_4. \tag{6.2}$$

Here $\hat{T}$ and $\hat{U}_n$ are kinetic energy operator and nth order potential energy operator respectively. Let us define the renormalised frequencies which diagonalise $\hat{H}_0$ as $\tilde{\omega}(\mathbf{k}_j)$ and the frequencies in the harmonic approximation as $\omega(\mathbf{k}_j)$. The exact free energy F of the system $\hat{H}_0 + \hat{H}_1$ satisfies the Gibbs-Bogoliubov inequality [181, 182]

$$F \leq F_0 + \langle \hat{H}_1 \rangle_0, \tag{6.3}$$

where

$$F_0 = -\frac{1}{\beta} \ln(Z_0) \text{ and} \tag{6.4}$$

$$\langle \hat{H}_1 \rangle_0 = \mathrm{tr}\left[\hat{H}_1 \exp\{-\beta \hat{H}_0\}\right]/Z_0. \tag{6.5}$$

Here $\beta = 1/(k_\mathrm{B}\mathrm{T})$ and the partition function Z_0 is equal to $\mathrm{tr}(\exp\{-\beta \hat{H}_0\})$. As can be seen from the relation in Eq.(6.3), the minimum of the right hand side can be considered as an approximation to the free energy of the system. An expression for the $\tilde{\omega}(\mathbf{k}_j)$ can be obtained by minimising this right hand side with respect to $\tilde{\omega}(\mathbf{k}_j)$ [182]. Fourth order force constants are required for evaluating the $\tilde{\omega}(\mathbf{k}_j)$ using this expression.

The fourth order force constants are calculated *ab initio* using a frozen phonon method and finite differencing [179]. The symmetry of the crystal and dynamical matrices can be used to reduce the number of fourth order force constants to be evaluated. Even after this reduction, the force constants calculations take most of the computational time of this method. However, once these force constants are available, phonon dispersion and free energy at any temperature can be calculated easily. In this respect this method contrasts with the SCAILD method, where, although there are fewer of them, the force constants have to be recalculated for each iteration and temperature.

Errea et al. [181] used this method for studying effect of anharmonicity on the stability of a simple cubic (SC) phase of Ca at a pressure of 50 GPa. The calculated frequency of a normal mode was imaginary at M in the harmonic approximation. On including the anharmonic effects, all the renormalised frequencies are found to be real and the SC structure is stabilised even at 0 K. This method could in principle be used for studying the effect of anharmonicity on the stability of B2 in TiNi-based SMAs, although the preliminary work required to analyse the symmetry and number of fourth order force constants seems not trivial.

6.2.3 Thermodynamic integration

An attractive alternative might be to calculate the anharmonic part of the free energy non-perturbatively, by using thermodynamic integration. In this method, we might make a similar division of the *exact* Hamiltonian, following the notation of the SCHA described previously:

$$\hat{H}_0 = \hat{T} + \hat{U}_0 + \hat{U}_2^0 \quad \text{and} \tag{6.6}$$

$$\hat{H}_1 = (\hat{U} - \hat{U}_2^0) \tag{6.7}$$

where $\hat{U}$ is now the full potential energy, to all orders beyond $\hat{U}_0$ in atomic displacements. Now the exact potential is 'switched on' slowly during an equilibrated molecular dynamics run, with a parameter λ [183] such that at each value of λ:

$$\hat{H}_\lambda = \hat{H}_0 + \lambda \hat{H}_1. \tag{6.8}$$

At a sequence of values of λ in the range $0 \leq \lambda \leq 1$, the average values $\langle \hat{H}_1 \rangle_\lambda$ are evaluated. Then the exact free energy is given in terms of the harmonic free energy (which is evaluated initially from the standard formulae as in the SCHA) by:

$$F = F_0 + \int_0^1 \mathrm{d}\lambda \langle \hat{H}_1 \rangle_\lambda. \tag{6.9}$$

The free energy up to a martensitic transformation can be studied by calculating the free energy as a function of temperature in different phases. Although the description in terms of renormalised phonons is not available, this could be recovered if required by projection of the displacements onto normal coordinates during a molecular dynamics run. Clearly such a thermodynamic integration method can only be implemented if the total energy and force evaluations are computationally fast enough.

Appendix A

Normal mode symmetries in a CsCl crystal

Symmetry information of a soft mode is required for determining all the possible martensite structures using group-subgroup relations. Normal modes in a given space group have symmetries belong to one of the irreps of the space group. By taking CsCl and Mg crystals as examples, Warren [47] explained procedures for decomposing any representation at a wave vector into irreps, and determining the compatibility relations along different paths in the BZ. However, as noticed by Saxena et al. [46], the mode symmetries at M belong to M_5^-, M_3^-, and M_2^- irreps instead of M_5^-, M_2^-, and M_4^- irreps respectively, as suggested by Warren [47], in case of a CsCl crystal. It means the corresponding compatibility relations are also need to be corrected. Mode symmetries at high symmetry points and compatibility relations along high symmetry directions in the BZ of a CsCl crystal are derived in this Appendix. All the normal mode symmetries presented in this thesis are labelled using the irrep decompositions derived in this Appendix and according to the symmetry properties of polarisation vectors of normal modes [184]. Miller and Love convention is used to denote the irreps.

A.1 Irreducible representations

The symmetry properties of a normal mode are determined by the symmetry elements in the point group of normal mode wave vector, $G_0(\mathbf{k})$ [125]. The number of times an irreducible representation Γ_i occurs in a given representation Γ at a wave vector $\mathbf{k}$, a_i, is given by the following relation [148]:

$$a_i = \frac{1}{h}\sum_c N_c \chi_i(\mathbf{k}; R_c)^* \chi(\mathbf{k}; R_c). \tag{A.1}$$

Here h is the order of $G_0(\mathbf{k})$, c is the number of classes, N_c is the number of symmetry elements in a class c, $\chi(\mathbf{k}; R)$ is the character of a symmetry element R in the Γ representation, and $\chi_i(\mathbf{k}; R)$ is the character of a symmetry element R in the irrep Γ_i. $\chi(\mathbf{k}; R)$ is the trace of a $3r \times 3r$ matrix $T(\mathbf{k}; R)$ representing a symmetry element R at a wave vector $\mathbf{k}$ in a crystal with r atoms in a unit cell.

Maradudin et al. derived an expression for the representation matrix $T(\mathbf{k}; R)$ in terms of $\mathbf{k}$-vector, atomic positions (s) and symmetry elements ($R_{\alpha\beta}$) [125]:

$$T_{\alpha\beta}(ss'|\mathbf{k}; R) = R_{\alpha\beta}\delta(s, F_0(s'; R)) \exp\{i\mathbf{k}.[\mathbf{x}(s) - \mathbf{R}\mathbf{x}(s')]\}. \tag{A.2}$$

Here $F_0(s'; R)$ is a function which determines the type of atom onto which s' atom is moved by symmetry operation R and $R_{\alpha\beta}$ are elements of a matrix which transform the coordinates of a general point according to symmetry operation R. The point group of a CsCl crystal is $m\bar{3}m$. It is a symmorphic group and all elements will move an atom of given type to a site occupied by similar atom. Hence $F_0(s'; R) = s'$ and

$$T_{\alpha\beta}(ss'|\mathbf{k}; R) = R_{\alpha\beta}\delta(s, s') \exp\{i\mathbf{k}.[\mathbf{x}(s) - \mathbf{R}\mathbf{x}(s')]\}. \tag{A.3}$$

In a CsCl structure, there are two atoms in a unit cell (s=1,2) located at $\mathbf{x}(1) =$ [0,0,0] and $\mathbf{x}(2) = \frac{a}{2}[1, 1, 1]$. Hence,

$$T(\mathbf{k}; R) = \begin{pmatrix} R & 0 \\ 0 & \bar{\theta}R \end{pmatrix}.$$

Here $\bar{\theta} = \exp\{i\mathbf{k}.[\mathbf{x}(2) - \mathbf{R}\mathbf{x}(2)]\}$.

$\chi_i(\mathbf{k}; R)$ is the trace of an irreducible representation matrix $T_i(\mathbf{k}; R)$. As cited by Maradudin et al. [125], Kovalev [185] tabulated the irreducible representation matrices for different space groups. Tools on a crystallographic server [157] are used for generating these irreducible representation matrices and calculating the characters $\chi_i(\mathbf{k}; R)$. Labels of high symmetry points the FBZ of a B2 crystal are shown in Fig.(A.1). Complete character tables are determined at high symmetry points in the BZ of a CsCl crystal. From the character tables, irreducible decompositions are determined using the Eq.(A.1). They are presented in the following subsections. Symmetry elements are described in the notation of

Altmann and Cracknell [186].

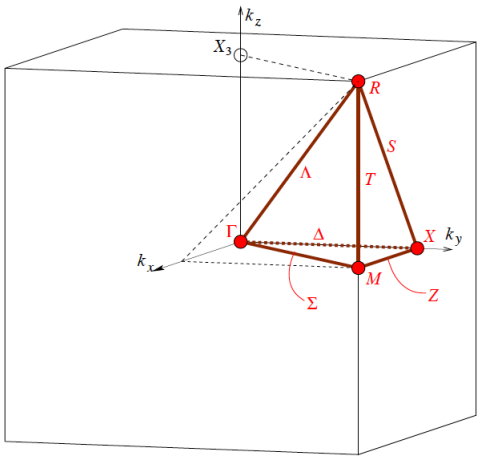


Figure A.1: First Brillouin zone of a B2 crystal and labels of high symmetry points in it (generated on a crystallographic server [157]).

$\mathbf{k} = \frac{2\pi}{a}[0,0,0](\Gamma)$

The group of Γ is $m\bar{3}m$. It has 48 elements. These elements are divided among 10 classes. Hence there are 10 irreps. At Γ the representation matrix in Eq.(A.3) simplifies to [47]

$$T_{\alpha\beta}(ss'|\mathbf{k};R) = R_{\alpha\beta}\delta(s,s'). \tag{A.4}$$

Complete character table at Γ is presented in Table(A.1). From this table it is apparent that the representation at Γ consists of two three dimensional Γ_4^- representations: One corresponds to triply degenerate acoustic modes and other to optic modes of degeneracy 3.

$$\Gamma_\Gamma = 2\Gamma_4^-. \tag{A.5}$$

$\mathbf{k} = \frac{2\pi}{a}[\frac{1}{2},\frac{1}{2},\frac{1}{2}](\mathbf{R})$

The group of the wave vector R is same as that of Γ. The character table is shown in Table(A.2). From this table it can be concluded that a representation at R point can be decomposed into two three dimensional irreps R_5^+ and R_4^-.

$$\Gamma_\mathrm{R} = \mathrm{R}_5^+ \oplus \mathrm{R}_4^-. \tag{A.6}$$

Table A.1: Character table for irreps at Γ

$R \rightarrow$ irrep $\downarrow$	E	$8C_3$	$6C_2$	$6C_4$	$3C_2$	i	$6S_4$	$8S_6$	$3\sigma_h$	$6\sigma_d$	a_i
Γ_1^+	1	1	1	1	1	1	1	1	1	1	0
Γ_2^+	1	1	-1	-1	1	1	-1	1	1	-1	0
Γ_3^+	2	-1	0	0	2	2	0	-1	2	0	0
Γ_4^+	3	0	-1	1	-1	3	1	0	-1	-1	0
Γ_5^+	3	0	1	-1	-1	3	-1	0	-1	1	0
Γ_1^-	1	1	1	1	1	-1	-1	-1	-1	-1	0
Γ_2^-	1	1	-1	-1	1	-1	1	-1	-1	1	0
Γ_3^-	2	-1	0	0	2	-2	0	1	-2	0	0
Γ_4^-	3	0	-1	1	-1	-3	-1	0	1	1	2
Γ_5^-	3	0	1	-1	-1	-3	1	0	1	-1	0
$\chi(\mathbf{k};R) \longrightarrow$	6	0	-2	2	-2	-6	-2	0	2	2	
N_c	1	8	6	6	3	1	6	8	3	6	

Table A.2: Character table for irreps at R

$R \rightarrow$ irrep $\downarrow$	E	$8C_3$	$6C_2$	$6C_4$	$3C_2$	i	$6S_4$	$8S_6$	$3\sigma_h$	$6\sigma_d$	a_i
R_1^+	1	1	1	1	1	1	1	1	1	1	0
R_2^+	1	1	-1	-1	1	1	-1	1	1	-1	0
R_3^+	2	-1	0	0	2	2	0	-1	2	0	0
R_4^+	3	0	-1	1	-1	3	1	0	-1	-1	0
R_5^+	3	0	1	-1	-1	3	-1	0	-1	1	1
R_1^-	1	1	1	1	1	-1	-1	-1	-1	-1	0
R_2^-	1	1	-1	-1	1	-1	1	-1	-1	1	0
R_3^-	2	-1	0	0	2	-2	0	1	-2	0	0
R_4^-	3	0	-1	1	-1	-3	-1	0	1	1	1
R_5^-	3	0	1	-1	-1	-3	1	0	1	-1	0
$\chi(\mathbf{k};R)$	6	0	0	0	-2	0	-2	0	0	2	
N_c	1	8	6	6	3	1	6	8	3	6	

$\mathbf{k} = \frac{2\pi}{a}[\frac{1}{2}, \frac{1}{2}, 0]\mathbf{(M)}$

The group of the wave vector M is $D_{4h}(4/mmm)$. It has sixteen elements divided among ten classes: { $\{E\}, \{C_{2z}\}, \{C_{4z}+, C_{4z}-\}, \{C_{2x}, C_{2y}\}, \{C_{2a}, C_{2b}\}, \{i\}, \{\sigma_z\}$, $\{S_{4z}+, S_{4z}-\}, \{\sigma_x, \sigma_y\}$, and $\{\sigma_{da}, \sigma_{db}\}$ }. The character table is shown in Table(A.3). Any representation at M point can be decomposed according to the following equation.

$$\Gamma_{\mathrm{M}} = \mathrm{M}_2^- \oplus \mathrm{M}_3^- \oplus 2\mathrm{M}_5^- . \tag{A.7}$$

Table A.3: Character table for irreps at M

$R \rightarrow$ irrep $\downarrow$	E	C_{2z}	$C_{4z}+$	C_{2x}	C_{2a}	i	σ_z	$S_{4z}+$	σ_x	σ_{da}	a_i
M_1^+	1	1	1	1	1	1	1	1	1	1	0
M_2^+	1	1	-1	1	-1	1	1	-1	1	-1	0
M_3^+	1	1	1	-1	-1	1	1	1	-1	-1	0
M_4^+	1	1	-1	-1	1	1	1	-1	-1	1	0
M_5^+	2	-2	0	0	0	2	-2	0	0	0	0
M_1^-	1	1	1	1	1	-1	-1	-1	-1	-1	0
M_2^-	1	1	-1	1	-1	-1	-1	1	-1	1	1
M_3^-	1	1	1	-1	-1	-1	-1	-1	1	1	1
M_4^-	1	1	-1	-1	1	-1	-1	1	1	-1	0
M_5^-	2	-2	0	0	0	-2	2	0	0	0	2
$\chi(\mathbf{k}; R)$	6	-2	0	0	-2	-6	2	0	0	2	
N_c	1	1	2	2	2	1	1	2	2	2	

$\mathbf{k} = \frac{2\pi}{a}[0, 0, \frac{1}{2}]\mathbf{(X)}$

The group of the wave vector X is $D_{4h}(4/mmm)$. It has sixteen elements divided among ten classes: $\{ \{E\}, \{C_{2z}\}, \{C_{4z}+, C_{4z}-\}, \{C_{2x}, C_{2y}\}, \{C_{2a}, C_{2b}\}, \{i\}, \{\sigma_z\}, \{S_{4z}+, S_{4z}-\}, \{\sigma_x, \sigma_y\},$ and $\{\sigma_{da}, \sigma_{db}\}$ $\}$. The character table is shown in Table(A.4). Any representation at X point can be decomposed according to the following equation.

$$\Gamma_{\mathrm{X}} = \mathrm{X}_1^+ \oplus \mathrm{X}_5^+ \oplus \mathrm{X}_3^- \oplus \mathrm{X}_5^-. \tag{A.8}$$

Table A.4: Character table for irreps at X

$R \rightarrow$ irrep $\downarrow$	E	C_{2z}	$C_{4z}+$	C_{2x}	C_{2a}	i	σ_z	$S_{4z}+$	σ_x	σ_{da}	a_i
X_1^+	1	1	1	1	1	1	1	1	1	1	1
X_2^+	1	1	-1	1	-1	1	1	-1	1	-1	0
X_3^+	1	1	1	-1	-1	1	1	1	-1	-1	0
X_4^+	1	1	-1	-1	1	1	1	-1	-1	1	0
X_5^+	2	-2	0	0	0	2	-2	0	0	0	1
X_1^-	1	1	1	1	1	-1	-1	-1	-1	-1	0
X_2^-	1	1	-1	1	-1	-1	-1	1	-1	1	0
X_3^-	1	1	1	-1	-1	-1	-1	-1	1	1	1
X_4^-	1	1	-1	-1	1	-1	-1	1	1	-1	0
X_5^-	2	-2	0	0	0	-2	2	0	0	0	1
$\chi(\mathbf{k}; R)$	6	-2	2	0	0	0	0	0	2	2	
N_c	1	1	2	2	2	1	1	2	2	2	

$\mathbf{k} = \frac{2\pi}{a}[\frac{1}{3}, \frac{1}{3}, 0](\Sigma)$

The group of the wave vector $\frac{2\pi}{3a}[1,1,0]$ is $C_{2v}(mm2)$. It has four classes each having one element: $\{\ \{E\}, \{C_{2a}\}, \{\sigma_z\}, \{\sigma_{db}\}\ \}$. The character table is shown in Table(A.5). Any representation at $\frac{2\pi}{3a}[1,1,0]$ point can be decomposed according to the following equation.

$$\Gamma_\Sigma = 2\Sigma_1 \oplus 2\Sigma_2 \oplus 2\Sigma_3. \tag{A.9}$$

There is no Σ_4 irrep in the decomposition. The TA_2 soft mode symmetry at $\frac{2\pi}{3a}[1,1,0]$ belong to a Σ_2 irrrep.

Table A.5: Character table for irreps at $\frac{2\pi}{3a}[1,1,0]$

$R \rightarrow$ irrep $\downarrow$	E	C_{2a}	σ_z	σ_{db}	a_i
Σ_1	1	1	1	1	2
Σ_2	1	-1	1	-1	2
Σ_3	1	-1	-1	1	2
Σ_4	1	1	-1	-1	0
$\chi(\mathbf{k}; R)$	6	-2	2	2	
N_c	1	1	1	1	

$\mathbf{k} = \frac{2\pi}{a}[0, \frac{1}{3}, 0](\Delta)$

The group of the wave vector $\frac{2\pi}{3a}[0,1,0]$ is $C_{4v}(4mm)$. It has five classes and eight elements: $\{\ \{E\}, \{C_{2y}\}, \{C_{4y}+, C_{4y}-\}, \{\sigma_z, \sigma_x\}, \{\sigma_{de}, \sigma_{dc}\}\ \}$. The character table is shown in Table(A.6). Any representation at $\frac{2\pi}{3a}[0,1,0]$ point can be decomposed according to the following equation.

$$\Gamma_\Delta = 2\Delta_1 \oplus 2\Delta_5. \tag{A.10}$$

$\mathbf{k} = \frac{2\pi}{a}[\frac{1}{3}, \frac{1}{3}, \frac{1}{3}](\Lambda)$

The group of the wave vector $\frac{2\pi}{3a}[1,1,1]$ is $C_{3v}(3m)$. It has three classes and six elements: $\{\ \{E\}, \{C_{31}+, C_{31}-\}, \{\sigma_{db}, \sigma_{df}, \sigma_{de}\}\ \}$. The character table is shown in Table(A.7). Any representation at $\frac{2\pi}{3a}[1,1,1]$ can be decomposed according to the following equation.

$$\Gamma_\Lambda = 2\Lambda_1 \oplus 2\Lambda_3. \tag{A.11}$$

Table A.6: Character table for irreps at $\frac{2\pi}{3a}[0,1,0]$

$R \rightarrow$ irrep $\downarrow$	E	C_{2y}	$C_{4y}+$	σ_z	σ_{de}	a_i
Δ_1	1	1	1	1	1	2
Δ_2	1	1	-1	1	-1	0
Δ_3	1	1	-1	-1	1	0
Δ_4	1	1	1	-1	-1	0
Δ_5	2	-2	0	0	0	2
$\chi(\mathbf{k};R)$	6	-2	2	2	2	
N_c	1	1	2	2	2	

Table A.7: Character table for irreps at $\frac{2\pi}{3a}[1,1,1]$

$R \rightarrow$ irrep $\downarrow$	E	$C_{31}+$	σ_{db}	a_i
Λ_1	1	1	1	2
Λ_2	1	1	-1	0
Λ_3	2	-1	0	2
$\chi(\mathbf{k};R)$	6	0	2	
N_c	1	2	3	

A.2 Compatibility relations

High symmetry points are also points on high symmetry lines. Therefore compatibility relations are expected between the irrep at Γ, X, M, R and the connecting high symmetry lines [187]. Mode labelling is easy if compatibility relations are available. Comparability relations in a CsCl structure are determined using a programme called ISOTROPY [188].

Table A.8: Compatibility relations at Γ for representations in B2 crystals

Irrep at $\Gamma\downarrow$	Δ	Σ	Λ
Γ_4^-	$\Delta_1 \oplus \Delta_5$	$\Sigma_1 \oplus \Sigma_2 \oplus \Sigma_3$	$\Lambda_1 \oplus \Lambda_3$

Table A.9: Compatibility relations at X for representations in B2 crystals

Irrep at X $\downarrow$	Δ	Z	S
X_1^+	Δ_1	Z_1	S_1
X_5^+	Δ_5	$Z_2 \oplus Z_4$	$S_3 \oplus S_4$
X_3^-	Δ_1	Z_4	S_3
X_5^-	Δ_5	$Z_1 \oplus Z_3$	$S_1 \oplus S_2$

Table A.10: Compatibility relations at M for representations in B2 crystals

Irrep at M $\downarrow$	Σ	Z	T
M_2^-	Σ_3	Z_2	T_3
M_3^-	Σ_3	Z_3	T_1
M_5^-	$\Sigma_1 \oplus \Sigma_2$	$Z_1 \oplus Z_4$	T_5

Table A.11: Compatibility relations at R for representations in B2 crystals

Irrep at R $\downarrow$	Λ	S	T
R_5^+	$\Lambda_1 \oplus \Lambda_3$	$S_1 \oplus S_3 \oplus S_4$	$T_3 \oplus T_5$
R_4^-	$\Lambda_1 \oplus \Lambda_3$	$S_1 \oplus S_2 \oplus S_3$	$T_1 \oplus T_5$

Appendix B

Homogeneous deformation method for cubic crystals

Strain tensors used for determining the elastic constants of a cubic crystal following a homogeneous deformation method are described in this Appendix. For the chosen strain tensors, the linear relations between the elastic constants and curvature values are derived. There are only three independent elastic stiffness tensor elements. Therefore, three independent strain tensors are required to completely determine the elastic stiffness tensor.

Matrix notation introduced by Voigt is used for representing tensor elements in the following discussions [189]. In this notation, a single suffix is used in place of two suffixes to represent the strain tensor elements. *i.e.*

$$\begin{pmatrix} \epsilon_1 & \frac{1}{2}\epsilon_6 & \frac{1}{2}\epsilon_5 \\ \frac{1}{2}\epsilon_6 & \epsilon_2 & \frac{1}{2}\epsilon_4 \\ \frac{1}{2}\epsilon_5 & \frac{1}{2}\epsilon_4 & \epsilon_3 \end{pmatrix} \equiv \begin{pmatrix} \epsilon_{11} & \epsilon_{12} & \epsilon_{13} \\ \epsilon_{21} & \epsilon_{22} & \epsilon_{23} \\ \epsilon_{31} & \epsilon_{32} & \epsilon_{33} \end{pmatrix}.$$

Similarly, the first pair of suffixes of elastic tensor elements C_{ijkl} are abbreviated into one suffix and the last pair into another suffix according to following Table(B.1).

Table B.1: Equivalence of indices in the tensor notation and the matrix notation

Tensor notation	11	22	33	23,32	31,13	12,21
Matrix notation	1	2	3	4	5	6

In the matrix notation, the elastic strain energy in Eq.(3.117) is written as

$$E^{\text{ela}} = \frac{1}{2}\sum_{ij} \mathrm{C}_{ij}\epsilon_i\epsilon_j. \tag{B.1}$$

Using this expansion the total energy of a strained cubic crystal per unit volume can be written in terms of elastic tensor elements and strain tensor elements.

$$E^{\text{tot}} = E^{\circ} + \frac{1}{2}\mathrm{C}_{11}(\epsilon_1^2+\epsilon_2^2+\epsilon_3^2) + \mathrm{C}_{12}(\epsilon_1\epsilon_2+\epsilon_2\epsilon_3+\epsilon_3\epsilon_1) + \frac{1}{2}\mathrm{C}_{44}(\epsilon_4^2+\epsilon_5^2+\epsilon_6^2). \tag{B.2}$$

Depending on the choice of the strain tensors this equation can be further simplified. For a given strain tensor, twenty strains of magnitude between -0.02 and 0.02 are applied to the unit cell. Atoms in the strained unit cells are relaxed to the minimum energy positions and the total energies are calculated. A fifth order polynomial is fitted to the total energy versus strain profiles. Curvature value of energy versus strain profiles is calculated at the equilibrium configuration. The curvature values are related to combinations of elastic constants. In the following sections the strain tensors used for calculating elastic constants in cubic crystals are described. For the chosen strain tensors the relations between the elastic constants and curvature values are derived.

Within elastic limit the stress and the strain are linearly related and this relation is the generalised Hooke's law:

$$\sigma_{ij} = \sum_{kl} \mathrm{C}_{ijkl}\epsilon_{kl}. \tag{B.3}$$

In the matrix notation a single index is used in place of two indices for the stress tensor elements in the tensor notation. Equivalence of the elements in both these notations is shown in the following matrices.

$$\begin{pmatrix} \sigma_1 & \sigma_6 & \sigma_5 \\ \sigma_6 & \sigma_2 & \sigma_4 \\ \sigma_5 & \sigma_4 & \sigma_3 \end{pmatrix} \equiv \begin{pmatrix} \sigma_{11} & \sigma_{12} & \sigma_{13} \\ \sigma_{21} & \sigma_{22} & \sigma_{23} \\ \sigma_{31} & \sigma_{32} & \sigma_{33} \end{pmatrix}.$$

In the matrix notation the Hooke's law is written as

$$\sigma_i = \sum_{j} \mathrm{C}_{ij}\epsilon_j. \tag{B.4}$$

For a chosen strain tensor a linear combination of elastic constants can be calcu-

lated from the stress values on a unit cell using this relation. These relations are also written for the chosen strain tensors in the following sections.

B.1 Bulk modulus calculation

Bulk modulus is defined as the resistance to a hydrostatic pressure. In cubic crystal it is equal to $(C_{11} + 2C_{12})/3$. The following strain tensor was used for calculating the bulk modulus.

$$\begin{pmatrix} \epsilon_1 & \frac{1}{2}\epsilon_6 & \frac{1}{2}\epsilon_5 \\ \frac{1}{2}\epsilon_6 & \epsilon_2 & \frac{1}{2}\epsilon_4 \\ \frac{1}{2}\epsilon_5 & \frac{1}{2}\epsilon_4 & \epsilon_3 \end{pmatrix} = \gamma \begin{pmatrix} 1.0 & 0.0 & 0.0 \\ 0.0 & 1.0 & 0.0 \\ 0.0 & 0.0 & 1.0 \end{pmatrix}. \tag{B.5}$$

Here γ is the magnitude of the applied strain. For this strain tensor the total energy expansion is reduced to

$$E^{\text{tot}} = E^{\circ} + \frac{3}{2}\gamma^2(C_{11} + 2C_{12}). \tag{B.6}$$

Using this relation the bulk modulus values can be calculated from the curvature values:

$$(C_{11} + 2C_{12}) = \frac{1}{9V_0}\frac{\partial^2 E^{\text{tot}}}{\partial \gamma^2}. \tag{B.7}$$

$$\sigma_1 = \sigma_2 = \sigma_3 = (C_{11} + 2C_{12})\gamma, \text{ and} \tag{B.8}$$

$$\sigma_4 = \sigma_5 = \sigma_6 = 0. \tag{B.9}$$

B.2 C′ calculation

C′ is another shear modulus and it determines the resistance to a (110) shear. It is related the elastic constants C_{11} and C_{12}: $C' = \frac{1}{2}(C_{11} - C_{12})$. A volume conserving strain tensor described by the following matrix can be used for C′ calculations.

$$\begin{pmatrix} \epsilon_1 & \frac{1}{2}\epsilon_6 & \frac{1}{2}\epsilon_5 \\ \frac{1}{2}\epsilon_6 & \epsilon_2 & \frac{1}{2}\epsilon_4 \\ \frac{1}{2}\epsilon_5 & \frac{1}{2}\epsilon_4 & \epsilon_3 \end{pmatrix} = \gamma \begin{pmatrix} 1.0 & 0.0 & 0.0 \\ 0.0 & -0.5 & 0.0 \\ 0.0 & 0.0 & -0.5 \end{pmatrix}. \tag{B.10}$$

The total energy of the strained crystal corresponding to this distortion is reduced

to the following Eq.(B.11). From the curvature value of the total energy versus strain profiles corresponding to this distortion, C′ values are calculated using the Eq.(B.12).

$$E^{\text{tot}} = E^{\circ} + \frac{3}{4}(\mathrm{C}_{11} - \mathrm{C}_{12})\gamma^2. \tag{B.11}$$

$$\mathrm{C}' = \frac{1}{3V_0}\frac{\partial^2 E^{\text{tot}}}{\partial \gamma^2}. \tag{B.12}$$

$$\begin{aligned} \sigma_1 &= (\mathrm{C}_{11} - \mathrm{C}_{12})\gamma = 2\mathrm{C}'\gamma, && \text{(B.13)} \\ \sigma_2 = \sigma_3 &= -(\frac{\mathrm{C}_{11} - \mathrm{C}_{12}}{2})\gamma = -\mathrm{C}'\gamma, \text{ and} && \text{(B.14)} \\ \sigma_4 = \sigma_5 = \sigma_6 &= 0. && \text{(B.15)} \end{aligned}$$

B.3 C_{44} calculation

C_{44} determines the resistance to a (100) shear in cubic crystals. It is calculated by applying a rhombohedral shear to the unit cell. It is equivalent to stretching of a cube along the [111] direction. The following matrix is the homogeneous strain matrix corresponding to this shear.

$$\begin{pmatrix} \epsilon_1 & \frac{1}{2}\epsilon_6 & \frac{1}{2}\epsilon_5 \\ \frac{1}{2}\epsilon_6 & \epsilon_2 & \frac{1}{2}\epsilon_4 \\ \frac{1}{2}\epsilon_5 & \frac{1}{2}\epsilon_4 & \epsilon_3 \end{pmatrix} = \gamma \begin{pmatrix} 0.0 & 0.5 & 0.5 \\ 0.5 & 0.0 & 0.5 \\ 0.5 & 0.5 & 0.0 \end{pmatrix}. \tag{B.16}$$

The total energy expression for this distortion is given by the Eq.(B.17). The C_{44} value can be calculated from the curvature value of the energy versus strain profiles corresponding to this distortion.

$$E^{\text{tot}} = E^{\circ} + \frac{3}{2}\mathrm{C}_{44}(\gamma^2), \text{and} \tag{B.17}$$

$$\mathrm{C}_{44} = \frac{1}{3V_0}\frac{\partial^2 E^{\text{tot}}}{\partial \gamma^2}. \tag{B.18}$$

$$\begin{aligned} \sigma_1 = \sigma_2 = \sigma_3 &= 0, \text{ and} && \text{(B.19)} \\ \sigma_4 = \sigma_5 = \sigma_6 &= \mathrm{C}_{44}\gamma. && \text{(B.20)} \end{aligned}$$

References

[1] S. M. Shapiro, *Neutron Scattering Studies of Anomalous Phonon Behavior in Functional Materials*, vol. 79 of *Materials science*, pp. 93–112. Springer Berlin Heidelberg, 2005. 10.1007/3-540-31631-0-6. 1

[2] Y. Bellouard, "Shape memory alloys for microsystems: A review from a material research perspective," *Materials Science and Engineering: A*, vol. 481-482, pp. 582 – 589, 2008. Proceedings of the 7th European Symposium on Martensitic Transformations, ESOMAT 2006. 1, 2, 4

[3] K. Otsuka and X. Ren, "Physical metallurgy of Ti-Ni based shape memory alloys," *Progress in Materials Science*, vol. 50, no. 5, pp. 511 – 678, 2005. 1, 5, 7, 9, 14, 15, 24, 89

[4] R. W. Cahn, "Metallic rubber bounces back," *Nature*, vol. 374, pp. 120–121, Mar 1995. 4

[5] A. Ölander *Zeitschrift für Kristallographie*, vol. A83, p. 145, 1932. 4

[6] A. Ölander, "An electrochemical investigation of solid Cadmium-Gold alloys," *Journal of the American Chemical Society*, vol. 54, no. 10, pp. 3819–3833, 1932. 4

[7] A. Byström and K. E. Almin, "X-ray investigation of Gold-Cadmium alloys rich in Gold," *Acta Chemica Scandinavica*, vol. 1, pp. 76–89, 1947. 4

[8] W. J. Buehler, J. V. Gilfrich, and R. C. Wiley, "Effect of low-temperature phase changes on the mechanical properties of alloys near composition TiNi," *Journal of Applied Physics*, vol. 34, no. 5, pp. 1475–1477, 1963. 4

[9] van Humbeeck, J., "Shape memory materials : State of the art and requirements for future applications," *J. Phys. IV France*, vol. 07, no. C5, pp. C5–3–C5–12, 1997. 4

[10] R. Noebe, T. Biles, and S. Padula, *NiTi-Based High-Temperature Shape-Memory Alloys*. CRC Press, 2012/01/25 2006. 4, 5, 24, 27, 28, 121

[11] J. Ryhänen, *Biocompatibility evaluation of Nickel-Titanium shape memory alloys*. PhD thesis, University of Oulu, 1999. 4

[12] Cederström, J. and Van Humbeeck, J., "Relationship between shape memory material properties and applications," *J. Phys. IV France*, vol. 05, no. C2, pp. C2–335–C2–341, 1995. 4

[13] P. Pietrokowsky, "Ordering in the intermediate phases TiFe, TiCo, and TiNi," *Journal of applied physics*, vol. 31, no. 10, 1960. 7

[14] C. Zener, "Contributions to the theory of beta-phase alloys," *Phys. Rev.*, vol. 71, pp. 846–851, Jun 1947. 7, 20, 21

[15] Petry, W., "Dynamical precursors of martensitic transitions," *J. Phys. IV France*, vol. 05, no. C2, pp. C2–15–C2–28, 1995. 7

[16] T. V. Philip and P. A. Beck *Transactions of AIME*, vol. 209, p. 1269, 1957. 8, 75

[17] K. Chandra and G. R. Purdy, "Observations of thin crystals of TiNi in premartensitic states," *Journal of Applied Physics*, vol. 39, no. 5, pp. 2176–2181, 1968. 8

[18] T. B. Massalski, *Binary Alloy Phase Diagrams*. ASM International. 8

[19] K. Otsuka and X. Ren, "Recent developments in the research of shape memory alloys," *Intermetallics*, vol. 7, no. 5, pp. 511 – 528, 1999. 8, 29

[20] H. Morawiec, D. Stróż, T. Goryczka, and D. Chrobak, "Two-stage martensitic transformation in a deformed and annealed NiTi alloy," *Scripta Materialia*, vol. 35, no. 4, pp. 485 – 490, 1996. 9, 92, 94

[21] J. Zhang, W. Cai, X. Ren, K. Otsuka, and M. Asai, "The nature of reversible change in M_s temperatures of Ti-Ni alloys with alternating aging," *Materials transactions JIM*, vol. 40, pp. 1367–1375, DEC 1999. 9

[22] W. Bührer, R. Gotthardt, A. Kulik, O. Mercier, and F. Staub, "Powder neutron diffraction study of Nickel-Titanium martensite," *Journal of Physics F: Metal Physics*, vol. 13, no. 5, p. L77, 1983. 9

[23] Y. Kudoh, M. Tokonami, S. Miyazaki, and K. Otsuka, "Crystal structure of the martensite in Ti-49.2 at.%Ni alloy analyzed by the single crystal X-ray diffraction method," *Acta Metallurgica*, vol. 33, no. 11, pp. 2049 – 2056, 1985. 9, 76, 77

[24] J. Kim, Y. Liu, and S. Miyazaki, "Ageing-induced two-stage R-phase transformation in Ti-50.9at.%Ni," *Acta Materialia*, vol. 52, no. 2, pp. 487 – 499, 2004. 9, 94

[25] X. Ren, N. Miura, J. Zhang, K. Otsuka, K. Tanaka, M. Koiwa, T. Suzuki, Y. I. Chumlyakov, and M. Asai, "A comparative study of elastic constants of Ti-Ni based alloys prior to martensitic transformation," *Materials Science and Engineering A*, vol. 312, no. 1-2, pp. 196 – 206, 2001. 10, 21, 22

[26] L. Mañosa, D. Ríos-Jara, J. Ortín, A. Planes, and X. Bohigas, "Calorimetric and ultrasonic investigation of the R-phase formation in a TiNi:Fe alloy," *Journal of Physics: Condensed Matter*, vol. 4, no. 34, p. 7059, 1992. 10

[27] Z. Lekston and E. Łągiewka, "X-ray diffraction studies of NiTi shape memory alloys," *Archives of Materials Science and Engineering*, vol. 28, no. 11, pp. 665–672, 2007. 10, 92, 94

[28] T. Hara, T. Ohba, E. Okunishi, and K. Otsuka, "Structural study of R-phase in Ti-50.23 at. %Ni and Ti-47.75 at.%Ni - 1.50 at. %Fe alloys," *Materials transactions - JIM*, vol. 38, no. 1, pp. 11–17, 1997. 10, 77, 78, 92, 94

[29] T. Goryczka and H. Morawiec, "Structure studies of the R-phase using X-ray diffraction methods," *Journal of Alloys and Compounds*, vol. 367, no. 1-2, pp. 137 – 141, 2004. Proceedings of the VIII International Conference on Crystal Chemistry of Intermetallic Compounds. 10, 94

[30] T. Nam, T. Saburi, and K. Shimizu, "Cu-content dependence of shape memory characteristics in Ti-Ni-Cu alloys," *Materials transactions JIM*, vol. 31, pp. 959–967, Nov 1990. 10, 11

[31] T. Saburi, Y. Watanabe, and S. Nenno, "Morphological characteristics of the orthorhombic martensite in a shape memory Ti-Ni-Cu alloy," *ISIJ International*, vol. 29, no. 5, pp. 405–411, 1989. 10

[32] T. Nam, T. Saburi, Y. Nakata, and K. Shimizu, "Shape memory characteristics and lattice deformation in Ti-Ni-Cu alloys," *Materials transactions JIM*, vol. 31, pp. 1050–1056, Dec 1990. 10, 11, 89, 91

[33] P. Potapov, A. Shelyakov, and D. Schryvers, "On the crystal structure of TiNi-Cu martensite," *Scripta Materialia*, vol. 44, no. 1, pp. 1 – 7, 2001. 11

[34] X. Huang, G. J. Ackland, and K. M. Rabe, "Crystal structures and shape-memory behaviour of NiTi," *Nature Materials*, vol. 2, pp. 307–311, 2003. 11, 76, 77, 79, 99

[35] H. Tietze, M. Müllner, and B. Renker, "Dynamical properties of premartensitic NiTi," *Journal of Physics C: Solid State Physics*, vol. 17, no. 21, p. L529, 1984. 13, 14, 15, 92, 93

[36] R. Bruinsma, "Electron-phonon interaction in Ni-Ti," *Phys. Rev. B*, vol. 25, pp. 2951–2954, Feb 1982. 13, 14, 19, 81

[37] H. Tietze, M. Müllner, P. Selgert, and W. Assmus, "The intermediate phase of the shape-memory alloy NiTi," *Journal of Physics F: Metal Physics*, vol. 15, no. 2, p. 263, 1985. 13

[38] T. Ohba, T. Fukuda, T. Tabata, and T. Kakeshita, "Neutron scattering study on equi-atomic TiNi alloy," *J. Phys. IV France*, vol. 112, pp. 639–642, 2003. 14, 92, 93

[39] W. Petry, A. Heiming, J. Trampenau, M. Alba, C. Herzig, H. R. Schober, and G. Vogl, "Phonon dispersion of the BCC phase of group-IV metals. I. BCC Titanium," *Phys. Rev. B*, vol. 43, pp. 10933–10947, May 1991. 14

[40] A. Heiming, W. Petry, J. Trampenau, M. Alba, C. Herzig, H. R. Schober, and G. Vogl, "Phonon dispersion of the BCC phase of group-IV metals. II. BCC Zirconium, a model case of dynamical precursors of martensitic transitions," *Phys. Rev. B*, vol. 43, pp. 10948–10962, May 1991. 14

[41] J. Trampenau, A. Heiming, W. Petry, M. Alba, C. Herzig, W. Miekeley, and H. R. Schober, "Phonon dispersion of the BCC phase of group-IV metals. III. BCC Hafnium," *Phys. Rev. B*, vol. 43, pp. 10963–10969, May 1991. 14

[42] P. Moine, J. Allain, and B. Renker, "Observation of a soft-phonon mode and a pre-martensitic phase in the intermetallic compound $Ti_{50}Ni_{47}Fe_3$ stud-

ied by inelastic neutron scattering," *Journal of Physics F: Metal Physics*, vol. 14, no. 11, p. 2517, 1984. 14, 15, 92

[43] S. K. Satija, S. M. Shapiro, M. B. Salamon, and C. M. Wayman, "Phonon softening in $Ni_{46.8}Ti_{50}Fe_{3.2}$," *Phys. Rev. B*, vol. 29, pp. 6031–6035, Jun 1984. 14, 92

[44] X. Ren, K. Taniwaki, K. Otsuka, and Y. Morii, "Unpublished work," 14, 89

[45] R. Cowley, "Structural phase transitions I. Landau theory," *Advances in Physics*, vol. 29, no. 1, pp. 1–110, 1980. 16

[46] A. Saxena, G. R. Barsch, and D. M. Hatch, "Lattice dynamics representation theory versus isotropy subgroup method with application to M_5^- mode instability in CsCl structure," *Phase Transitions*, vol. 46, no. 2, pp. 89–142, 1994. 16, 88, 130

[47] J. L. Warren, "Further considerations on the symmetry properties of the normal vibrations of a crystal," *Rev. Mod. Phys.*, vol. 40, pp. 38–76, Jan 1968. 16, 130, 132

[48] G. R. Barsch, "Landau theory of the displacive phase transformations in Gold-Cadmium and Titanium-Nickel alloys," *Materials Science Forum*, vol. 327 - 328, pp. 367–376, 2000. 16, 17, 23, 88, 94, 99, 100, 102

[49] G. R. Barsch, T. Ohba, and D. M. Hatch, "Landau theory of structural transformations in Titanium-Nickel and Gold-Cadmium alloys," *Materials Science and Engineering A*, vol. 273-275, pp. 161 – 165, 1999. 16, 89

[50] D. M. Hatch and H. T. Stokes, "Complete listing of order parameters for a crystalline phase transition: A solution to the generalized inverse Landau problem," *Phys. Rev. B*, vol. 65, p. 014113, Dec 2001. 16

[51] K. Parlinski and M. Parlinska-Wojtan, "Lattice dynamics of NiTi austenite, martensite, and R phase," *Phys. Rev. B*, vol. 66, p. 064307, Aug 2002. 16, 17, 76, 77, 78, 79, 88, 89, 94, 99, 102

[52] G.-L. Zhao, T. C. Leung, B. N. Harmon, M. Keil, M. Müllner, and W. Weber, "Electronic origin of the intermediate phase of NiTi," *Phys. Rev. B*, vol. 40, pp. 7999–8001, Oct 1989. 16, 19, 20, 83, 94

[53] X. Huang, C. Bungaro, V. Godlevsky, and K. M. Rabe, "Lattice instabilities of cubic NiTi from first principles," *Phys. Rev. B*, vol. 65, p. 014108, Dec 2001. 17, 89

[54] Z. Y. Zeng, C. E. Hu, L. C. Cai, X. R. Chen, and F. Q. Jing, "Lattice dynamics and phase transition of NiTi alloy," *Solid State Communications*, vol. 149, no. 47-48, pp. 2164 – 2168, 2009. 17

[55] C. M. Varma and W. Weber, "Phonon dispersion in transition metals," *Phys. Rev. Lett.*, vol. 39, pp. 1094–1098, Oct 1977. 17, 18, 19

[56] C. M. Varma and W. Weber, "Phonon dispersion in transition metals," *Phys. Rev. B*, vol. 19, pp. 6142–6154, Jun 1979. 17, 18, 19, 20, 83

[57] G. L. Zhao and B. N. Harmon, "Electron-phonon interactions and the phonon anomaly in β-phase NiTi," *Phys. Rev. B*, vol. 48, pp. 2031–2036, Jul 1993. 19, 81, 83

[58] P. Souvatzis, O. Eriksson, M. I. Katsnelson, and S. P. Rudin, "Entropy driven stabilization of energetically unstable crystal structures explained from first principles theory," *Phys. Rev. Lett.*, vol. 100, p. 095901, Mar 2008. 20, 66, 70

[59] A. der Wissenschaften in Göttingen, *Festschrift zur Feier des zweihundertjährigen Bestehens der Akademie der Wissenschaften in Göttingen*. No. v. 1 in Festschrift zur Feier des zweihundertjährigen Bestehens der Akademie der Wissenschaften in Göttingen, Springer, 1951. 20, 66, 127

[60] P. Souvatzis, D. Legut, O. Eriksson, and M. I. Katsnelson, "Ab initio study of interacting lattice vibrations and stabilization of the β phase in Ni-Ti shape-memory alloy," *Phys. Rev. B*, vol. 81, p. 092201, Mar 2010. 20, 82, 107

[61] O. Mercier, K. N. Melton, G. Gremaud, and J. Hagi, "Single-crystal elastic constants of the equiatomic NiTi alloy near the martensitic transformation," *Journal of Applied Physics*, vol. 51, no. 3, pp. 1833–1834, 1980. 21, 59, 85

[62] X. Ren, K. Taniwaki, K. Otsuka, T. Suzuki, K. Tanaka, and T. Chumlyakov, Yu. I.and Ueki, "Elastic constants of $Ti_{50}Ni_{30}Cu_{20}$ alloy prior to martensitic transformation," *Philosophical Magazine A*, vol. 79, no. 1, pp. 31–41, 1999. 21

[63] J. Zhang, X. Ren, K. Otsuka, K. Tanaka, Y. Chumlyakov, and M. Asai, "Elastic constants of Ti-48 at%Ni-2 at%Fe single crystal prior to B2 → R transformation," *Materials transactions JIM*, vol. 40, pp. 385–388, MAY 1999. Autumn Meeting of Japan-Institute-of-Metals, EHIME, JAPAN, SEP 28, 1998. 21

[64] W. Cao, A. Saxena, and D. M. Hatch, "Antiphase structures of an improper ferroelastic phase transition driven by an M_5^- zone boundary phonon in $RAg_{1-x}In_x$," *Phys. Rev. B*, vol. 64, p. 024106, Jun 2001. 21

[65] X. Ren and K. Otsuka, "The role of softening in elastic constant C_{44} in martensitic transformation," *Scripta Materialia*, vol. 38, no. 11, pp. 1669 – 1675, 1998. 21, 91

[66] G. Bihlmayer, R. Eibler, and A. Neckel, "Elastic properties of B2-NiTi and B2-PdTi," *Phys. Rev. B*, vol. 50, pp. 13113–13117, Nov 1994. 24, 85

[67] M.-X. Wagner and W. Windl, "Lattice stability, elastic constants and macroscopic moduli of NiTi martensites from first principles," *Acta Materialia*, vol. 56, no. 20, pp. 6232 – 6245, 2008. 24, 85

[68] T. Biggs, M. Cortie, M. Witcomb, and L. Cornish, "Martensitic transformations, microstructure, and mechanical workability of TiPt," *Metallurgical and Materials Transactions A*, vol. 32, pp. 1881–1886, 2001. 10.1007/s11661-001-0001-5. 24

[69] G. S. Firstov, J. V. Humbeeck, and Y. N. Koval, "High-temperature shape memory alloys: Some recent developments," *Materials Science and Engineering A*, vol. 378, no. 1-2, pp. 2 – 10, 2004. European Symposium on Martensitic Transformation and Shape-Memory. 25, 29, 30

[70] K. Gupta, "The Ni-Ti-Zr system (Nickel-Titanium-Zirconium)," *Journal of Phase Equilibria*, vol. 20, pp. 441–448, 1999. 10.1361/105497199770335604. 25, 26, 109, 112

[71] K. Gupta, "The Hf-Ni-Ti (Hafnium-Nickel-Titanium) system," *Journal of Phase Equilibria*, vol. 22, pp. 69–72, 2001. 10.1361/105497101770339328. 25, 26, 75

[72] V. N. Eremenko, E. L. Semenova, and L. A. Tret'yachenko, "Liquidus surface and solidification scheme for alloys of the system Ti-Ni-Zr containing

up to 50% Ni," *Powder Metallurgy and Metal Ceramics*, vol. 30, pp. 664–668, 1991. 10.1007/BF01172044. 26

[73] T. Tokunaga, S. Matsumoto, H. Ohtani, and M. Hasebe, "Thermodynamic calculation of phase equilibria in the Nb-Ni-Ti-Zr quaternary system," *Materials transactions*, vol. 48, pp. 89–96, FEB 2007. 26

[74] B. W. David N. AbuJudom, II, C. W. Paul E. Thoma, F. P. W. Ming-Yuan Kao, and W. A. W. David R. Angst, "High transformation temperature shape memory alloy." Patent, 05 1992. US 5114504. 25

[75] D. Angst, P. Thoma, and M. Kao, "The effect of Hafnium content on the transformation temperatures of $Ni_{49}Ti_{51-x}Hf_x$ shape memory alloys," *Journal de Physique IV*, vol. 5, pp. 747–752, DEC 1995. International Conference on Martensitic Transformation (ICOMAT 95), Lausanne, Switzerland, Aug 20-25, 1995. 25, 27, 121

[76] S. Sanjabi, Y. Cao, and Z. Barber, "Multi-target sputter deposition of $Ni_{50}Ti_{50-x}Hf_x$ shape memory thin films for high temperature microactuator application," *Sensors and Actuators A: Physical*, vol. 121, no. 2, pp. 543 – 548, 2005. 27, 108

[77] P. L. Potapov, A. V. Shelyakov, A. A. Gulyaev, E. L. Svistunov, N. M. Matveeva, and D. Hodgson, "Effect of Hf on the structure of Ni-Ti martensitic alloys," *Materials Letters*, vol. 32, no. 4, pp. 247 – 250, 1997. 27, 109, 112, 117

[78] M. Zarinejad, Y. Liu, and T. J. White, "The crystal chemistry of martensite in NiTiHf shape memory alloys," *Intermetallics*, vol. 16, no. 7, pp. 876 – 883, 2008. 27, 108, 109, 117

[79] P. E. Thoma and J. J. Boehm, "Effect of composition on the amount of second phase and transformation temperatures of $Ni_xTi_{90-x}Hf_{10}$ shape memory alloys," *Materials Science and Engineering: A*, vol. 273–275, no. 0, pp. 385 – 389, 1999. 27

[80] Y. Wang, Y. Zheng, W. Cai, and L. Zhao, "The tensile behavior of $Ti_{36}Ni_{49}Hf_{15}$ high temperature shape memory alloy," *Scripta Materialia*, vol. 40, no. 12, pp. 1327 – 1331, 1999. 27

[81] X. Meng, W. Cai, L. Wang, Y. Zheng, L. Zhao, and L. Zhou, "Microstructure of stress-induced martensite in a TiNiHf high temperature shape memory alloy," *Scripta Materialia*, vol. 45, no. 10, pp. 1177 – 1182, 2001. 27

[82] X. Meng, W. Cai, Y. Zheng, Y. Tong, L. Zhao, and L. Zhou, "Stress-induced martensitic transformation behavior of a Ti-Ni-Hf high temperature shape memory alloy," *Materials Letters*, vol. 55, no. 12, pp. 111 – 115, 2002. 27

[83] Pu, Z and Tseng, H and Wu, K, "Martensite transformation and shape memory effect of NiTi-Zr high temperature shape memory alloys," in *Smart materials: smart structures and materials 1995* (Jardine, AP, ed.), vol. 2441 of *Proceedings of the society of photo-optical instrumentation engineers (SPIE)*, (PO Box 10, Bellingham, WA 98227-0010), pp. 171–178, Soc Photo Opt Instrumentat Engineers; Amer Soc Mech Engineers; Mat Res Soc; Soc Exptl Mech Inc; IEEE, Control Syst Soc; Amer Phys Soc, Div Mat Phys; Ceram Soc Japan; Amer Inst Chem Engineers, SPIE - Int soc opt engieering, 1995. Conference on Smart Materials, San diego, CA, Feb 27-28, 1995. 28, 121

[84] S. Hsieh and S. Wu, "Room-temperature phases observed in $Ti_{53-x}Ni_{47}Zr_x$ high-temperature shape memory alloys," *Journal of Alloys and Compounds*, vol. 266, no. 1–2, pp. 276 – 282, 1998. 28

[85] Beyer, J., "Recent advances in the martensitic transformations of Ti-Ni alloys," *J. Phys. IV France*, vol. 05, pp. C2–433–C2–442, 1995. 28, 108, 109, 117

[86] S. Hsieh and S. Wu, "Martensitic transformation of quaternary $Ti_{50.5-x}Ni_{49.5}Zr_{x/2}Hf_{x/2}$ (x=0–20 at.%) shape memory alloys," *Materials Characterization*, vol. 45, no. 2, pp. 143 – 152, 2000. 28, 29, 114

[87] X. Meng, Y. Zheng, W. Cai, and L. Zhao, "Two-way shape memory effect of a TiNiHf high temperature shape memory alloy," *Journal of Alloys and Compounds*, vol. 372, no. 1-2, pp. 180 – 186, 2004. 28, 29

[88] G. Firstov, J. V. Humbeeck, and Y. Koval, "Comparison of high temperature shape memory behaviour for ZrCu–based, Ti–Ni–Zr and Ti–Ni–Hf alloys," *Scripta Materialia*, vol. 50, no. 2, pp. 243 – 248, 2004. Viewpoint Set No. 33. Shape Memory Alloys. 28

[89] S. Besseghini, E. Villa, and A. Tuissi, "Ni-Ti-Hf shape memory alloy: effect of aging and thermal cycling," *Materials Science and Engineering: A*, vol. 273-275, no. 0, pp. 390 – 394, 1999. 29

[90] X. Meng, Y. Zheng, Z. Wang, and L. Zhao, "Effect of aging on the phase transformation and mechanical behavior of $Ti_{36}Ni_{49}Hf_{15}$ high temperature shape memory alloy," *Scripta Materialia*, vol. 42, no. 4, pp. 341 – 348, 2000. 29

[91] E. Hornbogen, "The effect of variables on martensitic transformation temperatures," *Acta Metallurgica*, vol. 33, no. 4, pp. 595 – 601, 1985. 29, 30, 114

[92] E. Schrödinger, "Quantisierung als Eigenwertproblem," *Ann. Phys.*, vol. 384, no. 4, pp. 361–376, 1926. 32

[93] M. Born and R. Oppenheimer, "Zur quantentheorie der molekeln," *Annalen der Physik*, vol. 389, no. 20, pp. 457–484, 1927. 32

[94] R. G. Parr and W. Yang, *Density-Functional Theory of atoms and molecules*. Oxford science publications, 1989. 33, 34

[95] P. Hohenberg and W. Kohn, "Inhomogeneous electron gas," *Phys. Rev.*, vol. 136, pp. B864–B871, Nov 1964. 35

[96] W. Kohn and L. J. Sham, "Self-consistent equations including exchange and correlation effects," *Phys. Rev.*, vol. 140, pp. A1133–A1138, Nov 1965. 36, 39

[97] U. von Barth and L. Hedin, "A local exchange-correlation potential for the spin polarized case : I," *Journal of Physics C: Solid State Physics*, vol. 5, no. 13, p. 1629, 1972. 39

[98] P. A. M. Dirac, "Note on exchange phenomena in the Thomas atom," *Mathematical Proceedings of the Cambridge Philosophical Society*, vol. 26, no. 03, pp. 376 – 385, 1930. 40

[99] D. M. Ceperley and B. J. Alder, "Ground state of the electron gas by a stochastic method," *Phys. Rev. Lett.*, vol. 45, pp. 566–569, Aug 1980. 40

[100] J. P. Perdew and A. Zunger, "Self-interaction correction to density-functional approximations for many-electron systems," *Phys. Rev. B*, vol. 23, pp. 5048–5079, May 1981. 40

[101] J. P. Perdew, K. Burke, and Y. Wang, "Generalized gradient approximation for the exchange-correlation hole of a many-electron system," *Phys. Rev. B*, vol. 54, pp. 16533–16539, Dec 1996. 40

[102] C. Filippi, C. J. Umrigar, and M. Taut, "Comparison of exact and approximate density functionals for an exactly soluble model," *The Journal of Chemical Physics*, vol. 100, no. 2, pp. 1290–1296, 1994. 40

[103] D. R. Hamann, "Generalized gradient theory for Silica phase transitions," *Phys. Rev. Lett.*, vol. 76, pp. 660–663, Jan 1996. 40

[104] J. P. Perdew, J. A. Chevary, S. H. Vosko, K. A. Jackson, M. R. Pederson, D. J. Singh, and C. Fiolhais, "Atoms, molecules, solids, and surfaces: Applications of the generalized gradient approximation for exchange and correlation," *Phys. Rev. B*, vol. 46, pp. 6671–6687, Sep 1992. 40

[105] J. P. Perdew, K. Burke, and M. Ernzerhof, "Generalized gradient approximation made simple," *Phys. Rev. Lett.*, vol. 77, pp. 3865–3868, Oct 1996. 41

[106] M. C. Payne, M. P. Teter, D. C. Allan, T. A. Arias, and J. D. Joannopoulos, "Iterative minimization techniques for *ab initio* total-energy calculations: molecular dynamics and conjugate gradients," *Rev. Mod. Phys.*, vol. 64, pp. 1045–1097, Oct 1992. 41, 43, 50

[107] C. G. Broyden, "A class of methods for solving nonlinear simultaneous equations," *Math. Comp.*, vol. 19, pp. 577–593, 1965. 42

[108] P. Pulay, "Convergence acceleration of iterative sequences. The case of SCF iteration," *Chemical Physics Letters*, vol. 73, no. 2, pp. 393 – 398, 1980. 42

[109] P. Bendt and A. Zunger, "New approach for solving the density-functional self-consistent-field problem," *Phys. Rev. B*, vol. 26, pp. 3114–3137, Sep 1982. 42

[110] G. Kresse and J. Furthmüller, "Efficient iterative schemes for *ab initio* total-energy calculations using a plane-wave basis set," *Phys. Rev. B*, vol. 54, pp. 11169–11186, Oct 1996. 42, 46

[111] M. T. Yin and M. L. Cohen, "Theory of *ab initio* pseudopotential calculations," *Phys. Rev. B*, vol. 25, pp. 7403–7412, Jun 1982. 43, 44

[112] J. D. Joannopoulos and M. L. Cohen, "Electronic charge densities for ZnS in the wurtzite and zincblende structures," *Journal of Physics C: Solid State Physics*, vol. 6, no. 9, p. 1572, 1973. 43, 44

[113] D. R. Hamann, M. Schlüter, and C. Chiang, "Norm-conserving pseudopotentials," *Phys. Rev. Lett.*, vol. 43, pp. 1494–1497, Nov 1979. 44

[114] J. Ihm, A. Zunger, and M. L. Cohen, "Momentum-space formalism for the total energy of solids," *Journal of Physics C: Solid State Physics*, vol. 12, no. 21, p. 4409, 1979. 44, 51

[115] G. Kresse and D. Joubert, "From ultrasoft pseudopotentials to the projector augmented-wave method," *Phys. Rev. B*, vol. 59, pp. 1758–1775, Jan 1999. 44

[116] O. K. Andersen, "Linear methods in band theory," *Phys. Rev. B*, vol. 12, pp. 3060–3083, Oct 1975. 44

[117] M. Methfessel, "Elastic constants and phonon frequencies of Si calculated by a fast full-potential linear-muffin-tin-orbital method," *Phys. Rev. B*, vol. 38, pp. 1537–1540, Jul 1988. 44

[118] M. Methfessel, C. O. Rodriguez, and O. K. Andersen, "Fast full-potential calculations with a converged basis of atom-centered linear muffin-tin orbitals: Structural and dynamic properties of Silicon," *Phys. Rev. B*, vol. 40, pp. 2009–2012, Jul 1989. 44

[119] P. Blöchl, C. Först, and J. Schimpl, "Projector augmented wave method: *ab initio* molecular dynamics with full wave functions," *Bulletin of Materials Science*, vol. 26, pp. 33–41, 2003. 10.1007/BF02712785. 44

[120] P. E. Blöchl, "Projector augmented-wave method," *Phys. Rev. B*, vol. 50, pp. 17953–17979, Dec 1994. 44, 45, 46, 47

[121] P. Giannozzi, S. Baroni, N. Bonini, M. Calandra, R. Car, C. Cavazzoni, D. Ceresoli, G. L. Chiarotti, M. Cococcioni, I. Dabo, A. D. Corso, S. de Gironcoli, S. Fabris, G. Fratesi, R. Gebauer, U. Gerstmann, C. Gougoussis, A. Kokalj, M. Lazzeri, L. Martin-Samos, N. Marzari, F. Mauri, R. Mazzarello, S. Paolini, A. Pasquarello, L. Paulatto, C. Sbraccia, S. Scandolo, G. Sclauzero, A. P. Seitsonen, A. Smogunov, P. Umari, and R. M. Wentzcovitch, "Quantum espresso: a modular and open-source

software project for quantum simulations of materials," *Journal of Physics: Condensed Matter*, vol. 21, no. 39, p. 395502 (19pp), 2009. 46

[122] N. Holzwarth, A. Tackett, and G. Matthews, "A projector augmented wave (PAW) code for electronic structure calculations, part I: atompaw for generating atom-centered functions," *Computer Physics Communications*, vol. 135, no. 3, pp. 329 – 347, 2001. 47

[123] F. Bloch, "Über die quantenmechanik der elektronen in kristallgittern," *Zeitschrift fr Physik A Hadrons and Nuclei*, vol. 52, pp. 555–600, 1929. 10.1007/BF01339455. 47

[124] N. W. Ashcroft and D. N. Mermin, *Solid State Physics*. Toronto: Thomson Learning, 1 ed., Jan. 1976. 47

[125] A. A. Maradudin and S. H. Vosko, "Symmetry properties of the normal vibrations of a crystal," *Rev. Mod. Phys.*, vol. 40, pp. 1–37, Jan 1968. 47, 53, 130, 131

[126] D. J. Chadi and M. L. Cohen, "Special points in the Brillouin zone," *Phys. Rev. B*, vol. 8, pp. 5747–5753, Dec 1973. 50

[127] H. J. Monkhorst and J. D. Pack, "Special points for Brillouin-zone integrations," *Phys. Rev. B*, vol. 13, pp. 5188–5192, Jun 1976. 50

[128] H. Hellmann, *Einführung in die quantenchemie*. Leipzig und Wien: F. Deuticke, 1937. 51

[129] R. P. Feynman, "Forces in molecules," *Phys. Rev.*, vol. 56, pp. 340–343, Aug 1939. 51

[130] M. T. Dove, *Introduction to Lattice Dynamics*. Cambridge University Press, 1993. 52, 59, 69, 92, 93

[131] M. Born and K. Huang, *Dynamical Theory of Crystal Lattices*. Clarendon Press, Oxford, 1996. 52, 53, 54, 55, 57, 58, 59, 60, 61, 68, 125

[132] D. Alfè, G. D. Price, and M. J. Gillan, "Thermodynamics of hexagonal-close-packed Iron under earth's core conditions," *Phys. Rev. B*, vol. 64, p. 045123, Jul 2001. 54

[133] W. Frank, C. Elsässer, and M. Fähnle, "Ab initio force-constant method for phonon dispersions in alkali metals," *Phys. Rev. Lett.*, vol. 74, pp. 1791–1794, Mar 1995. 54

[134] G. Kresse, J. Furthmüller, and J. Hafner, "Ab initio force constant approach to phonon dispersion relations of diamond and graphite," *EPL (Europhysics Letters)*, vol. 32, no. 9, p. 729, 1995. 54

[135] D. Alfè, "Phon: A program to calculate phonons using the small displacement method," *Computer Physics Communications*, vol. 180, no. 12, pp. 2622 – 2633, 2009. 40 YEARS OF CPC: A celebratory issue focused on quality software for high performance, grid and novel computing architectures. 54, 55, 58, 59

[136] G. J. Ackland, M. C. Warren, and S. J. Clark, "Practical methods in ab initio lattice dynamics," *Journal of Physics: Condensed Matter*, vol. 9, no. 37, p. 7861, 1997. 54, 55

[137] K. Kunc and P. G. Dacosta, "Real-space convergence of the force series in the lattice dynamics of Germanium," *Phys. Rev. B*, vol. 32, pp. 2010–2021, Aug 1985. 55

[138] K. Parlinski, Z. Q. Li, and Y. Kawazoe, "First-principles determination of the soft mode in cubic ZrO_2," *Phys. Rev. Lett.*, vol. 78, pp. 4063–4066, May 1997. 56

[139] S. Baroni, P. Giannozzi, and E. Isaev, "Density-functional perturbation theory for quasi-harmonic calculations," *Reviews in Mineralogy and Geochemistry*, vol. 71, no. 1, pp. 39–57, 2010. 58, 96

[140] D. C. Wallace, *Thermodynamics of Crystals*. Dover Pubns, Jan. 1998. 58

[141] P. Carrier, R. Wentzcovitch, and J. Tsuchiya, "First-principles prediction of crystal structures at high temperatures using the quasiharmonic approximation," *Phys. Rev. B*, vol. 76, p. 064116, Aug 2007. 59

[142] S. Narasimhan and S. de Gironcoli, "*Ab initio* calculation of the thermal properties of Cu: Performance of the LDA and GGA," *Phys. Rev. B*, vol. 65, p. 064302, Jan 2002. 59

[143] A. Togo, F. Oba, and I. Tanaka, "First-principles calculations of the ferroelastic transition between rutile-type and $CaCl_2$ -type SiO_2 at high pressures," *Phys. Rev. B*, vol. 78, p. 134106, Oct 2008. 59

[144] C. Kittel, *Introduction to Solid State Physics*, vol. 2011. John Wiley & Sons, Inc., 1995. 59

[145] J. de Launay, "Lattice dynamics of body-centered and face-centered cubic metallic elements," *The Journal of Chemical Physics*, vol. 21, no. 11, pp. 1975–1986, 1953. 59

[146] Y. Murakami, "Lattice softening, phase stability and elastic anomaly of the β-Au-Cu-Zn alloys," *Journal of the Physical Society of Japan*, vol. 33, no. 5, pp. 1350–1360, 1972. 59

[147] M. Aroyo and H. Wondratschek, "Crystallographic viewpoints in the classification of space-group representations," in *International Tables for Crystallography Volume B: Reciprocal space* (U. Shmueli, ed.), vol. B of *International Tables for Crystallography*, pp. 162–188, Springer Netherlands, 2006. 62

[148] M. Tinkham, *Group Theory and Quantum Mechanics*. Dover Publications, Dec. 2003. 63, 64, 130

[149] H. T. Stokes, E. H. Kisi, D. M. Hatch, and C. J. Howard, "Group-theoretical analysis of octahedral tilting in ferroelectric perovskites," *Acta Crystallographica Section B*, vol. 58, no. 6, pp. 934–938, 2002. 65

[150] C. J. Howard and H. T. Stokes, "Group-theoretical analysis of octahedral tilting in perovskites," *Acta Crystallographica Section B*, vol. 54, no. 6, pp. 782–789, 1998. 65

[151] H. Wondratschek, "General introduction to the subgroups of space groups," in *International Tables for Crystallography Volume A1: Symmetry relations between space groups* (H. Wondratschek, U. Müller, H. Fuess, T. Hahn, , U. Shmueli, E. Prince, A. Authier, V. Kopský, D. Litvin, M. Rossmann, E. Arnold, S. Hall, and B. McMahon, eds.), vol. A1 of *International Tables for Crystallography*, pp. 6–23, Springer Netherlands, 2004. 10.1107/97809553602060000538. 66

[152] P. Souvatzis and S. P. Rudin, "Dynamical stabilization of cubic ZrO_2 by phonon-phonon interactions: Ab initio calculations," *Phys. Rev. B*, vol. 78, p. 184304, Nov 2008. 66, 70

[153] P. Souvatzis, O. Eriksson, M. Katsnelson, and S. Rudin, "The self-consistent ab initio lattice dynamical method," *Computational Materials Science*, vol. 44, no. 3, pp. 888 – 894, 2009. 66, 70

[154] P. Souvatzis, *Electronic Structure and Lattice Dynamics of Elements and Compounds*. PhD thesis, Uppsala University, Department of Physics, 2007. 69, 70

[155] M. Finnis, *Interatomic forces in condensed matter*. Oxford University Press, USA, 2003. 71, 72

[156] S. Baroni, S. de Gironcoli, A. Dal Corso, and P. Giannozzi, "Phonons and related crystal properties from density-functional perturbation theory," *Rev. Mod. Phys.*, vol. 73, pp. 515–562, Jul 2001. 75, 96

[157] M. I. Aroyo, A. Kirov, C. Capillas, J. M. Perez-Mato, and H. Wondratschek, "Bilbao Crystallographic Server. II. Representations of crystallographic point groups and space groups," *Acta Crystallographica Section A*, vol. 62, pp. 115–128, Mar 2006. 99, 102, 131, 132

[158] X.-Q. Wang, "Twinned structure for shape memory: First-principles calculations," *Phys. Rev. B*, vol. 78, p. 092103, Sep 2008. 77

[159] G. Lehmann and M. Taut, "On the numerical calculation of the density of states and related properties," *physica status solidi (b)*, vol. 54, no. 2, pp. 469–477, 1972. 79

[160] T. Fukuda, T. Kakeshita, H. Houjoh, S. Shiraishi, and T. Saburi, "Electronic structure and stability of intermetallic compounds in the Ti-Ni system," *Materials Science and Engineering: A*, vol. 273-275, no. 0, pp. 166 – 169, 1999. 79

[161] Y. Y. Ye, C. T. Chan, and K. M. Ho, "Structural and electronic properties of the martensitic alloys TiNi, TiPd, and TiPt," *Phys. Rev. B*, vol. 56, pp. 3678–3689, Aug 1997. 79

[162] A. E. Carlsson and P. J. Meschter, "Relative stability of $L1_2$, DO_{22}, and DO_{23} structures in MAl_3 compounds," *Journal of Materials Research*, vol. 4, pp. 1060–1063, Sept. 1989. 79

[163] N. Hatcher, O. Y. Kontsevoi, and A. J. Freeman, "Martensitic transformation path of NiTi," *Phys. Rev. B*, vol. 79, p. 020202, Jan 2009. 82

[164] B. Fultz, "Vibrational thermodynamics of materials," *Progress in Materials Science*, vol. 55, no. 4, pp. 247 – 352, 2010. 85

[165] W. Cai, C. Tan, T. Shen, and X. Tian, "First-principles study on alloying effect on martensitic transformation behavior of TiNi alloy," *Journal of Alloys and Compounds*, vol. 438, no. 1-2, pp. 30 – 33, 2007. 85

[166] M. W. Finnis and V. Heine, "A simple theory of some phase transitions," *Journal of Physics F: Metal Physics*, vol. 4, no. 7, p. 960, 1974. 88

[167] G. M. Michal and R. Sinclair, "The structure of TiNi martensite," *Acta Crystallographica Section B*, vol. 37, pp. 1803–1807, Oct 1981. 91

[168] Z. Lekston, V. E. Naish, T. V. Novoselova, and I. V. Sagaradze, "Structure of the alloy $Ti_{50}Ni_{48.7}Co_{1.3}$," *Acta Crystallographica Section A*, vol. 55, no. 5, pp. 803–810, 1999. 94

[169] J. Uchil, K. Mohanchandra, K. G. Kumara, K. Mahesh, and T. P. Murali, "Thermal expansion in various phases of Nitinol using TMA," *Physica B: Condensed Matter*, vol. 270, no. 34, pp. 289 – 297, 1999. 98

[170] P. Souvatzis, "The self-consistent ab initio lattice dynamics method." http://www.anst.uu.se/pesou087/UU-SITE/Webbplats_2/SCAILD.html, 2002. 103

[171] S. Hsieh and S. Wu, "Lattice parameters of martensite in $Ti_{50.5x}Ni_{49.5}Zr_{x/2}Hf_{x/2}$ quaternary shape memory alloys," *Journal of Alloys and Compounds*, vol. 312, no. 12, pp. 288 – 294, 2000. 109

[172] D. Góra and K. Parlinski, "Ab initio calculation of $Ni_{50-x}Fe_xTi_{50}$," *Journal of Physics and Chemistry of Solids*, vol. 66, no. 10, pp. 1748 – 1754, 2005. 118

[173] A. Alam, S. Ghosh, and A. Mookerjee, "Phonons in disordered alloys: Comparison between augmented-space-based approximations for configuration averaging to integration from first principles," *Phys. Rev. B*, vol. 75, pp. 134202–1–11, 2007. 122

[174] K. Bhattacharya, *Microstructure of Martensite: Why It Forms and How It Gives Rise to the Shape-Memory Effect*. Oxford Series on Materials Modelling, Oxford University Press, USA, 2004. 126

[175] G. J. Ackland, A. Jones, and R. Noble-Eddy, "Molecular dynamics simulations of the martensitic phase transition process," *Materials Science and Engineering: A*, vol. 481–482, pp. 11 – 17, 2008. Proceedings of the 7th European Symposium on Martensitic Transformations, ESOMAT 2006. 126

[176] A. P. Bartók, M. C. Payne, R. Kondor, and G. Csányi, "Gaussian approximation potentials: The accuracy of quantum mechanics, without the electrons," *Phys. Rev. Lett.*, vol. 104, p. 136403, Apr 2010. 126

[177] A. P. Bartók, *Gaussian approximation potential : an interatomic potential derived from first principles quantum mechanics*. PhD thesis, Cavendish laboratory, University of Cambridge, November 2009. 127

[178] G. Csányi, T. Albaret, M. C. Payne, and A. De Vita, ""learn on the fly": A hybrid classical and quantum-mechanical molecular dynamics simulation," *Phys. Rev. Lett.*, vol. 93, p. 175503, Oct 2004. 127

[179] B. Rousseau and A. Bergara, "Giant anharmonicity suppresses superconductivity in AlH_3 under pressure," *Phys. Rev. B*, vol. 82, p. 104504, Sep 2010. 127, 128

[180] T. R. Koehler, "Theory of the self-consistent harmonic approximation with application to solid Neon," *Phys. Rev. Lett.*, vol. 17, pp. 89–91, Jul 1966. 127

[181] I. Errea, B. Rousseau, and A. Bergara, "Anharmonic stabilization of the high-pressure simple cubic phase of Calcium," *Phys. Rev. Lett.*, vol. 106, p. 165501, Apr 2011. 128

[182] I. Errea, *Pressure induced complexity in simple elements and alloys from first-principles calculations*. PhD thesis, University of the Basque Country, Department of Condensed Matter Physics, October 2011. 128

[183] B. Grabowski, T. Hickel, and J. Neugebauer, "Formation energies of point defects at finite temperatures," *physica status solidi (b)*, vol. 248, no. 6, pp. 1295–1308, 2011. 129

[184] M. S. Dresselhaus, "Applications of group theory to the physics of solids." stuff.mit.edu/afs/athena/course/6/6.734j/www/group-full02.pdf, 2002. 130

[185] O. V. Kovalev, *Irreducible Representations of the Space Groups*. Academy of Sciences of the Ukrainian SSR, Kiev, 1961. 131

[186] S. L. Altmann and A. P. Cracknell, "Lattice harmonics I. cubic groups," *Rev. Mod. Phys.*, vol. 37, pp. 19–32, Jan 1965. 132

[187] V. Heine, *Group theory in quantum mechanics : an introduction to its present usage*. Pergamon Press, Oxford ; Sydney :, 1977. 136

[188] C. J. Howard and H. T. Stokes, "Structures and phase transitions in perovskites – a group-theoretical approach," *Acta Crystallographica Section A*, vol. 61, no. 1, pp. 93–111, 2005. 136

[189] J. Nye, *Physical properties of crystals : their representation by tensors and matrices*. Oxford University Press, 2004. 138